# DEVELOPMENT OF PEPTIDE-BASED METHODS FOR CONTROLLING THE STRUCTURES, COMPOSITIONS, AND PROPERTIES OF COMPLEX NANOPARTICLE SUPERSTRUCTURES

By

**Chengyi Song**

B.S., Fudan University, 2008

Submitted to the Graduate Faculty of

the Kenneth P. Dietrich School of Arts and Sciences

in partial fulfillment

of the requirements for the degree of

Doctor of Philosophy

University of Pittsburgh

2013

UNIVERSITY OF PITTSBURGH

KENNETH P. DIETRICH SCHOOL OF ARTS AND SCIENCES

This dissertation was presented

by

Chengyi Song

It was defended on

August 8th, 2013

and approved by

Tara Y. Meyer, PhD, Associate Professor, Department of Chemistry

Alexander Star, PhD, Associate Professor, Department of Chemistry

Peijun Zhang, PhD, Associate Professor, Department of Structural Biology

Dissertation Advisor: Nathaniel L. Rosi, PhD, Associate Professor, Department of Chemistry

Prof. Nathaniel L. Rosi

**DEVELOPMENT OF PEPTIDE-BASED METHODS FOR CONTROLLING THE STRUCTURES, COMPOSITIONS, AND PROPERTIES OF COMPLEX NANOPARTICLE SUPERSTRUCTURES**

Chengyi Song, PhD

University of Pittsburgh, 2013

This dissertation describes the development of a nanoparticle assembly methodology based on the use of peptide conjugate molecules. The aim of this research was to explore how this methodology could be used to control the structure, metrics, and properties of product nanoparticle superstructures.

Specifically, this document describes mechanistic studies aimed at understanding the key factors that govern the nanoparticle synthesis and assembly process. Using what we learned from these studies, we prepared high-quality helical nanoparticle superstructures and studied their chirooptical properties. We coupled theory and experiment to show how tuning the metrics and structure of the helices results in predictable and tailorable circular dichroism (CD) properties. We also describe how the composition of the peptide conjugate can influence both the structure of the nanoparticle assembly and detail how peptide conjugates can be utilized to prepare 'hollow' sub-100nm gold nanoparticle spheres. Finally, to expand the composition scope of the methodology, we present a new cobalt-binding peptide conjugate, which could be used to direct the synthesis and assembly of hollow CoPt nanospherical superstructures exhibiting electrocatalytic activity for methanol oxidation.

**TABLE OF CONTENTS**

**LIST OF FIGURES**

## First Chapter

## Second Chapter

## Third Chapter

## Fourth Chapter

## Fifth Chapter

## Appendix

**LIST OF SCHEMES**

## First Chapter



## Second Chapter



## Third Chapter

## Fourth Chapter



## Fifth Chapter

**PREFACE**

## Acknowledgements

I would like to particularly thank my research advisor and mentor, Prof. Nathaniel L. Rosi or "the boss" for taking me on and being a great supervisor who has encouraged and guided me through my graduate student life. Honestly, Dr. Rosi is a perfectionist. His passion for perfection prompted us to pursue high quality results and publication. His perfectionism makes us realize that scientific research is a rather serious business and we have pay 120% attention to what we are doing. It is fair to say I wouldn't have achieved a tenth of the publications that I have without his guidance and strictness.

I would also like to thank the esteemed Dr. Chun-long Chen for all his help and getting me started in the lab before he moved to Lawrence National Laboratory. Also, I would like to thank Dr. Leekyoung Hwang as well for helping me as I was a young graduate student and collaborating with me on the research projects. Thanks Tao Li, Chen Zhang, Chong Liu, Ryan Ruenroeng and Andre Merg for being great colleagues.

I would like to thank Prof. Peijun Zhang and her posdocs (past and present): Dr. Gongpu Zhao and Dr. Haiying Huang for analyzing my nanoparticle superstructures and peptide soft assembly!

I would like to thank Prof. George C. Schatz and his posdocs (past and present): Dr. Martin G. Blaber and Dr. Yong Zhao for simulating circular dichroism of gold nanoparticle double helices and UV-Vis of nanospherical nanoparticle superstructures.

I also need to thank all the scientists who have worked with me and/or helped to analyse my samples: Dr. Susheng Tan for the High Resolution TEM and STEM; Dr. Cole M. Van Ormer for the regular TEM; Dr. Joel Gillespie for AFM measurements; Prof. David H. Waldeck and his student Yang Wang for the electrocatalysis measurements; Tao Li for the powder XRD diffraction; Prof. W. Seth Horne for circular dichroism measurements; Dr. H. Christopher Fry for the peptide synthesis.

Lastly I would also like to thank all my family, Mom, Dad, Grandpa and Grandma for understanding my wishes to be a graduate student and keeping me in good supply of spirits and chat! I can say that I will not become a qualified PhD without their support.

Thanks!

# 1.0 INTRODUCTION

## 1.1 METALLIC NANOPARTICLES

Metallic nanoparticles exhibit unique size, shape and composition dependent properties. For example, Faraday[1] observed the red color of colloidal gold particles which is strikingly different compared to the yellow color of bulk gold. Now, synthetic methods exist to control the optical properties of colloidal solutions by controlling the size, shape, and composition of their constituent particles. Nanoscale characterization tools such as AFM and TEM allow for careful study of nanoparticles' size, dimensions, and crystalline nature. The unique properties of metallic nanoparticles are often a result of their surface-to-volume ratio. Because nano-objects have a size that is intermediate between atoms and bulk matter, a cluster comprising 1000 atoms has more than one-quarter of its atoms lying on the surface. This can result in unique optical and catalytic properties.[2,3]

## 1.2 ASSEMBLIES OF METALLIC NANOPARTICLES AND THEIR PROPERTIES

New collective physical properties emerge when nanoparticles are assembled together into superstructures,[4,5] which is due to the strong interactions between the excitons,[6,7] magnetic moments,[8,9] and surface plasmons of individual nanoparticles.[10-12] These collective properties depend not only on the size, shape,[13,14] and compositions[2,10] of the particles but also on the

arrangement of particles and interparticle distances within the assembly. In order to control these collective properties, one must be able to precisely control nanoparticle assembly. Herein, we will mainly review optical and catalytic properties and potential applications of self-assembled structures of nanoparticles and show that the ability to precisely control the assembly of nanoparticles is significantly important to tune the optical properties of assemblies.

### 1.2.1 Optical properties of metallic nanoparticle assemblies

Surface Plasmon resonance (SPR) is known as resonance of the incident light frequency with the coherent oscillation of the conduction band electrons induced by the applied electromagnetic field. This effect only occurs when the size of particles is very small (nanoscale) (**Figure 1.1a**).[3] Noble metal nanoparticles such as Au have strong absorbance around 520 nm which corresponds to the plasmon frequency of gold nanoparticles (diameter ~ 9 nm).[3]

When single plasmonic nanoparticles assemble and form nanoparticle superstructures, the SPR absorbance band red-shifts due to the strong dipole-dipole interaction between two adjacent metallic nanoparticles.[15] **Figure 1.1b** shows that the absorbance peak dramatically red-shifts when gold nanoparticles aggregate[16] and the solution color changes from red to purple. The surface plasmon phenomenon of noble metals is useful in detecting trace amounts of chemicals and biomolecules.[17,18]

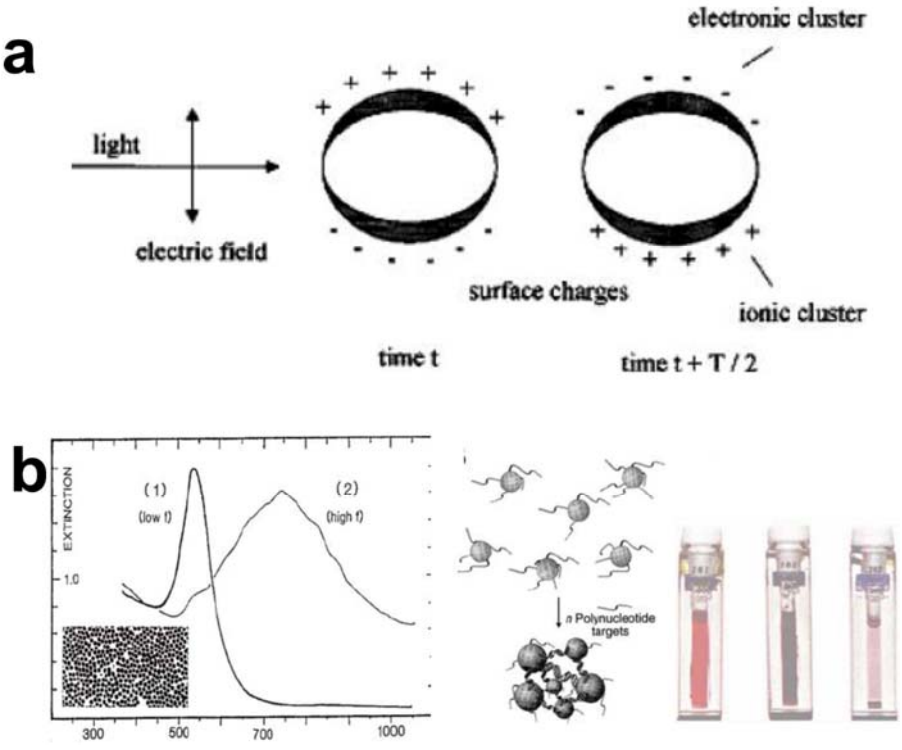


**Figure 1.1**. (a) schematic presentation of surface plasmon generated in metallic nanoparticles owing to the interaction of applied electromagnetic radiation (Adapted from ref.3); (b) optical spectra of a sparse Au nanoparticle and a dense Au nanoparticle film (Adapted from ref.17); schematic presentation of oligonucleotide-induced aggregation of oligonucleotide-functionalized gold nanoparticles (Adapted from ref.19) and pictures of dispersed colloid, linked colloid and fully aggregated nanoparticles (Adapted from ref.18).

2D and 3D gold nanoparticle assemblies are broadly useful in surface plasmon resonance sensor devices[2,19] and photothermal therapy.[20] **Figure 1.2** is a typical nanoparticle colorimetric DNA sensor based on a 2D monolayer of two different sets of DNA-modified gold nanoparticles at an equal ratio which were absorbed on a lipid layer.[19] Owing to the 2D fluidity of the lipid layer, the gold nanopaticles were allowed to migrate across the surface. The DNA-modified gold nanoparticles were able to recognize targets containing complementary DNA sequences, which lead to particle cross-linking events (**Figure 1.2b**). Cross-linked gold nanoparticles exhibited detectable localized surface plasmon resonance effect, resulting in a red-shift of the absorption peak.

Nie et al. recently reported a photothermal therapy experiment using a 4T1 tumor xenograft model.[20] A dose of gold nanoparticle vesicular assemblies (**Figure 1.3a,b**) was injected into a mice bearing 4T1 tumor; thereafter, the mouse was exposed to a 808 nm laser. After NIR irradiation, the temperature of tumors treated with vesicular assemblies dramatically increased and tumor growth was inhibited, leaving black scars at the tumor sites (**Figure 1.3c,d**).

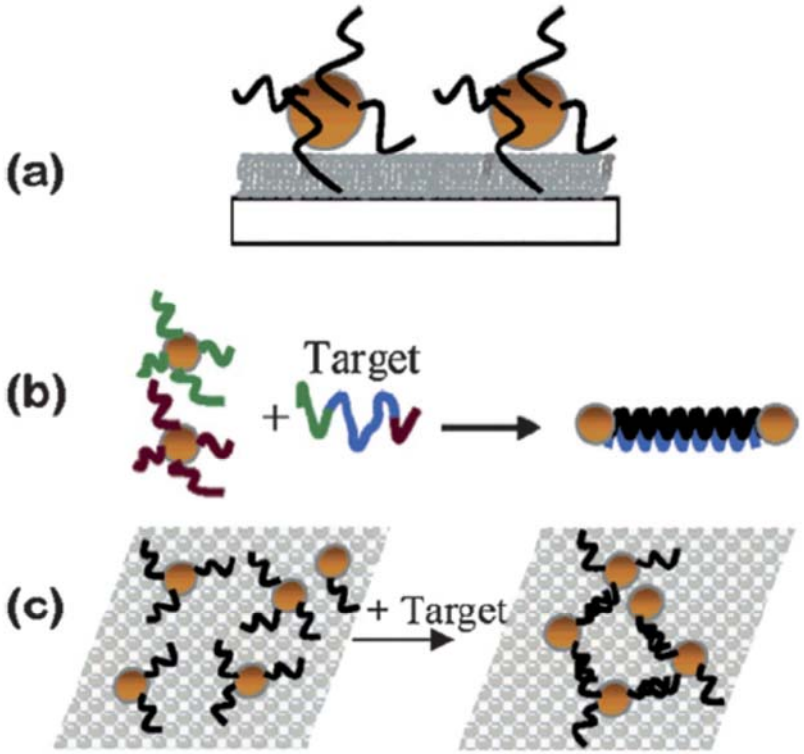


**Figure 1.2**. (a) Scheme of the detection device. (b) NPs assembling via DNA hybridization. (c) Top view of the system before and after hybridization (Adapted from ref.19).

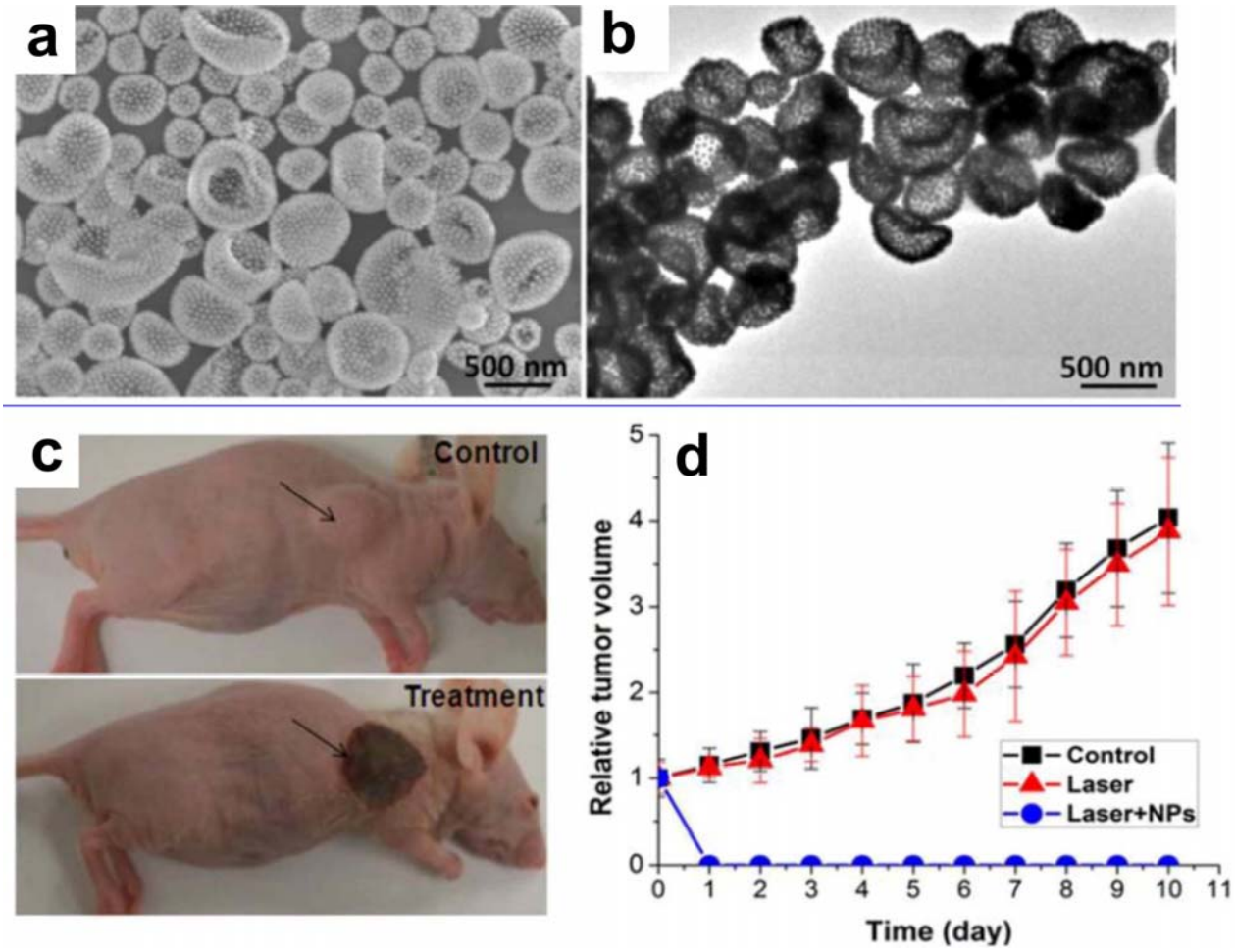


**Figure 1.3**. (a) SEM image of gold nanoparticle vesicular assemblies. (b) TEM image of gold nanoparticle vesicular assemblies. (c) Mice were treated with and without gold nanoparticle vesicles under laser irradiation. (d) The tumor growth curves of different groups of mice after treatment (Adapted from ref. 20).

Circular dichroism (CD) means the differential absorption of left- and right-handed circularly polarized light when shedding circularly polarized light on chirooptically active molecules.[21-23] Naturally occurring chiral molecules such as proteins usually exhibit different secondary structures (i.e. alpha helix, beta sheets and random coil). CD is frequently used to test their chirality and determine their secondary structures and their folding properties due to the distinctive UV CD signatures of these biomoleucles.[22]

Recently, it has been found that chiral plasmonic nanostructures can exhibit CD response in the near UV, visible and ultra infrared region.[24-26] **Figure 1.4** shows that a chiral arrangement of gold nanoparticles should exhibit well-defined circular dichroism spectra at visible wavelength due to the collective plasmon-plasmon interaction between nanoparticles.[25,26] The spectra of left- and right-handed gold nanostructures were vertically dip-peak mirrored. It has been experimentally and theoretically proven that tuning and tailoring the structural metrics of chiral nanostructures should dramatically influence the intensity and position of CD signals.

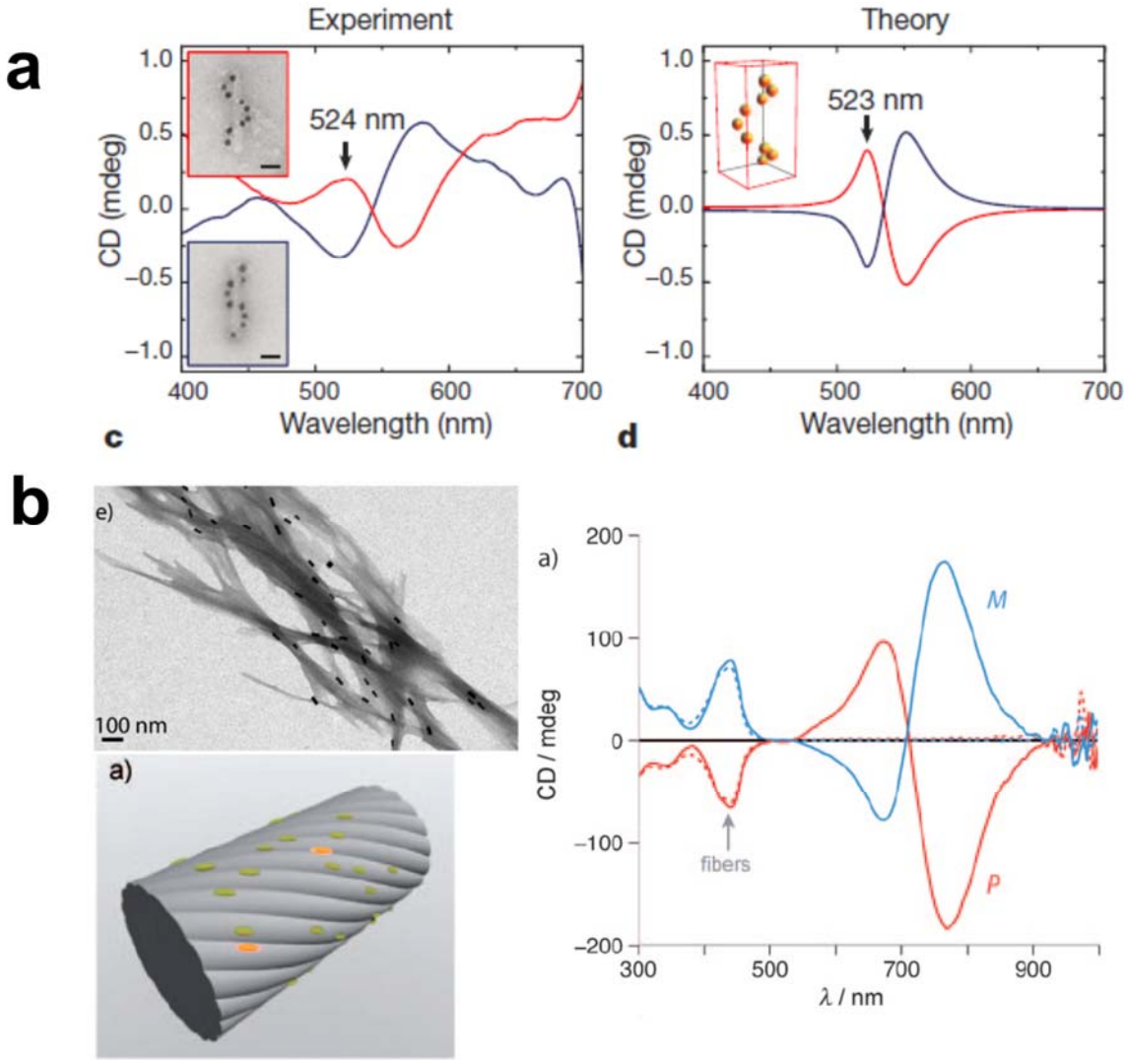


**Figure 1.4**. Chirooptical properties of plasmonic nanostructures: (a) TEM images of left-(blue) and right-(red) gold nanohelices composed of 9 gold nanoparticles each pitch. Experimental and theoretical CD spectra showed vertically mirrored CD peaks (Adapted from ref.25); (b) TEM image of twisted fibers with adsorbed nanorods and CD spectra of left- and right-handed nanocomposites (Adapted from ref.26).

### 1.2.2 Catalytic properties of metallic nanoparticle assemblies

Pd, Pt and Ru nanoparticles are widely used for organic reaction catalysis.[27,28] Among these nanoparticle catalysts, Pt has been reported as a catalyst for methanol oxidation in the direct methanol fuel cell (DMFC).[29-31] Bai and coworkers presented an approach to prepare hollow Pt nanospheres and studied their electrocatalytic activity for the oxidation of methanol.[31] **Figure 1.5** reveals that hollow Pt nanospheres exhibited enhanced catalytic activity compared to the solid Pt nanospheres with similar size. They attributed the remarkable high oxidation current for hollow sphere catalysts to their higher surface area (i.e. the sum of interior and exterior surface area).

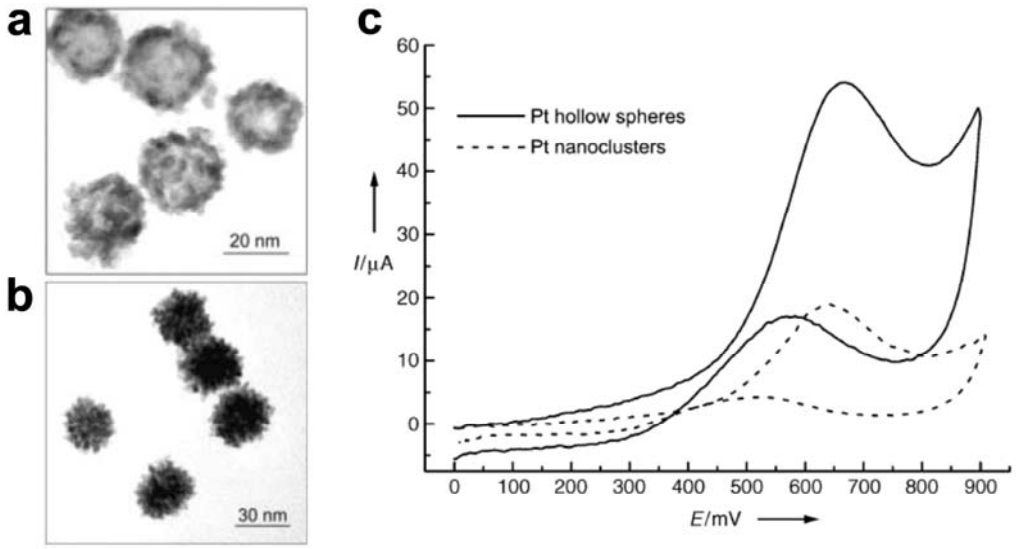


**Figure 1.5**. (a) TEM image of hollow Pt nanospheres; (b) TEM image of solid Pt nanoclusters; (c) Cyclic voltammograms of Pt solid nanoclusters and hollow nanospheres on a glass carbon disk electrode in $H_2SO_4$ and methanol. Scan rate=50 $mVs^{-1}$ (Adapted from ref.31).

.

## 1.3 WELL-ESTABLISHED NANOPARTICLE ASSEMBLY METHODS

A practical nanoparticle-assembly methodology should meet the following criteria: 1) it should have few synthetic steps, which would save synthetic materials and time and reduce the synthetic cost; 2) it should allow for the construction of topologically complex multidimensional nanoparticle superstructures; 3) it should allow for the synthesis and assembly of nanoparticle superstructures with various inorganic composition; and 4) it should allow one to control the superstructure metrics (i.e. nanoparticle size, nanoparticle shape, interparticle distances, and superstructure diameter). My research is focused on developing new methods for precisely controlling the assembly of nanoparticles into nanoparticle superstructures. In the following section, I will detail existing nanoparticle assembly methods and discuss some of their limitations.

## 1.4 SOLUTION-BASED METHODS FOR ASSEMBLING NANOPARTICLES

Inorganic nanoparticle assemblies are mainly prepared using either of the two following strategies: the "top-down" approach[32,33] or the "bottom-up" approach.[34-37] Top-down strategies reduce bulk materials into nanoscale objects. To date, several excellent top–down approaches including photolithography,[38] electron-beam lithography, thin film technologies, and molecular bean epitaxy, have been used to produce nanostructures. The typical approach to top-down assembly is photolithography, which is used in modern semiconductor manufacturing, while the other methods, including electron beam lithography (e-beam lithography), are better suited to research labs. Top-down processes can offer precise size and shape control, but they are generally useful only for constructing 2-D superstructures and they can be costly. The bottom-up approach is based on getting chemical components to assemble into desired multidimensional

nanostructures, much like biological assembly processes. Self-assembly in solution is controlled by the balance of attractive forces (such as covalent or hydrogen bonding, electrostatic attraction between oppositely charged molecules, or dipole-dipole interactions) and repulsive forces (such as steric forces and electrostatic repulsion between molecules of like charge).[39] In this chapter, I will focus on bottom-up strategies for assembling nanoparticles into superstructures in solution.

### 1.4.1 Assembly at interfaces

The assembly of nanoparticles at interfaces is achieved by the Langmuir-Blodgett technique,[40-42] evaporation induced self-assembly,[43-45] and the adsorption of nanoparticles on surfaces.[46] The interface interaction usually is liquid to liquid, liquid to air, or liquid to solid. **Scheme 1.1** shows a typical Langmuir-Blodgett technique.[40] Nanoparticles are deposited from the surface of a liquid onto a solid by immersing the solid substrate into the liquid to form one or more monolayers. **Figure 1.6** shows several examples of close-packed Langmuir-Blodgett monolayers of nanocrystals and nanowires. A water-filled Langmuir-Blodgett (**Scheme 1.1**) is used to form nanoparticle monolayers (**Figure 1.6**) at the water-air interface.

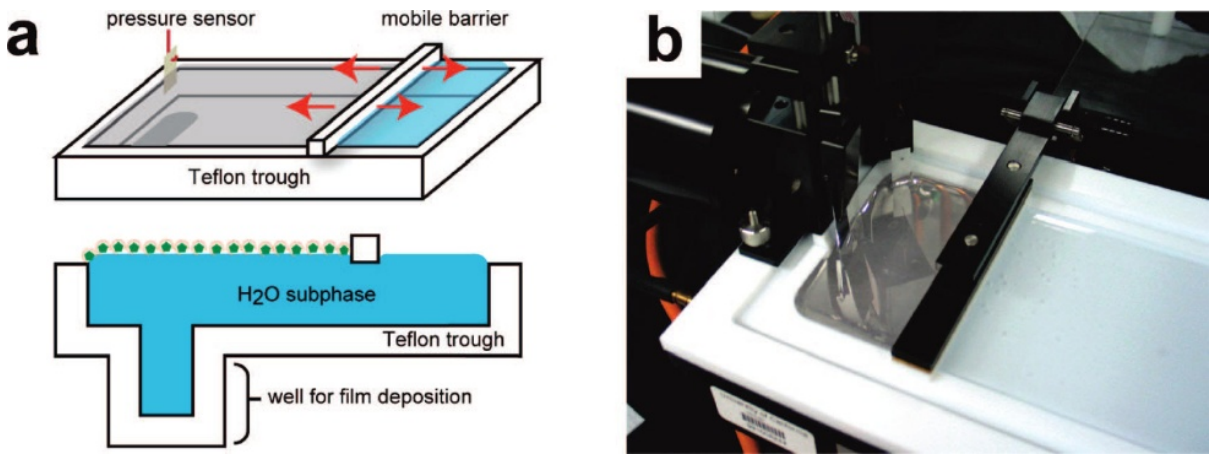


**Scheme 1.1**. Langmuir-Blodgett trough: (a) schematic of a water-filled Langmuir-Blodgett trough from the top and side views; (b) image of a substrate being pulled vertically through a Langmuir monolayer of silver nanowires. The speed of both the dip-coater and the mobile barrier are mechanically (Adapted from ref.40).

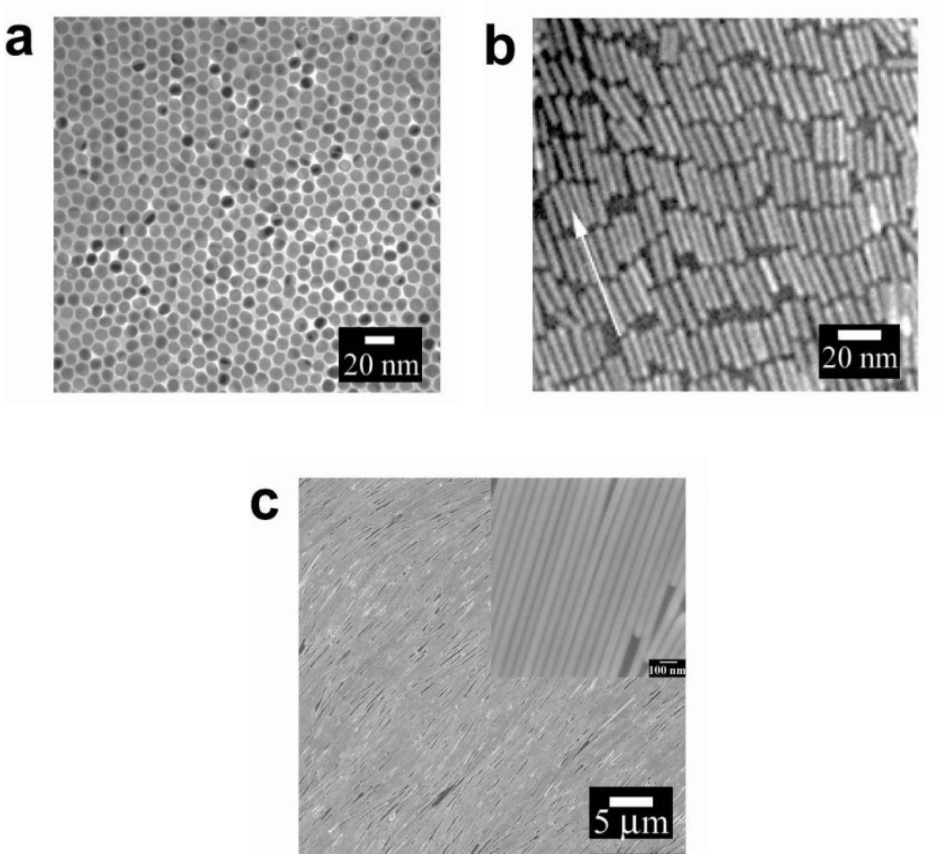


**Figure 1.6**. Selected examples of close-packed Langmuir-Blodgett monolayers of nanocrystals and nanowires: (a) Pt nanocrystal arrays used as 2D model catalysts; (b) $BaCrO_4$ nanorods arranged into liquid crystalline patterns; (c) densely packed Ag nanowire arrays for molecular sensing using surface-enhanced Raman spectroscopy. (The inset shows an area of close-packed nanowires.) (Adapted from ref.40).

### 1.4.2 Assembly via colloidal crystalization

Colloidal crystallization can provide a general and low-cost method to assemble nanoparticles of two different materials into a binary nanoparticle superlattice with precisely controlled chemical composition and spatial arrangement of nanoparticles. The formation of nanoparticle superlattice in colloidal solutions is driven by solvent evaporation,[43] electrostatic interactions[47] or DNA base paring.[48,49] **Figure 1.7** shows different types of binary superlattices self-assembled from different nanoparticles and their molded unit cell.[43] These binary assemblies were formed upon evaporation of solvent.

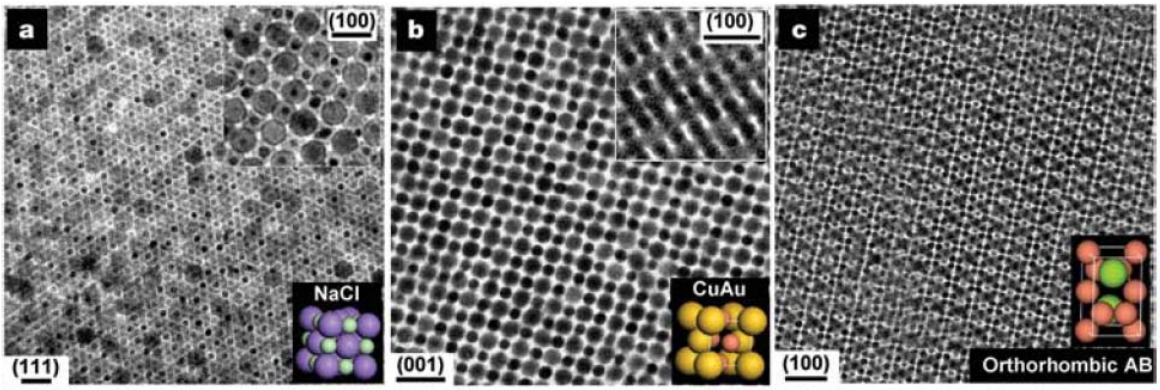


**Figure 1.7**. TEM images of the characteristic projections of the binary superlattices, self-assembled from different nanoparticles and modeled unit cells of the corresponding three-dimensional structures. The superlattices are assembled from a, 13.4 nm g-$Fe_2O_3$ and 5.0 nm Au; b, 7.6 nm PbSe and 5.0 nm Au; c, 6.2 nm PbSe and 3.0 nm Pd (Adapted from ref.43).

### 1.4.3 Template-based assembly

Interactions between a template and nanoparticles lead to the arrangement of nanoparticles into structures that are prearranged by the shape of the template. In terms of the property of templates, they can be categorized as: 1) Hard templates (such as chemically functionalized carbon nanotubes) provide well-organized shapes for nanoparticle assembly but the nanoparticles are typically not precisely-arranged on the surface of the templates.[50-52] The Siegel group chemically functionalized nitrogen-doped carbon nanotubes to selectively make gold nanoparticles attach on the surface (**Figure 1.8a**).[52] 2) Soft templates (such as synthetic polymers,[53] viruses[54] or biomolecules[55-57]) possess extraordinary chemical structures, and they provide multiple binding sites for the attachment of nanoparticles. For example, some groups have used pre-prepared polymer nanofibers as templates for the assembly of gold nanorods (**Figure 1.8b**).[58] Various peptide-based self-assembled structures and viruses can also be used as templates for directing nanoparticle assembly (**Figure 1.8c and 1.8d**).[54,59] However, these typically result in structures with good long range nanoparticle order but poor local nanoparticle order.

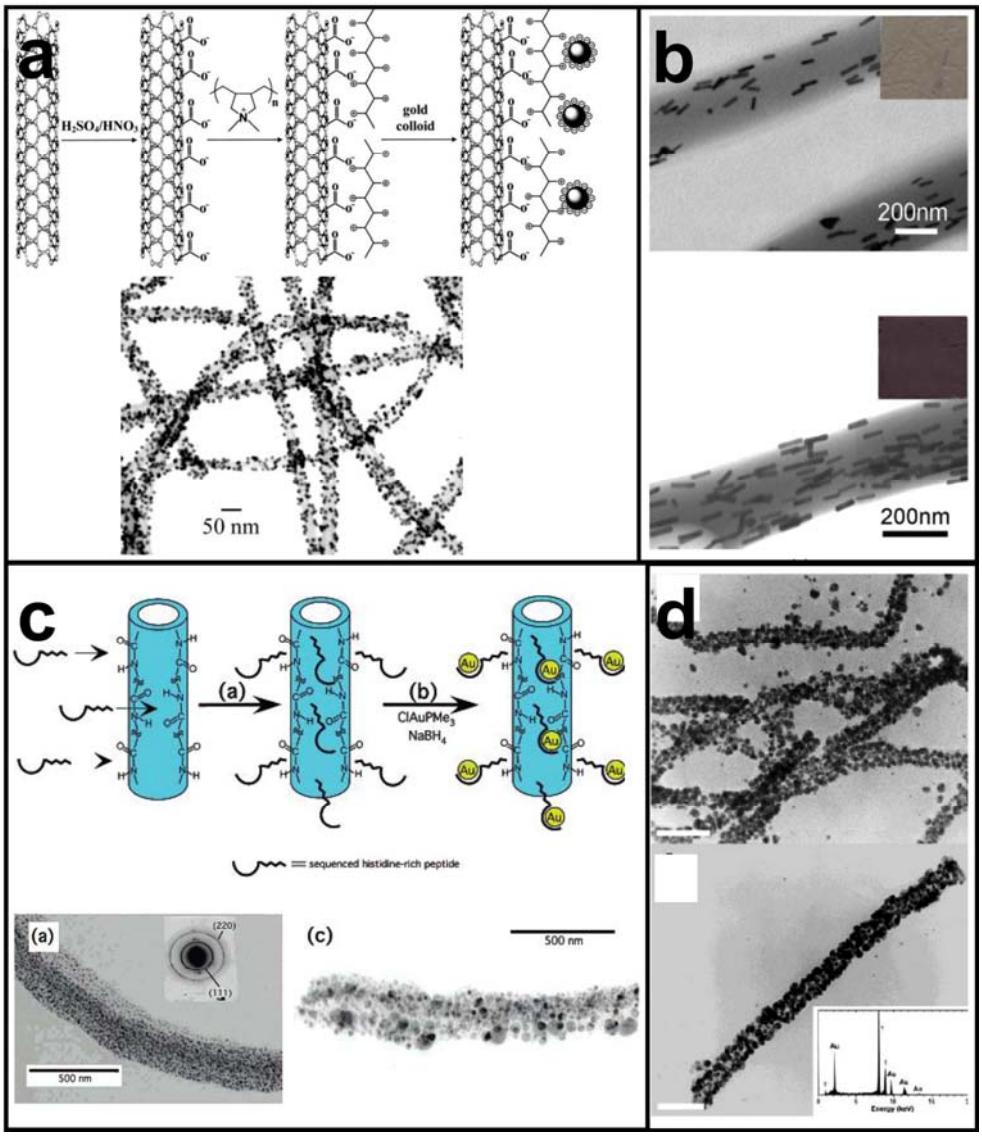


**Figure 1.8**. Templated-based nanoparticle assemblies (a) nitrogen doped carbon nanotubes selectively decorated with gold nanoparticles (Adapted from ref.52); (b) assemblies of gold nanorods in Poly(vinyl alcohol) (PVA) nanofiber matrix (Adapted from ref.58); (c) gold coating nucleated at the histidine sites of the heptanes dicarboxylate nanowire (Adapted from ref.59) and (d) Tobacco mosaic virus (TMV) rods with dense external coating of gold nanoparticles; scale bar= 100 nm (Adapted from ref.54).

## 1.5 A NEW METHOD FOR PEPTIDE-DIRECTED SYNTHESIS AND ASSEMBLY OF NANOPARTICLES

The existing methods are successful and useful for controlling nanoparticle assembly into well-organized complex superstructures and preparing superstructures with various nanoparticle compositions. However, the development of new methodology is still required because these typical methods suffer from several disadvantages. Self-assembly at interfaces produces close-packed 2-D nanoparticle lattices and 1D arrays,[60] but these methods are not useful for constructing more complex structures (e.g. chains, spheres, etc.). Assembly via colloidal crystallization provides binary nanoparticle assemblies with precisely controlled chemical composition and tight placement of nanoparticles. However, these methods generally require multiple steps. It exhibits similar weakness to assembly at interfaces: one cannot use colloidal crystallization to control the directional assembly of nanoparticles into complex superstructures. Template-based possesses yield superstructures with well-defined shapes and decent long-range order, yet they typically do not provide superstructures with good short-range nanoparticle order.[61] Developing more facile and efficient methods for rationally designing and fabricating well-organized nanoparticle superstructures is significantly important. Therefore, the Rosi group has developed a new peptide-based methodology to direct the synthesis and assembly of the nanoparticles into nanoparticle superstructures that aims to address some of the limitations of the existing methods of nanoparticle assembly.

### 1.5.1 Why Peptides?

Peptides possess several unique attributes that make them ideal for directing the assembly of inorganic nanoparticles. In particular, peptides have 1) *unique substrate specific recognition*

*capabilities* and 2) *unique self-assembly capacities*, both of which depend intrinsically on the specific amino-acid sequence within the peptide.

Phage display[62] and in vitro evolution methods have been applied to evolve new peptides that bind to specific inorganic materials in a sequence specific fashion. These methods have yielded new peptides that recognize and bind many different inorganic compositions.[62-64] For example, peptides, in a sequence-specific fashion, exhibit high binding affinities for gold,[59,65,66] silver,[67] zinc sulfide,[68] and other inorganic materials.[69-74] In some cases, peptides play a significant role in controlling the nucleation and growth of particular nanoparticles from precursor salt solutions.

Amino acids in peptides have the same basic structure and vary only in the R-group at the central carbon (C$\alpha$) position of the molecule. Peptides adopt specific configurations depending on which R-groups are near one another in a peptide chain. Additionally, the structure formed by a single peptide can interact with another complementary peptide via non-covalent interactions: ionic, hydrophobic, hydrogen bonding and $\pi$-stacking. When a large number of these building blocks with specific configurations assemble, supramolecular structures can be formed. In some peptide based nanomaterials, the native secondary structure of the peptides, such as $\beta$-sheets and turns, $\alpha$-helices and coiled coils, also strongly impact structure formation. Modifying peptides by attaching various molecules to peptides can also impact the structure formation and affect their self-assembly properties. Such peptides are often called "peptide conjugates". Different peptide conjugates have been designed and self assembled into particular well-organized nanostructures such as micelles, vesicles, nanotubes and nanoribbons.[63,75-79] For instance, peptide amphiphiles, which consist of oligopeptides that are modified with a hydrophobic alkyl tail (**Figure 1.9**), are widely used as building blocks for forming soft bionanomaterials. When these molecules are in

water they generally assemble into high ordered structures with a hydrophobic core consisting of the alkyl tails and a hydrophilic exterior consisting of the peptides.[80,81]

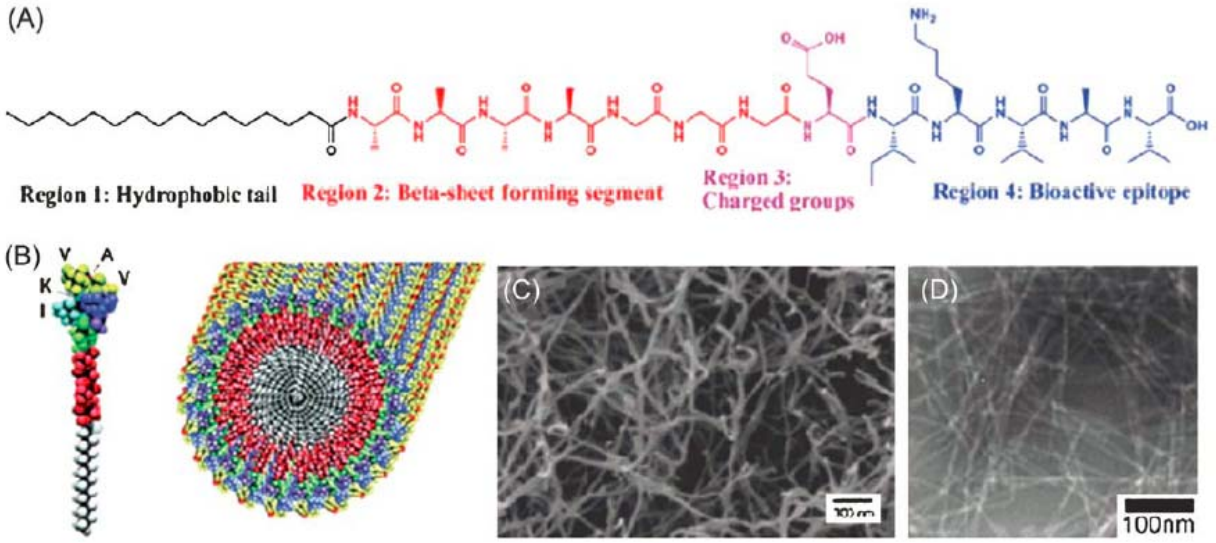


**Figure 1.9.** (a) Molecular structure of a typical PA studied by the Stupp group, incorporating motifs as indicated (the bioactive epitope in this case is the laminin IKVAV sequence), (b) Diagram of nanofibril structure, (c) SEM image of nanofibril network in DMEM cell medium and (d) TEM image (Adapted from ref.80 and ref.81).

### 1.5.2 New peptide-based methodology

The Rosi group's peptide-based method relies on peptide conjugates that direct a one-pot reaction that couples synthesis and assembly of nanoparticles into one simultaneous process.[66] We expect this new promising methodology could direct and assemble nanoparticle superstructures with fewer synthetic steps, good local order, well-controlled structural metrics, and diverse composition scope. In a first example, Chen et al. used this method to prepare 1-D nanoparticle double-helical structures (**Figure 1.10**). AYSSGAPPMPPF, a gold-binding peptide, was coupled to dodecanoic acid to generate $[C_{11}H_{23}CO]$-$PEP_{Au}$ ($PEP_{Au}$ = AYSSGAPPMPPF). In the presence of chloroauric acid and HEPES buffer, $C_{12}$-$PEP_{Au}$ directs the formation of gold nanoparticle double helices. The HEPES acts as a reducing agent.[65,82-84] This study showed that two processes, peptide self-assembly and peptide-based synthesis of discrete nanoparticles, could be coupled to occur simultaneously, resulting in a hierarchical assembly of nanoparticles.

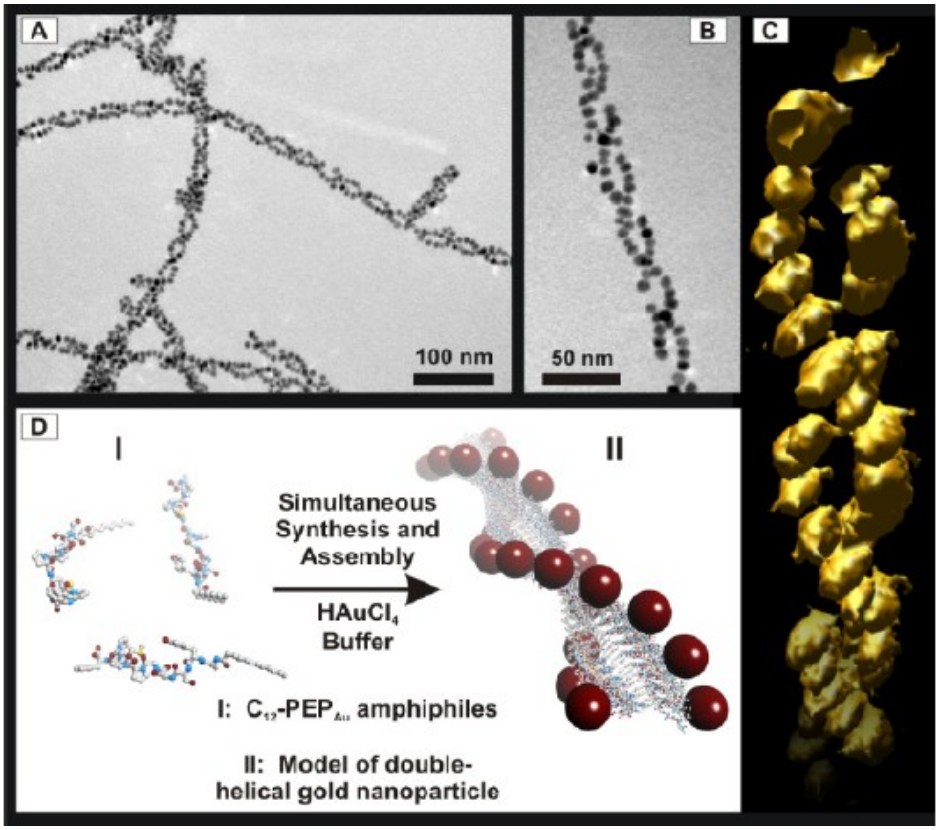


**Figure 1.10**. (a) and (b) TEM images of left-handed gold nanoparticle double helices; (c) Tomographic 3-D reconstruction image of left-handed gold nanoparticle double helices; (d) Schematic view of the formation of left-handed gold nanoparticle double helices by combining peptide self-assembly and peptide-based biomineralization (Adapted from ref. 66).

## 1.6 OBJECTIVES AND OUTLINES

The objectives of this dissertation are: 1) describe fundamental synthetic factors that impact the mechanism of this peptide-based nanoparticle assembly methodology; 2) explore the physical properties of nanoparticle superstructures via tuning and tailoring structure metrics (i.e. nanoparticle size, nanoparticle compositon, and interparticle distance); 3) expand the structural scope of this peptide-based methodology; and 4) expand the composition scope of the methodology so that it can be utilized to prepare nanoparticle superstructures of compositions other than gold.

Chapter 2 describes studies that aim to understand the important mechanistic factors that underline the peptide-directed assembly of gold nanoparticle double helices (*manuscript in preparation*). Chapter 3 utilizes information gleaned from the mechanistic studies to prepare larger quantities of high-quality gold nanoparticle double helices for property studies. In particular, we focus on the circular dichroism (CD) chirooptical properties of double helical nanoparticle superstructures. This chapter also details how tuning and tailoring the structure parameters of gold helices (i.e. nanoparticle size, interparticle distance, interhelical distance, and particle composition) impact the chirooptical properties. Theoretical models successfully simulate and can be used to predict the chirooptical behavior of gold helices (*Nano Letters* **2013**, 13(7), 3256). Chapter 4 describes peptide conjugates that are used to direct the synthesis and assembly of hollow gold nanospherical superstructures, which can be potentially used in drug delivery, photothermal therapy and surface enhanced Raman spectroscopy (SERS). In this chapter, modifications to both the peptide sequence and the organic tether group is critically important to control the morphology of soft assemblies, which eventually determine the overall structure of the gold nanoparticle assemblies (*Journal of the American Chemical Society* **2010**,

132(40), 14033). Chapter 5 describes the diverse compositional scope of our methodology. A new Co-binding peptide is employed to direct the synthesis and assembly of CoPt alloy nanoparticles. Hollow spherical CoPt nanoparticle superstructures are shown to exhibit high electrocatalytic activity for methanol oxidation compared with that of discrete CoPt nanoparticles (*Angewandte Chemie International Edition* **2013**, 52(14), 3993).

# 2.0 MECHANISM OF THE FORMATION OF GOLD NANOPARTICLE DOUBLE HELICES

This work was performed in collaboration with Leekyoung Hwang. A portion of this work was published in Hwang, Leekyoung. 2012. *Development and mechanistic study of a peptide based methodology for the preparation of nanoparticle superstructures.* Doctoral Dissertation, University of Pittsburgh. Ann Arbor: ProQuest/UMI. (UMI Number 3529534.)

## 2.1 INTRODUCTION

Nanoparticles assemblies exhibit ensemble chemical and physical properties owing to the nanoparticle size, shape, composition and the spatial arrangement within the assembly.[85-91] In previous work, the Rosi group introduced a peptide-based methodology that relies on designed peptide-conjugate molecules that direct the synthesis and assembly of one dimensional well-organized gold nanoparticle double helices.[66] Peptide conjugate molecules consist of a specific sequence of amino acids that recognize and bind specific inorganic nanoparticles[65,92] and an organic moiety that impacts the self-assembly of the peptides.[93]

In this previous report[66], $C_{12}$-$PEP_{Au}$ peptide-conjugates were employed to synthesize and directed the assembly of one dimensional left-handed gold nanoparticle double-helical superstructures with nanoscale widths and microscale lengths. They exhibit excellent local order

(i.e. uniform nanoparticle size and consistent interparticle distance, interhelical distance and pitch). These structures exhibit a characteristic surface plasmon peak at ~560 nm in the visible region, which implies that these chiral gold helices could potentially serve as nanoscale circular polarizers, chirooptical sensors, or negative refraction materials.[86,94-98] In principle, if one could precisely control the structural parameters of gold helices, one could then finely tune their chirooptical properties. In order to finely adjust the structural metrics, it would be helpful to understand the synthetic factors and mechanism that underline the assembly process.

Two important mechanistic factors will be reported in this chapter. We will show that the presence of (1) small gold nanoparticles and (2) well-dispersed peptide conjugates are the prerequisites to induce the assembly of well-ordered gold nanoparticle double helices. We also present the proposed mechanism underlying the assembly of nanoparticle superstructures. Upon completion of these studies, we were able to increase the yield of gold nanoparticle double helices via modifying the synthetic protocol. We believe that this understanding will not only improve and optimize the developed synthetic process but also allow the creation of new methodology for directing nanoparticle-assembly.

## 2.2 RESULTS AND DISSCUSSION

### 2.2.1 Comparison of two gold sources: $HAuCl_4$/TEAA vs. $HAuCl_4/H_2O$

The following reagents are used in the preparation of gold nanoparticle double helices: $C_{12}$-$PEP_{Au}$ ($C_{11}H_{23}CO$-AYSSGAPPMPPF), 0.1 M HEPES buffer (4-(2-hydroxyethyl)-piperazineethanesulfonic acid, pH = 7.3 ± 0.1) and an aqueous mixture of $HAuCl_4$/TEAA buffer (0.1M chloroauric acid ($HAuCl_4$) in 1.0 M triethylammonium acetate (TEAA; pH = 7.0). The $HAuCl_4$/TEAA buffer is incubated for 10 minutes at room temperature and then centrifuged (10 min., 5K rpm); aliquots of the supernatant are used in the synthesis. The HEPES serves as a buffer for assembly as well as a reducing agent. After an aliquot of the $HAuCl_4$/TEAA solution is added to the conjugate/HEPES solution, only two different products form: complete gold nanoparticle double helices and assembled fibers without any gold nanoparticles attached (**Scheme 2.1 and Figure 2.1**).

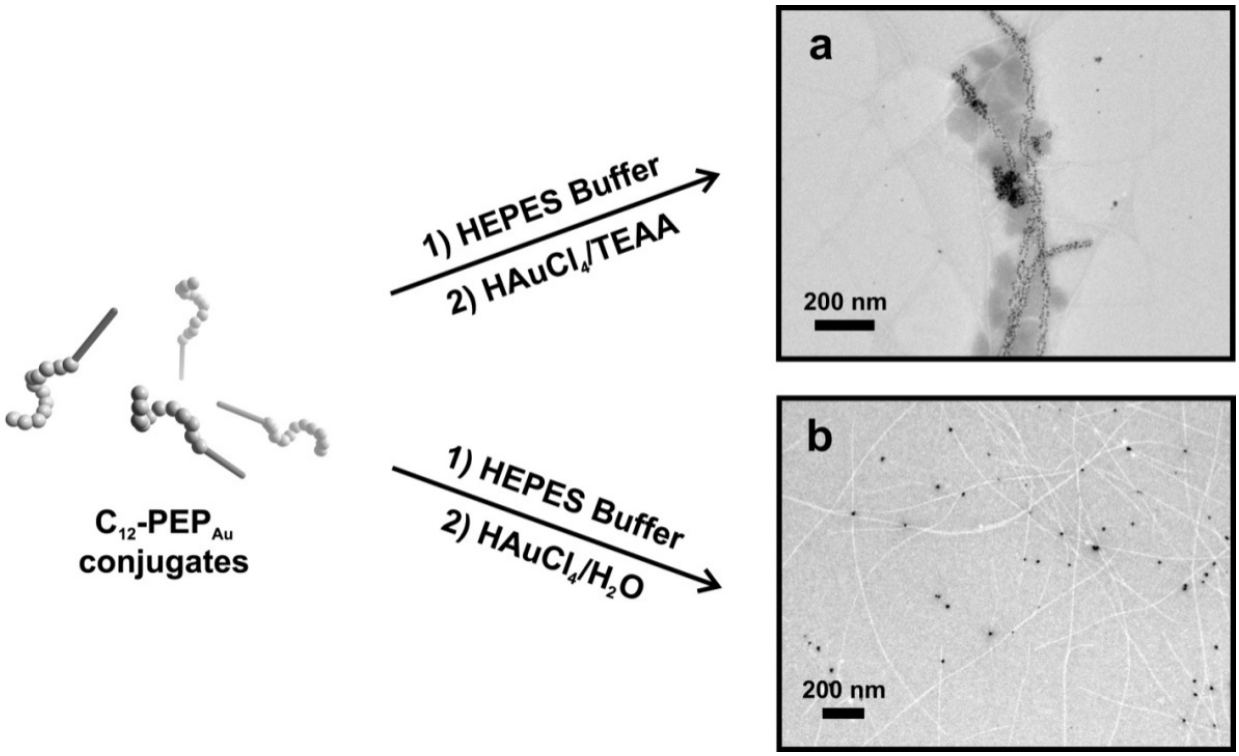


**Scheme 2.1.** (a) TEM image of gold nanoparticle double helices and 'naked' fibers obtained by adding $HAuCl_4$/TEAA (aq.) solution. (b) TEM image of free nanoparticles and 'naked' fibers formed by adding $HAuCl_4/H_2O$ (aq.) solution.

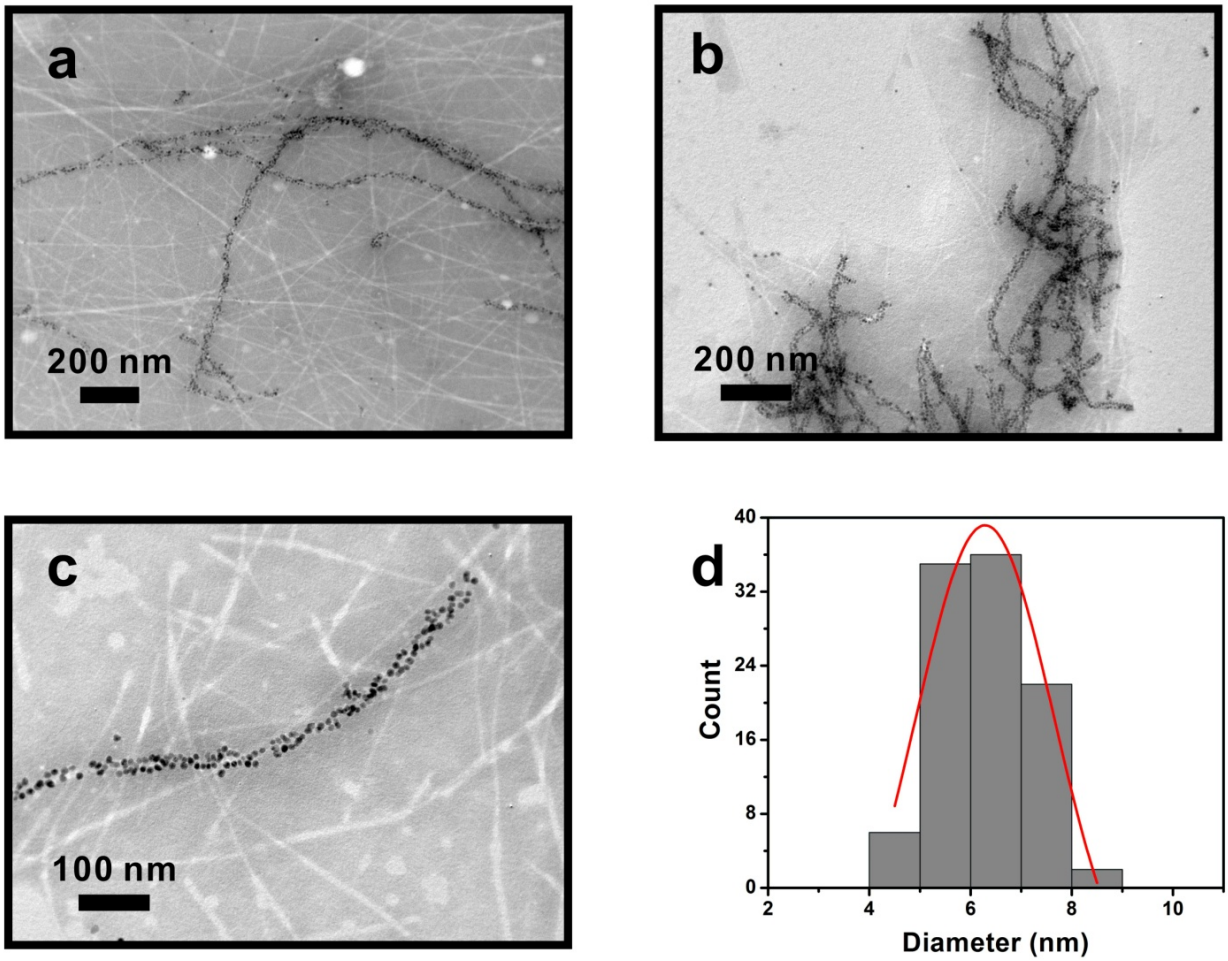


**Figure 2.1**. (a-c) TEM images of complete gold nanoparticle double helices and 'naked' fibers formed in HEPES buffer in the presence of $C_{12}$-$PEP_{Au}$ by adding an aliquot of $HAuCl_4$/TEAA buffer. (d) Nanoparticle size distribution of the complete gold nanoparticle double helices (based on 101 counts; diameter = 6.28 ± 1.37 nm).

It is important to note that this mixture of two products differs from the product distribution yielded by a typical peptide template approach to assembly. In a typical template based nanoparticle assembly method, multiple synthetic steps are required: 1) the soft-assembly template is prepared; 2) nanoparticles are pre-synthesized or nucleated *in situ*;[99] and 3) the particles and template are mixed together, which results in templates randomly decorated with nanoparticles.[100,101] The typical products of these methods are templates that are decorated with nanoparticles and free, non-assembled nanoparticles.[59] It is rare to observe two separate products consisting of 'naked' templates and fully-decorated templates. The unusual distribution of products in our case prompted us to understand the mechanism of gold nanoparticle double helix formation.

The gold precursor used in our synthesis is $HAuCl_4$/TEAA (aq.) solution, which differs from the $HAuCl_4/H_2O$ (aq.) solution, a commonly used gold source in nanoparticle synthesis methods.[65] We aimed to determine whether the gold helices would still form by using $HAuCl_4/H_2O$ (aq.) solution instead of $HAuCl_4$/TEAA (aq.); this would help us determine the role of the $HAuCl_4$/TEAA (aq.) precursor solution. We added $HAuCl_4/H_2O$ (aq.) to HEPES buffer in the presence of $C_{12}$-$PEP_{Au}$ conjugates in order to investigate whether these conditions would yield well-organized gold nanoparticle double helices. However, these synthetic conditions only produced 'naked' fibers and free nanoparticles (**Scheme 2.1 (b) and Figure 2.2**).

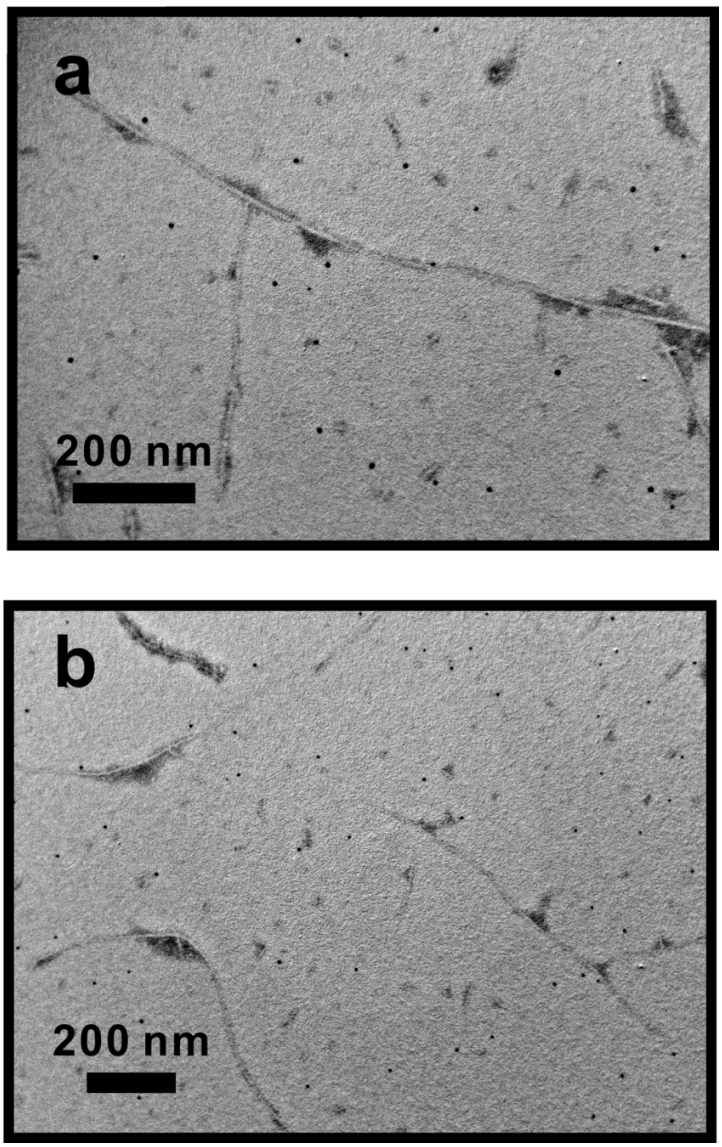


**Figure 2.2**. (a-b) TEM images of free gold nanoparticles and 'naked' fibers formed in HEPES buffer in the presence of $C_{12}$-$PEP_{Au}$ by adding an aliquot of $HAuCl_4/H_2O$. This simple study suggested that TEAA may play an important role in the synthesis and assembly process.

### 2.2.2 Role of $HAuCl_4$/TEAA

To determine the role of $HAuCl_4$/TEAA (aq.), we performed fundamental studies on the growth of nanoparticles using this gold ion source. To simplify the experiment, we used $PEP_{Au}$ instead of $C_{12}$-$PEP_{Au}$. $PEP_{Au}$ are used to cap and stabilize gold nanoparticles,[65] which would exclude the self-assembly capability of $C_{12}$-$PEP_{Au}$. We dissolved $PEP_{Au}$ in HEPES and added to this solution either an aliquot of $HAuCl_4$/TEAA or an aliquot of $HAuCl_4/H_2O$.

First, we measured UV-Vis spectra of $PEP_{Au}$/HEPES solutions 30 min after adding $HAuCl_4/H_2O$ (aq.) and $HAuCl_4$/TEAA (aq.) to each vial. Both solutions exhibit a $\lambda_{max}$ at ~525 nm (**Figure 2.3e**), owing to the suface plasmon of the free gold nanoparticles.[65,102,103] TEM images revealed that the spherical gold nanoparticles formed from these two gold sources had a similar nanoparticle size distribution (**Figure 2.3a,2.3c**).

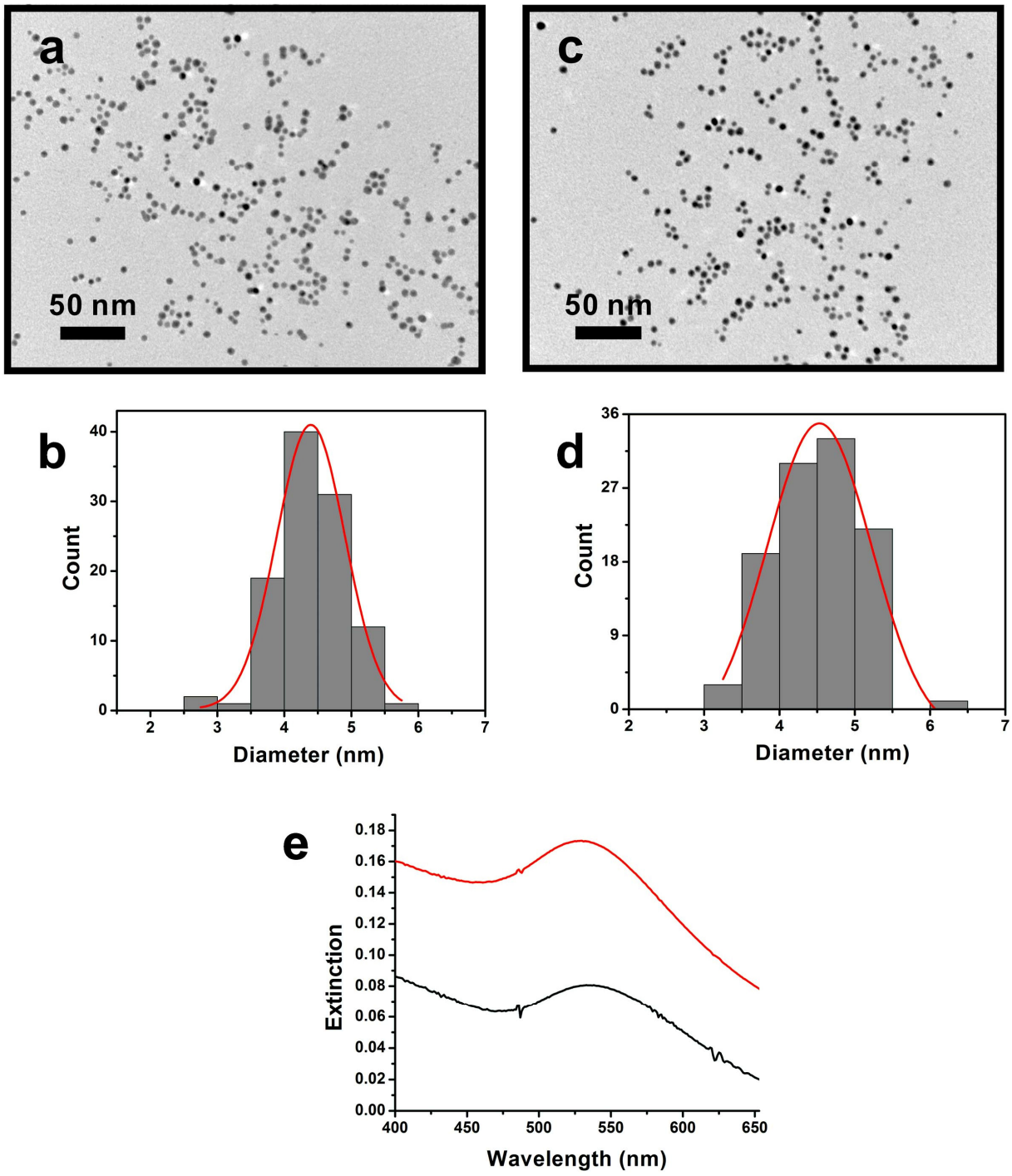


**Figure 2.3**. (a-b) TEM image and nanoparticle size distribution of spherical gold nanoparticles (based on 106 counts; diameter = 4.40 ± 0.51 nm) synthesized by adding an aliquot of $HAuCl_4$

/$H_2O$ to HEPES buffer in the presence of $PEP_{Au}$. (b-d) TEM image and nanoparticle size distribution of spherical gold nanoparticles (based on 108 counts; diameter = 4.53 ± 0.69 nm) synthesized by adding an aliquot of $HAuCl_4$/TEAA buffer to HEPES buffer in the presence of $PEP_{Au}$ (e) UV-Vis absorbance of the $PEP_{Au}$-stabilized gold nanoparticles prepared by $HAuCl_4/H_2O$ (aq.) and $HAuCl_4$/TEAA (aq.). (black spectrum: adding $HAuCl_4$ / $H_2O$. red spectrum: adding $HAuCl_4$/TEAA).

To further study the difference between $HAuCl_4$/TEAA (aq.) and $HAuCl_4/H_2O$ (aq.) solution, the same experiment was conducted, but we monitored the absorbance at 520 nm as a function of time from 0 to 1500 secs (25 mins). The UV-Vis absorbance at 520 nm for the $HAuCl_4/H_2O$ (aq.) sample remained nearly zero for the first 5 minutes of reaction, which implies that the reaction solution does not contain an appreciable amount of gold nanoparticles or that the nanoparticle size is less than 2 nm. Gold nanoparticles less than 2 nm in diameter do not exhibit a surface plasmon.[104,105] Over time, the absorbance at 520 nm increases as particles of sufficient size form in the reaction. In this case $Au^{3+}$ is the only source of gold and therefore there is a lag time for producing plasmonic nanoparticles. In contrast, the UV-Vis absorbance at 520 nm for the sample containing $HAuCl_4$/TEAA (aq.) was non-zero at the starting point and continuously increases over time (**Figure 2.4**). We reasoned that gold cations were reduced and formed > 2nm gold nanoparticles in the $HAuCl_4$/TEAA (aq.) solution. It is known that TEAA buffer is in an equilibrium state between triethylammonium acetate (TEA) and triethylamine and acetic acid. TEA can serve as reducing reagent to reduce gold cations[106] and acetic acid can bind and protect the fresh made metallic gold particles.[107] Therefore, it was not surprising that gold nanoparticles form in the $HAuCl_4$/TEAA (aq.) solution (**Figure 2.5a**). TEM images showed that pre-formed gold nanoparticles in the $HAuCl_4$/TEAA (aq.) solution were small with a size 3.02 ± 0.26 nm (Figure 5b–c); there were also some large gold nanoparticles (**Figure 2.5d-e**) because the products of this reaction are rapidly evolving. AFM analysis was also performed to further confirm that $HAuCl_4$/TEAA (aq.) provides small gold nanoparticles (height = 2.0 ± 0.22 nm) (**Figure 2.6**).

Based on our observation, we speculate that $C_{12}$-$PEP_{Au}$ could bind the pre-formed small gold nanoparticles after adding $HAuCl_4$/TEAA (aq.) solution and thereafter induce the assembly of gold helices.

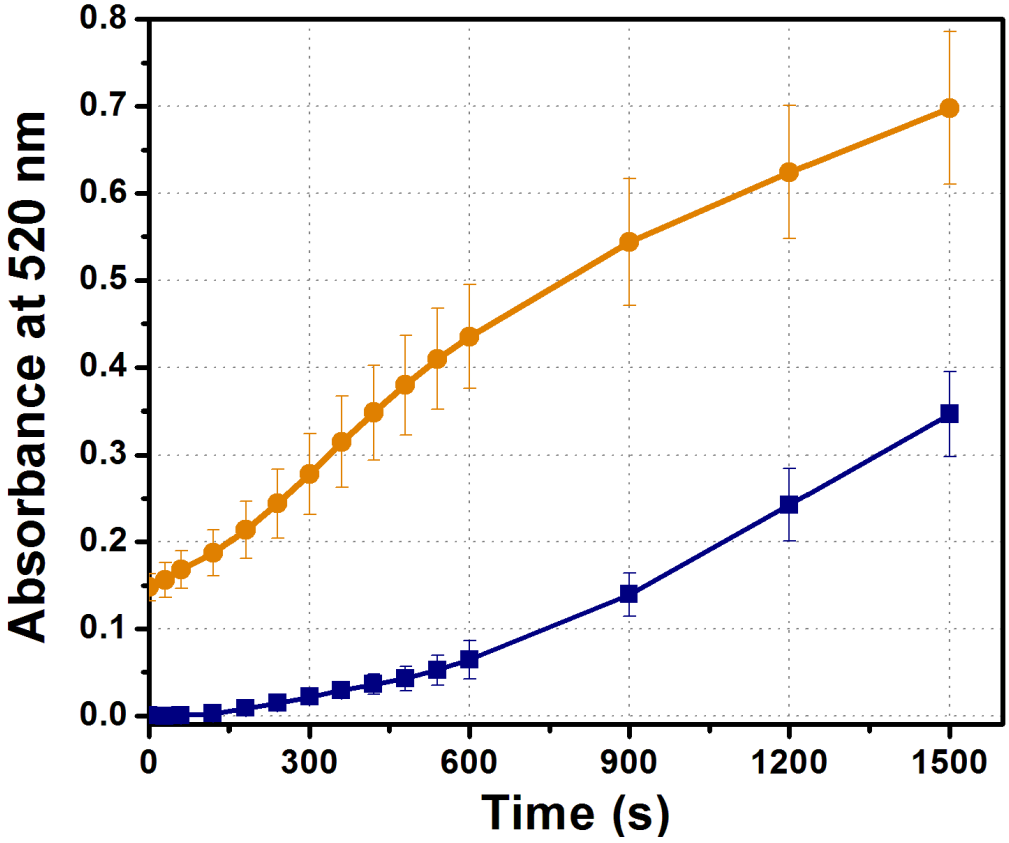


**Figure 2.4.** UV-Vis absorbance at 520 nm vs Nucleation and growth time of gold nanoparticles formed in $HAuCl_4/H_2O$ (aq.) ( navy line) and $HAuCl_4$/TEAA (aq.)( orange line) respectively.

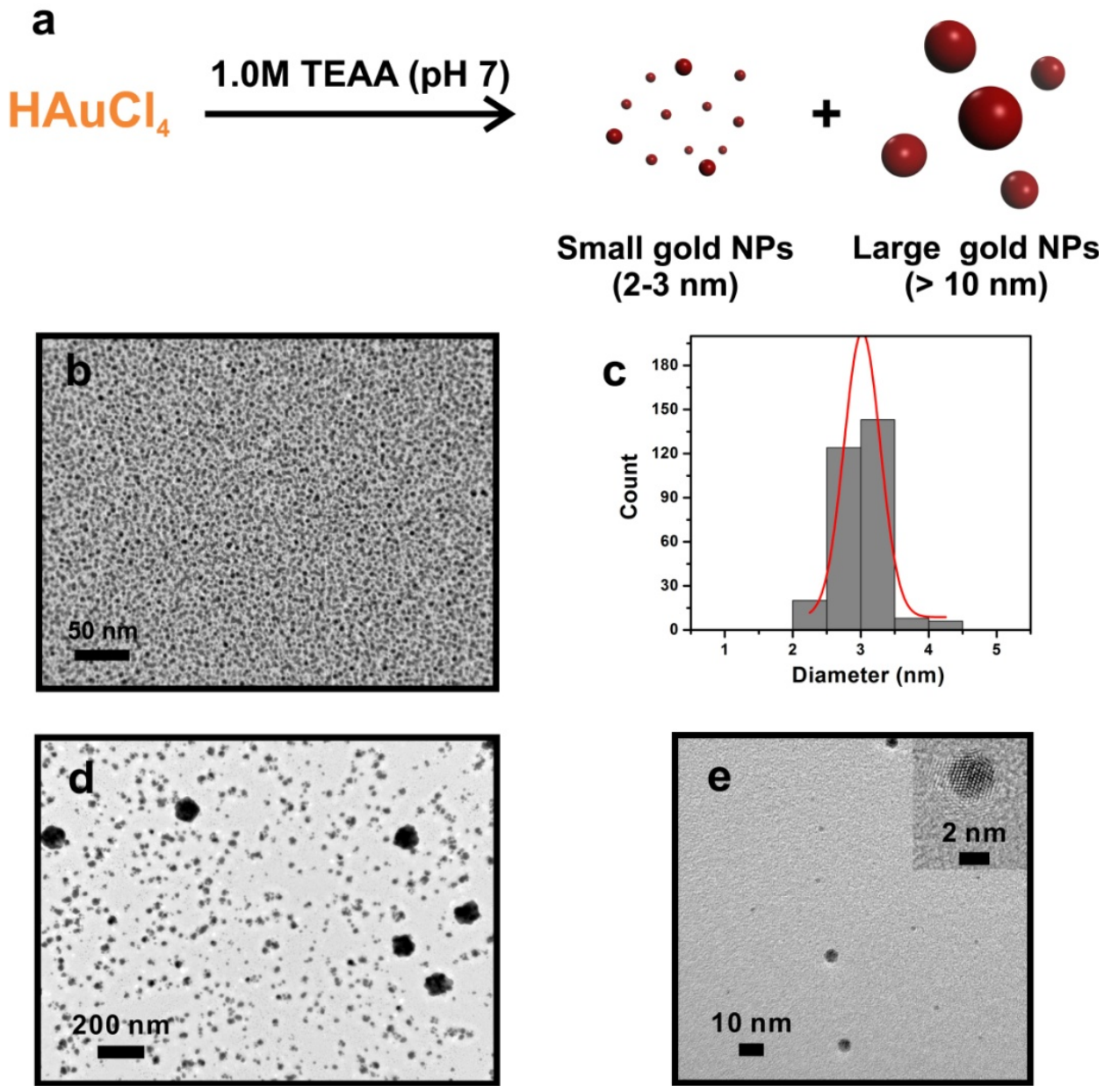


**Figure 2.5**. (a) schematic illustration of the formation of gold nanoparticles and large gold nanoparticles; (b) TEM image of the small gold nanoparticles obtained from $HAuCl_4$/TEAA (aq.); (c) the size distribution of the gold nanoparticles (based on 350 counts; Diameter = 3.02 ±

0.26 nm). Additional TEM images (d-e) of gold nanoparticle and gold clusters synthesized in TEAA buffer; the $HAuCl_4$/TEAA (aq.) solution was centrifuged at 5k rpm 10min after incubating the gold solution at room temperature, and then an aliquot of the solution was examined by TEM. The inset HRTEM image in (e) shows the lattice fringes of small gold seeds.

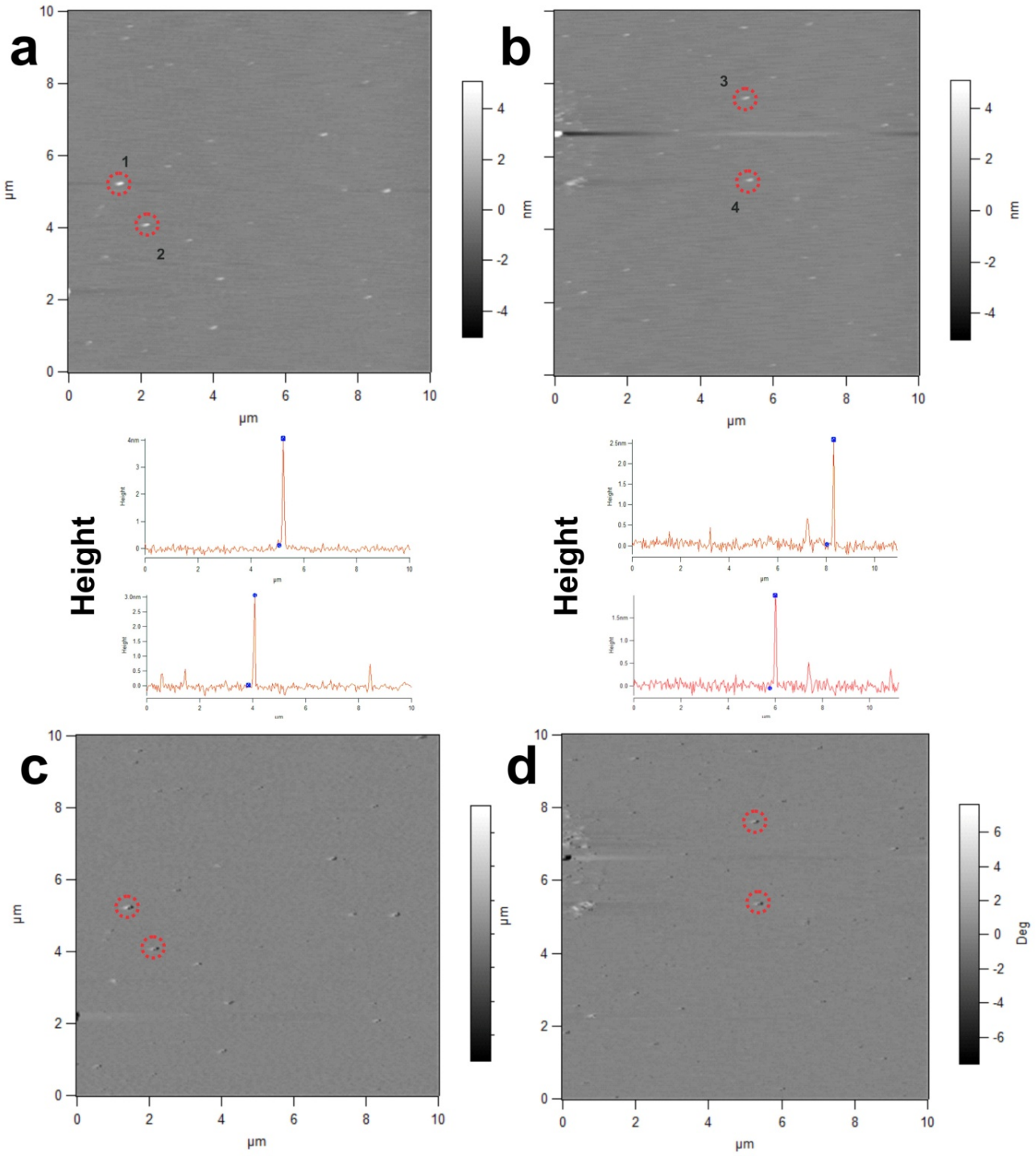


**Figure 2.6.** AFM height (a and b), phase (c and d) of gold nanoparticles formed by $HAuCl_4$/TEAA (aq.) solution. It exhibits height distribution of gold nanoparticles (height = 2.0 ±

0.22 nm; based on 15 counts from AFM images). Height of number 1–4 was marked here as representatives (height of 1, 2, 3, and 4 = 3.93 nm, 3.05 nm, 2.56 nm, and 2.03 nm).

### 2.2.3 Effect of monomers at the outset of reaction on forming double helical gold nanoparticle assembled structures

As detailed earlier, the reaction to form double helices yields two products: gold nanoparticle double helices and 'naked' fibers. We next asked the following question: how do the 'naked' fibers form and why do they not serve as a template for gold nanoparticle double-helical superstructures. As we mentioned in **section 2.2.2**, $HAuCl_4$/TEAA (aq.) contains both small gold nanoparticles and gold cations and $HAuCl_4/H_2O$ (aq.) contains only gold cations. Hence, we conclude that both gold precursors yield 'naked' fibers due to their common gold cations. We hypothesize that gold cations accelerate the speed of self-assembly of peptide-conjugate molecules. To investigate this further, we added an aliquot of calcium cations to determine whether they would accelerate the assembly of the peptide-conjugate molecules. After adding $Ca^{2+}$ to a solution of $C_{12}$-$PEP_{Au}$ in HEPES, fibers rapidly formed after 30 min incubation at room temperature, as revealed by TEM analysis (**Figure 2.7**). Without $Ca^{2+}$, the fibers form slowly over the course of 2 weeks. We reason that $Ca^{2+}$ assists the assembly of the conjugates owing to its strong interaction with carboxylate group of amino acids.[108] Samples in the presence of $Na^+$ and $Au^{3+}$ were also imaged via TEM, which clearly showed that there were more fibers formed than the sample in the absence of metal cations (**Figure 2.7**). To quantitatively prove that adding metal cations will indeed increase the yield of 'naked' fibers, we collected CD spectra for each sample. The CD signal is proportional to the concentration of fibers that contain β-sheet structures.[108,109]

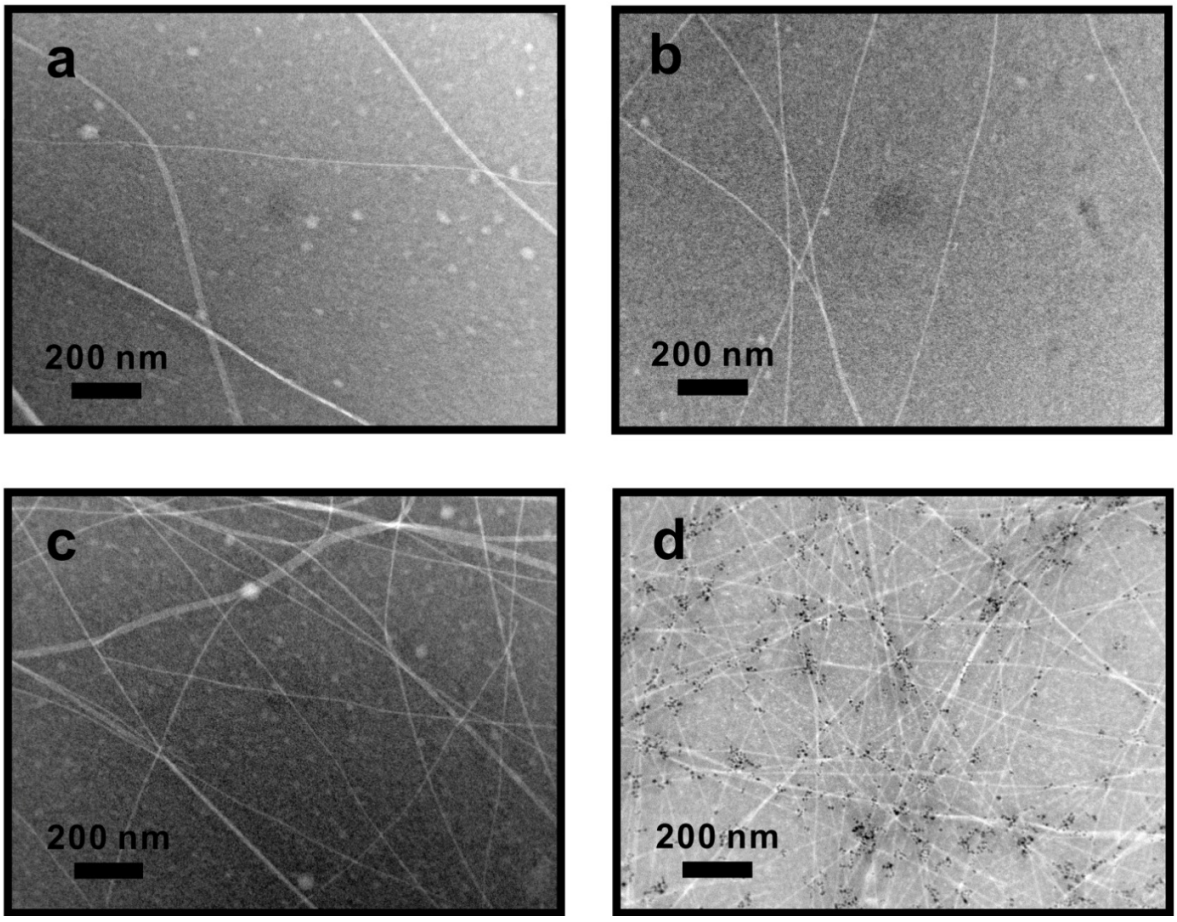


**Figure 2.7**. Negative stained TEM images of $C_{12}$-$PEP_{Au}$ fibers in the HEPES buffer incubating for 30 minutes. (a) $C_{12}$-$PEP_{Au}$ fibers/ HEPES buffer without any metal cations. (b) $C_{12}$-$PEP_{Au}$ fibers/ HEPES buffer in the presence of $Na^{+}$. (c) $C_{12}$-$PEP_{Au}$ fibers/ HEPES buffer in the presence of $Ca^{2+}$. (d) $C_{12}$-$PEP_{Au}$ fibers/ HEPES buffer in the presence of $Au^{3+}$.

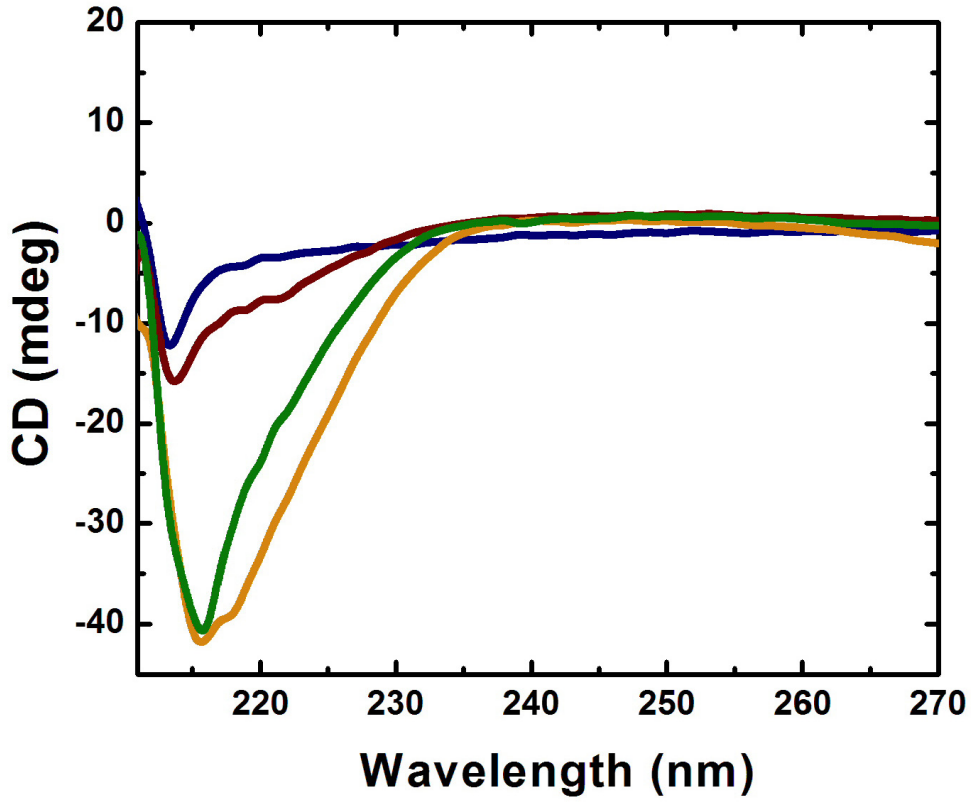


**Figure 2.8.** CD spectra of $C_{12}$-$PEP_{Au}$/HEPES buffer in the absence of additional metal cations for 30 mins incubation (navy) and $C_{12}$-$PEP_{Au}$/HEPES buffers incubate with aliquots of $Na^{+}$ (wine), $Ca^{2+}$ (orange) and $Au^{3+}$ (olive) for 30 minutes in the UV region (211 nm – 255 nm) respectively. The path length of the light is 1 mm.

**Figure 2.8** indicates that the addition of $Ca^{2+}$ or $Au^{3+}$ results in large negative bands, the addition of $Na^{+}$ results in a medium negative band, and the solution in the absence of metal cations showed the smallest negative band. CD measurements were consistent with what we observed from the negatively stained TEM images. These experiments indicate that $C_{12}$-$PEP_{Au}$ peptide-conjugate fibers and $C_{12}$-$PEP_{Au}$ 'monomers' (i.e. peptide-conjugate molecule) may coexist in the HEPES buffer and metal cations would accelerate the assembly speed of peptide-conjugate molecules.[108-110] $PEP_{Au}$ is slightly negative because the pI is 5.57 in HEPES (pH7) buffer.[111] We expected that the overall negatively charged peptide conjugates would result in electronic repulsion, which could prevent conjugate assembly. The addition of metal cations to solution can shield (or created a charge balance to) the negatively charged peptide conjugates.[110,112,113] When the charges on the C-termini are shielded, the peptides could aggregate, and then the hydrophobic interaction between the $C_{12}$ aliphatic tails would become a major driving force for assembly.[114] On the other hand, once the peptide conjugates assemble into fibers, the binding sites for the gold nanoparticles may become less accessible, which may explain why the 'naked' fibers are never decorated with gold nanoparticles. Therefore, the only way to construct complete gold helices is if the monomers directly bind small gold nanoparticles and then the particles and peptide conjugates assemble cooperatively.

To explore this hypothesis, we added aliquots of $HAuCl_4$/TEAA (aq.) and $HAuCl_4/H_2O$ (aq.), respectively, to $C_{12}$-$PEP_{Au}$/HEPES/$Au^{3+}$ solutions. TEM images showed that a low yield of gold nanoparticle superstructures formed after addition of $HAuCl_4$/TEAA (aq.) while only free nanoparticles were observed after addition of $HAuCl_4/H_2O$ (aq.) (**Figure 2.9**). This indicated that the synthetic process of gold nanoparticle double helices is different from a typical template-based method.

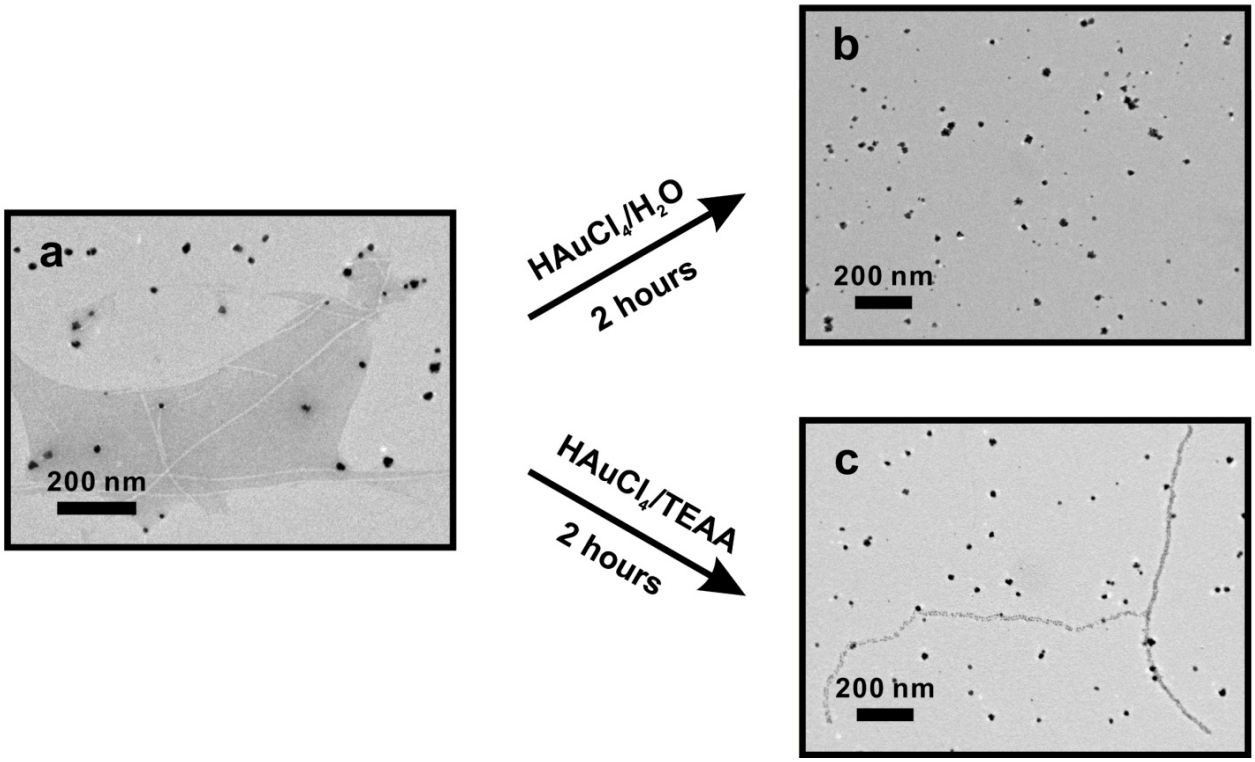


**Figure 2.9**. (a) TEM image show the 'naked' fibers and free gold nanoparticles after adding $HAuCl_4/H_2O$ into $C_{12}$-$PEP_{Au}$ /HEPES buffer incubating for one day. (b) Another aliquot of $HAuCl_4/H_2O$ was added to the solution (a) and incubated for 2 hours. TEM image showed only free gold nanoparticles. (c) Another aliquot of $HAuCl_4$/TEAA was added to the solution (a) and incubated for 2 hours. TEM image indicated the formation of gold nanoparticle double helical superstructures.

### 2.2.4 Proposed mechanism

Our main observations from this work are: 1) $HAuCl_4$/TEAA (aq.) solution provides pre-formed small gold nanoparticles as well as gold cations while $HAuCl_4/H_2O$ (aq.) solution provides only gold cations; 2) $C_{12}$-$PEP_{Au}$/HEPES buffer contains both $C_{12}$-$PEP_{Au}$ fibers and $C_{12}$-$PEP_{Au}$ free monomers or oligomers; and 3) the pre-assembled 'naked' fibers do not serve as a templates to produce double-helical nanoparticle assemblies.

In **section 2.2.2**, we mentioned that it took ~5 mins to nucleate small gold nanoparticles after adding $HAuCl_4/H_2O$ (aq.) to $PEP_{Au}$/HEPES buffer. However, $HAuCl_4$/TEAA (aq.) already provided small gold nanoparticles at the starting point and these gold nanoparicles continued growing in the presence of HEPES. Inorganic metal binding peptides ($PEP_{Au}$) bind to the surface [111] of spherical gold nanoparticles with varied sizes.[115-117] We proposed that $C_{12}$-$PEP_{Au}$ directs the assembly of gold nanoparticles. After $HAuCl_4$/TEAA (aq.) solution is added to the peptide conjugate/HEPES buffer solution, free peptide-conjugate molecules would meet small gold nanoparticles as well as gold cations ($Au^{3+}$). Once peptide conjugates coordinate $Au^{3+}$ they rapidly assemble into 'naked' fibers due to charge shielding and the hydrophobic interaction between the $C_{12}$ chains. After colliding with/sampling small gold nanoparticles in the reaction mixture, peptide conjugates could bind to their surface, creating peptide conjugate-nanoparticle complexes. These complexes could collide with each other and assemble into completed double-helical superstructures. This mechanism explains why the reaction yields only two distinct products: complete double helices and 'naked' fibers.[65,82-84] The synthetic pathway for forming double-helical gold nanoparticle superstructures is unique and promising in that they are prepared in a single step and have excellent local order and structural regularity (**Scheme 2.2**).

To test the proposed mechanism, $C_{12}$-$PEP_{Au}$/HEPES solutions were examined via TEM 5 minutes after adding aliquots of $HAuCl_4$/TEAA (aq.) and $HAuCl_4/H_2O$ (aq.). In 5 minutes, small gold nanoparticles had indeed assembled in the presence of $HAuCl_4$/TEAA (aq.) while only small free nanoparticles and 'naked' fibers appeared in the presence of $HAuCl_4/H_2O$ (aq.), as showed by negatively stained TEM images (**Figure 2.10**). To further prove the mechanism, cryo-TEM will be employed to trace the growth of gold nanoparticle double helices at different time point.

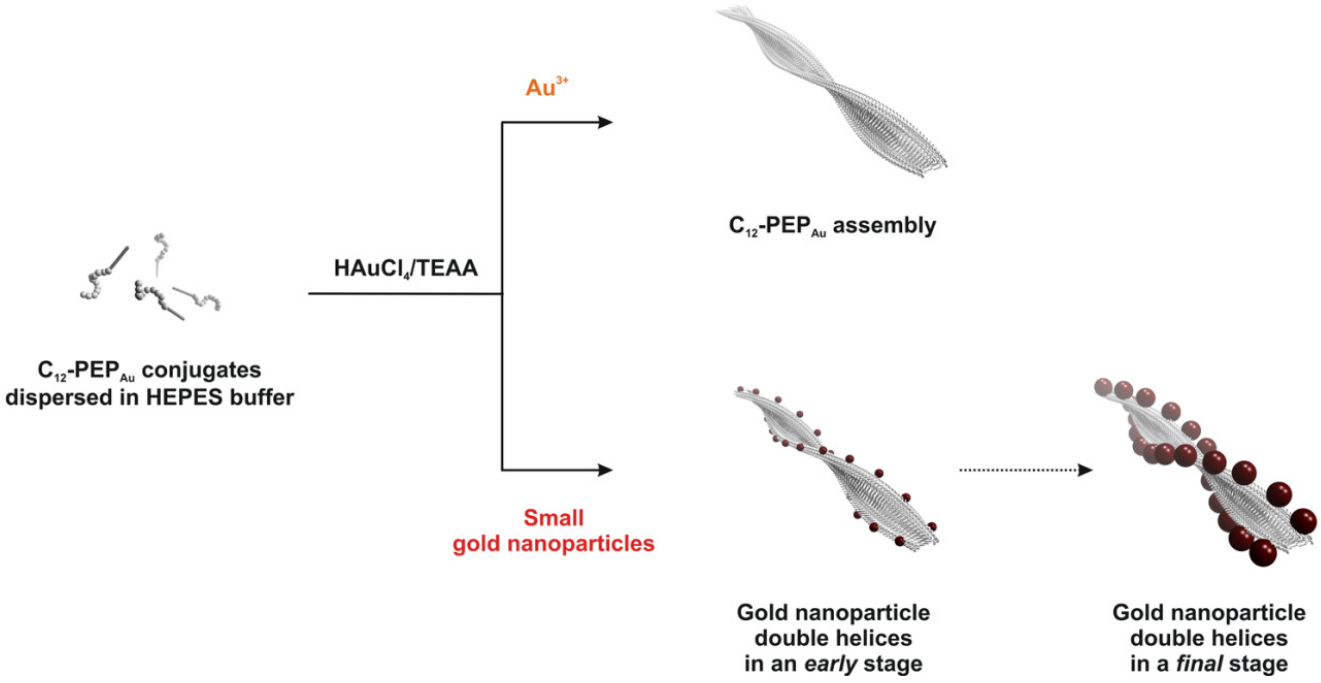


**Scheme 2.2.** Proposed schematic illustration of synthetic pathway for formation of well-organized gold nanoparticle double helices.

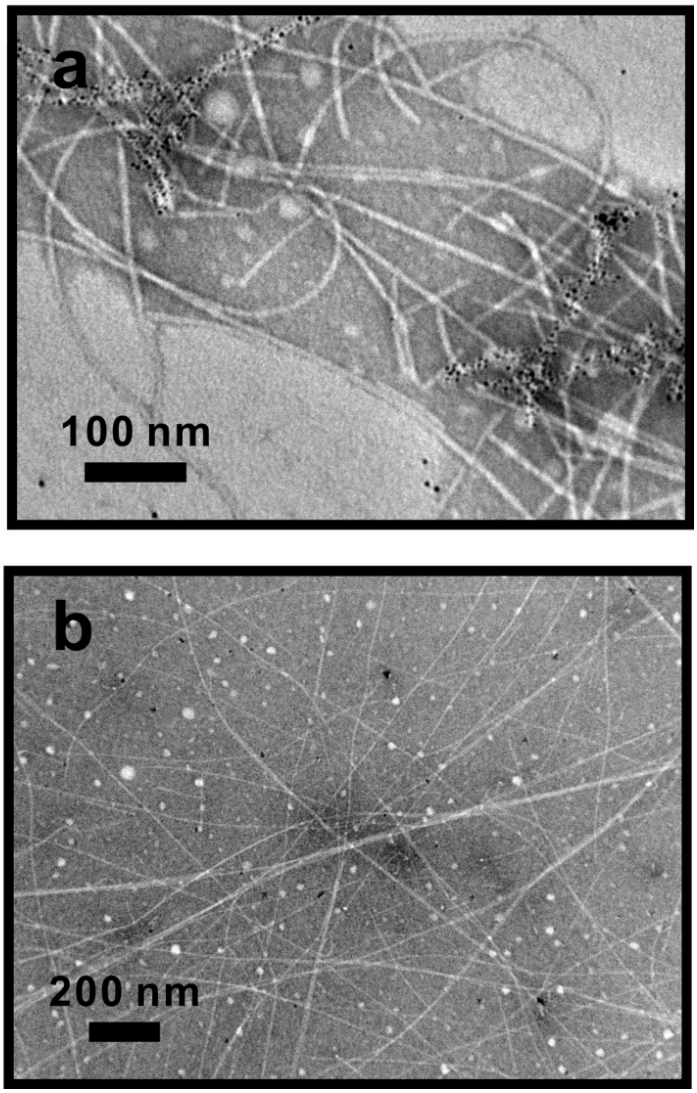


**Figure 2.10**. (a) Negatively stained TEM image shows 'naked' fibers and fibers completely decorated with small gold nanoparticles 5 mins after adding an aliquot of $HAuCl_4$/TEAA into $C_{12}$-$PEP_{Au}$/HEPES buffer. (b) Negatively stained TEM image shows only 'naked' fibers and free small gold nanoparticles 5 mins after adding $HAuCl_4/H_2O$ into $C_{12}$-$PEP_{Au}$/HEPES buffer.

### 2.2.5 Improving the synthetic procedure

On the basis of our proposed mechanism, after adding $HAuCl_4$/TEAA (aq.), free $C_{12}$-$PEP_{Au}$ monomers would bind to the pre-formed gold nanoparticles surface and serve to direct the assembly of the gold nanoparticles into helical superstructures. We next aimed to use what we learned about the mechanism to increase the yield of gold nanoparticle superstructures.

As stated in the proposed mechanism, large amounts of free monomers were consumed during the formation of 'naked' fibers with the assistance of gold cations. To reduce the concentration of gold cations and increase the amount of pre-formed small gold nanoparticles, it is necessary to improve our gold precursors or the reducing reagent (i.e. buffer solution). Here, we present a method that relies on modifying the buffer solution to produce a high yield of gold nanoparticle double helices.

We utilize citrate molecules in our improved synthetic method. Before we detail the method, we will show some preliminarily experimental results: free gold nanoparticles were synthesized and stabilized in $PEP_{Au}$/citrate buffer and $PEP_{Au}$/HEPES buffer solutions, respectively. As TEM images and distributions of nanoparticle size revealed, gold nanoparticles synthesized in $PEP_{Au}$/citrate buffer exhibited smaller average size compared to nanoparticles formed in $PEP_{Au}$/HEPES buffer (**Figure 2.11**). Citrate molecules are regularly used as capping and stabilizing agents for gold nanoparticles.[118,119] Highly negatively charged citrate molecules adhere to nanoparticle surfaces and prevent particle aggregation. The particles formed in citrate buffer were small (**Figure 2.11a, 2.11c**). However, HEPES is not a good particle stabilizing reagent. In the HEPES reaction, we expect that the resulting nanoparticles are capped only with $PEP_{Au}$, which led to faster particle growth and larger particle size (**Figure 2.11b, 2.11d**).

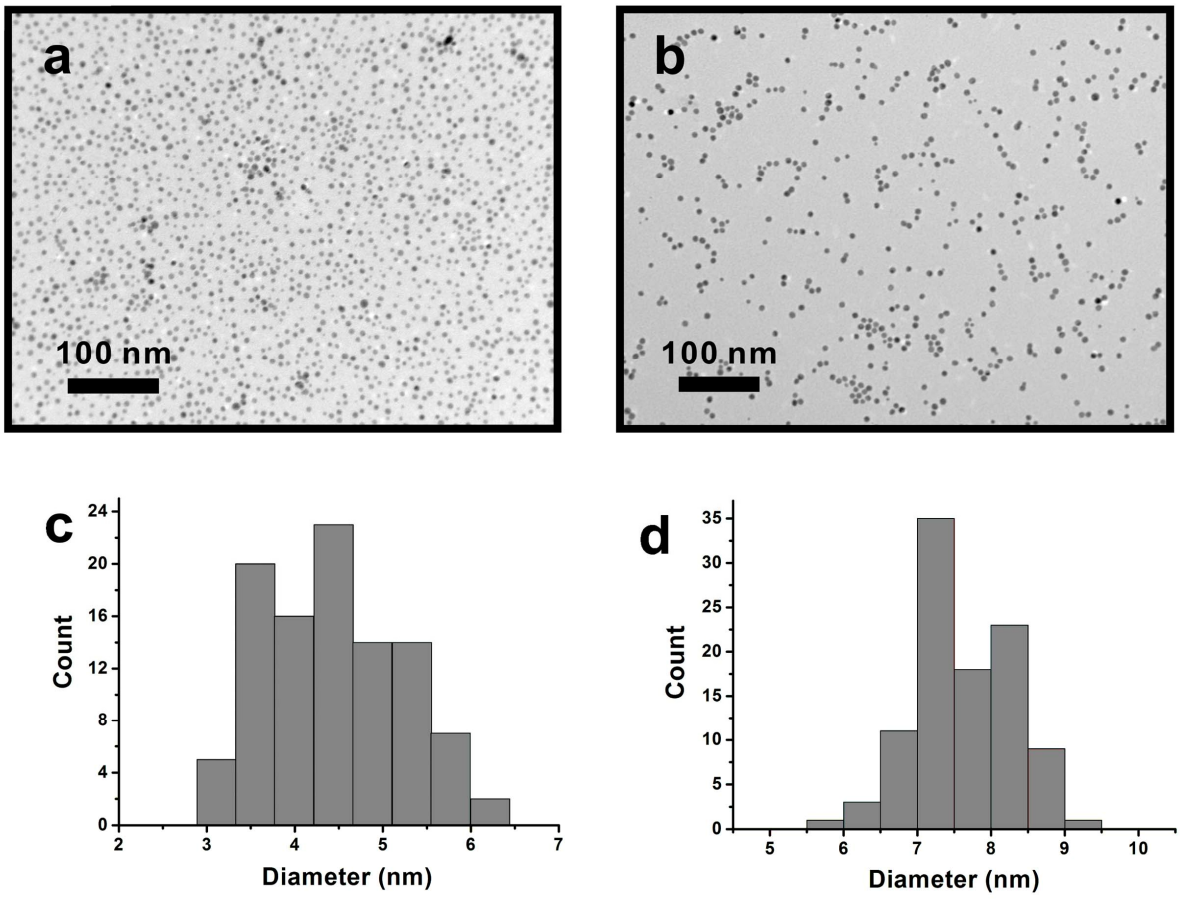


**Figure 2.11**. (a) TEM image of $PEP_{Au}$ capped gold nanoparticles in 0.10 M citrate buffer after one day incubation. (b) TEM image of $PEP_{Au}$ capped gold nanoparticles in 0.10 M HEPES buffer after one day incubation. (c) Distribution of nanoparticle size of (a) (based on 101 counts; diameter = 4.67 ± 0.76 nm). (d) Distribution of nanoparticle size of (b) (based on 101 counts; diameter = 7.59 ± 0.81 nm).

It is not difficult to speculate that the yield of gold helices in citrate buffer might be increased due to a large amount of small citrate-capped gold nanoparticles. Unfortunately, no well-organized nanoparticle superstructures were observed when the gold helices synthetic experiment was conducted in citrate buffer. We concluded that gold salts added to a solution of peptide in citrate buffer provides a large amount of small particles while gold salts added to solutions of peptide conjugates in HEPES buffer provide well-organized gold assemblies. We asked ourselves the following question: can we combine the merits of these two solutions by mixing citrate and HEPES buffer? To test our hypothesis, we mixed these two buffers at different volume ratios (HEPES buffer: citrate buffer=4:1, 3:2, 2:3, 1:4). When the volume ratio is HEPES: citrate=4:1 (i.e. 0.08 M HEPES and 0.02 M citrate buffer solution), TEM images revealed gold nanoparticle double helices consisting of spherical gold nanoparticles (diameter = 6.76 ± 0.89 nm). These helices exhibited regular pitch (~82 nm) and interhelical distance (~6.5 nm) and their length extended well into to the micrometer regime (**Figure 2.12**). The structural parameters of gold helices assembled under improved experimental condition were very similar to those of gold helices formed under conventional experimental condition (**Figure 2.13**).

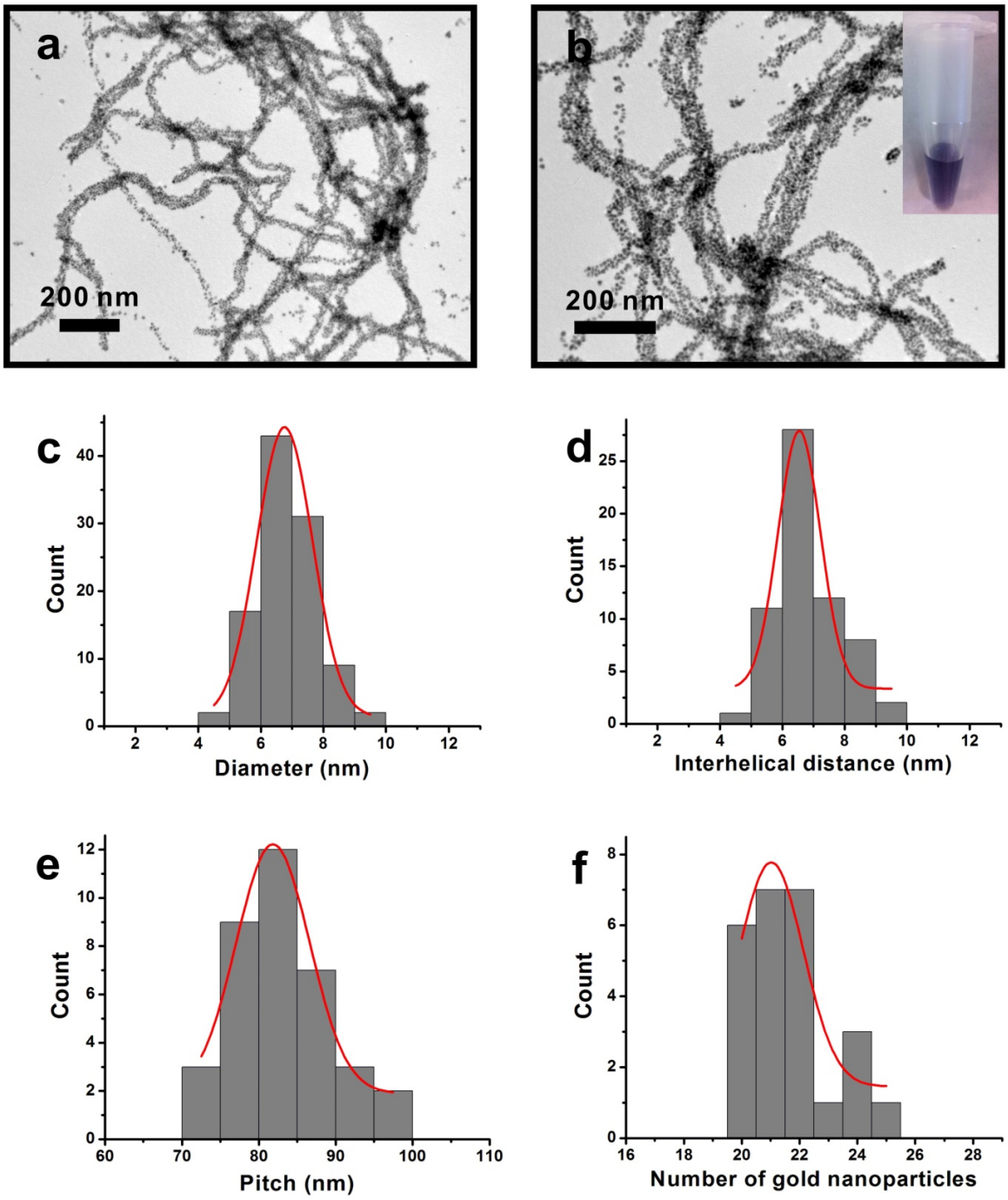


**Figure 2.12**. TEM images and statistics of gold nanoparticle double helices in 0.08 M HEPES and 0.02 M citrate buffer after one day incubation. (a) (b) TEM images of gold nanoparticle

double helices. (c) Distribution of nanoparticle size (based on 104 counts; diameter = 6.76 ± 0.89 nm). (d) Distribution of the interhelical distance (based on 62 counts; distance = 6.54 ± 0.68 nm). (e) Distribution of pitch (based on 36 counts; pitch = 81.83 ± 4.77 nm). (f) Distribution of number of gold nanoparticles per pitch of double helix (based on 25 counts; number = 21 ± 1).

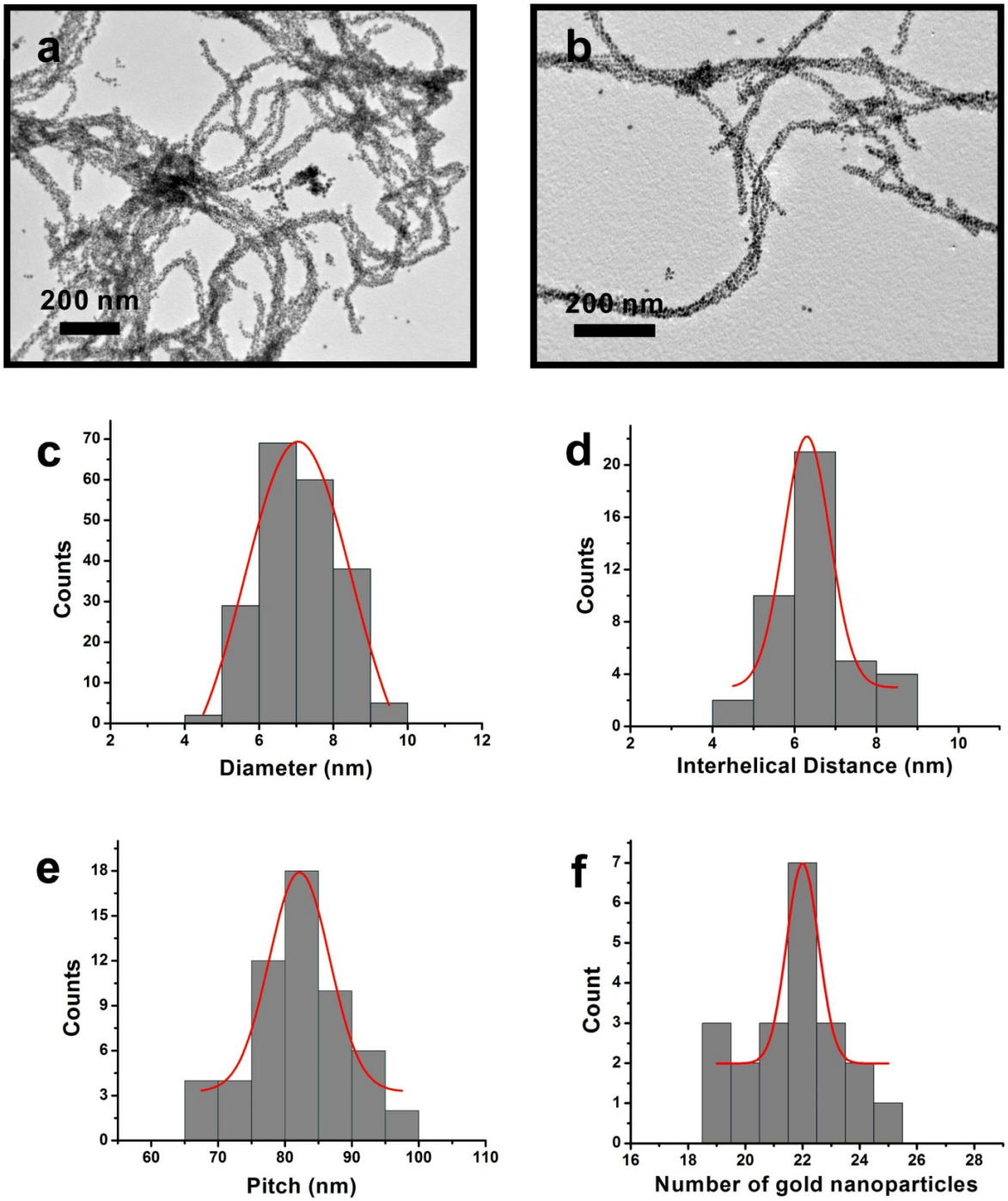


**Figure 2.13**. TEM images and statistics of gold nanoparticle double helices in 0.10 M HEPES buffer after one day incubation. (a) (b) TEM images of gold nanoparticle double helices. (c)

Distribution of nanoparticle size (based on 200 counts; diameter = 7.05 ± 1.44 nm). (d) Distribution of the interhelical distance (based on 42 counts; distance = 6.30 ± 0.56 nm). (e) Distribution of pitch (based on 56 counts; pitch = 82.17 ± 4.51 nm). (f) Distribution of number of gold nanoparticles per pitch of double helix (based on 30 counts; number = 22 ± 1).

Circular dichroism (CD) spectra were employed to examine if the yield of gold helices was increased. Chiral plasmonic nanomaterials such as gold nanoparticle double helices would exhibit well-defined CD signature within the visible region.[25,26] The characteristic CD signal intensity of chiral plasmonic helices is proportional to the concentration of helices if structural metrics are kept almost constant.[25,26] By carefully analysis of CD spectra of gold helices assembled in HEPES buffer and HEPES/citrate buffer, we observe that both of these CD spectra clearly show the same bisignate peak-dip shape, but the amplitudes of the CD signals are significantly different (**Figure 2.14**). The blue spectrum, corresponding to gold helices incubated in HEPES/citrate buffer, presented much stronger intensity than the red spectrum, corresponding to gold helices incubated in HEPES buffer. Hence, we concluded that the HEPES/citrate buffer indeed improved the yield of gold helices. In our future work, we will continuously explore new method to modify the gold precursors to generate size-controlled nanoparticles, which could be useful to assemble gold helices with varied structural parameters (including nanoparticle size, interhelical distance, internanoparticle distance and pitch).

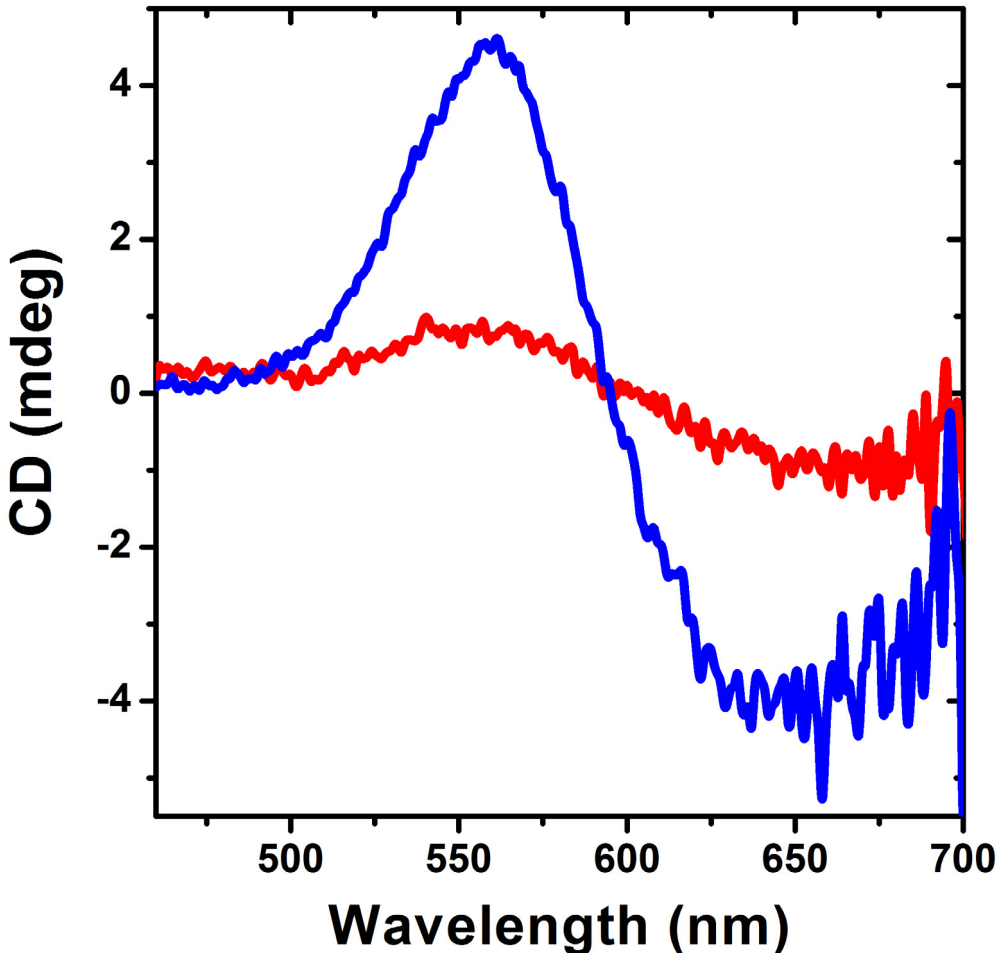


**Figure 2.14**. CD spectra of gold nanoparticle double helices one day after incubating in 0.1M HEPES buffer and 0.08 M HEPES/0.02 M citrate buffer, respectively. Red spectrum: gold helices incubated in 0.1 M HEPES buffer. Blue spectrum: gold helices incubated in 0.08 M HEPES/0.02 M citrate buffer. The optical path length is 1 mm.

## 2.3 CONCLUSION

Collectively, (1) small gold nanoparticles formed by $HAuCl_4$/TEAA (aq) solution and (2) dispersed peptide-conjugate molecules are key features to direct the assembly of peptides and gold nanoparticles into complex nanoparticle superstructures. This fundamental mechanistic insight will allow for rational design of various nanoparticle superstructures and for systematic and thoughtful control over their structural attributes.

## 2.4 EXPERIMENT SECTION

### 2.4.1 Materials and general methods

All solvents and chemicals were obtained from commercial sources and used without further purification. 0.1 M HEPES (4-(2-hydroxyethyl)-piperazineethanesulfonic acid) buffer was made with HEPES (free acid) powder (pH = 7.3 ± 0.1, pH was adjusted with NaOH; Promega) with water (NANOpure, Barnstead Diamond$^{TM}$ System.; 18.2 MΩ). All peptides were synthesized and purified by New England Peptide (NEP). Reverse-phase high pressure liquid chromatography (HPLC) was performed at ambient temperature with an Agilent 1200 liquid chromatographic system equipped with diode array and multiple wavelength detectors using a Grace Vydac protein C4 column (214TP1010, 1.0 cm × 25 cm). Matrix-assisted laser desorption ionization time-of-flight (MALDI-TOF) mass spectra were obtained on an Applied Biosystem Voyager System 6174 MALDI-TOF mass spectrometer using an α-cyano-4-hydroxy cinnamic acid (CHCA). Transmission electron microscopy (TEM) samples were prepared by pipetting one drop of solution onto a 3-mm-diameter copper grid with carbon film; 2% aqueous phosphotungstic acid. TEM was conducted on a JEOL 200CX instrument operated at 200kV and images were collected using a Gatan CCD image system. . Samples for atomic force microscopy (AFM) were prepared on freshly peeled MICA substrates that were treated with a 1% solution of 3-aminopropyl trimethoxysilane.[120] Tapping-mode AFM was performed on an Asylum MFP-3D. Peptide powders were mounted on a Bruker X8 Prospector Ultra diffractometer equipped with a Cu IMuS microfocus source (λ = 1.54184 Å) operated at 45 kV, 0.65ma). The X-ray intensities were measured at 298K; the detector was placed at a distance of 4 cm from the sample. A 360$^{o}$ Phi scan was collected for 60 seconds. The Brulter Program XRD$^{2}$ Eval was used to integrate the

powder pattern. Circular dichroism measurement was conducted on a Olis DSM 17 CD spectrometer. The scan rate was 8 nm/min. All CD was carried out in a 0.1 M HEPES buffer with a quartz cuvette (0.1 cm path length) at 25 °C. 2 µl of 0.1 M NaCl, 0.1 M $CaCl_2$ and 0.1 M $HAuCl_4$ aqueous solutions were added to 250 µl HEPES buffer in the presence of peptide conjugates with the concentration of ~ $3.75 \times 10^{-8}$ mol, respectively. After incubating 30 mins, samples are measured by CD spectrometer.

### 2.4.2 Preparation of peptide conjugate and gold nanoparticle superstructures

$C_{12}$-$PEP_{Au}$ peptide conjugate was synthesized, purified, and characterized using a published protocol.[66] Lyophilized $C_{12}$-$PEP_{Au}$ (~ $3.75 \times 10^{-8}$ mol) peptide conjugate was completely dissolved in 0.1M HEPES buffer (0.25 ml; pH = 7.3 ± 0.1) in a plastic vial. This solution was allowed to incubate at room temperature (30 min). Thereafter, a solution of 0.1M chloroauric acid ($HAuCl_4$) in 1.0 M triethylammonium acetate (TEAA; pH = 7.0) buffer was incubated for 10min at room temperature and followed by a centrifugation at 5k rpm. 2 µl of the supernatant was added to the peptide conjugate solution. The resulting mixture was vortexed for a few seconds as soon as the $HAuCl_4$/TEAA solution was added and then left undisturbed at room temperature (2 h).

### 2.4.3 Preparation of free gold nanoparticles

A gold ion precursor solution was prepared: 0.1M chloroauric acid ($HAuCl_4$) in 1.0 M triethylammonium acetate (TEAA; pH = 7.0) buffer was incubated for 10minutes at room temperature. Thereafter, this mixture was centrifuged (10 min., 5K rpm). Lyophilized $PEP_{Au}$ (~ $3.75 \times 10^{-8}$ mol) was completely dissolved in 250 µl 0.10 M HEPES and 0.10 M citrate buffer

(pH=7.3±0.1) in a plastic vial, respectively. This peptide solution was allowed to incubate for 30 minutes. Thereafter, 2 µl of the supernatant of the centrifuged gold ion precursor solution was added to the peptide conjugate solution. The mixture was vortexed for a few seconds and then left undisturbed at room temperature for 1 day. Solution turned to red after ~30 minutes.

### 2.4.4 Preparation of high yielded gold nanoparticle double helices

A gold ion precursor solution was prepared: 0.1M chloroauric acid ($HAuCl_4$) in 1.0 M triethylammonium acetate (TEAA; pH = 7.0) buffer was incubated for 10minutes at room temperature. Thereafter, this mixture was centrifuged (10 min., 5K rpm). Lyophilized $C_{12}$-L-$PEP_{Au}$ (~ $3.75 \times 10^{-8}$ mol) was completely dissolved in 250 µl 0.08 M HEPES and 0.02 M citrate buffer (pH=7.3±0.1) in a plastic vial. This peptide solution was allowed to incubate for 30 minutes. Thereafter, 2 µl of the supernatant of the centrifuged gold ion precursor solution was added to the peptide conjugate solution. The mixture was vortexed for a few seconds and then left undisturbed at room temperature for 1 day. Gold nanoparticle double helices were clearly observed as product after ~1 hour.

# 3.0 TAILORABLE PLASMONIC CIRCULAR DICHROISM PROPERTIES OF HELICAL NANOPARTICLE SUPERSTRUCTURES

This work, written in collaboration with Martin G. Blaber, Gongpu Zhao, Peijun Zhang, H. Christopher Fry, George C. Schatz and Nathaniel L. Rosi*, was published in *Nano Lett.,* **2013**, 13(7), 3256. 

Martin Blaber and George Schatz performed the theoretical modeling work, Gongpu Zhao and Peijun Zhang performed the electron tomography work, and H. Christopher Fry provided peptide synthesis.

## 3.1 INTRODUCTION

In Chapter 2 we have briefly introduced circular dichroism spectra which were applied to determine the relative yields of gold nanoparticle double helices formed from two different reaction conditions. In this Chapter, we will detail the chirooptical property studies of gold nanoparticle double helices.

Chiral plasmonic nanoparticle superstructures are attractive synthetic targets because of their potential applications as circular polarizers, chirooptical sensors, and negative refraction materials.[24,121-124] One of the most effective ways to finely adjust the chirooptical properties of such structures is to precisely control their metrics and structural parameters. Here we utilize a

peptide-based methodology to prepare a diverse collection of double-helical gold nanoparticle superstructures having controllable handedness and structural metrics. These materials exhibit well-defined circular dichroism (CD) signatures at visible wavelengths owing to the collective dipole-dipole interactions between the nanoparticles. We couple theory and experiment to show how tuning the metrics and structure of the helices results in predictable and tailorable chirooptical properties. Finally, we experimentally and theoretically demonstrate that the intensity, position, and nature of the chirooptical activity can be carefully adjusted via silver overgrowth. These studies illustrate the utility of peptide-based nanoparticle assembly platforms for designing and preparing complex plasmonic materials with tailorable optical properties.

Many approaches have been utilized to prepare chiral nanoparticle assemblies.[25,26,66,96,97,125-137] Of these, biomolecule-based approaches are the most common, because biomolecules, such as peptides and nucleic acids, can both be programmed to assemble into chiral architectures and also designed to bind or associate to specific nanoparticle surfaces.[25,66,96,97,125-132] Helical structures represent a unique sub-category of chiral nanoparticle assemblies.[25,66,97,130,132,134,136-138] Following early reports detailing peptide-directed assembly of helical gold nanoparticle superstructures[66] and nucleic-acid-directed assembly of helical nanoparticle archite,ctures[130] several groups employed peptides or nucleic acids to prepare helical nanoparticle superstructures that exhibit targeted chirooptical properties.[25,97,132] In order to control and tailor the chirooptical properties of helical nanoparticle assemblies, an assembly methodology should allow one to precisely and simultaneously control the position, organization, and size of the nanoparticles within the nanoparticle superstructure product.

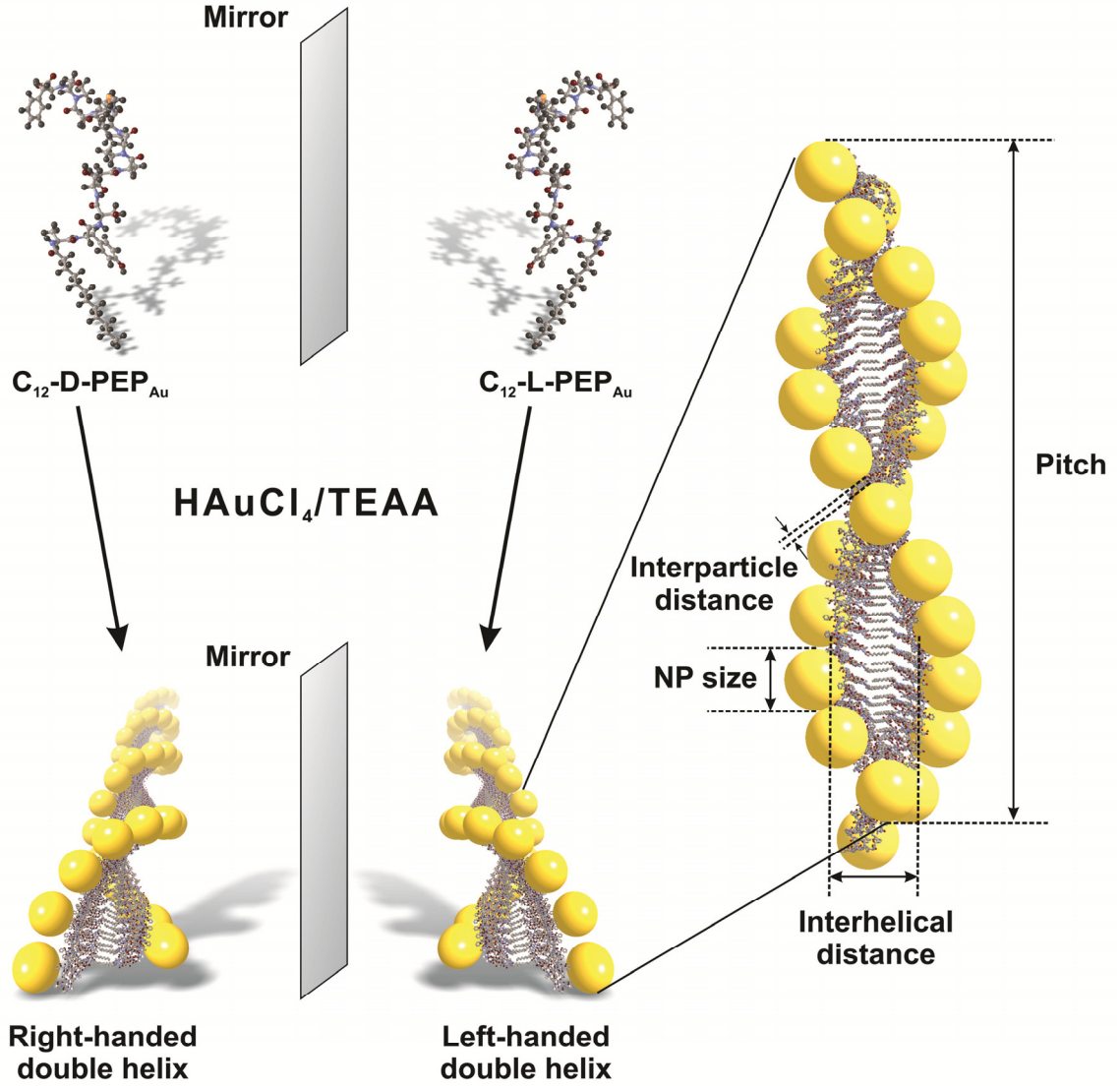


**Figure 3.1.** Scheme detailing the preparation of enantiomeric gold nanoparticle double helices. $C_{12}$-D-$PEP_{Au}$ and $C_{12}$-L-$PEP_{Au}$, when mixed with a gold precursor solution and HEPES buffer, direct the formation of, respectively, right- and left-handed double helices. Each double helix has quantifiable metrics, including nanoparticle size, interparticle distance, pitch, and interhelical distance.

We recently reported a conceptual framework and synthetic methodology for designing and preparing nanoparticle superstructures that utilizes carefully designed peptide conjugate molecules for precisely directing the synthesis and assembly of nanoparticles.[66] We demonstrated that these strategies and methods are very useful for targeting, preparing, and tailoring the metrics and structural parameters of a diverse family of 1D gold nanoparticle superstructures, including chiral double helices[66,139] and linear chains,[140] as well as a collection of discrete hollow spheres consisting of either gold[141,142] or cobalt-platinum nanoparticles.[143] The precision of nanoparticle placement and the structural integrity of the resulting nanoparticle superstructures are key distinguishing features of this methodology. In this report, we utilize a peptide-based toolkit to prepare a unique and diverse collection of chiral gold nanoparticle double-helical superstructures comprising both left- and right-handed structures with tailorable nanoparticle sizes (**Figure 3.1**) and compositions. We demonstrate for the first time that these materials exhibit chiral plasmonic optical behavior that can be carefully tuned by adjusting their structure and composition.

## 3.2 RESULTS AND DISCUSSION

$C_{12}$-L-$PEP_{Au}$ conjugates ($C_{12}$-$PEP_{Au}$ = [$C_{11}H_{23}CO$]-AYSSGAPPMPPF), comprising L amino acids, were used to construct left-handed gold nanoparticle double helices using established methods.[66,139] In previous work, we demonstrated that $C_{12}$-L-$PEP_{Au}$ conjugates, under certain conditions, assemble into left-handed twisted nanofibers having a regular pitch of ~84 nm.[66] We reasoned that the left-handed helicity of these fibers resulted from the chirality of the L-amino acid within the $C_{12}$-L-$PEP_{Au}$ conjugates. Therefore, $C_{12}$-D-$PEP_{Au}$ should assemble into compositionally identical fibers as $C_{12}$-L-$PEP_{Au}$, but with a right-handed twisted ribbon structure. We thus prepared $C_{12}$-D-$PEP_{Au}$ conjugates and used these to construct right-handed gold nanoparticle double helices.

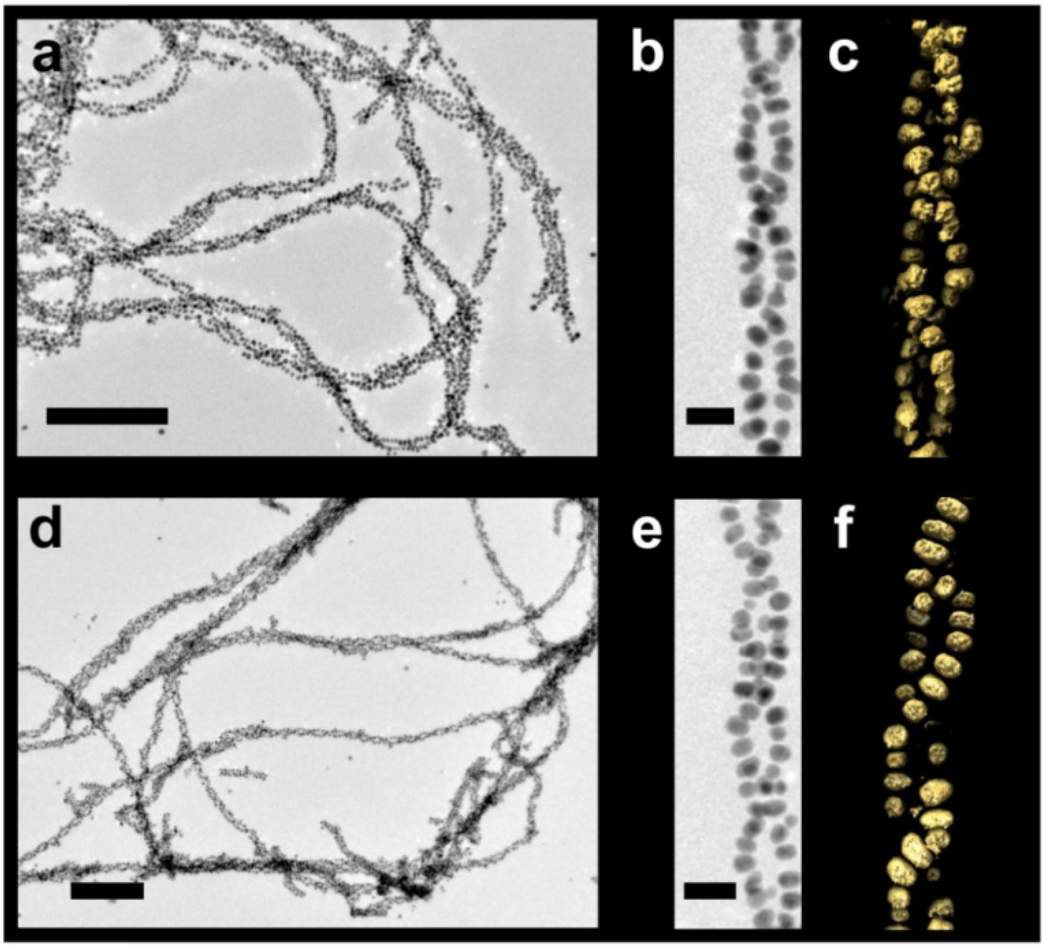


**Figure 3.2.** Transmission electron microscopy (TEM) and electron tomography data. TEM images of left- and right-handed (a,b and d,e, respectively) gold nanoparticle double helices (scale bars: a and d, 200 nm ; b and e, 20 nm). The 3-D surface renderings of the tomographic volumes reveal the left- or right-handed nature of double helices (c and f, respectively).

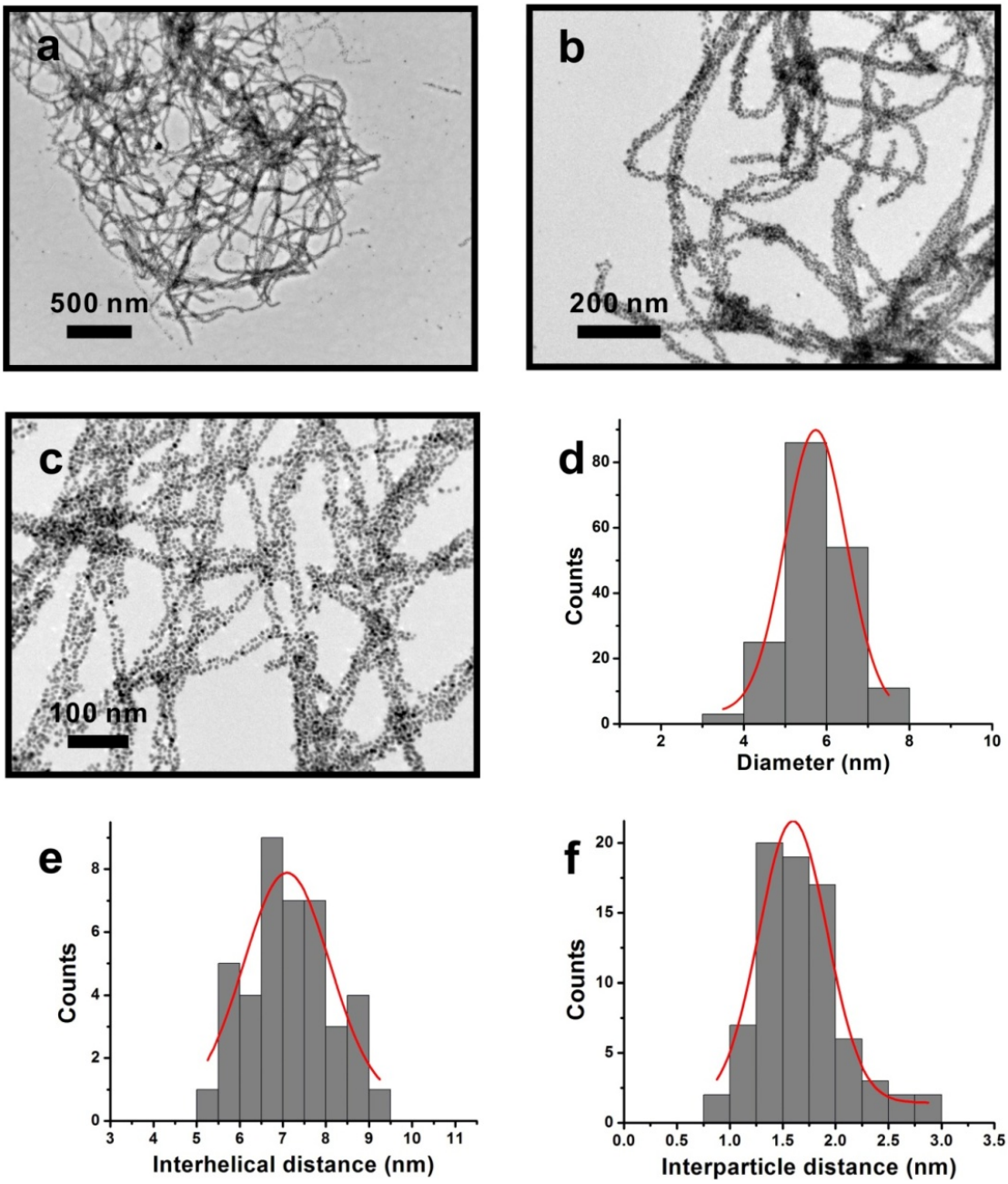


**Figure 3.3**. Additional TEM images (a-c)of left-handed nanoparticle double helices after one hour incubation. (d) Distribution of sizes of gold nanoparticles within the double helix (based on 179 counts; diameter = 5.74 ± 0.75 nm). (e) Distribution of the interhelical distance between particles along the width of the left-handed gold nanoparticle double helices (based on 41 counts;

distance = 7.09 ± 1.00 nm). (f) Distribution of the edge-to-edge distance betweennanoparticles along the longitudinal dimension of the gold nanoparticle double helices(based on 78 counts; distance = 1.60 ± 0.33 nm).

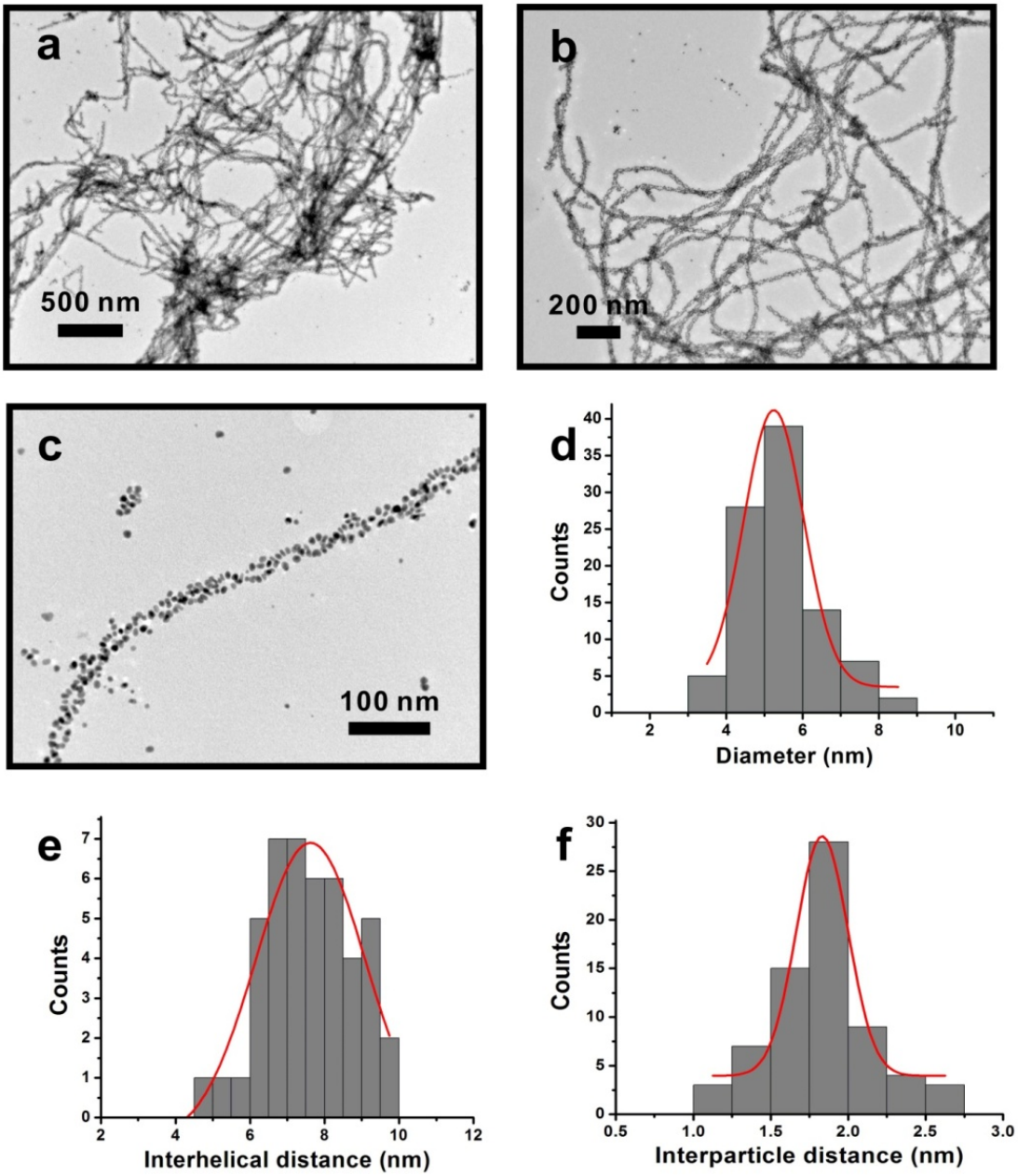

**Figure 3.4**. Additional TEM images (a-c)of right-handed nanoparticle double helices after one hour incubation. (d) Distribution of size of gold nanoparticles within the double helix (based on 95 counts; diameter = 5.25 ± 0.79 nm).(e) Distribution of the interhelical distance between particles along the width of the right-handed gold nanoparticle double helices (based on 45 counts; distance = 7.62 ± 1.48 nm).(f) Distribution of the edge-to-edge distance betweennanoparticles along the longitudinal dimension of the gold nanoparticle double helices(based on 69 counts; distance = 1.83 ± 0.17 nm).

Transmission electron microscopy (TEM) studies confirm that both samples of double helices consist of spherical gold nanoparticles (left-handed helices diameter = 5.74 ± 0.75 nm; right handed helices diameter = 5.25 ± 0.79 nm), exhibit a regular pitch (~84 nm), interhelical distance (~7.5 nm) and interparticle distance (~1.7 nm), extend lengthwise well into the micrometer regime, and remarkably, have very few defects (**Figure 3.2a-b, Figure 3.2d-e, Figure 3.3-3.4**). Tomograms constructed using electron tomography data definitively reveal the handedness of these structures: $C_{12}$-L-$PEP_{Au}$ derived double helices are left-handed (**Figure 3.2c**) and $C_{12}$-D-$PEP_{Au}$ derived double helices are right-handed (**Figure 3.2f**). To our knowledge, this is the first reported example of using a peptide-based nanoparticle assembly strategy to control the handedness of helical nanoparticle superstructures.

The gold nanoparticle double helices were incubated for one day in the gold salt precursor solution until the gold nanoparticles grew to ~8 nm in diameter (interhelical distance ~6.5 nm; interparticle distance ~1.4 nm; pitch ~84 nm; see **Figure 3.1**) (**Figure 3.5-3.8**). Circular dichroism (CD) spectroscopy was employed to examine the optical activity of the assembled structures in solution. In the ultraviolet region, the left-handed and the right-handed double helices have a negative and positive absorbance respectively at ~220nm (**Figure 3.9**), which results from the chirality of the self-assembled peptide conjugates underlying the gold nanoparticle assemblies. We expected that the double-helical structures would exhibit visible chirooptical activity at wavelengths corresponding to the collective surface plasmon resonance of the assembled gold nanoparticles.

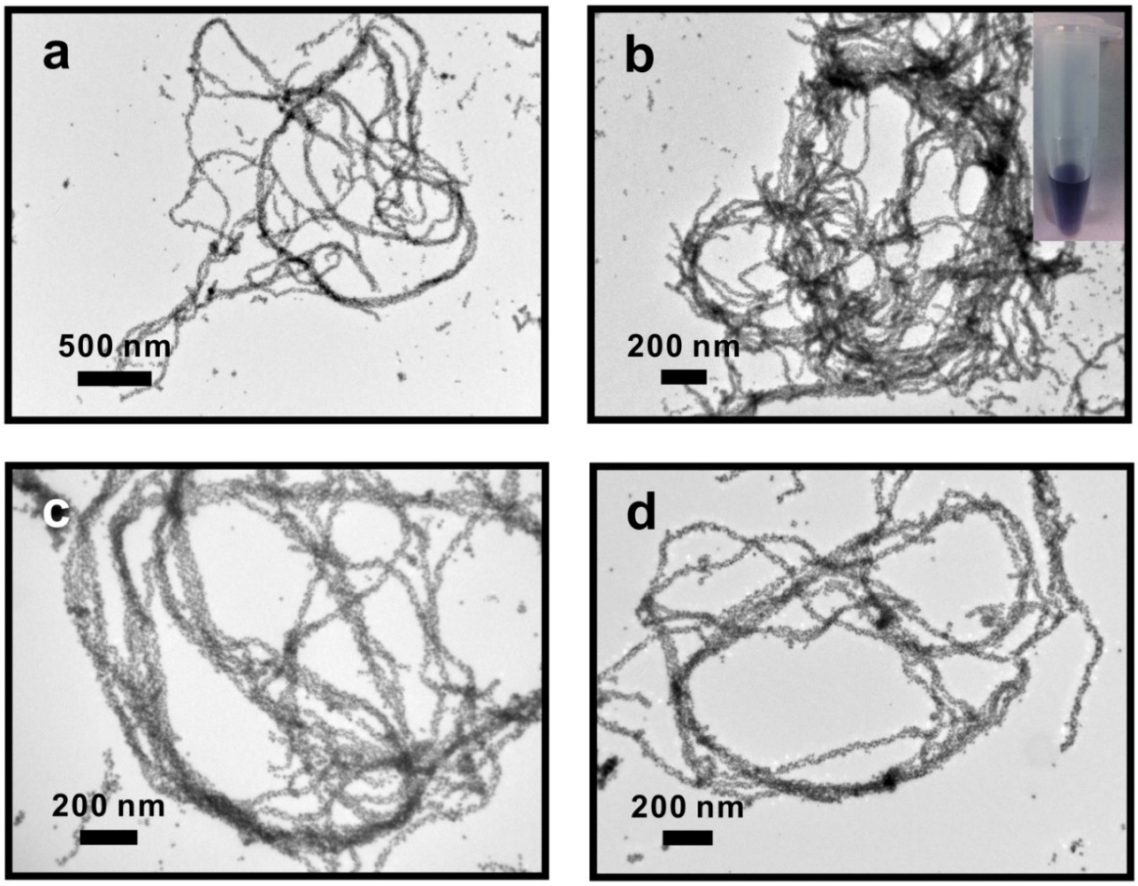


**Figure 3.5**. Additional TEM images (a-d) of left-handed gold nanoparticle double helices at different magnifications. The inset image of vial shows the purple color of gold nanoparticle double helices solution after one day incubation.

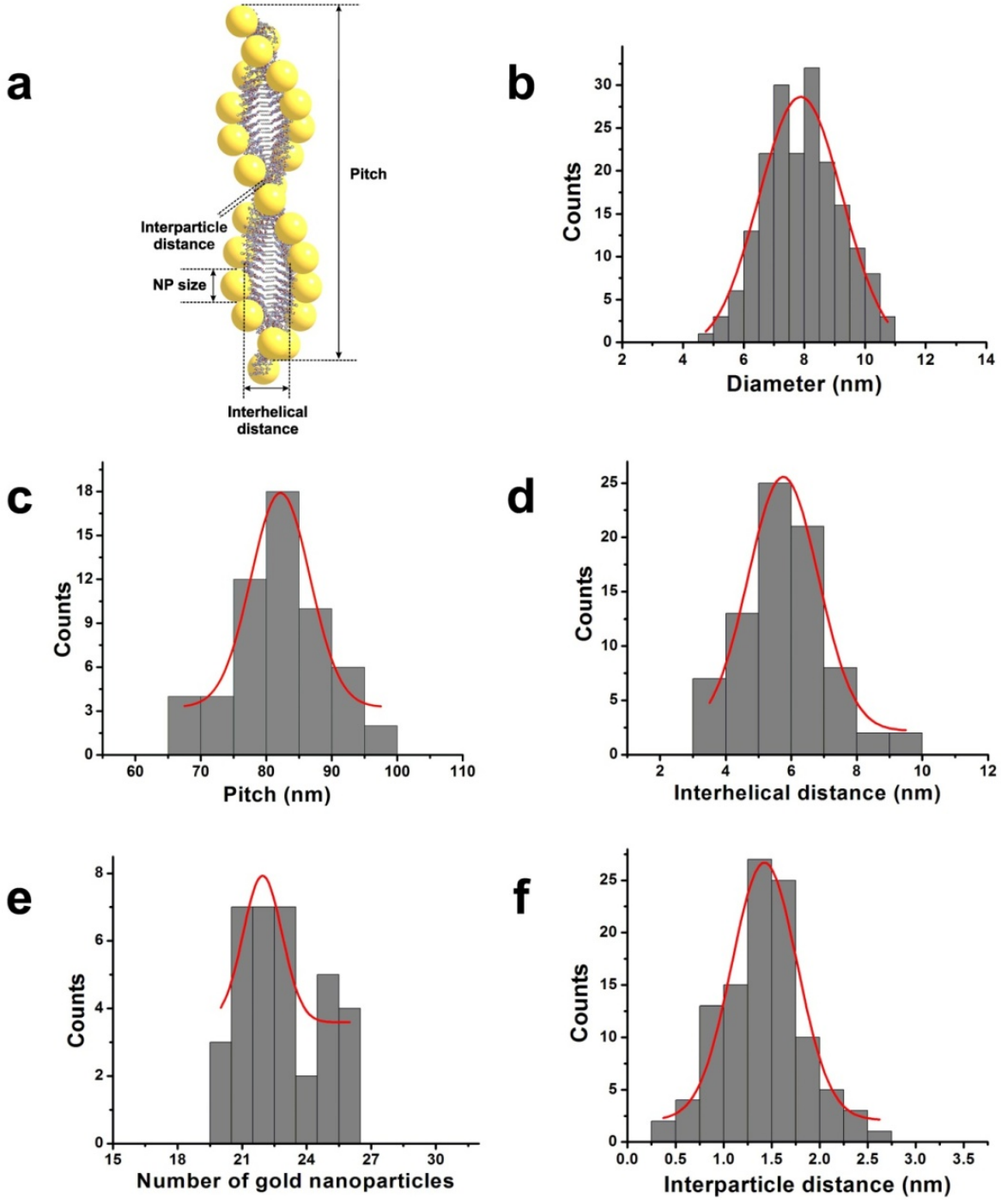


**Figure 3.6**. Statistics of left-handed gold nanoparticle double helices after one day incubation based on TEM images. (a)Illustration of left-handed gold nanoparticle double helix with relevant metrics indicated.(b) Distribution of nanoparticle size (based on 188 counts; diameter = 7.88 ±

1.38 nm). (c) Distribution of pitch (based on 56 counts; pitch = 82.17 ± 4.51 nm). (d) Distribution of the interhelical distance(based on 78 counts; distance = 5.75 ± 1.07 nm). (e) Distribution of number of gold nanoparticles per pitch of double helix (based on 35 counts; number = 22 ± 1).(f) Distribution of the edge-to-edge distance betweennanoparticles along the longitudinal dimension of the gold nanoparticle double helices(based on 105 counts; distance = 1.43 ± 0.34 nm).

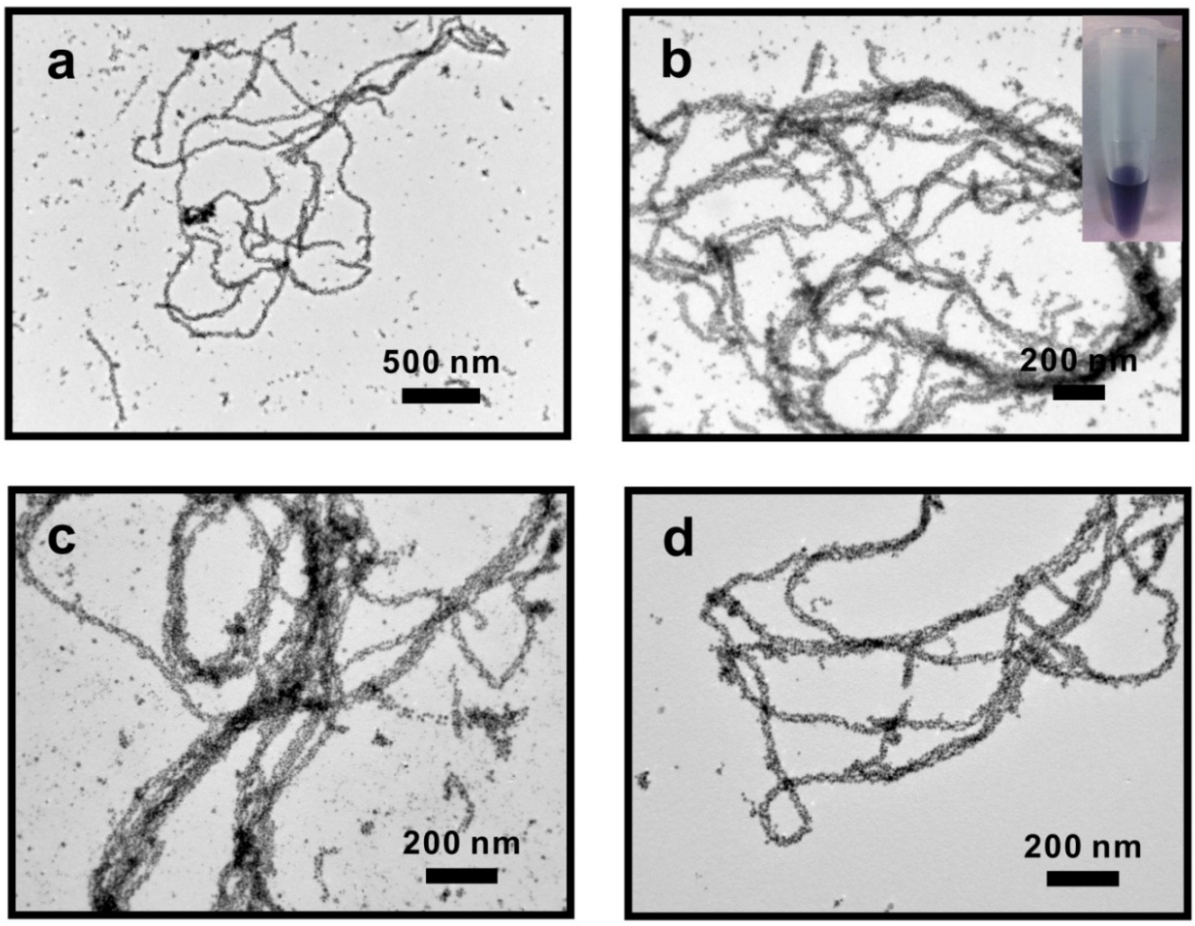


**Figure 3.7**. Additional TEM images (a-d)of right-handed gold nanoparticle double helices. The vial in the inset image shows the purple color of gold nanoparticle double helices solution after one day incubation.

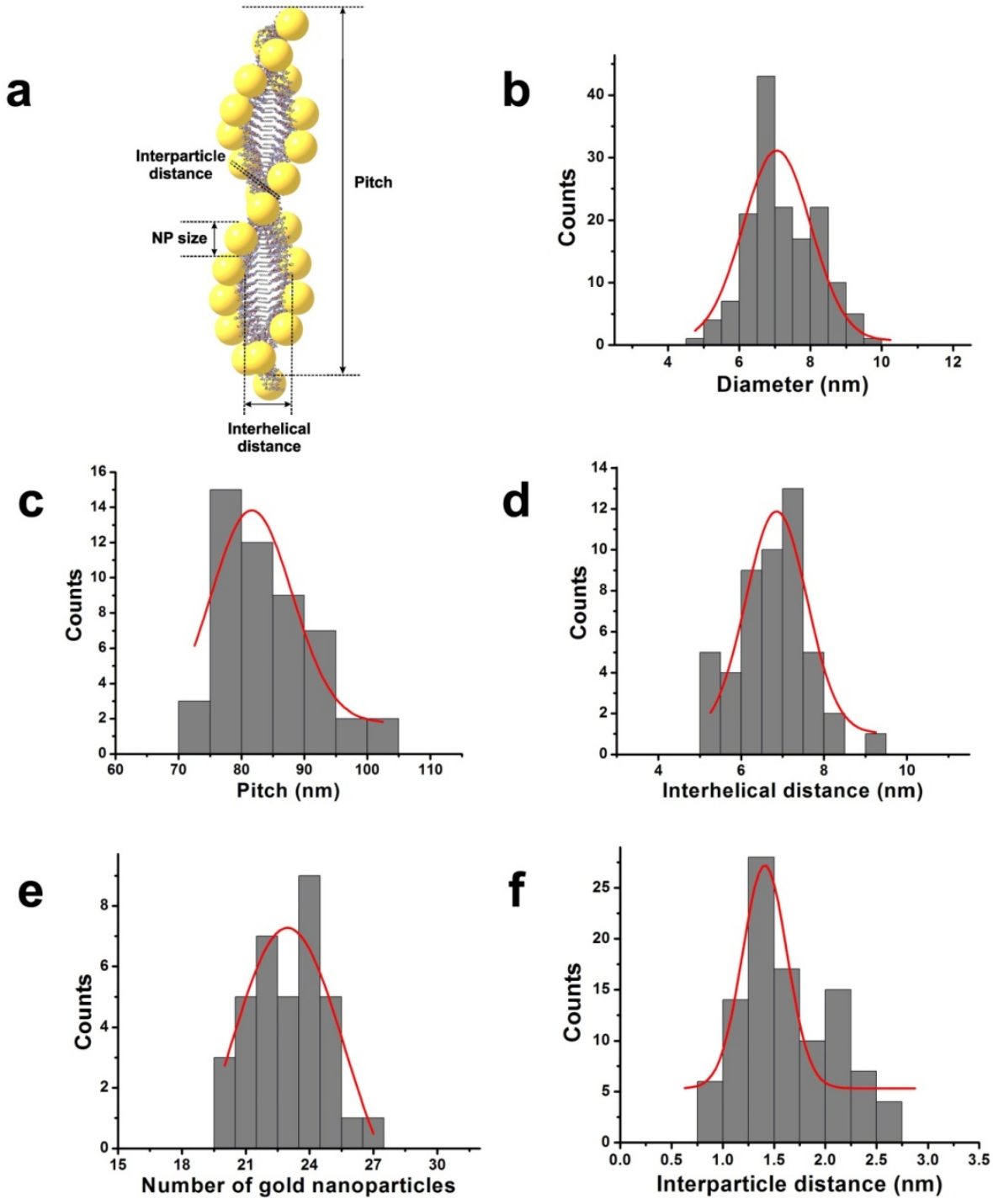


**Figure 3.8**. Statistics of right-handed gold nanoparticle double helices after one day incubation based from TEM images. (a)Illustration of right-handed gold nanoparticle double helix with

relevant metrics indicated.(b) Distribution of nanoparticle size (based on 153 counts; diameter = 7.06 ± 0.95 nm). (c) Distribution of pitch (based on 50 counts; pitch = 81.64 ± 6.42 nm). (d) Distribution of the interhelical distance(based on 49 counts; distance = 6.85 ± 0.74 nm). (e) Distribution of number of gold nanoparticles per pitch of double helix (based on 36 counts; number = 23± 2).(f) Distribution of the edge-to-edge distance betweennanoparticles along the longitudinal dimension of the gold nanoparticle double helices(based on 101 counts; distance = 1.41 ± 0.22 nm).

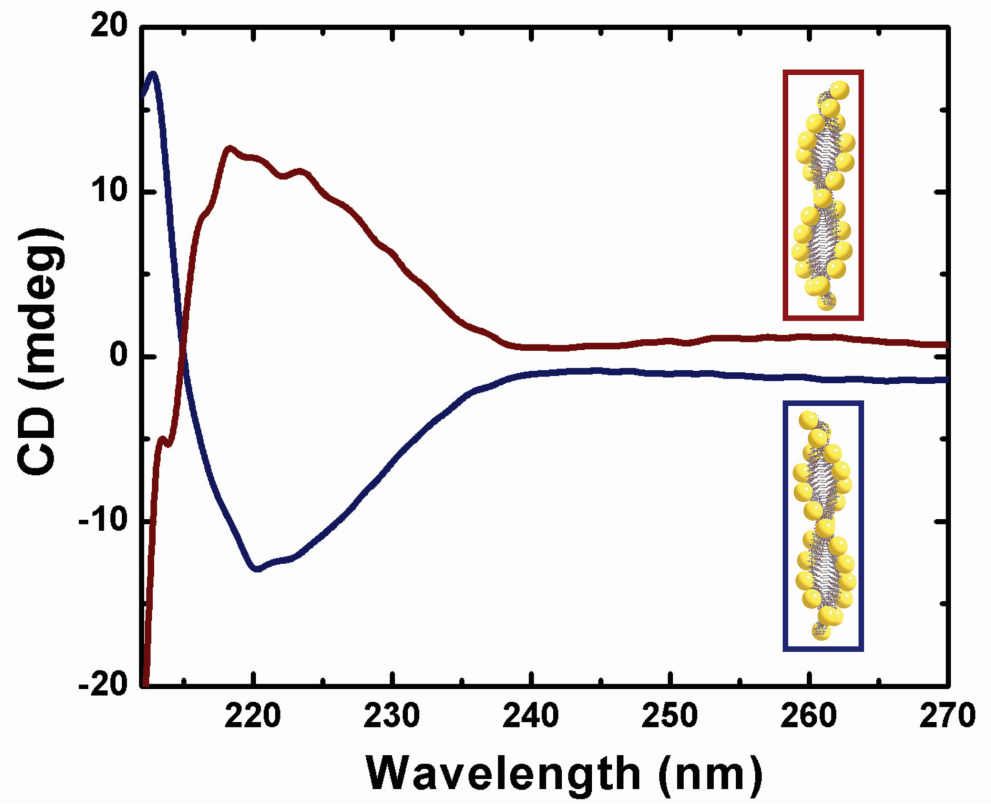


**Figure 3.9.** Circular Dichroism (CD) spectra of solutions of left- (blue) and right-handed (red) gold nanoparticle double helices after one day incubation. The path length of the light is 1 mm.

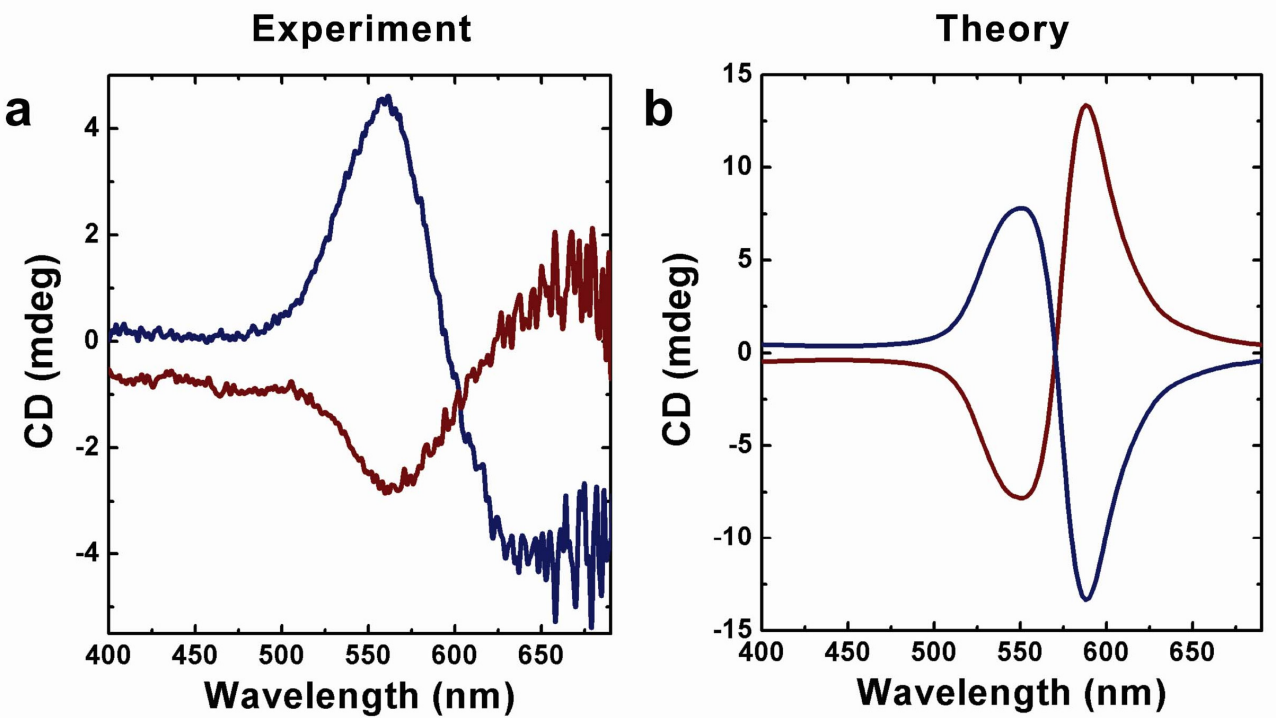


**Figure 3.10.** Experimental and theoretical circular dichroism data for left- and right-handed gold nanoparticle double helices. (a) CD spectra of left-handed (blue) and right-handed (red) gold nanoparticle double helices. Left-handed and right-handed double helices result in vertically mirrored CD signals at 562 nm. (b) CD spectra predicted by the theoretical model exhibit similar bisignate signatures to (a) in the visible region. The optical path length is 1 mm.

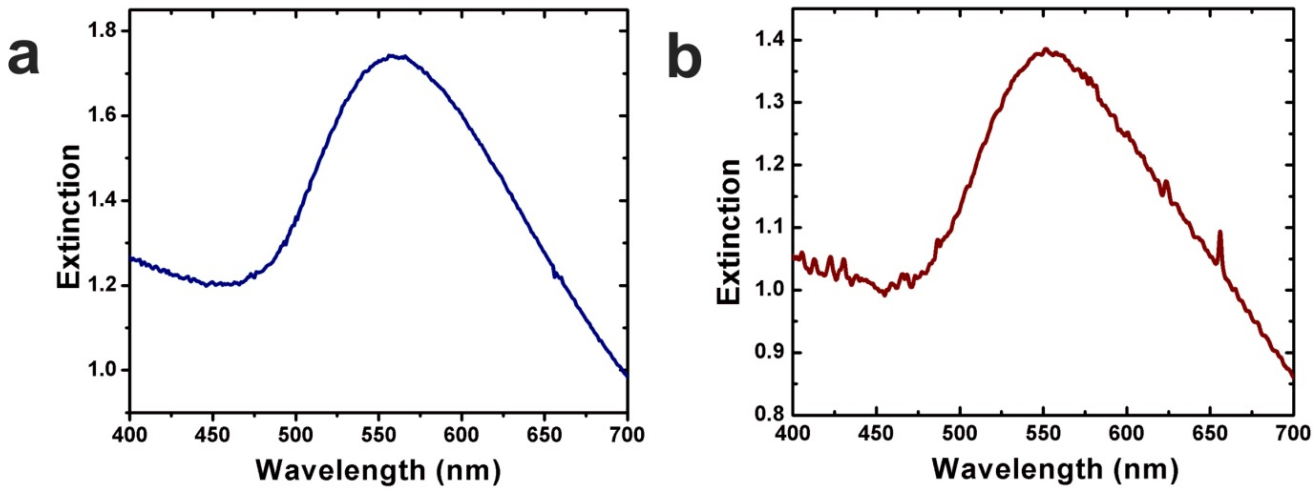


**Figure 3.11**. (a)UV-Vis spectrum of left-handed gold nanoparticle double helices in solution after one day incubation. (b) UV-Vis spectrum ofright-handed goldnanoparticle double helices in solution after one day incubation. The absorbance maximum is observed at 556 nm (blue) and 552 nm (red), which is consistent with our previous work.[66] The peaks are red-shifted compared to reported monodisperse gold colloidal solutionsof nanoparticles similar in size to what we observewithin the nanoparticle double helices[144].This effect results from the coupling of the surface plasmons between assembled gold nanoparticles. The path length of the light is 10 mm.

Indeed, the left- and right-handed helices respectively, produce vertically-mirrored negative and positive CD signals at 562 nm (**Figure 3.10a**), consistent with the existence of the collective surface plasmon resonance (**Figure 3.11**). Others have observed visible plasmonic circular dichroism for peptide-capped gold nanoparticles;[98] however, we do not observe a CD signal in the visible range for non-assembled $PEP_{Au}$-capped gold nanoparticles,[65] (**Figure 3.12**) which suggests that the observed circular dichroism effect results from the spatial arrangement of the gold nanoparticles within the superstructures. Having measured the visible chirooptical activity of these nanoparticle superstructures, we next used computational methods to first model the experimental results and then predict how changing the structural metrics of the assemblies might affect the chirooptical response. This work is similar to recent studies,[123,145] but we utilize a different approach.

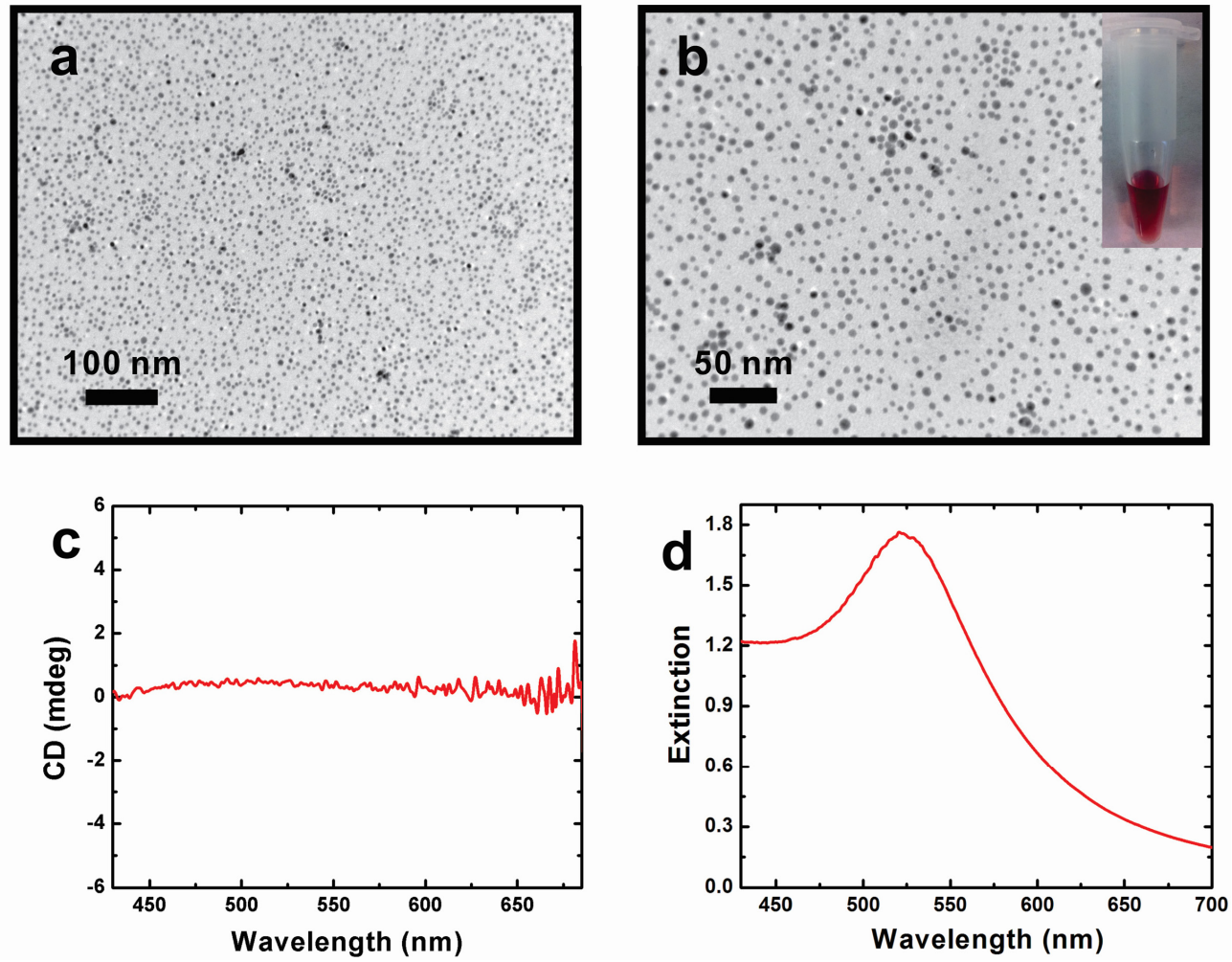


**Figure 3.12**. (a),(b)TEM images of free gold nanoparticles formed using $PEP_{Au}$ instead of $C_{12}$-L-$PEP_{Au}$.(Inset image shows the typical red colour of the free gold nanoparticle colloidal solution) (c) CD spectrum of the free gold nanoparticle colloidal solution.There is no significant CD feature within the visible light region. The path length of the light is 1mm. (d) UV-Vis spectrum of the free gold nanoparticle colloidal solution. It shows a typical surface plasmon peak at 520 nm.

Small metal nanoparticles interact primarily through dipole-dipole interactions, but higher order multipoles contribute to the position and strength of the ensemble localized surface plasmon resonance (LSPR) as the interparticle distance is reduced. For this reason, we chose to model the chiral ensemble of metallic nanoparticles within the framework of the discrete dipole approximation (DDA).[146,147] In this method, individual particles are described by thousands of dipoles, such that higher order multipole effects are accounted for. The CD response is determined by averaging the difference in extinction cross sections, *Q,* between left ($|\mathrm{L}\rangle$) and right ($|\mathrm{R}\rangle$) circularly polarized plane waves for many orientations of the helical superstructure:

$$\mathrm{CD} = \left\langle Q_{|\mathrm{L}\rangle} - Q_{|\mathrm{R}\rangle} \right\rangle_{\Omega} \qquad (1)$$

where Ω indicates the set of orientations of the helix with respect to the incident wave-vector (see the supplementary text for details on the choice of orientations[148-151]). A number of experimental and theoretical studies have been presented on one dimensional chains of spherical gold[152-155] and silver[154] nanoparticles, and simulations show that in general, the LSPR shift associated with increasing the length of a 1D chain of particles saturates at around 10 particles.[156,157] For this reason, we have chosen to simulate a short helix, consisting of only a single helical period of around 80 nm in length, or a minimum of 12 spheres per helix. The computational model accurately reproduces the experimental CD spectrum of the gold nanoparticle double helices (**Figure 3.10b**), particularly for the ~560 nm CD signature, which arises when the incident field propagates parallel to the helical axis. The red-shifted ~600 nm feature appears when the field propagates perpendicular to the helical axis. In the experiment, this feature appears further to the red (**Figure 3.10a**), primarily due to variations in interparticle distance. **Figure 3.13** shows that averaging the CD spectra from helices with interparticle

distances ranging from 1.0 nm to 2.0 nm leaves the 560 nm feature unchanged but causes the ~600 nm peak to red shift.

In 1D chains of particles, the longitudinal plasmon resonance ( $\lambda_p$ , polarization parallel to the long axis of the chain) is related to the plasmon resonance of an individual sphere in the chain ( $\lambda_s$ ) and the ratio of the particle diameter (*D*) to the interparticle gap (*G*) via the empirical relation[157]:

$$\lambda_p = \lambda_s A\left(\frac{D}{G}\right)^B + \lambda_s, \qquad (2)$$

Where *A* is a proportionality constant (typically around 0.01 $nm^{-1}$) and *B* is an exponent that depends on the length of the chain, and for sufficiently long chains, approaches 1 from below. For this reason, we posit that the interparticle spacing along the axis of the helix will play a larger role in determining the optical response of the assembly than the interhelical distance. Indeed, simulations show that when the interhelical distance is increased from the experimental mean of approximately 7.0 nm, only small variations in the position and intensity of the CD spectrum are evident (**Figure 3.14**). If the interhelical distance is reduced to 4.0 nm, the transverse resonance increases in magnitude by approximately 2%, and a slight blue shift of the high energy peak is apparent.

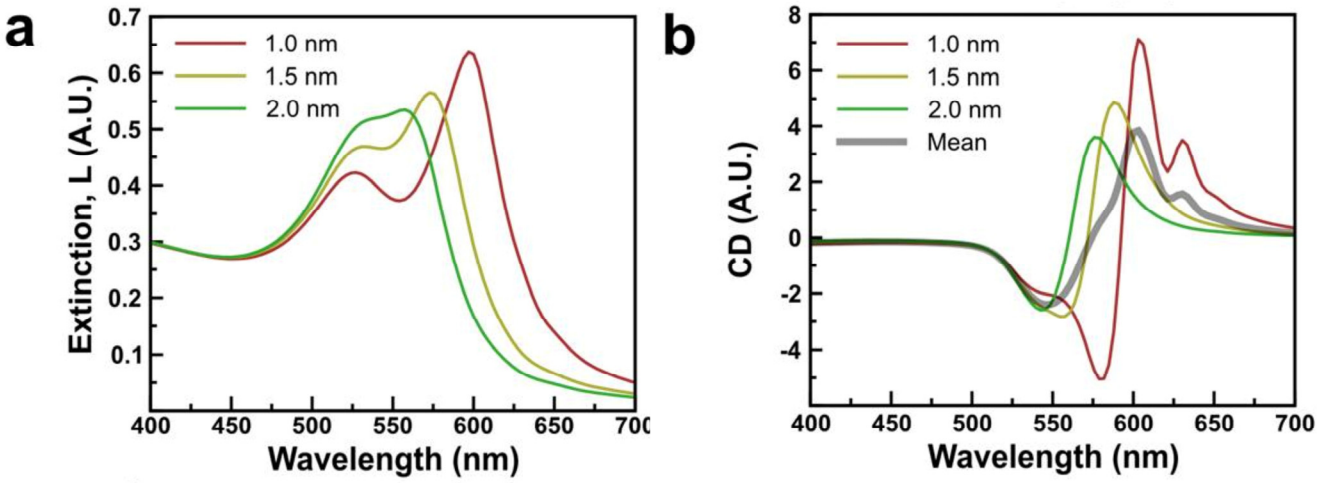


**Figure 3.13**. **Interparticle distance effect on CD response.** The simulated effect of interparticle distance on the extinction (a) and CD (b) of a right-handed double helix ensemble comprising 22 spheres. The double peaks in (a) represent the transverse surface plasmon resonance at around 525 nm (where the incident field polarization is perpendicular to the helical axis), and the longitudinal mode (where the incident field polarization is parallel to the helical axis), which red-shifts as the interparticle spacing decreases. See Equation 2 in the main text. The interparticle distance was sampled at 1.0 nm, 1.5 nm, the approximate experimental value, and 2.0 nm. The interhelical spacing is 7.0 nm and the sphere diameter is 8.0 nm.

Modifications to the interparticle gap (closest nearest neighbor distance) from 1.5 nm (close to the experimental value of 1.4 nm) can shift the high energy peak in the CD spectrum from 560 nm (**Figure 3.10b**) to approximately 540 nm for an interparticle distance of 2.0 nm (**Figure 3.13**). If the interparticle gap is reduced to 1.0 nm, the peak in the CD spectrum red-shifts to ~580 nm (**Figure 3.13**). As gold is more polarizable in the near infrared than in the visible,[158] shifting the LSPR to the red increases the extinction cross section of the assemblies, and hence increases the magnitude of the CD response.

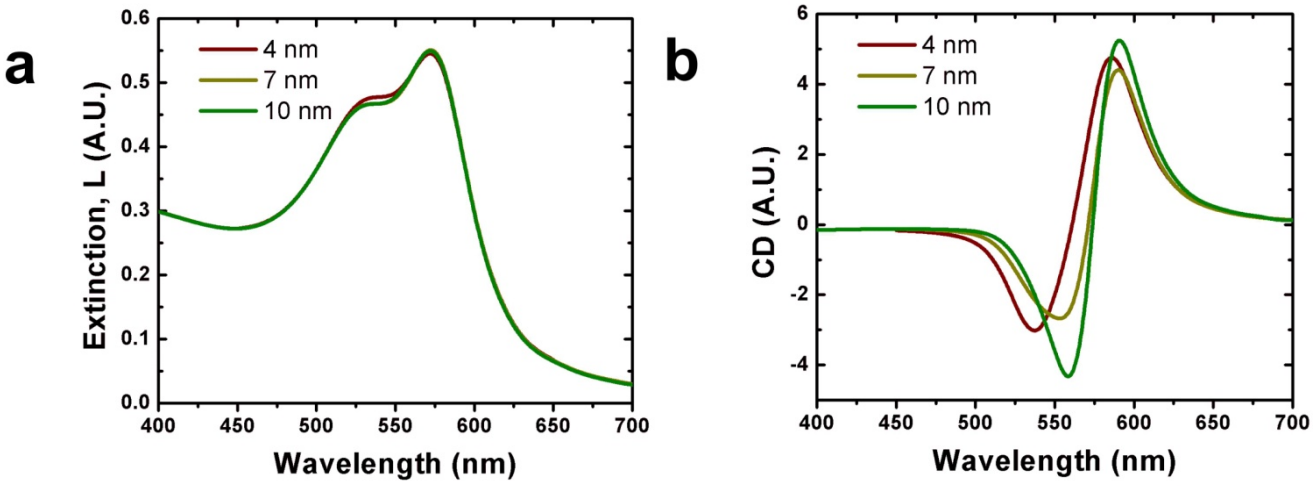


**Figure 3.14. Interhelical spacing effect on CD response.** The simulated effect of interhelical spacing on the extinction (a) and CD (b) of a right-handed double helix ensemble comprising 22 spheres. The interhelical spacing was sampled at 4.0 nm, 7.0 nm, the approximate experimental value, and 10.0 nm. The sphere diameter is 8.0 nm and the interparticle spacing is 1.5 nm.

Our model predicts that increasing the radius of the nanoparticles will have the same effect as decreasing the interparticle distance (namely a redshift of the longitudinal LSPR and increase in the extinction cross section). As such, we added additional aliquots of $HAuCl_4/H_2O$ to samples of left- and right-handed gold helices (particle diameters: left-handed helices = 8.64 ± 1.43 nm; right handed helices = 7.59 ± 1.22 nm) (**Figure 3.15 – 3.16**) suspended in HEPES buffer to yield product helices with larger nanoparticles (particle diameters: left-handed helices = 10.55 ± 0.75 nm; right handed helices = 10.70 ± 2.07 nm) (**Figure 3.17 – 3.18**). CD measurements of these samples showed that signal intensity dramatically increased and the CD peak shifted to longer wavelength (**Figure 3.19**). The CD signal for left-handed helices shifted from 571 to 594 nm while the CD signal for right-handed helices shifted from 566 nm to 602 nm (**Figure 3.19**). These results were consistent with our simulations which showed that when the particle diameter of left-handed gold helices is increased from the mean experimental value of approximately 8.0 nm to 11.0 nm, the ~560 nm dip shifts to above ~575 nm and the magnitude of the peak approximately doubles (**Figure 3.20**). In summary, carefully controlling structural parameters allows one to tune the macrooptical activity of these nanohelical assemblies. Our theoretical model based on classical electrodynamics provides a means of interpreting and predicting the chirooptical behavior.

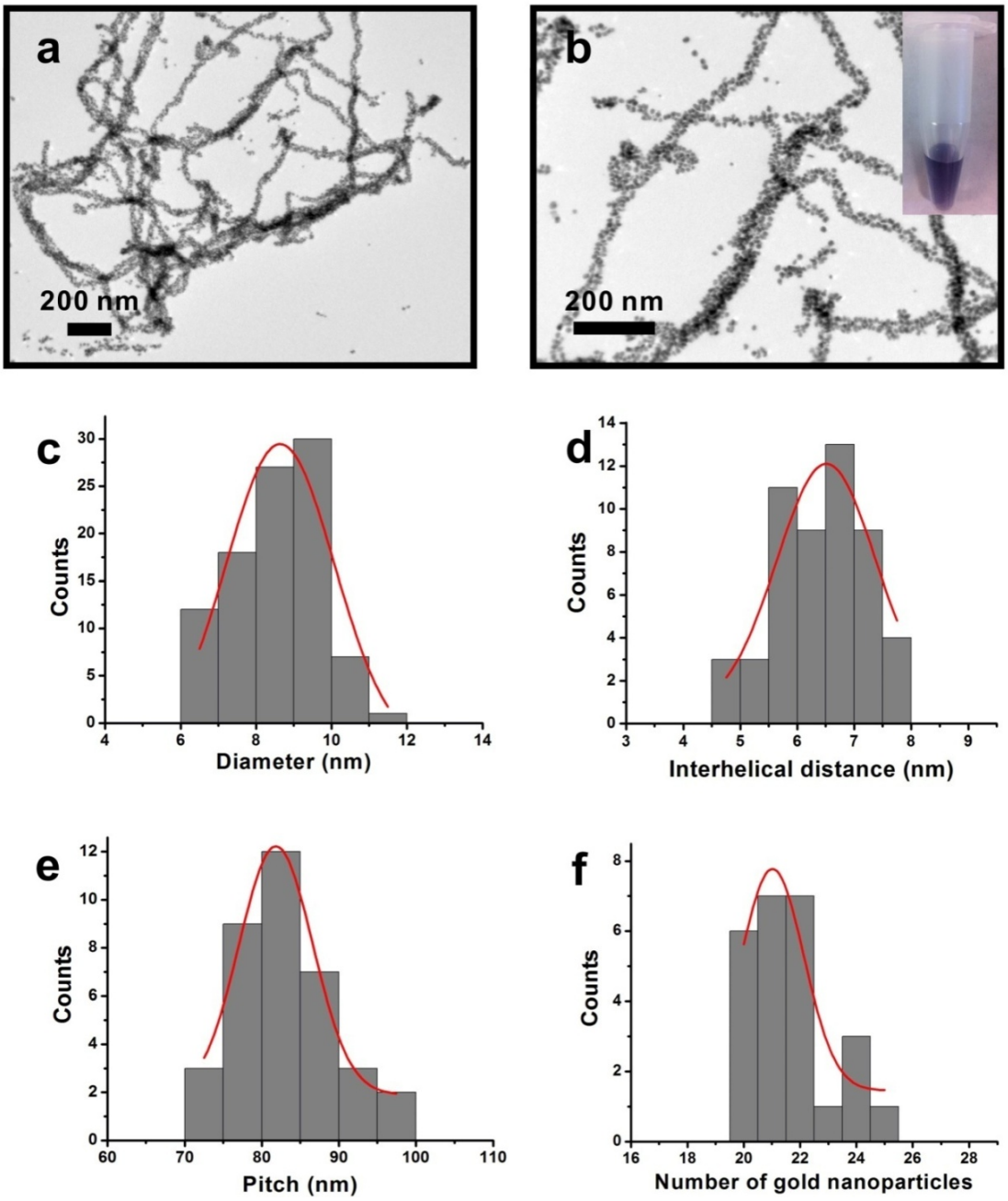


**Figure 3.15**. TEM images and statistics of left-handed gold nanoparticle double helices in 0.08 M HEPES and 0.02 M citrate buffer after one day incubation. (a) (b) TEM images of left-handed gold nanoparticle double helices.The inset image of the vial shows the purple color of the gold nanoparticle double helices solution. (c) Distribution of nanoparticle size (based on 95counts;

diameter = 8.64 ± 1.43nm). (d) Distribution of the interhelical distance (based on 52 counts; distance = 6.51 ± 0.87 nm). (e) Distribution of pitch (based on 36 counts; pitch = 81.83 ± 4.77 nm). (f) Distribution of number of gold nanoparticles per pitch of double helix (based on 25 counts; number = 21 ± 1).

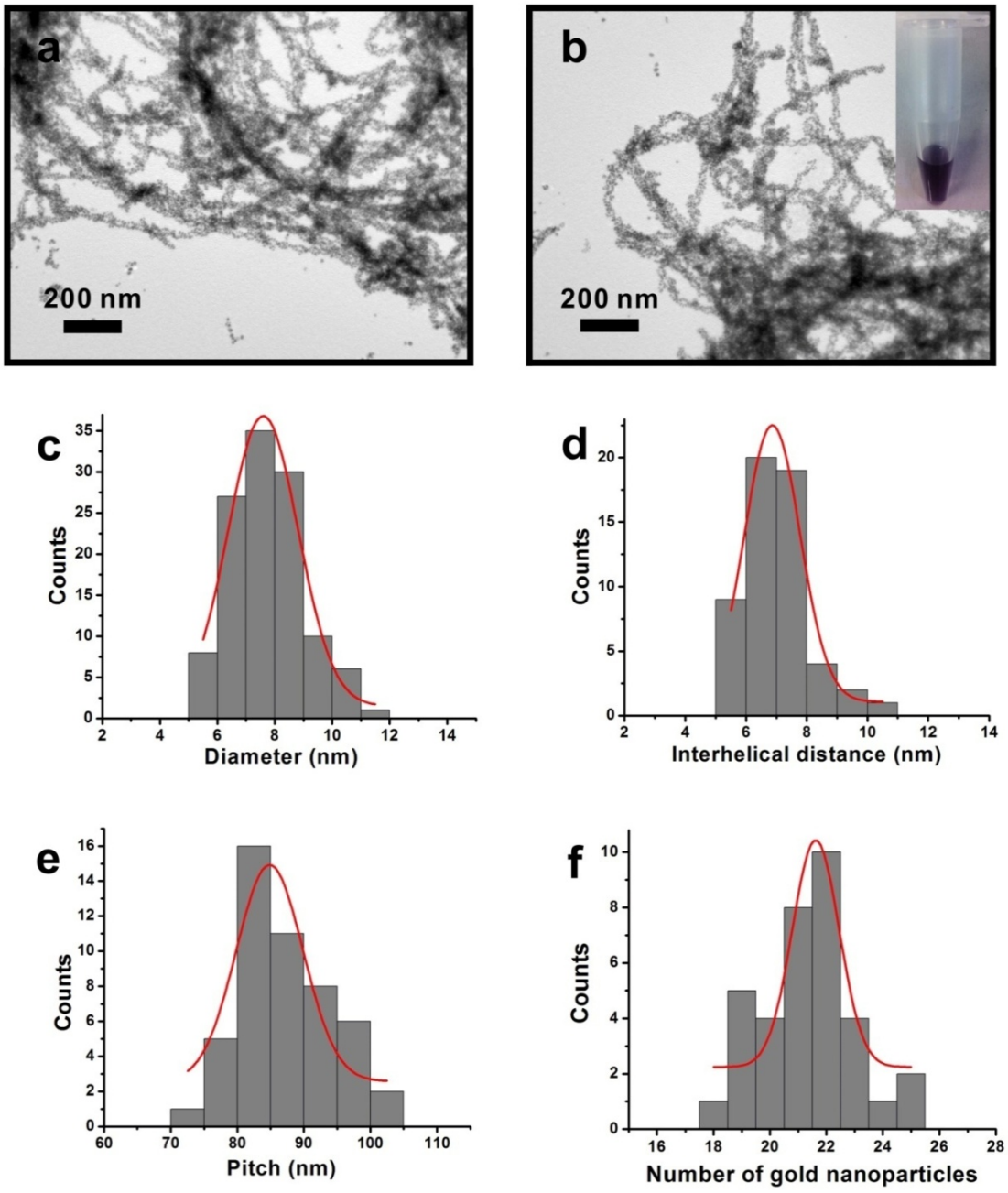

**Figure 3.16**. TEM images and statistics of right-handed gold nanoparticle double helices in 0.08 M HEPES and 0.02 M citrate buffer after one day incubation. The inset image of the vial shows the purple color of gold nanoparticle double helices solution. (a) (b) TEM images of right-handed gold nanoparticle double helices.(c) Distribution of nanoparticle size (based on 117 counts; diameter = 7.59 ± 1.22 nm). (d) Distribution of the interhelical distance (based on 55 counts; distance = 6.86 ± 0.92 nm). (e) Distribution of pitch (based on 49 counts; pitch = 84.86 ± 5.00 nm). (f) Distribution of number of gold nanoparticles per pitch of double helix (based on 35 counts; number = 22 ± 1).

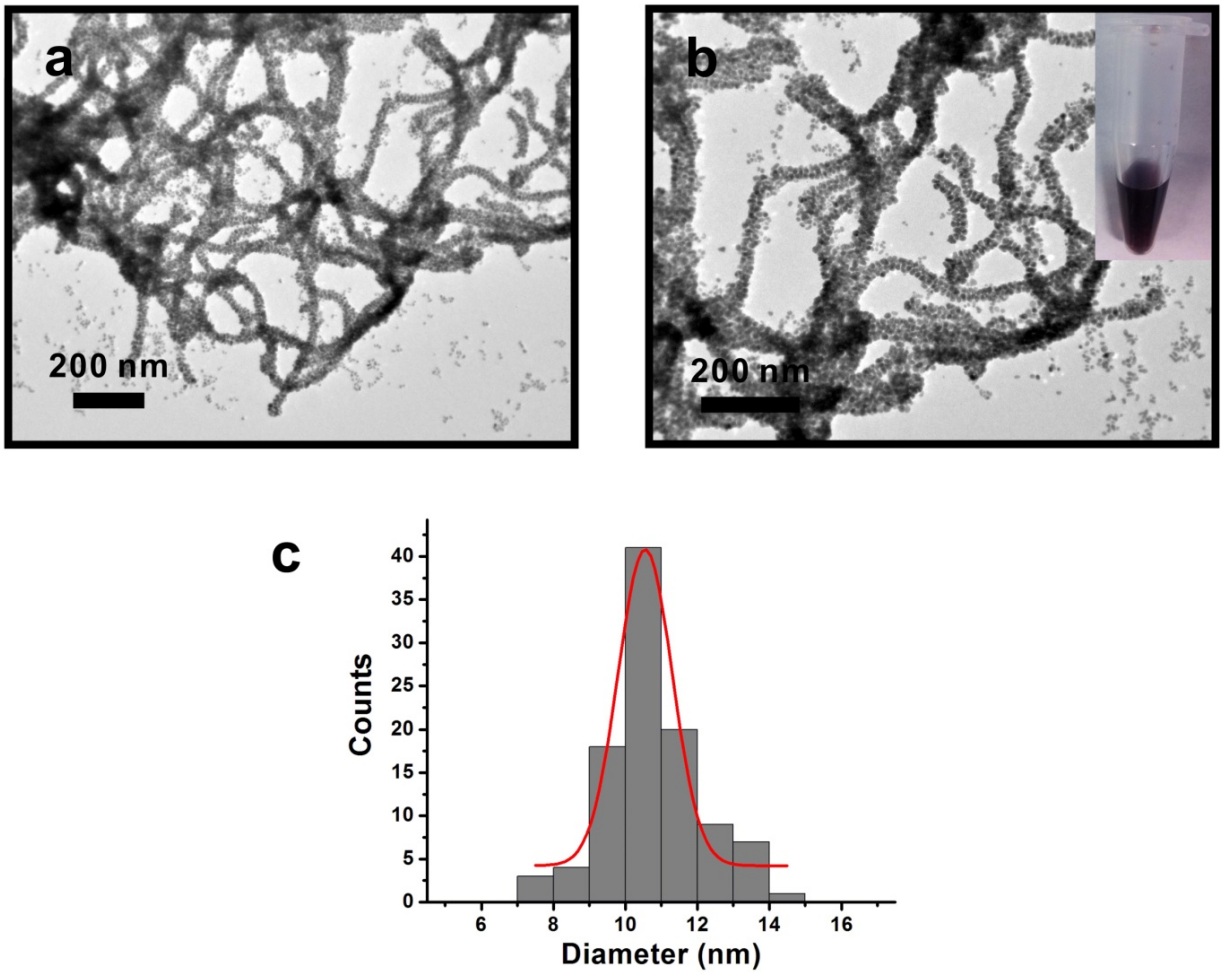


**Figure 3.17**. (a-b) TEM images of gold enhanced left-handed nanoparticle double helices.The inset image of the vial shows the dark purple color of gold nanoparticle double helices solution. (c) Distribution of nanoparticle size(based on 100 counts; diameter = 10.55 ± 0.75 nm).

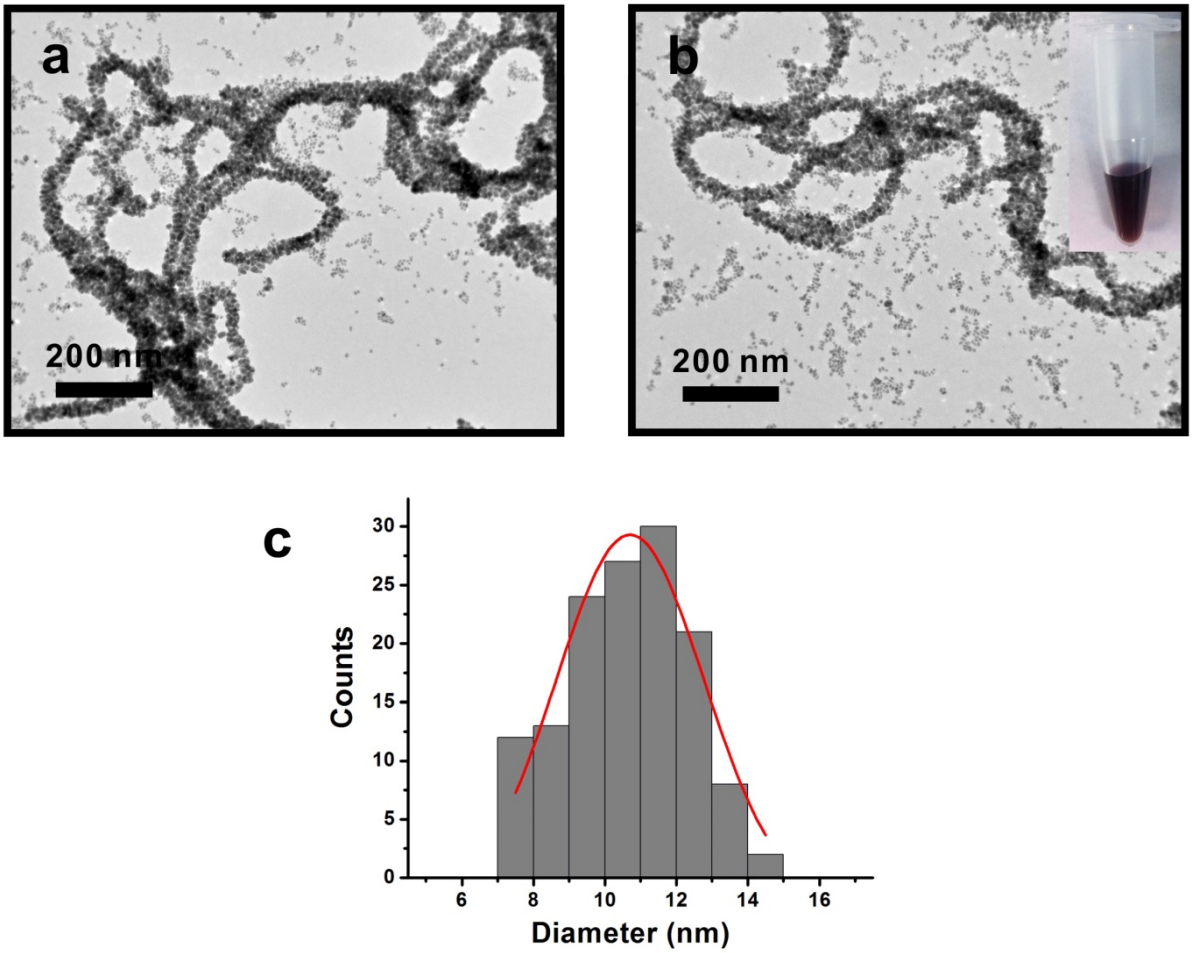


**Figure 3.18**. (a-b) TEM images of gold enhanced right-handed nanoparticle double helices.The inset image of the vial shows the dark purple color of gold nanoparticle double helices solution. (c) Distribution of nanoparticle size (based on 137 counts; diameter = 10.70 ± 2.07 nm).

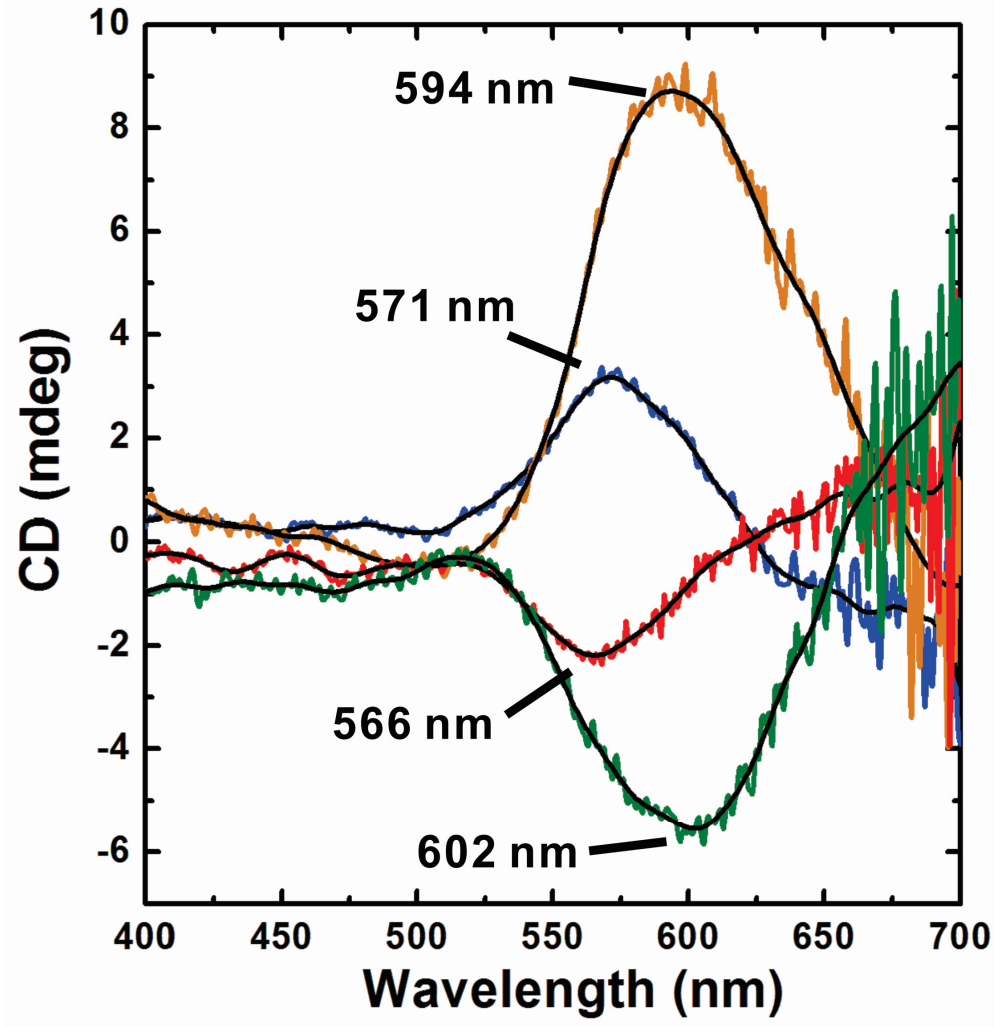


**Figure 3.19**. CD spectra of left- and right-handed gold nanoparticle double helices solutions. Blue line: left-handed gold double helices without gold enhancement; Red line: right-handed gold double helices without gold enhancement; Orange line: left-handed gold double helices enhanced by gold aqueous solution; Green line: right-handed gold double helices enhanced by gold aqueous solution. The path length of the light is 1 mm.

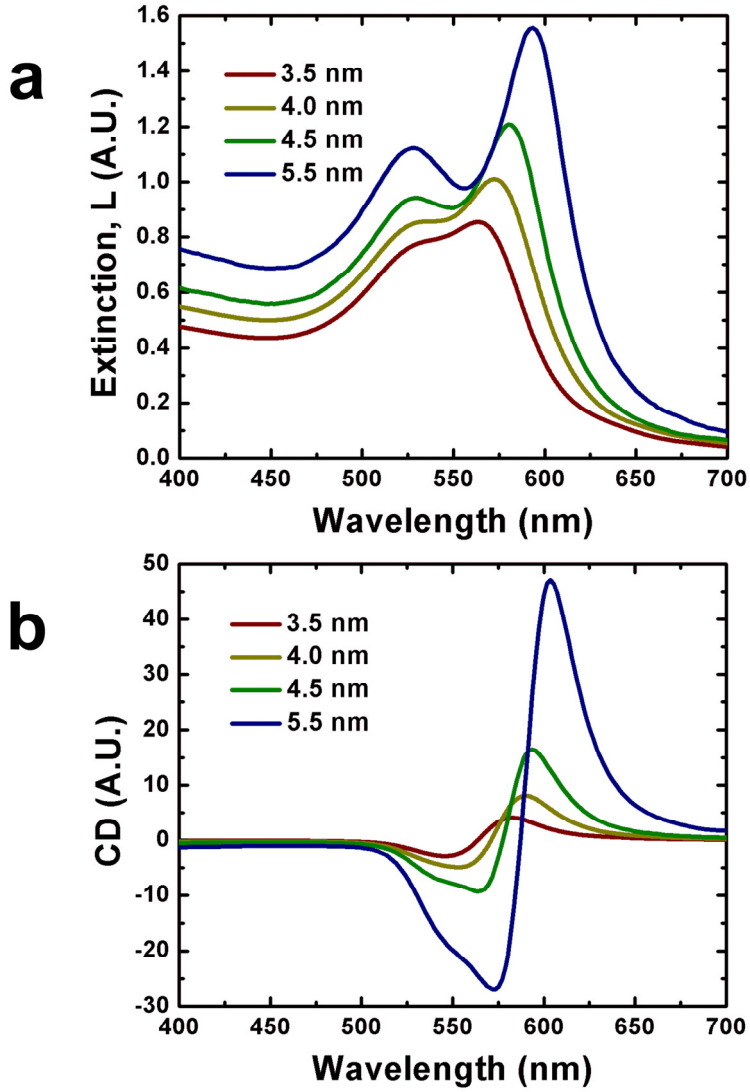


**Figure 3.20**. **Sphere diameter effect on CD response**. The simulated effect of sphere diameter on the extinction (a) and CD (b) of a left-handed double helix ensemble comprising 22 spheres. The double peaks in (a) represent the transverse surface plasmon resonance at around 525 nm (where the incident field polarization is perpendicular to the helical axis), and the longitudinal mode (where the incident field polarization is parallel to the helical axis), which red-shifts as the particle size increases. See Equation 2 in the main text. The sphere diameter was sampled at 7.0 nm, 8.0 nm, the approximate experimental value, 9.0 nm and 11.0 nm. The interhelical distance is 7.0 nm and the interparticle distance is 1.5 nm.

Based on our theoretical prediction, double helices consisting of small gold nanoparticles should result in a CD signal shift to shorter wavelength along with a concomitant decrease in signal intensity. Our experimental data bears this out, to some extent: as we decrease the nanoparticle size, we observe a decrease in the CD signal along with a slight blue shift, although the CD signal is quite weak (**Figure 3.21 – 3.22**).

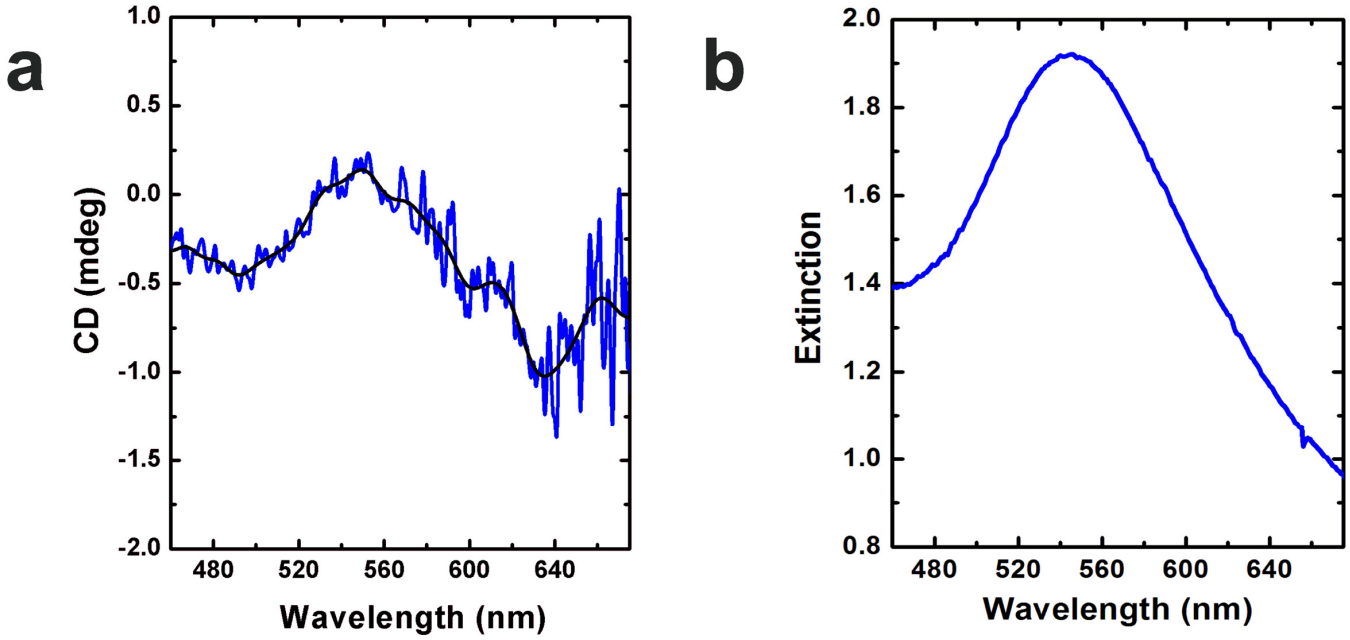


**Figure 3.21**. (a) CD spectrum of left-handed gold nanoparticle double helicesincubated in 0.04 M citratebuffer and 0.06 M HEPES buffer for one day. The path length of the light is 1 mm. (b) UV-Vis spectrum of the left-handed gold nanoparticle double helices solution. It shows a surface plasmonic peak of gold assemblies at 545 nm which is consistent with the CD positive signal at 549 nm.

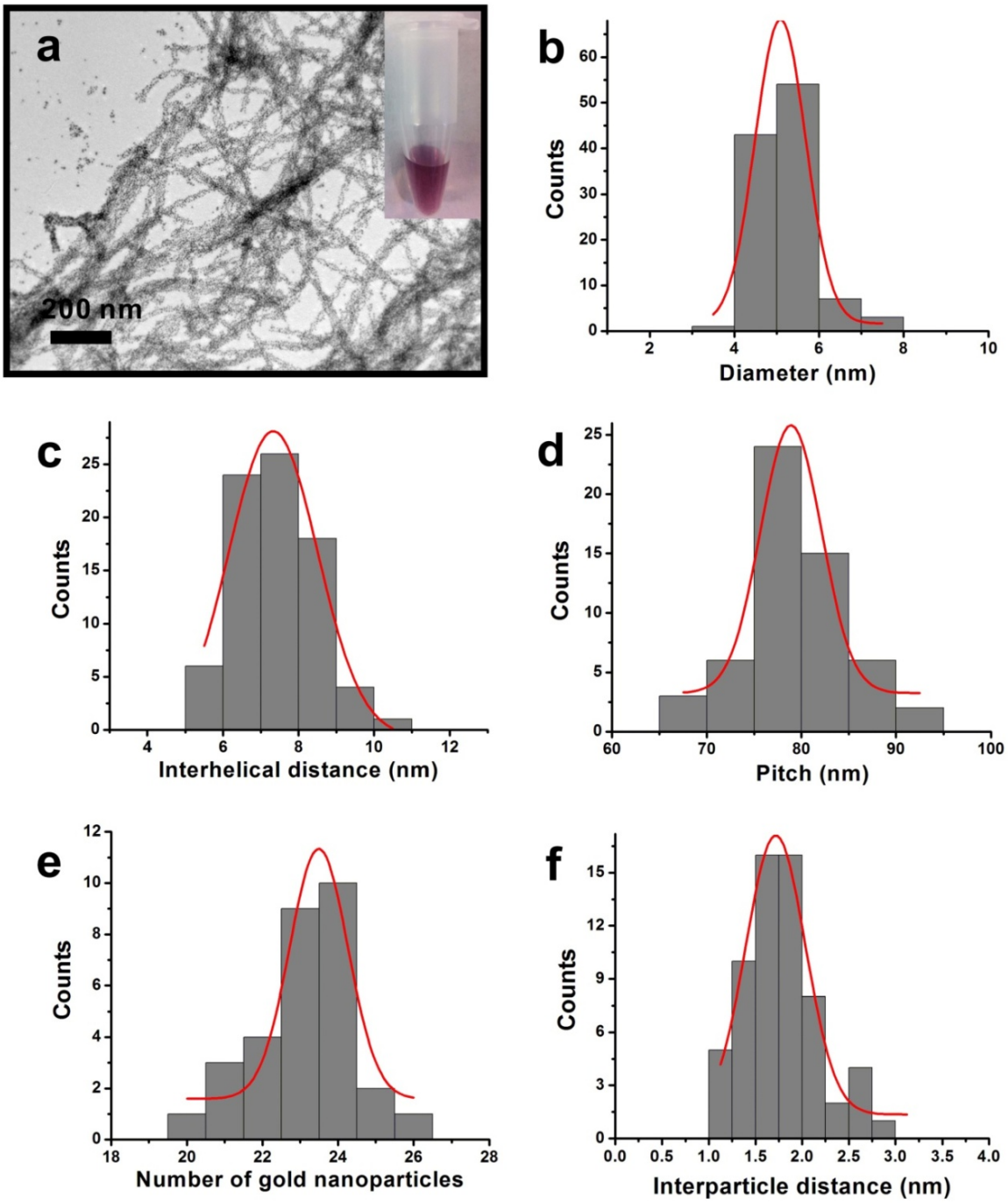


**Figure 3.22**. TEM image and statistics of left-handed gold nanoparticle double helices incubated in 0.04 M citrate buffer and 0.06 M HEPES buffer for one day. (a) TEM image of left-handed gold nanoparticle double helices.(b) Distribution of nanoparticle size (based on 108 counts;

diameter = 5.09 ± 0.60 nm). (c) Distribution of the interhelical distance(based on 79 counts; distance = 7.33 ± 1.17 nm). (d) Distribution of pitch (based on 56 counts; pitch = 78.89 ± 3.23 nm). (e) Distribution of number of gold nanoparticles per pitch of double helix (based on 30 counts; number = 23 ± 2).(f) Distribution of the edge-to-edge distance betweennanoparticles along the longitudinal dimension of the gold nanoparticle double helices(based on 62 counts; distance = 1.72 ± 0.32 nm).

In order to generate a strong blue shifted CD response, we coated the gold nanoparticle double helices with silver. Specifically, we deposited varying amounts of silver onto freshly prepared gold nanoparticle double helices (~8 nm particle diameters) to control the thickness of the silver shell. Scanning TEM (STEM) image and energy dispersive spectroscopy (EDS) data indicate that the silver-coated double helices consist of gold nanoparticles (white core) coated with silver (grey shell) (**Figure 3.23**).

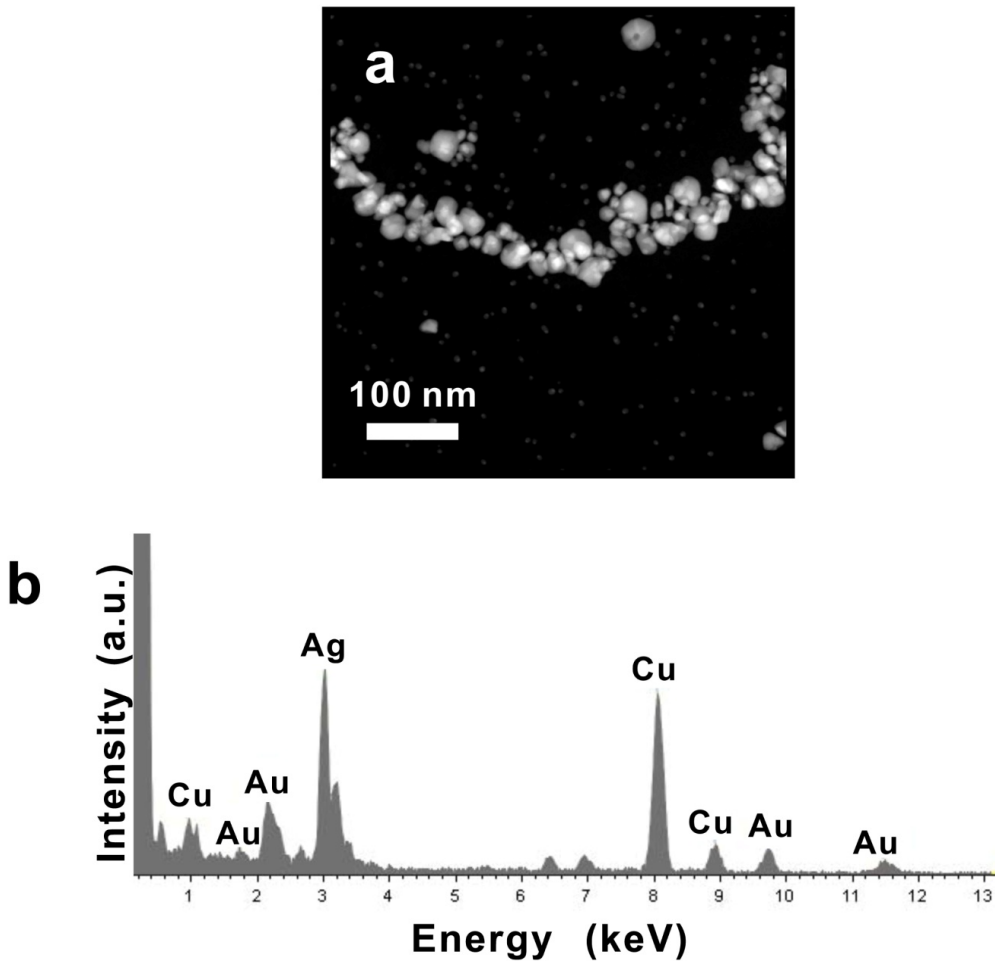


**Figure 3.23**. (a) STEM image of left-handed gold nanoparticle double helices enhanced by 108 µl Ag enhancer. It shows a white core (heavy metal:Au) surrounded by a gray shell (lighter metal: Ag). (b) EDS data of gold nanoparticle double helices (Cu is from the TEM grid).

CD spectra and TEM images (**Figure 3.24a, Figure 3.24c and Figure 3.25 – 3.30,** respectively) reveal that double helices with larger particles exhibit stronger CD signal at shorter wavelength. When the double helices are coated with a very thin silver shell (~0.5 nm), the CD intensity increases and exhibits the same sign as the original gold nanoparticle helices. However, if the gold nanoparticle double helices are coated with a thick silver shell, the CD intensity appears to significantly increase yet with the opposite sign of the original gold helices. Again, to confirm that the observed CD response results from the assembled superstructure, we collected CD data for non-assembled peptide-coated gold particles coated with silver; these particles did not exhibit a CD signal in the visible (**Figure 3.31 – 3.32**). We employed theory and simulation to understand the CD data from the silver-coating experiments. We present the simulated extinction spectra for a double helix consisting of just gold spheres, and of gold spheres coated with 1.0 nm, 1.5 nm, and 2.0 nm of silver (**Figure 3.33**). The introduction of silver onto the gold spheres causes the appearance of a band at around 375 nm that is associated with the silver. Additionally, the longitudinal resonance shifts to the blue as the silver thickness increases, which is a direct effect of the difference in the wavelength position of the interband transitions between the two metals: those in silver are in the UV, and those of gold are in the blue region of the spectrum. As more silver is added, the polarizability (and hence the extinction) of the nanoparticles increases as silver is more polarizable than gold in this region of the spectrum.[158] These effects conspire to blue shift the CD spectrum (**Figure 3.24b and Figure 3.24d**) and the 550 nm dip in **Figure 3.4a** and 3.**4c** appears to change sign when the silver coating thickness increases from approximately 0.5 nm to above approximately 1.0 nm. The simulations (**Figure 3.24b, Figure 3.24d**) indicate that this effect can be explained by a large blue shift in the

resonances of the double-helices when silver is introduced into the system together with the increase in intensity.

The experimental CD spectra (**Figure 3.24a, Figure 3.24c**) exhibit only small CD response in the blue in comparison to the features at approximately 550 nm, whereas the simulated spectra exhibit peaks and troughs of approximately equal magnitude. This can be explained by variations in the interparticle gap along the helix. **Figure 3.34** shows the effect of varying the interparticle gap between 0.5 nm and 1.5 nm, reducing the gap causes the CD response to red shift. Regions of the spectra which show negative CD signal at gaps of 1.5 nm (for example: purple trace, **Figure 3.24d**) are reduced in magnitude because the negative signal in this region is offset by positive CD response by locations on the helix where the particles are 0.5 nm apart. This amounts to an interference like effect between helices with larger (~1.5 nm) and smaller (~0.5 nm) interparticle gaps.

If the particles are touching (or conjoined) for long regions of the helix then the CD response is flat across the visible due to a lack of dipole-dipole coupling between particles (i.e. the system resembles a twisted nanowire with a plasmonic response that has shifted to the IR, see **Figure 3.34**).

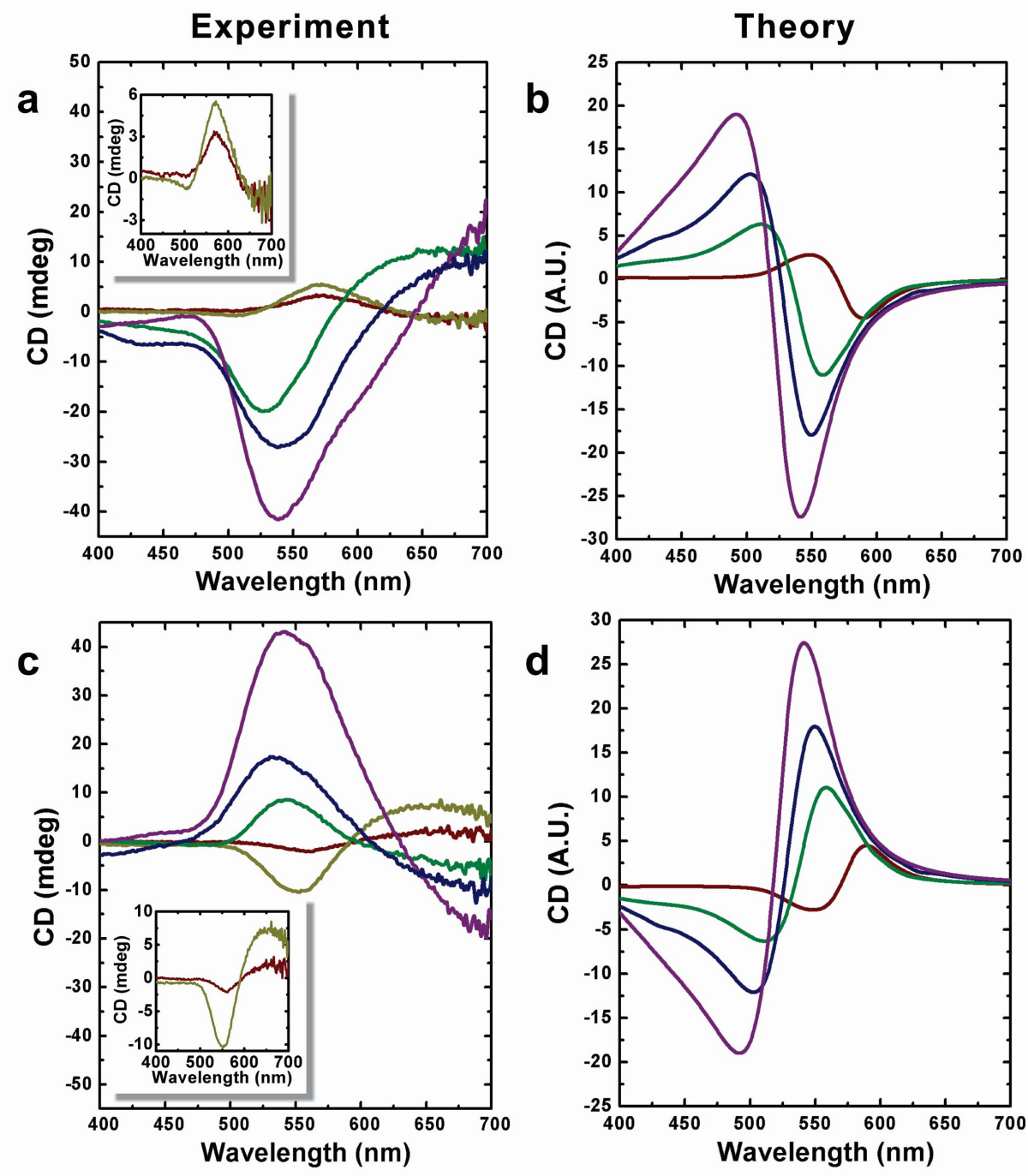
Experiment
Theory
a
b
c
d
CD (mdeg)
CD (A.U.)
Wavelength (nm)

**Figure 3.24.** Experimental and theoretical circular dichroism of gold nanoparticle double helices enhanced by silver. Left- (a) and right-handed (c) gold nanoparticle double helices coated with varied thickness of silver exhibit different CD intensities and wavelengths from the typical gold nanoparticle double helices. A significant blue shift of the peaks (from ~560 nm to ~530 nm) and dramatically increased amplitudes in the CD spectra were obtained by coating gold nanoparticles with increasing amounts of silver (red: no silver shell; yellow: ~0.5 nm silver shell; green: ~1 nm silver shell; blue: ~2 nm silver shell; purple: ~3 nm silver shell). The insets in (a) and (c) are provided for clarity. Simulated CD spectra for left- (b) and right-handed (d) gold nanoparticle double helices coated with varied thickness of silver shells (red: no silver shell; green: ~1 nm silver shell; blue: ~1.5 nm silver shell; purple: ~2 nm silver shell).

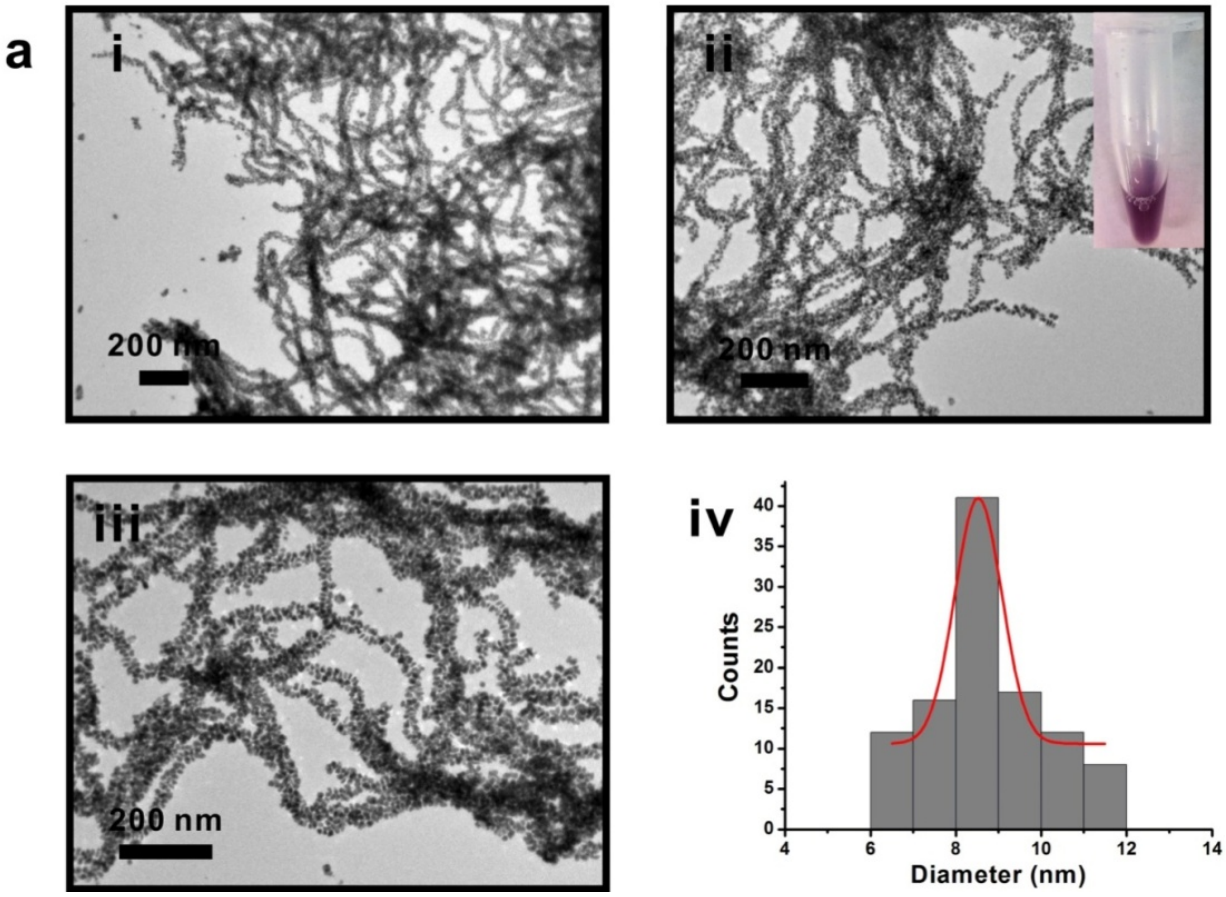


**Figure 3.25a**. (i-iii) TEM images ofleft-handed gold nanoparticle double helices enhanced with 9 μl Ag enhancer solution.The inset image of the vial shows the purple color of the gold nanoparticle double helices solution. (iv)Distribution of gold nanoparticle size on the double helices (based on 106 counts; diameter = 8.53 ± 0.55 nm).

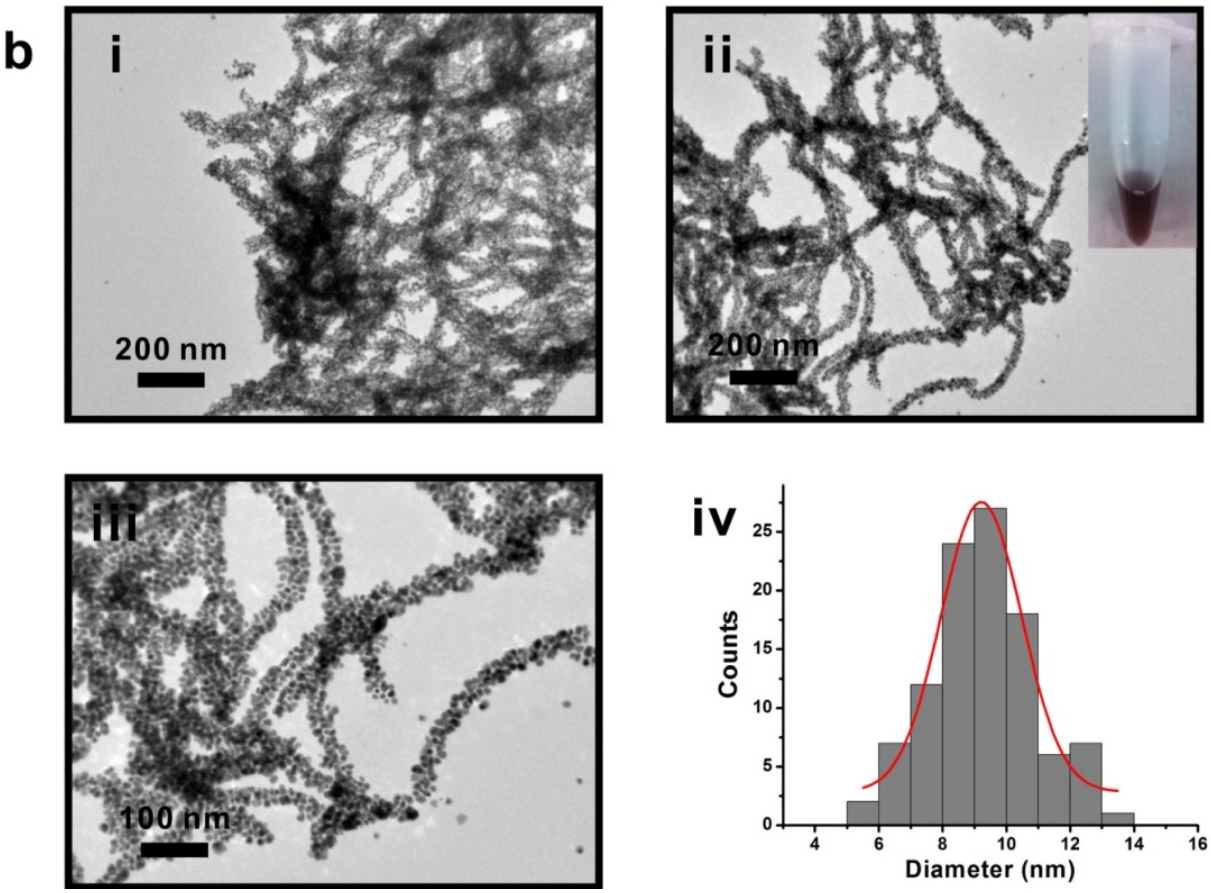


**Figure 3.25b**. (i-iii) TEM images of left-handed gold nanoparticle double helices enhanced with 27 µl Ag enhancer solution. The inset image of the vial shows the brown color of the gold nanoparticle double helices solution. (iv) Distribution of gold nanoparticle size on the double helices (based on 104 counts; diameter = 9.21 ± 1.27 nm).

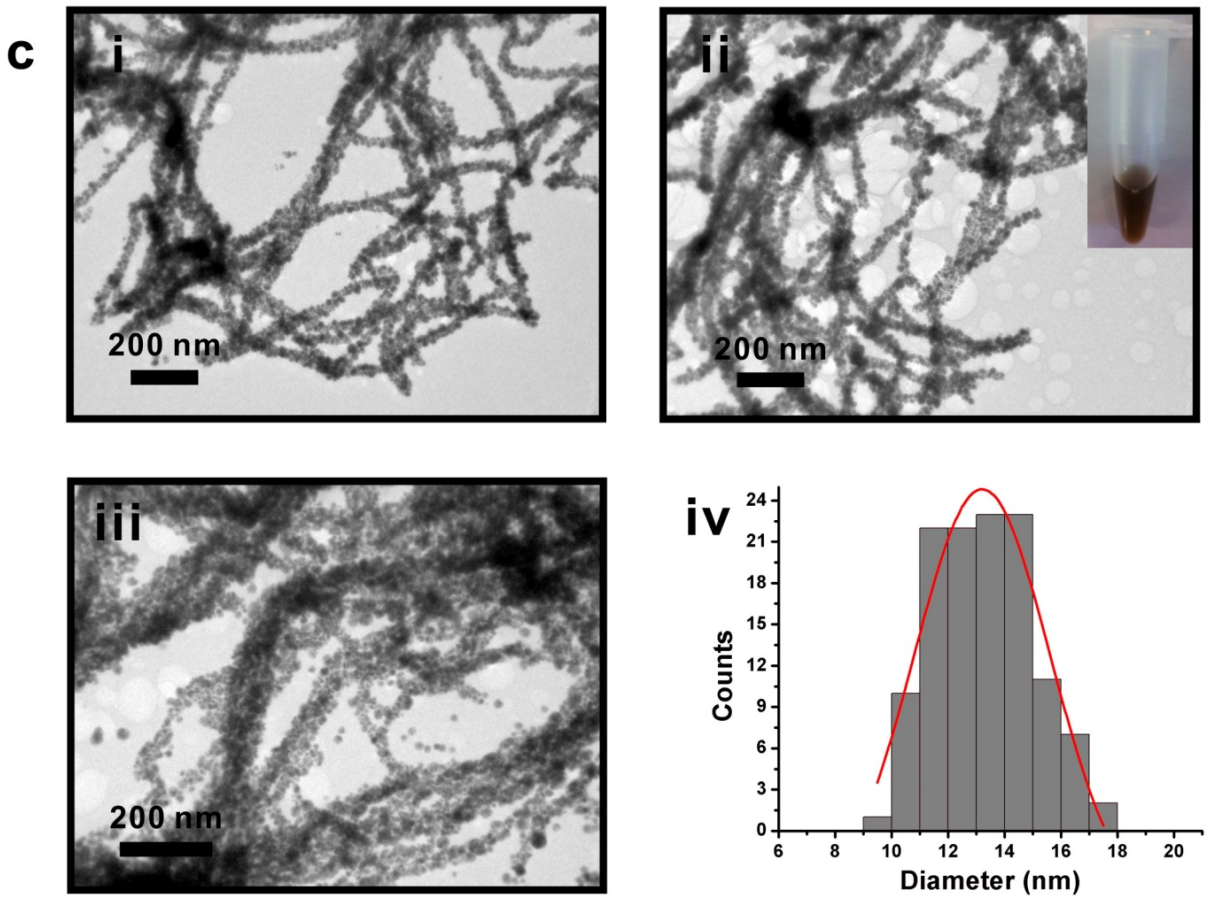


**Figure 3.25c**. (i-iii) TEM images of left-handed gold nanoparticle double helices enhanced with 54 µl Ag enhancer solution.The inset image of the vial shows the brown color of the gold nanoparticle double helices solution. (iv) Distribution of gold nanoparticlesize on the double helices (based on 121 counts; diameter = 13.20 ± 2.41 nm).

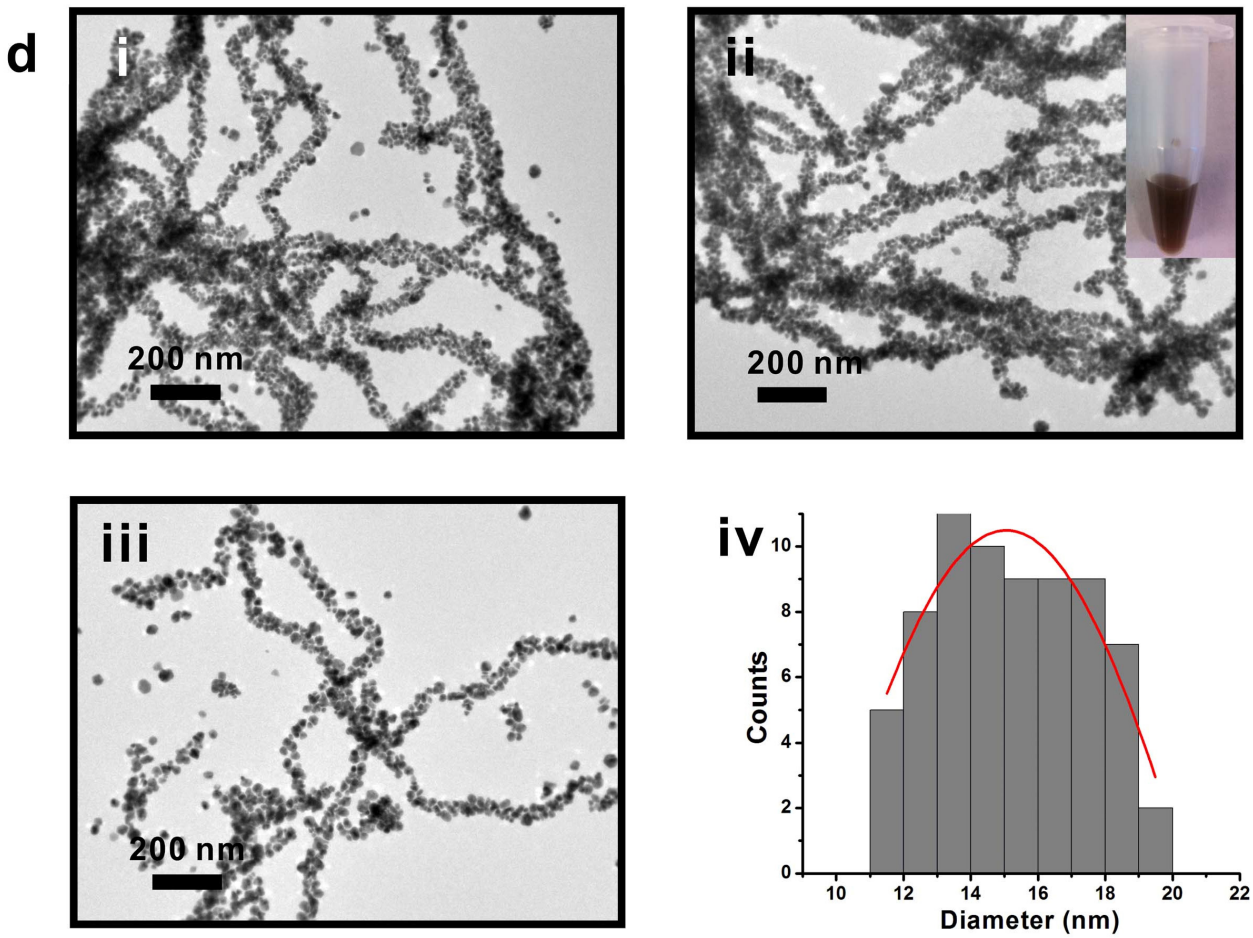


**Figure 3.25d**. (i-iii) TEM images of left-handed gold nanoparticle double helices enhanced with 108 µl Ag enhancer solution. The inset image of the vial shows the brown color of the gold nanoparticle double helices solution. (iv) Distribution of gold nanoparticle size on the double helices (based on 70 counts; diameter = 15.05 ± 6.90 nm).

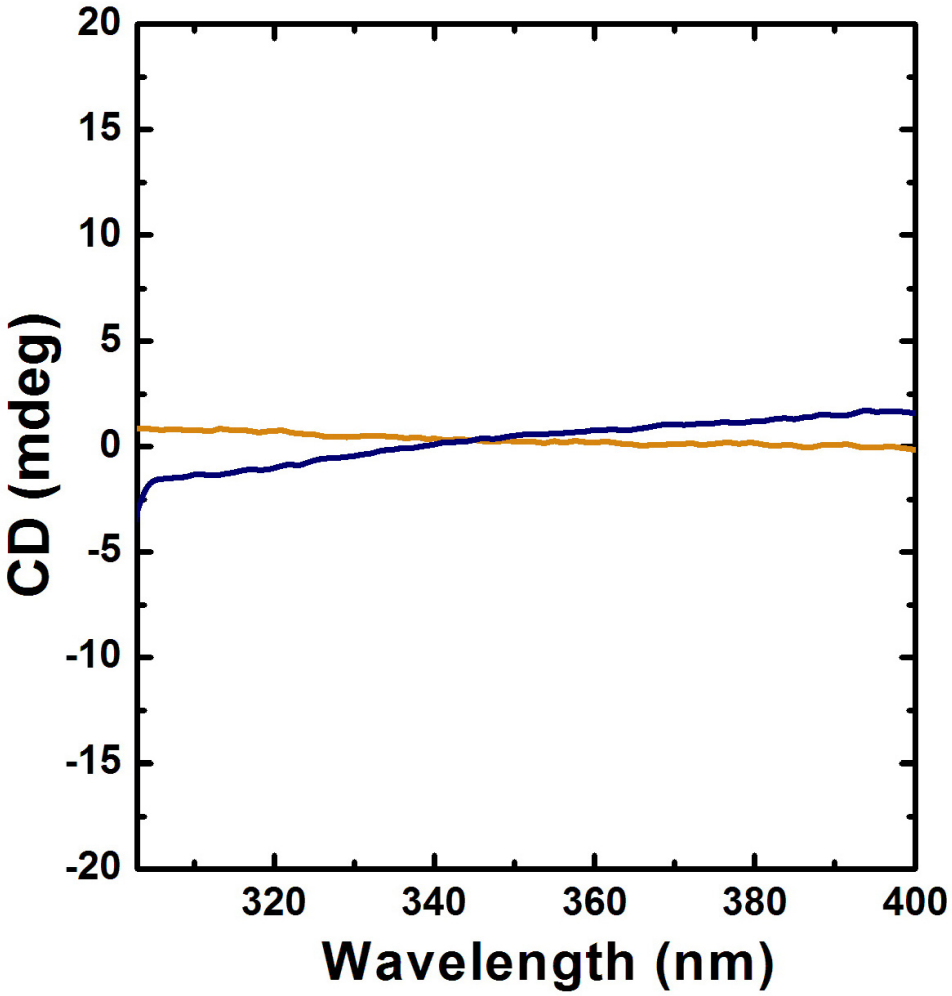


**Figure 3.26**. CD spectrum of left-handed gold nanoparticle double helices enhanced with 9 µl (yellow) and 108 µl (blue) Ag enhancer solution within the UV region (300nm – 400nm). The path length of the light is 1 mm. (note: graphs are not corrected for dilution effects)

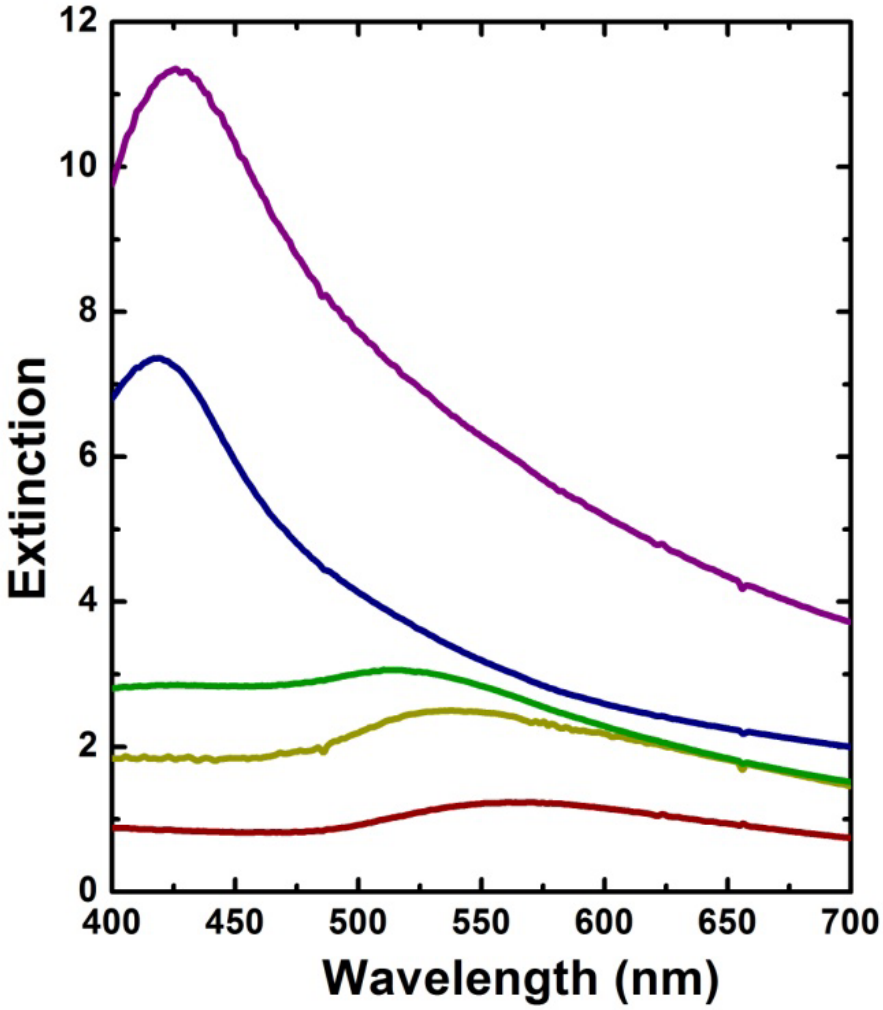


**Figure 3.27**. UV/Vis spectra of left-handed gold nanoparticle double helicessolutions. No silver enhancement (red) and helices enhanced with 9 µl (yellow), 27 µl (green), 54 µl (blue) and 108 µl (purple) Ag enhancer solution within the visible region (400nm – 700nm). The path length of the light is 10 mm. (note: graphs are not corrected for dilution effects)

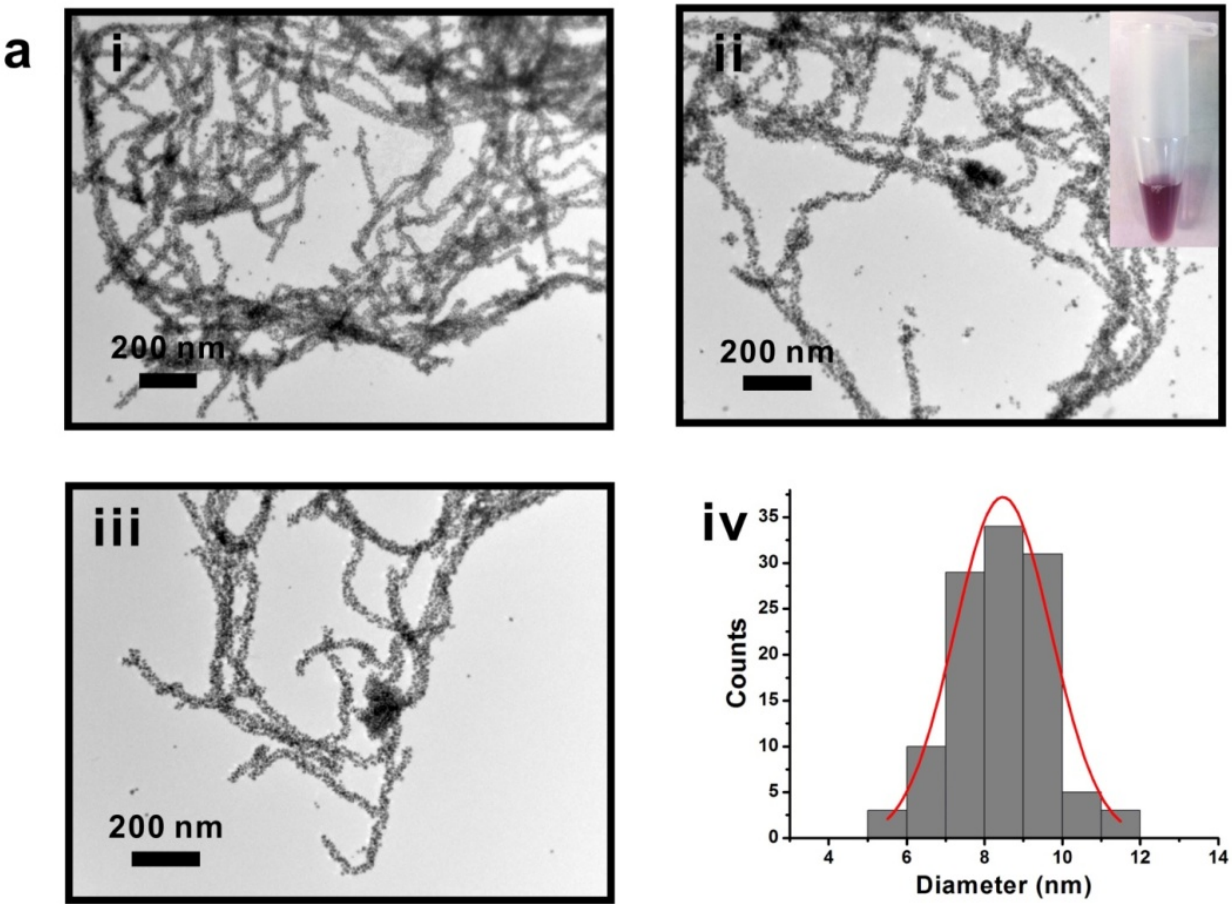


**Figure 3.28a**. (i-iii) TEM images of right-handed gold nanoparticle double helices enhanced with 9 µl Ag enhancer solution. The inset image of the vial shows the purple color of the gold nanoparticle double helices solution. (iv) Distribution of gold nanoparticlesize on the double helices (based on 115 counts; diameter = 8.47 ± 1.24 nm).

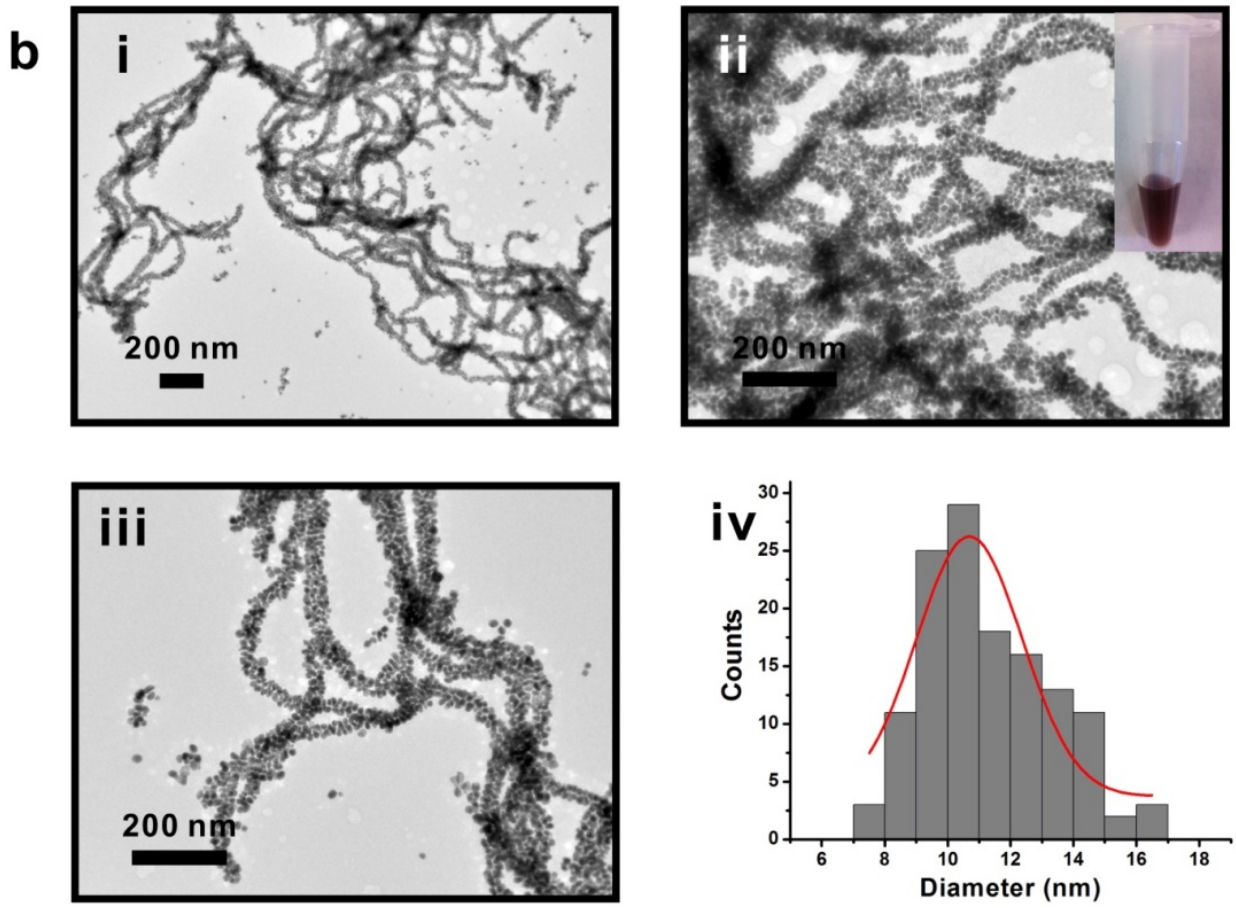


**Figure 3.28b**. (i-iii) TEM images of right-handed gold nanoparticle double helices enhanced with 27 μl Ag enhancer solution. The inset image of the vial shows the brown color of the gold nanoparticle double helices solution. (iv) Distribution of gold nanoparticle size on the double helices (based on 110 counts; diameter = 9.45 ± 1.23nm).

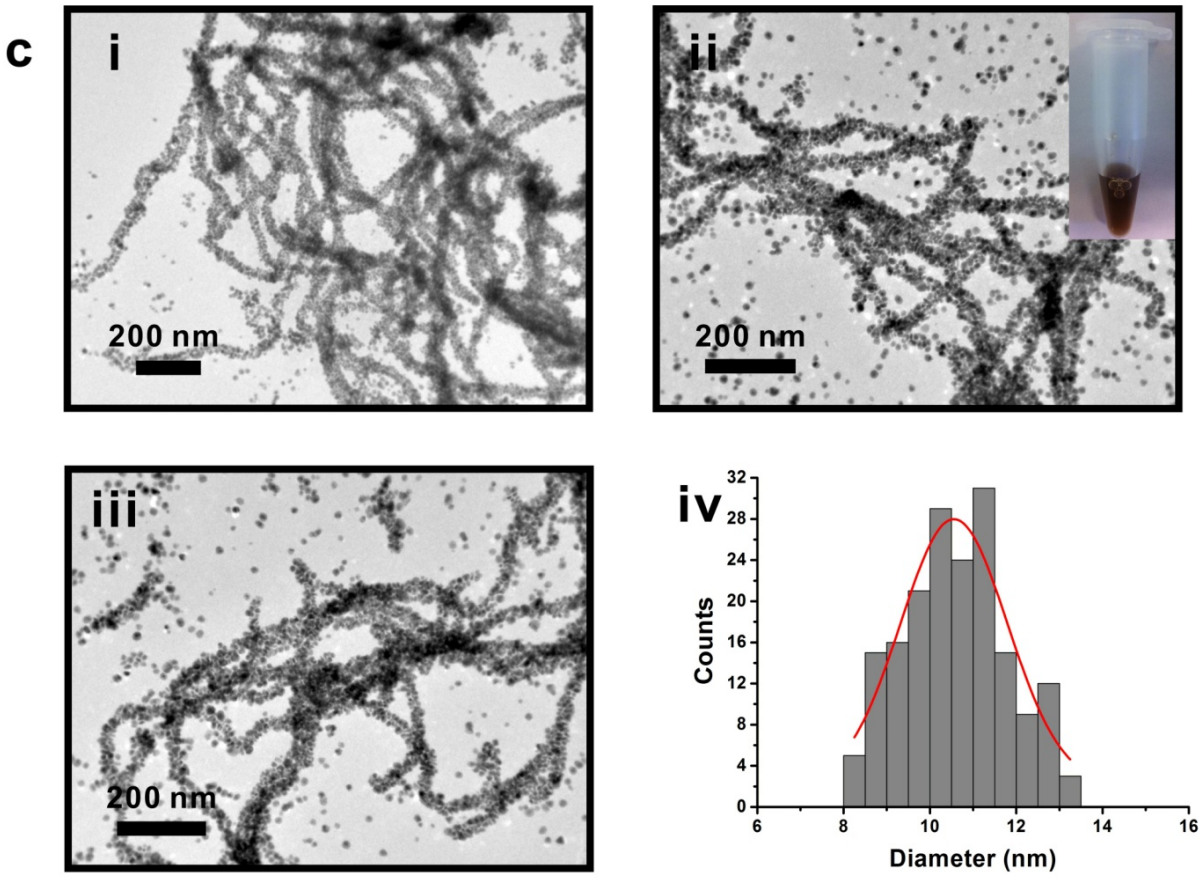


**Figure 3.28c**. (i-iii) TEM images of right-handed gold nanoparticle double helices enhanced with 54 µl Ag enhancer solution.The inset image of the vial shows the brown color of the gold nanoparticle double helices solution. (iv) Distribution of gold nanoparticlesize on the double helices (based on 180 counts; diameter = 10.56 ± 1.24 nm).

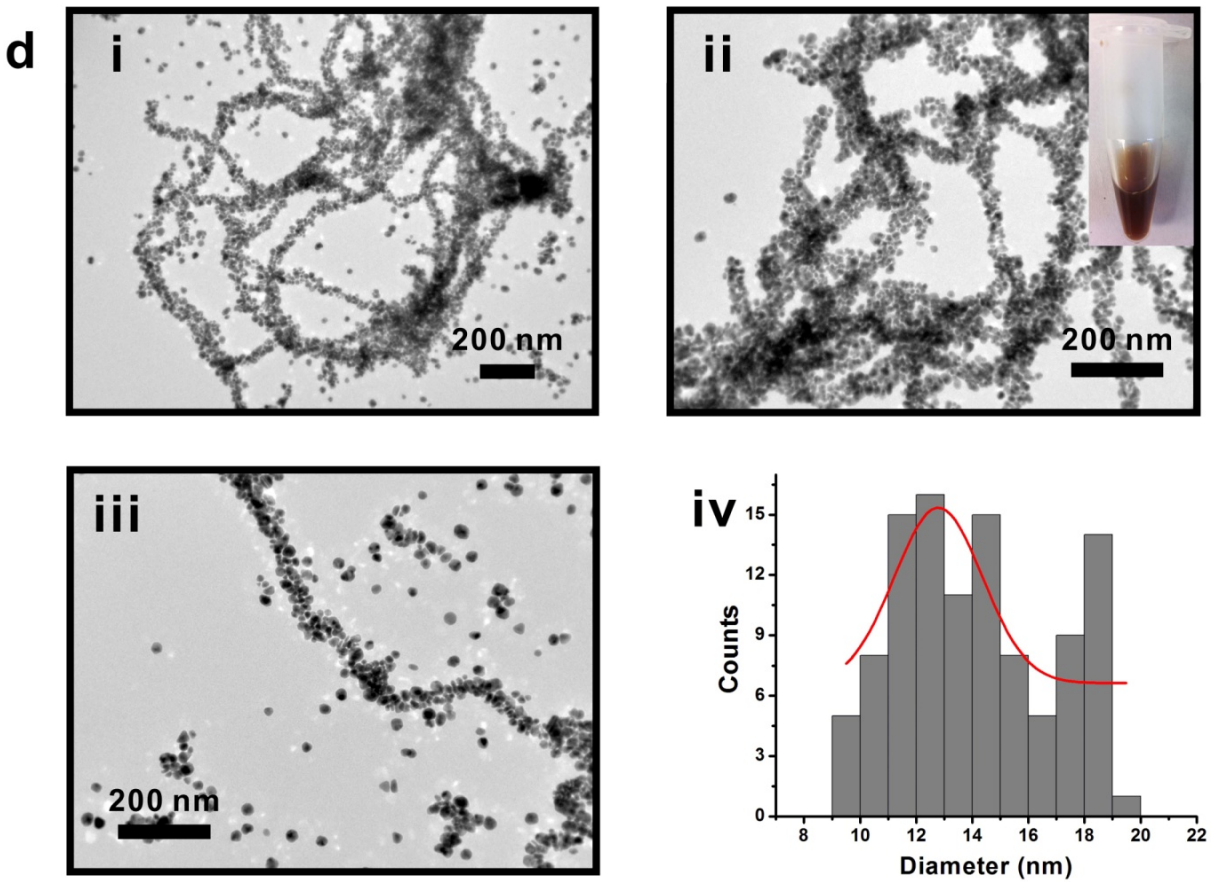


**Figure 3.28d**. (i-iii) TEM images of right-handed gold nanoparticle double helices enhanced with 108 µl Ag enhancer solution. (iv) Distribution of size of gold nanoparticles on the double helices (based on 107 counts; diameter = 12.79 ± 1.57 nm).

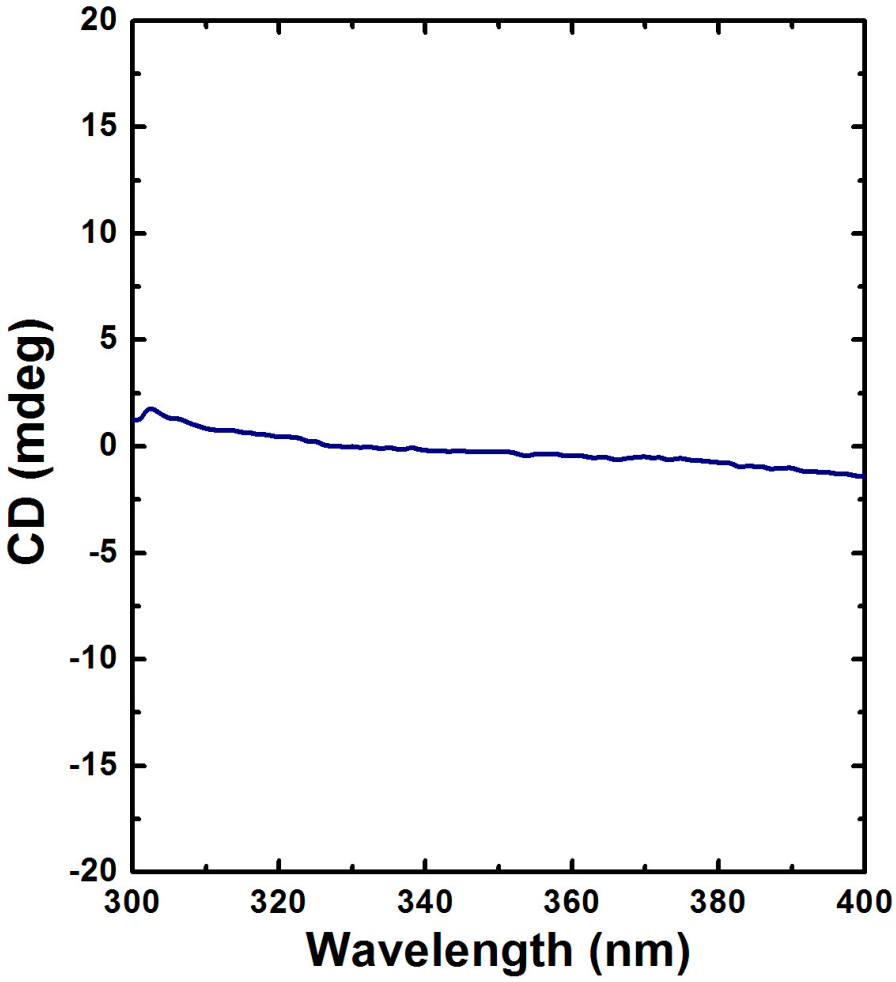


**Figure 3.29**. CD spectra of right-handed gold nanoparticle double helices enhanced with 108 µl Ag enhancer solution within UV region (300nm – 400nm). The path length of the light is 1 mm.

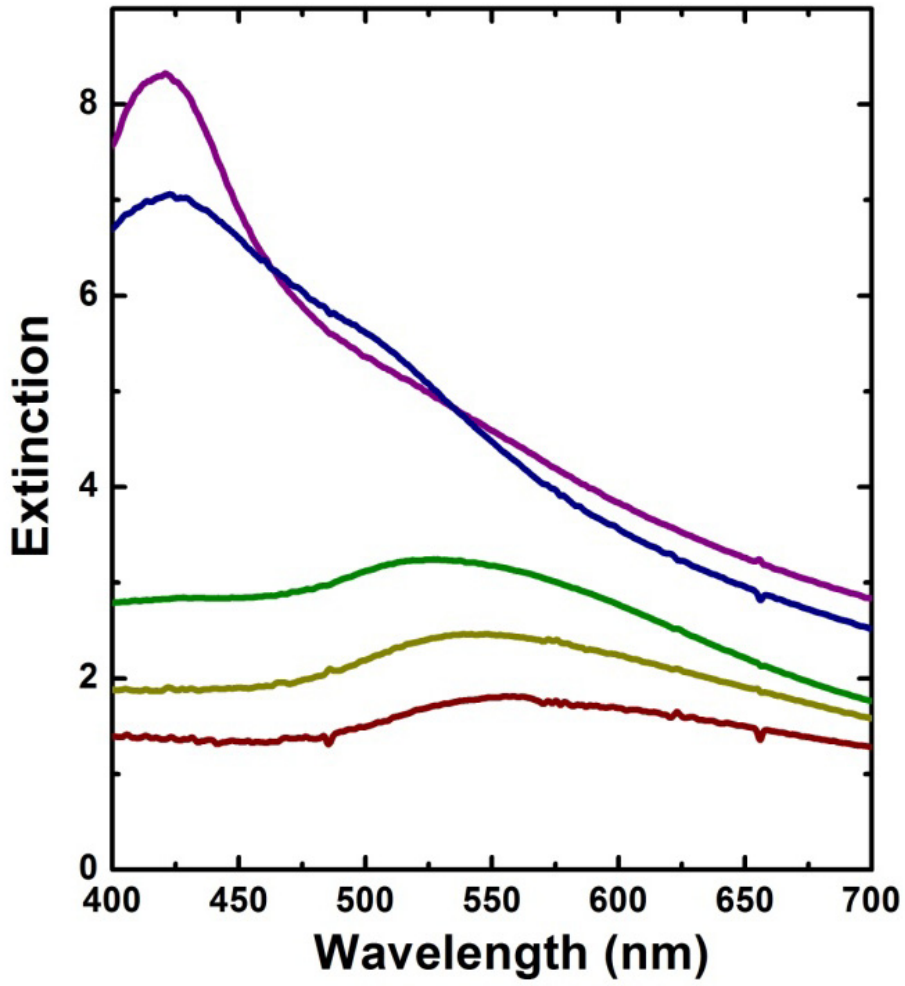


**Figure 3.30**. UV/Vis spectra of right-handed gold nanoparticle double helices solution. No silver enhancement (red) and helices enhanced with 9 µl (yellow), 27µl (green), 54 µl (blue) and 108 µl (purple) Ag enhancer solution within UV-Vis region (400nm – 700nm). The path length of the light is 10 mm. (note: graphs are not corrected for dilution effects).

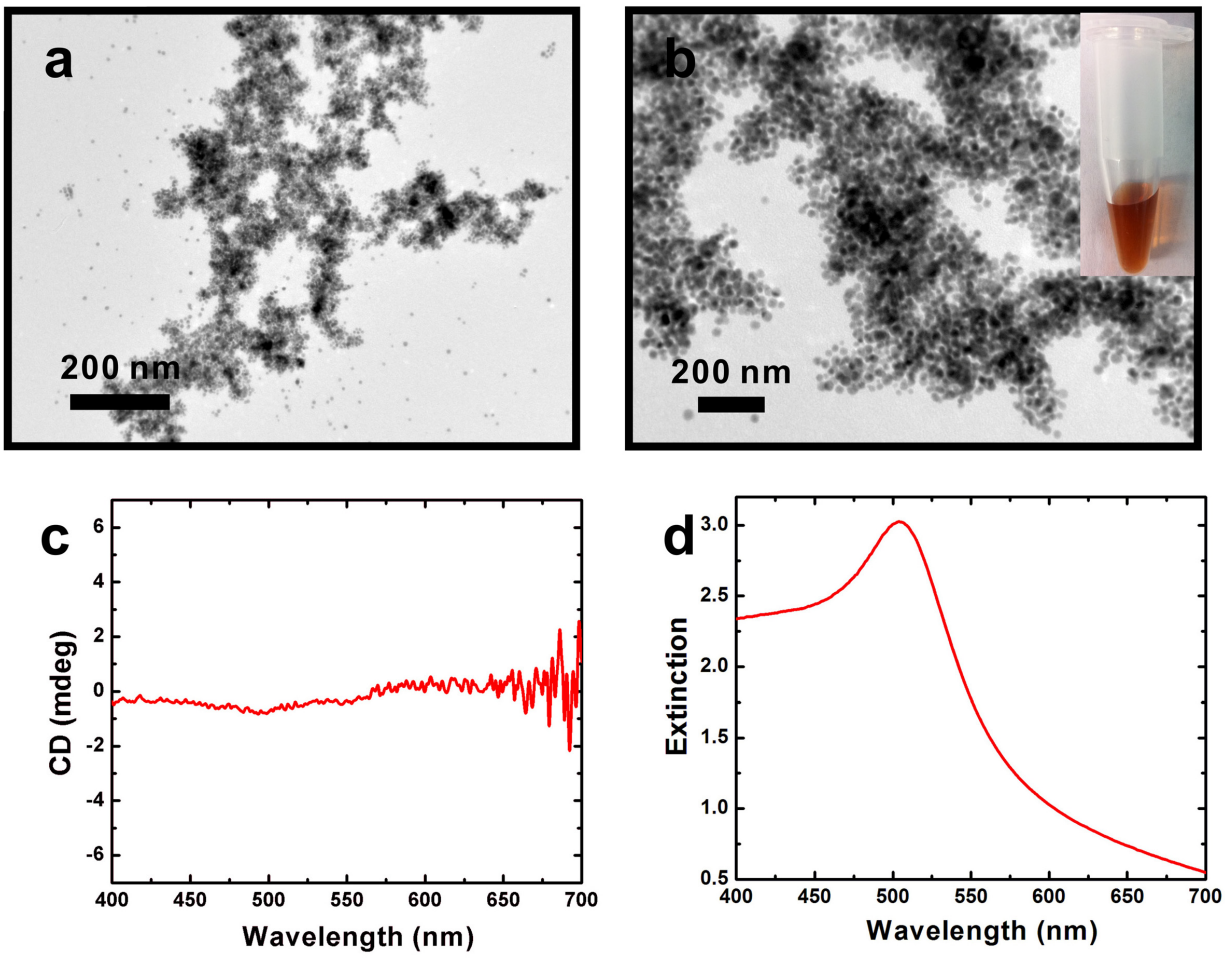


**Figure 3.31**. ((a),(b)TEM images of $PEP_{Au}$ capped free gold nanoparticles enhanced by 27 µl Ag enhancer solution.(Inset image shows the orange color of Ag enhanced free gold NP solution) (c) CD spectrum of Ag enhanced free gold NP solution. The path length of the light is 1 mm. (d) UV/Vis spectrum of Ag enhanced free gold NP solution. The surface plasmon peak is blue shifted to 503 nm compared with the typical peak (520 nm) of free gold NPs[144]. The path length of the light is 10 mm. (note: graphs are not corrected for dilution effects)

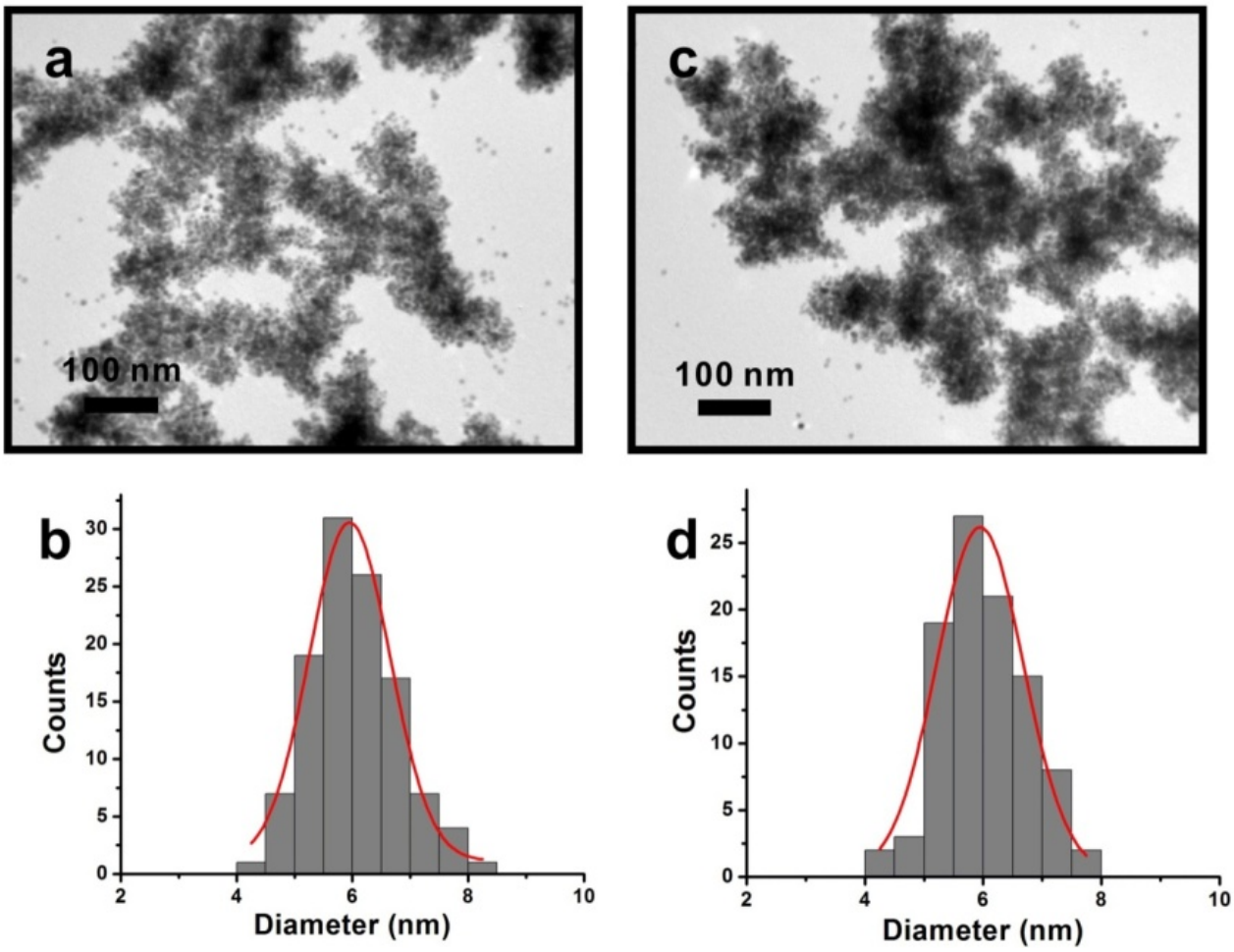


**Figure 3.32**. TEM images reveal that the size of silver coated gold nanoparticles is almost constant within one hour. (a)TEM image of $PEP_{Au}$ capped free gold nanoparticles enhanced by 27 µl Ag enhancer solution incubating for one hour. (b) Distribution of size of Ag enhanced free gold NP solution after one hour incubation (based on 97 counts; diameter = 5.95 ± 0.73 nm).(c)TEM image of $PEP_{Au}$ capped free gold nanoparticles enhanced by 27 µl Ag enhancer solution incubating for two hours. (d) Distribution of size of Ag enhanced free gold NP solution

after two hours incubation (based on 113 counts; diameter = 5.95 ± 0.70 nm).We provide this comparison, because the CD data were collected on a sample that had been incubated with silver for 1 h. After the 1 h, the sample was taken to the instrument and CD was measured. We wanted to determine whether the particles would change significantly during transfer time and data collection time (after the 1 h incubation). This study indicates that the particles do not significantly change after the course of 1 h incubation with silver.

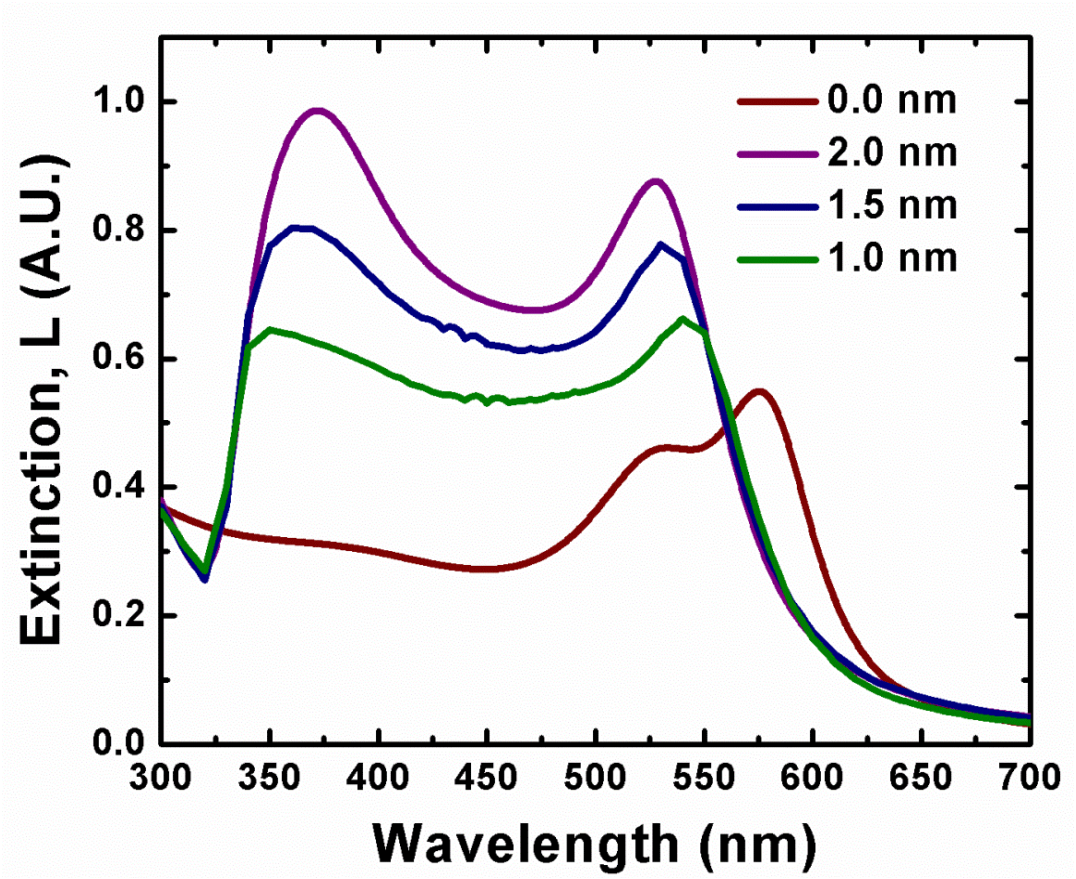


**Figure 3.33**. The simulated effect of silver shell thickness on the extinction of a double helix ensemble comprising 22 spheres. The silver shell thickness was sampled at 1.0 nm, 1.5 nm and 2.0 nm. The interhelical spacing is 7.0 nm, the gold sphere diameter is 8.0 nm and the interparticle spacing is 1.5 nm.

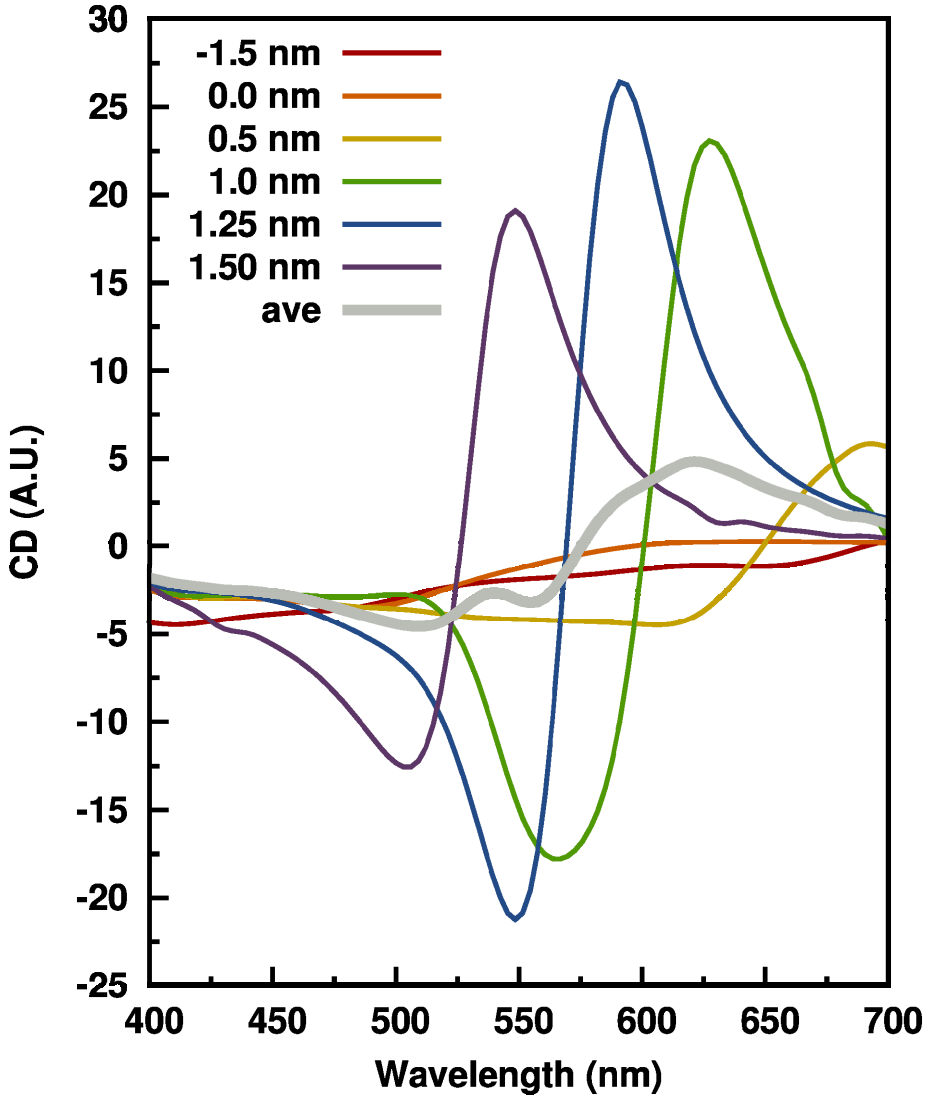


**Figure 3.34**. The simulated effect of interparticle gap on a 4.0 nm radius gold spheres with 1.5nm silver shell on the CD response of a double helix ensemble comprising 22 spheres. The legend indicates the changing interparticle gap. When the gap is -1.5 nm, the shells overlap, and the gold cores are separated by 1.5 nm. The interhelical spacing is 7.0 nm. The figure shows that by averaging a distribution of interparticle spacings leads to an interference style effect that results in a flat CD response below 500 nm.

## 3.3 CONCLUSION

The peptide-based assembly toolkit allows for the construction of a diverse set of gold nanoparticle double helices with tunable structures, handedness, and physical properties. We used this toolkit to prepare left- and right-handed gold nanoparticle double helices which exhibit well-defined plasmonic circular dichroism signals. By coupling predictions from theory and simulation with experiment, we demonstrated that tuning the nanoparticle size can affect the chirooptical properties and that altering the composition of the helices can dramatically affect the position and intensity of the plasmonic CD signal. In future experiments, we aim to orient and assemble the helices in to obtain a much higher chirooptical response. Also, we aim to design peptide conjugates for preparing helices with different pitch, interparticle distance, and interhelical distance to further experimentally assess how these parameters affect the CD response. The work reported herein indicates that this peptide-based nanoparticle assembly methodology is a powerful means of preparing tailorable plasmonic nanostructures with carefully tunable chirooptical properties.

## 3.4 EXPERIMENTAL SECTION

### 3.4.1 Materials and general methods

All solvents and chemicals were obtained from commercial sources and used without further purification. 0.1M HEPES Buffer (HEPES = 4-(2-hydroxyethyl)-1-piperazineethanesulfonic acid) was made by directly diluting 1.0M HEPES buffer (pH = 7.3 ± 0.1; Fisher Scientific) with water (NANOpure, Barnstead DiamondTM System.; 18.2 MΩ). 0.1 M citrate buffer was made using citric acid powder (pH = 7.3 ± 0.1, pH was adjusted with NaOH) andNANOpure water. Peptides with sequences of all L amino acids AYSSGAPPMPPF (L-$PEP_{Au}$) and all D amino acids AYSSGAPPMPPF (D-$PEP_{Au}$) were synthesized and purified by New England Peptide and Argonne National Laboratory, respectively, with final purity of 99%.Reverse-phase high-pressure liquid chromatography (HPLC) was performed at ambient temperature with an Agilent 1200 liquid chromatographic system equipped with diode array and multiple wavelength detectors using a Grace Vydac protein C4 column (214TP1010, 1.0 cm × 25 cm). Matrix-assisted laser desorption ionization time-of-flight (MALDI-TOF) mass spectra were obtained on an Applied Biosystem Voyager System 6174 MALDI-TOF mass spectrometer using α-cyano-4-hydroxy cinnamic acid (CHCA) as the matrix. Transmission electron microscopy (TEM) samples were prepared by depositing one drop of solution (5 μl) onto a 3-mm-diameter copper grid coated with Formvar/Carbon film. After deposition, the excess solution was wicked from grid with a piece of filter paper. Then, the grid was washed with NANOpure water. TEM analysis was conducted on a JEOL 200CX instrument operated at 200 kV and images were collected using a Gatan charge-coupled device (CCD) image system. STEM was performed on the JEM-2100F HR-TEM operated with a Schottky field-emission electron gun (FEG) at 200 kV

and images were collected using a Gatan CCD image system. The projection images from electron tomography studies were recorded with a Gatan 4K × 4K CCD camera mounted on a Tecnai F20 electron microscope (FEI Corporation, Hillsboro, Oreg.) equipped with a field emission gun (FEG) operating at 200 kV. For electron tomography, a series of images were recorded at room temperature at a nominal magnification of 80,000 x by tilting the specimen from −56° to 70° in increments of 1°. Images were recorded at an underfocus value of1.5 μm along the tilt axis. A back-projection algorithm, as implemented in the IMOD reconstruction package[159],was used to convert the information present in the series of tilted projection images into three-dimensional density maps. The surface rendering was generated using the UCSF Chimera software[160]. Circular dichroism measurementswere conducted on a Olis DSM 17 CD spectrometer. The scan rate was 8 nm/min. All CD experiments were carried out in a 0.08 M HEPES and 0.02 M citrate buffer (pH=7.3±0.1) with a quartz cuvette (0.1 cm path length) at 25 °C.

### 3.4.2 Preparation of N-hydroxyl-succinimide ester and peptide conjugate

**N-hydroxyl-succinimide esters.** Dodecanoic acid (1.200 g, 6.0 mmol) and N-hydroxysuccinimide (0.730 g, 6.3 mmol) were dissolved in 30 mL dry $CH_3COOC_2H_5$ under an argon atmosphere. After addition of dicyclohexyl carbodiimide (DCC) (1.47 g, 6.6 mmol) at 0ºC, the solution was stirred overnight at room temperature. The reaction mixture was processed by removing the precipitate via filtration. The solvent was removed under reduced pressure and the crystalline residue recrystallized from isopropanol (iPrOH) to yield the N-hydroxyl-succinimide ester (0.495g, 1.7 mmol, 28%).

**Peptide Conjugates.** L-AYSSGAPPMPPF (1.26 mg, 1.03 $\times 10^{-6}$ mol) was dissolved in 60 µL DMF. After addition of dodecanoic N-hydroxyl-succinimide ester (0.6 mg, $4.91 \times 10^{-7}$ mol) in 60µL DMF and 1 µL $Et_3N$ under stirring, the solution was stirred at room temperature for 12 hours. Pure $C_{12}$-L-$PEP_{Au}$ (Scheme S1) was obtained by conducting reversed-phase HPLC eluting with a linear gradient of 0.05% formic acid in $CH_3CN$ and 0.1% formic acid in water (5/95 to 95/5 over 30 minutes). The molecular weight for $C_{12}$-L-$PEP_{Au}$ was confirmed by MALDI-TOF mass spectrometry. Concentration of the peptide was determined spectrophotometrically in water/acetonitrile (1:1) using the molar extinction coefficient of tyrosine (1280 $M^{-1}cm^{-1}$) at 280 nm.

**NOTE:** $C_{12}$-D-$PEP_{Au}$ (Scheme S1) was prepared, purified, and characterized in a similar fashion.

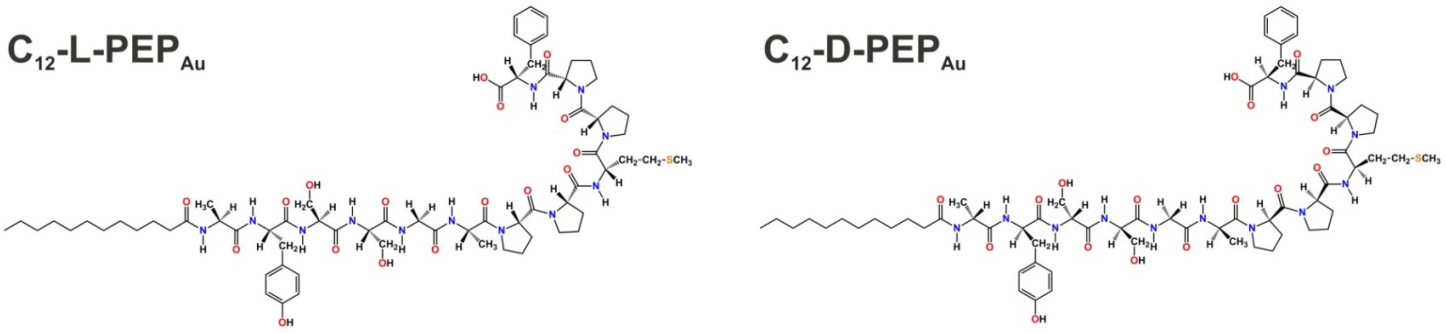


**Scheme 3.1**. Structural formula of peptide conjugates $C_{12}$-L-$PEP_{Au}$ and $C_{12}$-D-$PEP_{Au}$.

### 3.4.3 Preparation of left and right-handed gold nanoparticle double helices

A gold ion precursor solution was prepared: 0.1M chloroauric acid ($HAuCl_4$) in 1.0 M triethylammonium acetate (TEAA; pH = 7.0) buffer was incubated for 10minutes at room temperature. Thereafter, this mixture was centrifuged (10 min., 5K rpm). Lyophilized $C_{12}$-L-$PEP_{Au}$ (~ $3.75 \times 10^{-8}$ mol) was completely dissolved in 250 µl 0.08 M HEPES and 0.02 M citrate buffer (pH=7.3±0.1) in a plastic vial. This peptide solution was allowed to incubate for 30 minutes. Thereafter, 2 µl of the supernatant of the centrifuged gold ion precursor solution was added to the peptide conjugate solution. The mixture was vortexed for a few seconds and then left undisturbed at room temperature for 1 day. Gold nanoparticle double helices were clearly observed as product after ~1 hour.

**NOTE**: When $C_{12}$-D-$PEP_{Au}$ was used to prepare right-handed helices similar reaction conditions were employed.

### 3.4.4 Preparation of left and right-handed double helices comprising large gold nanoparticles

A gold ion precursor solution was prepared: 0.1M chloroauric acid ($HAuCl_4$) in 1.0 M triethylammonium acetate (TEAA; pH = 7.0) buffer was incubated for 10minutes at room temperature. Thereafter, this mixture was centrifuged (10 min., 5K rpm). Lyophilized $C_{12}$-L-$PEP_{Au}$ (~ $3.75 \times 10^{-8}$ mol) was completely dissolved in 250 µl 0.08 M HEPES and 0.02 M citrate buffer (pH=7.3±0.1) in a plastic vial. This peptide solution was allowed to incubate for 30 minutes. Thereafter, 2 µl of the supernatant of the centrifuged gold ion precursor solution was added to the peptide conjugate solution. The mixture was vortexed for a few seconds and then

left undisturbed at room temperature for 1 day. At this point, 4 µl of 0.1M chloroauric acid ($HAuCl_4$) aqueous solution was added to the above solution and then vortexed for 5 seconds. After incubation of the above mixture solution for 1 minute, 250 µl 0.1 M Hydroquinone, 0.08 M HEPES and 0.02 M citrate buffer was added. The mixture solution was vortexed for 3 minutes and the color became dark purple. Double helices with large gold nanoparticles were clearly observed as product after ~1 hour.

**NOTE**: When $C_{12}$-D-$PEP_{Au}$ was used, similar reaction conditions were employed.

### 3.4.5 Preparation of left-handed double helices comprising small gold nanoparticles

A gold ion precursor solution was prepared: 0.1M chloroauric acid ($HAuCl_4$) in 1.0 M triethylammonium acetate (TEAA; pH = 7.0) buffer was incubated for 10minutes at room temperature. Thereafter, this mixture was centrifuged (10 min., 5K rpm). Lyophilized $C_{12}$-L-$PEP_{Au}$ (~ $3.75 \times 10^{-8}$ mol) was completely dissolved in 250 µl 0.06 M HEPES and 0.04 M citrate buffer (pH=7.3±0.1) in a plastic vial. This peptide solution was allowed to incubate for 30 minutes. Thereafter, 2 µl of the supernatant of the centrifuged gold ion precursor solution was added to the peptide conjugate solution. The mixture was vortexed for a few seconds and then left undisturbed at room temperature for 1 day.

### 3.4.6 Preparation of silver coated left and right-handed gold nanoparticle double helices

A gold ion precursor solution was prepared: 0.1M chloroauric acid ($HAuCl_4$) in 1.0 M triethylammonium acetate (TEAA; pH = 7.0) buffer was incubated for 10minutes at room temperature. Thereafter, this mixture was centrifuged (10 min., 5K rpm). Lyophilized $C_{12}$-L-$PEP_{Au}$ (~ $3.75 \times 10^{-8}$ mol) was completely dissolved in 250 µl 0.08 M HEPES and 0.02 M citrate

buffer (pH=7.3±0.1) in a plastic vial. This peptide solution was allowed to incubate for 30 minutes. Thereafter, 2 µl of the supernatant of the centrifuged gold ion precursor solution was added to the peptide conjugate solution. The mixture was vortexed for a few seconds and then left undisturbed at room temperature for 1 day.A commercially available silver enhancement kit (HQ Silver Enhancement, Nanoprobes, USA) was used for the silver enhancement experiments. There are three kinds of solutions (i.e. "Enhancer", "Activator" and "Initiator") provided by the company. "Enhancer", "Activator", and "Initiator" solutions were mixed in a 1:1:1 volume ratio.Either 9 µl, 27 µl, 54 µl,or108 µl of the pre-mixed silver enhancer solution was added to the nanoparticle double helixmixture. The resulting mixtures were vortexed for 3 minutes and then left undisturbed for 1 hour. CD spectra were measured without any further treatment.

**NOTE**: When $C_{12}$-D-$PEP_{Au}$ was used, similar reaction conditions were employed.

### 3.5 Theoretical Models

Classical electrodynamics simulations were performed using the Discrete Dipole Approximation (DDA).[146,147] The DDA is an approximate method, but is well known to reproduce essential spectral features[161] of plasmonic nanostructures. Within the framework of the DDA, a target structure is represented by a set of *N* polarizable point dipoles which sit on a cubic lattice. The polarizability, $\alpha_i$, of the $i^{th}$ point is given by a modified version of the Clausius-Mossotti relationship that relates the macroscopic dielectric function of the metals to the microscopic polarizability of the point dipoles. The modified relationship is often referred to as a lattice dispersion relationship (LDR), and here we have used a version called the Gutkowicz-Krusin & Draine Lattice Dispersion Relation (GKD-LDR)[162] as it corrects for an error in previously published LDRs.[163] Returning to the choice of macroscopic dielectric function, the optical

constants of Johnson and Christy[164] were used, after the inclusion of modifications to account for a confined electron mean free path.[165] All simulations were performed in a background medium of water (n=1.333).

In the DDA, the polarizability is used to relate the local electric field at each lattice site, $\mathbf{E}_{loc,i,}$ to the instantaneous dipole moment, $\mathbf{P}_i$, of each dipole: [166]

$$\mathbf{P}_i = \alpha_i \mathbf{E}_{loc,i} \qquad (1)$$

The local electric field, $\mathbf{E}_{loc,i}$, at each point is the sum of the incident field, $\mathbf{E}_{inc,i}$, and the fields from the remaining $N$-1 dipoles, $\mathbf{E}_{dip,i}$:

$$\mathbf{E}_{dip,i} = \sum_{j \neq i} \frac{e^{i\mathbf{k}\mathbf{r}_{ij}}}{\mathbf{r}_{ij}^3} \left\{ k^2 \mathbf{r}_{ij} \times (\mathbf{r}_{ij} \times \mathbf{P}_j) + \frac{(1 - i\mathbf{k}\mathbf{r}_{ij})}{\mathbf{r}_{ij}^2} [\mathbf{r}_{ij}^2 \mathbf{P}_j - 3\mathbf{r}_{ij}(\mathbf{r}_{ij}.\mathbf{P}_j)] \right\} = \sum_{j \neq i} \mathbf{A}_{ij}.\mathbf{P}_j \,, \qquad (2)$$

where the contribution to the field at position i from the radiating dipole at position j is contained in the 3x3 matrix $\mathbf{A}_{ij}$. The final set of linear equations to be solved can then be written in terms of the incident field, $\mathbf{E}_{inc}$, at the position of each dipole $\mathbf{r}_i$:[167]

$$\mathbf{E}_{inc,i} = \frac{\mathbf{P}_i}{\alpha_i} + \sum_{j \neq i} \mathbf{A}_{ij}.\mathbf{P}_j \,. \qquad (3)$$

The incident field circularly polarized light is given by $\mathbf{E}_{inc,i} = \mathbf{e}_H \, e^{i\mathbf{k}\mathbf{r}_i}$ where handedness, $H$, takes values L (left) and R (right), which - for a plane wave propagating in the positive x direction - gives polarization vectors:

$$\mathbf{e}_L = \begin{bmatrix} 0 \\ i \\ 1 \end{bmatrix} / \sqrt{2} \text{ and } \mathbf{e}_R = \begin{bmatrix} 0 \\ 1 \\ i \end{bmatrix} / \sqrt{2} \,. \qquad (4)$$

**Selection of Orientations**

Simulated CD spectra are very sensitive to the method used to perform orientational averaging. We chose to fix the position and orientation of the helix and rotate the wavevector (**k**) of the incident field for convenience. The list of incident wavevectors was generated using an algorithm that produces quasi-equidistant points on a sphere for an arbitrary number of orientations.[148-151] This ensures that all orientations of the helix with respect to the incident wavevector had equivalent weight. In all the simulations here, we found that 34 wave-vectors on a single octant of the sphere were sufficient to ensure convergence of the CD spectrum.

# 4.0 EXPEDITIOUS SYNTHESIS AND ASSEMBLY OF SUB-100 NM HOLLOW SPHERICAL GOLD NANOPARTICLE SUPERSTRUCTURES

This work, written in collaboration with Gongpu Zhao, Peijun Zhang, and Nathaniel L.Rosi*, was published in *J. Am. Chem. Soc.* **2010**, 132(40), 14033. 

Gongpu Zhao and Peijun Zhang performed the electron tomography studies.

## 4.1 INTRODUCTION

Individual nanoparticles have size, shape, and composition-dependent properties. Nanoparticle assemblies can exhibit unique ensemble properties which depend on the organization of the nanoparticles.[86,168-170] Therefore, to control the ensemble properties of a nanoparticle assembly, methods must be developed to precisely control the placement of nanoparticles within the assembly. Achieving rational control of nanoparticle assembly from the 'bottom-up' is a significant synthetic challenge and represents one of the most important hurdles in modern nanoscience. Practical methods which address this challenge would ideally 1) allow for expeditious construction of arbitrarily complex nanoparticle superstructures, 2) enable assembly

of nanoparticles of any composition, 3) permit precise control over structural attributes, including nanoparticle size and position, and 4) require few preparative steps.

We recently introduced new methodology for designing and assembling nanoparticle superstructures which begins to address these important criteria.[171,172] This methodology relies on unique peptide conjugate molecules comprising peptides with sequences of amino acids that recognize and bind specific inorganic compositions and organic tethers designed to influence the self-assembly of these peptides.[173] In the presence of inorganic salts and reducing agents, properly designed peptide conjugate molecules can orchestrate a one-pot reaction in which the synthesis and assembly of nanoparticles into complex superstructures occurs simultaneously. From the outset of our studies in this area, we targeted hollow spherical nanoparticle superstructures[89,174-178] because of their potential practical application as capsules or delivery agents[179,180] and because of the inherent challenge of expeditiously generating such structures in a directed one-pot synthesis. Here, we introduce a new peptide conjugate which directs the construction of such structures (**Scheme 4.1**). Importantly, we demonstrate that, when using this methodology, small modifications to the peptide conjugate can dramatically impact the topology of the final nanoparticle superstructure.

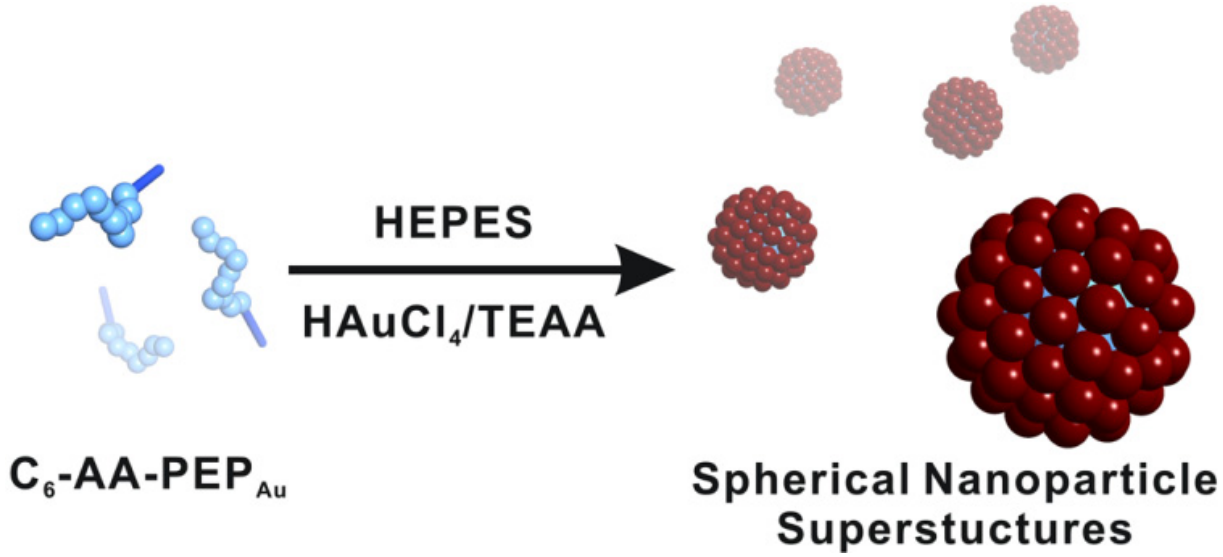


**Scheme 4.1**. Direct preparation of hollow spherical gold nanoparticle superstructures (red spheres = gold nanoparticles).

## 4.2 RESULTS AND DISSCUSSION

In our previous work, we showed that $C_{12}$-$PEP_{Au}$ conjugates ($PEP_{Au}$ [65] = AYSSGAPPMPPF), when mixed with a gold salt and a reducing agent, direct the synthesis and assembly of 1-D gold nanoparticle double helices exhibiting tailorable metrics and structures.[171,172] These results prompted us to systematically investigate how shortening the length of the aliphatic tether would impact the synthesis and assembly process and the ultimate structure of the product nanoparticle superstructure. Accordingly, we prepared $C_{10}$-$PEP_{Au}$, $C_8$-$PEP_{Au}$, and $C_6$-$PEP_{Au}$ using established methods. Each conjugate was individually dissolved in 0.1 M HEPES buffer (pH = 7.3 ± 0.1; HEPES = 4-(2- hydroxyethyl)-1-piperazineethanesulfonic acid) and an aliquot of chloroauric acid/triethylammonium acetate ($HAuCl_4$/TEAA) buffer solution (0.1 M $HAuCl_4$ in 1.0 M TEAA, pH = 7.0) was added to each solution. In this system, HEPES serves as the primary reducing agent.[83,181,182] $C_{10}$-$PEP_{Au}$ reactions yielded 1-D nanoparticle superstructures, while $C_6$-$PEP_{Au}$ and $C_8$-$PEP_{Au}$ reactions only yielded dispersed individual nanoparticles or nanoparticle aggregates (**Figure 4.1**). Based on these observations, we concluded that the $C_6$ and $C_8$ tethers were not sufficient for directing either the assembly of the peptide conjugate or the organization of the nanoparticles.

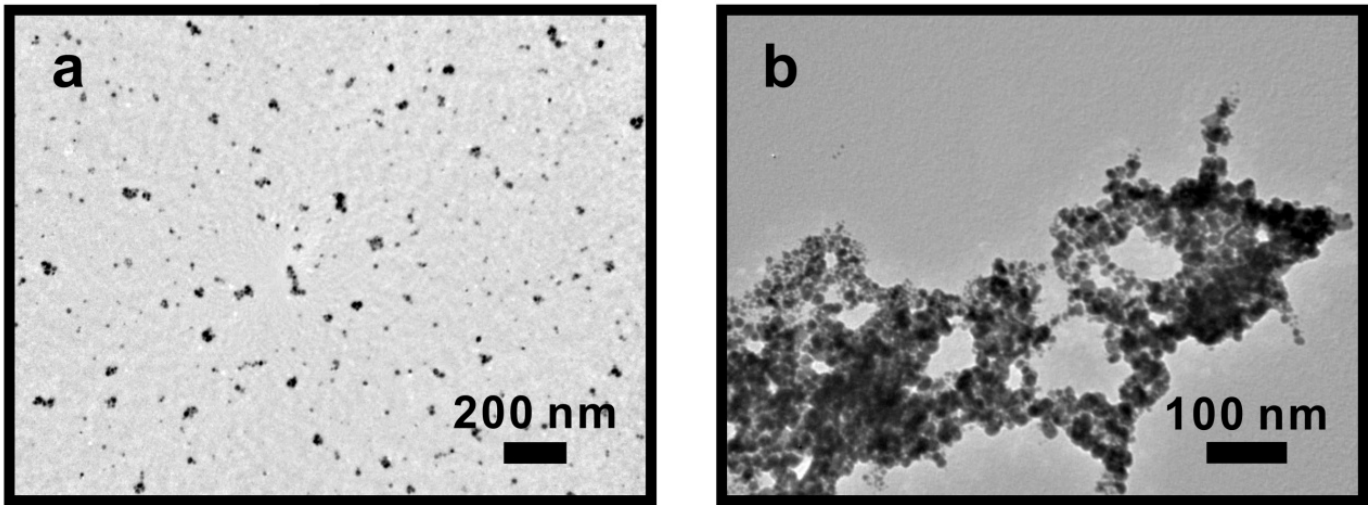


**Figure 4.1.** (a) TEM image of nanoparticles formed from reaction using $C_6$-$PEP_{Au}$. (b) TEM image of nanoparticles formed from reaction using $C_8$-$PEP_{Au}$.

We note that both the amino acid sequence and the organic tether can influence the self-assembly of the peptide conjugate. Therefore, we prepared $C_6$-AA-$PEP_{Au}$, reasoning that the alanine residues attached to the N-terminus of $PEP_{Au}$ could impact the self-assembly of the conjugate.[183] We found that $C_6$-A-$PEP_{Au}$ $C_6$-AA-$PEP_{Au}$ and $C_6$-AAA-$PEP_{Au}$ all direct the formation of spherical gold nanoparticle superstructures (**Figure 4.2**). Of these, $C_6$-AA-$PEP_{Au}$ yielded the best structures, therefore we explored this system in more detail. $C_6$-AA-$PEP_{Au}$ self-assembles into spherical structures (diameter = 136.5 ± 2.6 nm) upon incubation in water (24 h), as evidenced by TEM (**Figure 4.3**) and AFM (**Figure 4.4**). However, no self-assembly was observed in HEPES (**Figure 4.5**). AFM height images suggest that the spheres spread onto the MICA surface, resulting in broader and flatter structures (height = 29.3 ± 1.0 nm and diameter = 525.2 ± 8.9 nm; **Figure 4.4**). AFM phase images collected of the structures after TEM imaging and consequent exposure to high vacuum revealed that the structures had collapsed in the middle (**Figure 4.6**).

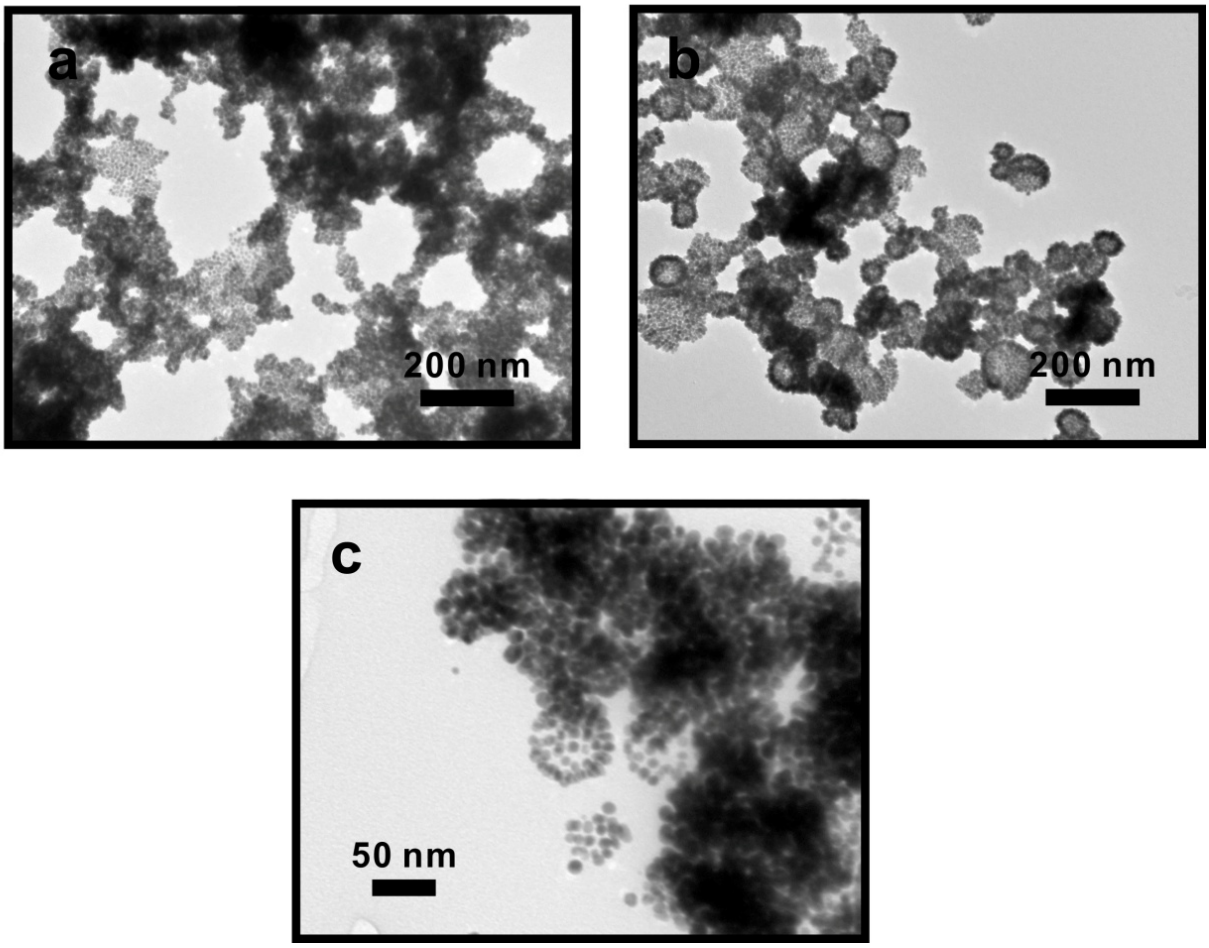


**Figure 4.2.** (a) TEM image of nanoparticles formed from reaction using $C_6$-A-$PEP_{Au}$. (b) TEM image of nanoparticles formed from reaction using $C_6$-AA-$PEP_{Au}$. (c) TEM image of nanoparticles formed from reaction using $C_6$-AAA-$PEP_{Au}$.

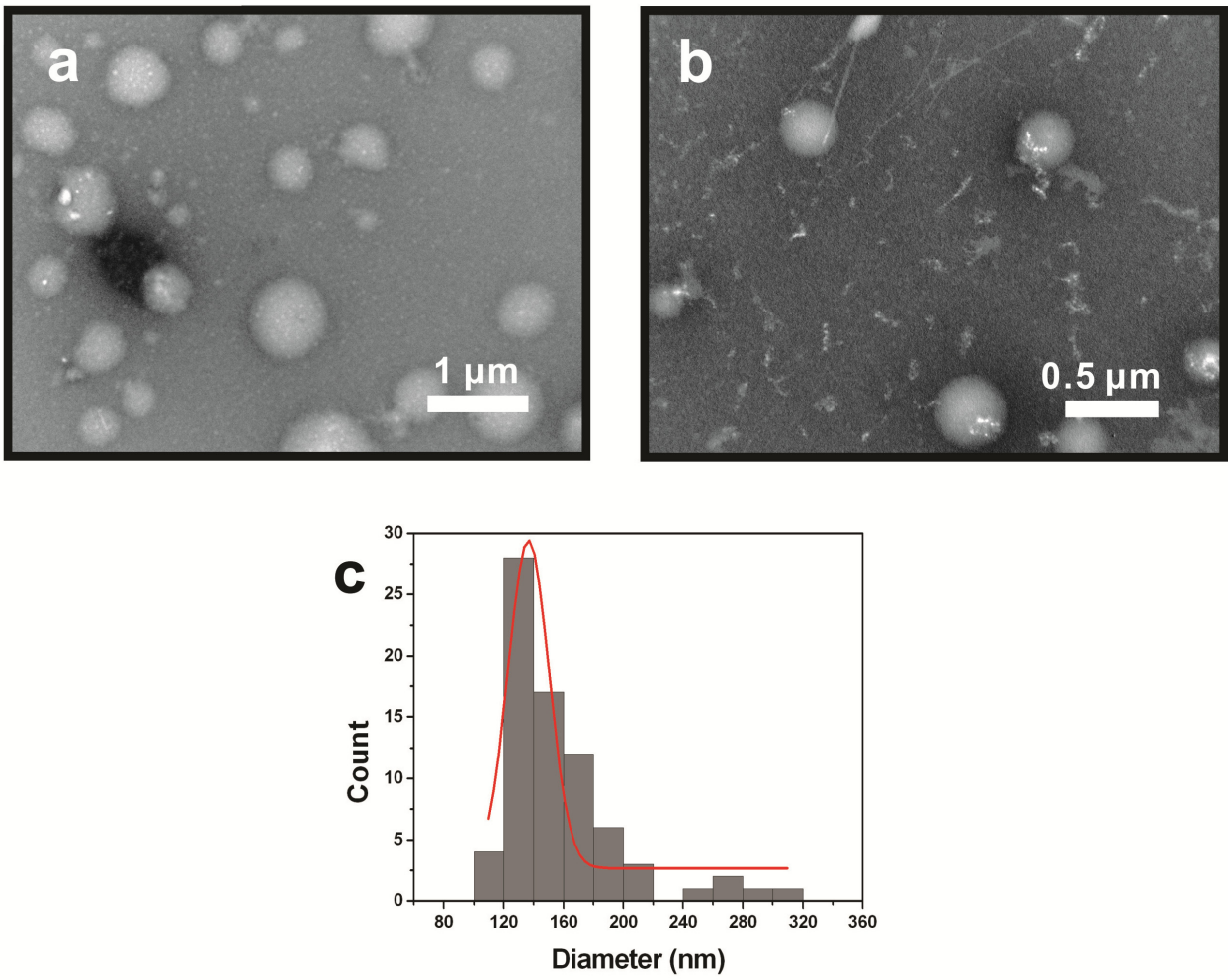


**Figure 4.3**. (a) (b) Additional TEM images of $C_6$-AA-$PEP_{Au}$ nanospherical structures obtained from dissolving $C_6$-AA-$PEP_{Au}$ in pure water. (c) Diameter distribution of the $C_6$-AA-$PEP_{Au}$ self-assembled spherical structures (based on 80 counts; diameter = 136.5 ± 2.6 nm).

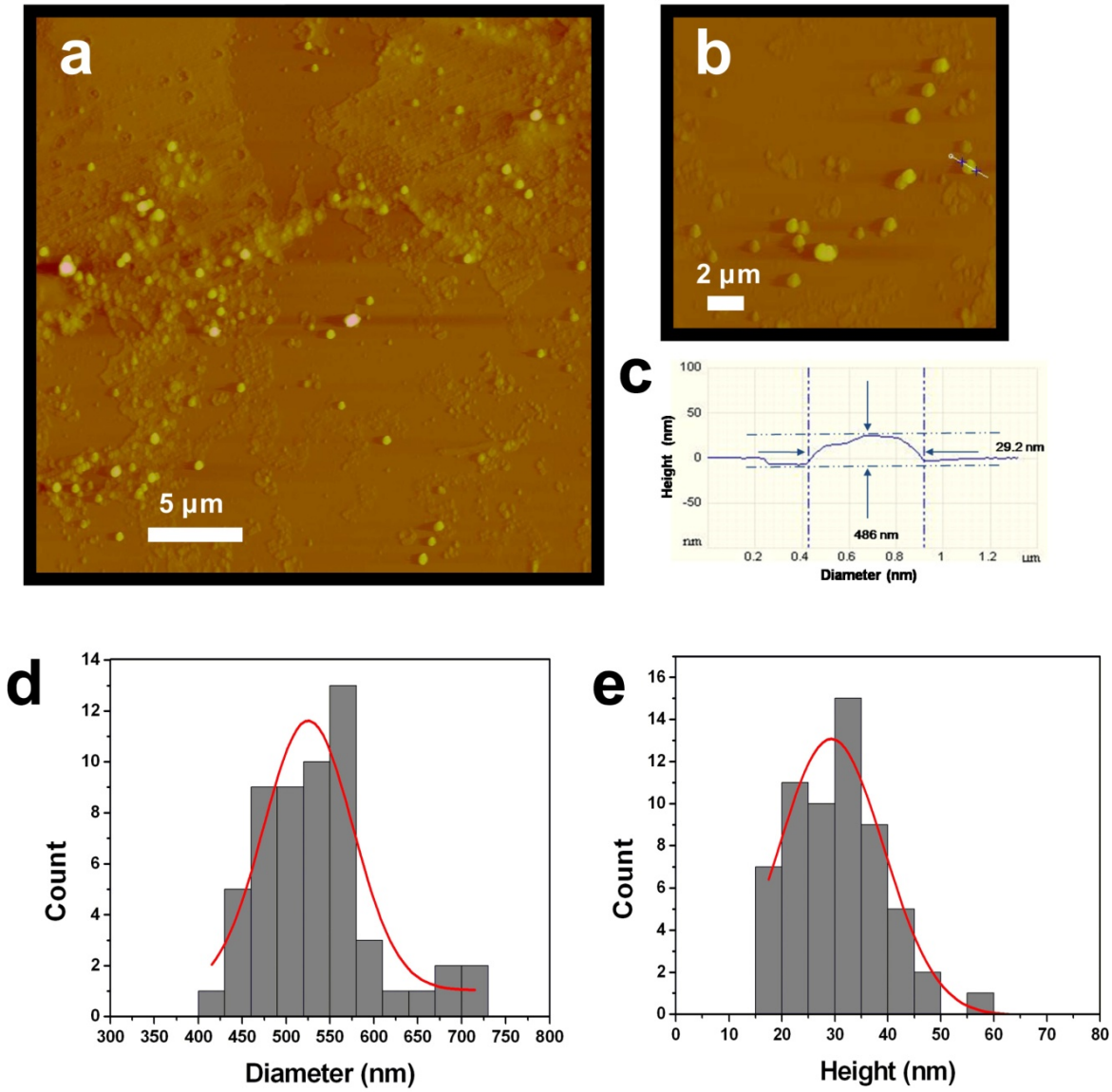


**Figure 4.4.** AFM height images of $C_6$-AA-$PEP_{Au}$ spherical structures (a) and height measurements (b),(c). e) Diameter distribution of the $C_6$-AA-$PEP_{Au}$ spherical structures (based on 60 counts from AFM images; diameter = 525.2 ± 8.9 nm). f) Height distribution of the $C_6$-AA-$PEP_{Au}$ spherical structures (based on 60 counts from AFM images; height = 29.3 ±1.0 nm). We note that AFM does not provide accurate width/diameter measurements. However, we

include these measurements because they indicate that the structures are ‘soft’ and tend to spread-out on the MICA surface.

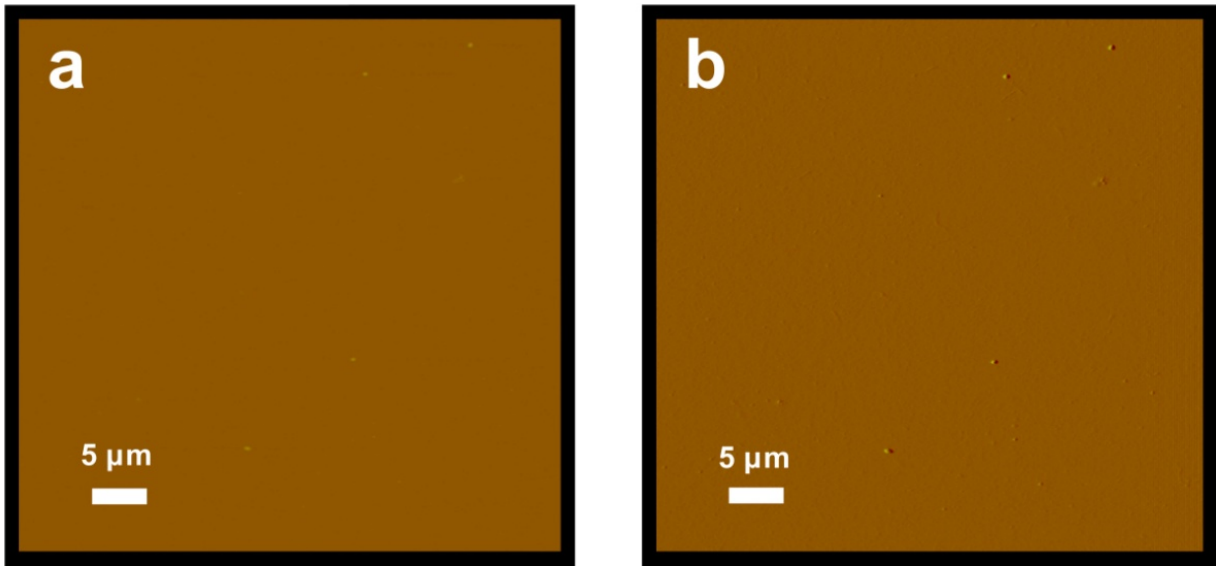


**Figure 4.5.** AFM height and amplitude images of samples taken from a solution of $C_6$-AA-$PEP_{Au}$ in 0.1 M HEPES buffer. (a) is a height image and (b) is an amplitude image.

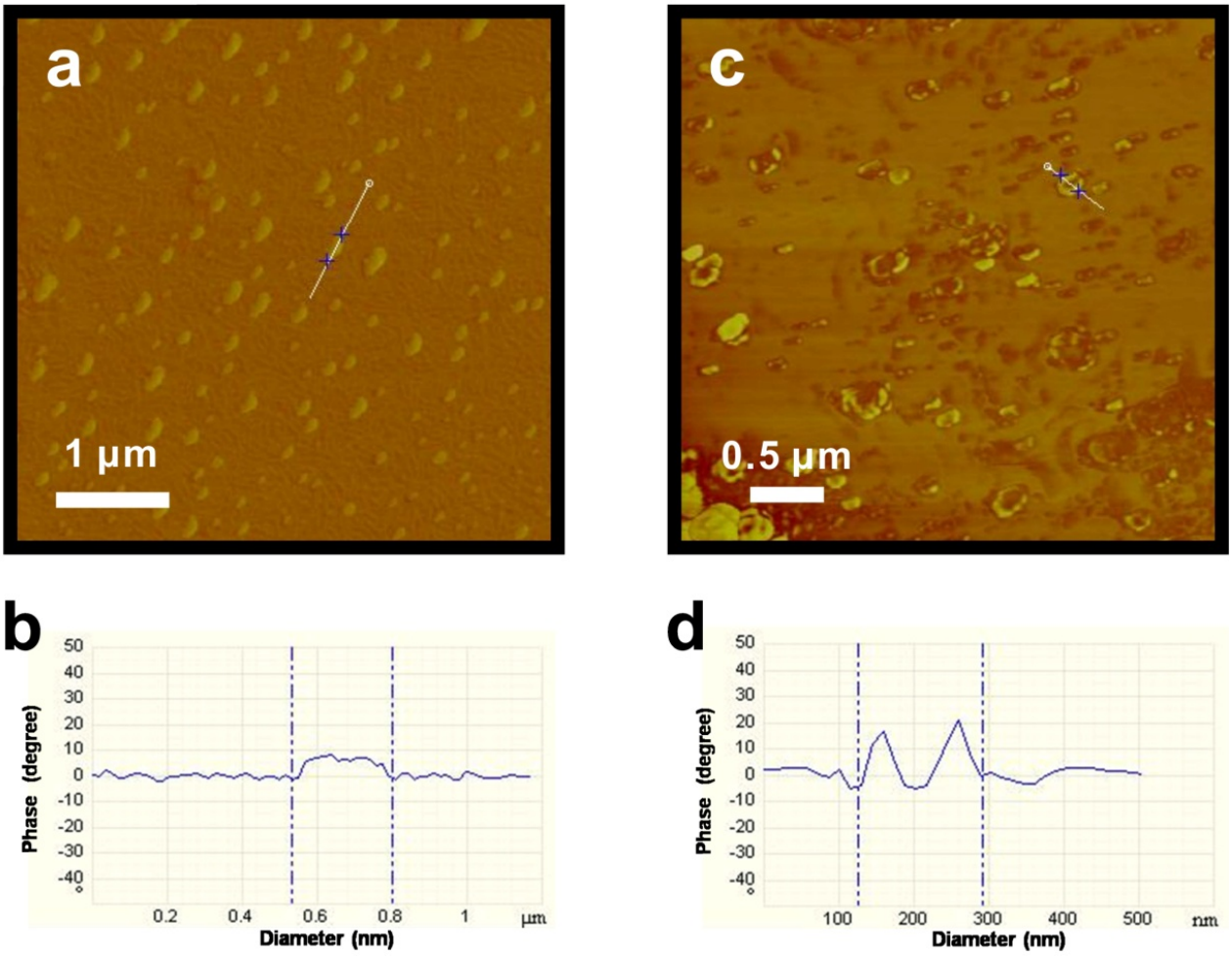


**Figure 4.6**. (a) AFM phase image of $C_6$-AA-$PEP_{Au}$ spherical structures deposited on a Formvar-carbon film copper TEM grid (AFM collected prior to TEM analysis and accompanying high vacuum treatment) and (b) cross-sectional analysis of this sample. (c) AFM phase image the same sample as that in (a), yet the AFM was collected after TEM analysis (d) cross-sectional analysis of this sample.

Collectively these AFM data suggest that the self-assembled $C_6$-AA-$PEP_{Au}$ spherical structures are hollow. Encouraged by these observations, we proceeded to evaluate whether $C_6$-AA-$PEP_{Au}$ could direct the self-assembly of gold nanoparticles into hollow spherical superstructures. $HAuCl_4$/TEAA was added to a solution of $C_6$-AA-$PEP_{Au}$ in HEPES buffer to yield a colorless solution. After incubating at room temperature for 24 h, the solution became light purple, suggesting the formation of gold nanoparticle aggregates. TEM analysis of samples of this solution revealed exclusive formation of spherical structures comprising gold nanoparticles (8.3 ± 0.2nm) (**Figure 4.7**). The UV-Vis spectrum of the spherical superstructures exhibits a maximum absorbance at 540 nm (**Figure 4.8**), which, as expected, is red-shifted compared to that of colloidal solutions of 9 nm gold nanoparticles (~517 nm). Close examination of the TEM images indicated that, with dark edges and light interiors, the structures likely consisted of a self-assembled $C_6$-AA-$PEP_{Au}$ core (35.3 ± 1.0 nm) surrounded by a monolayer gold nanoparticle shell (51.6 ± 0.8 nm) (**Figure 4.9**).

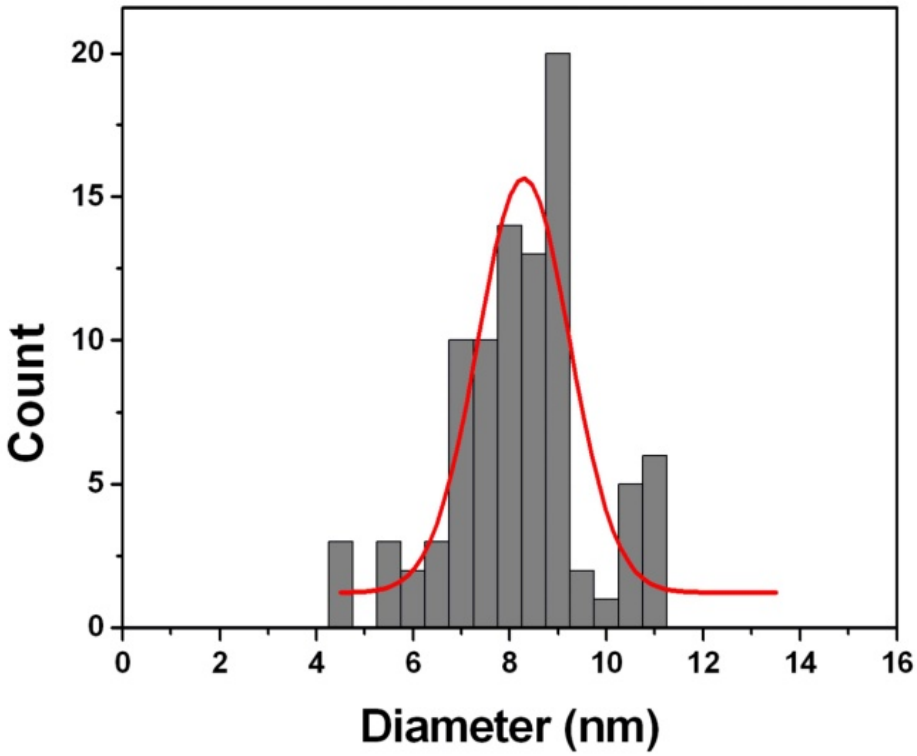


**Figure 4.7.** Additional TEM images (a) of spherical gold nanoparticle superstructures. (d) Size distribution of gold nanoparticles within the superstructures (based on 100 counts; diameter = 8.3 ± 0.2 nm).

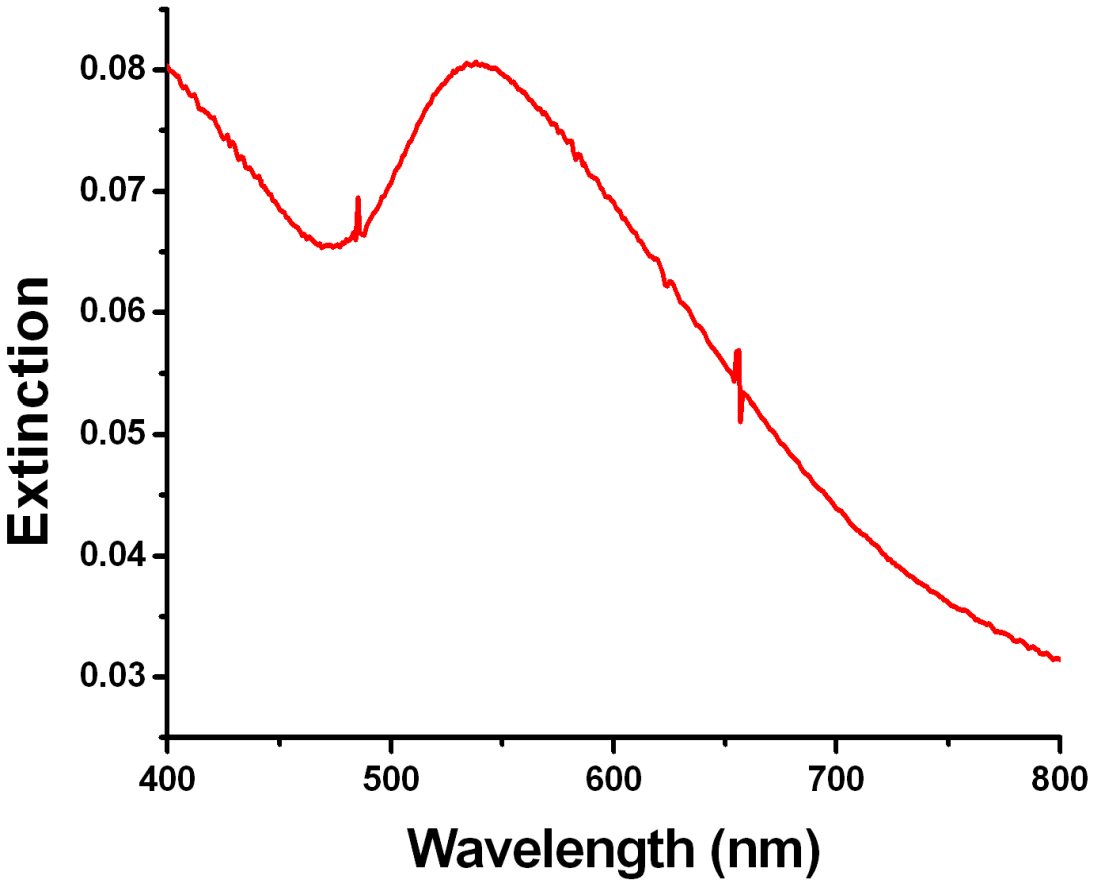


**Figure 4.8.** The UV-Vis spectrum of the spherical gold nanoparticle superstructures in solution. The absorbance maximum is observed at 540 nm. The peak is significantly red-shifted and broadened compared to what is typically observed for monodisperse colloidal solutions of gold nanoparticles having particle sizes similar to those within the spherical superstructures. This is expected due to the plasmonic coupling between the assembled nanoparticles.

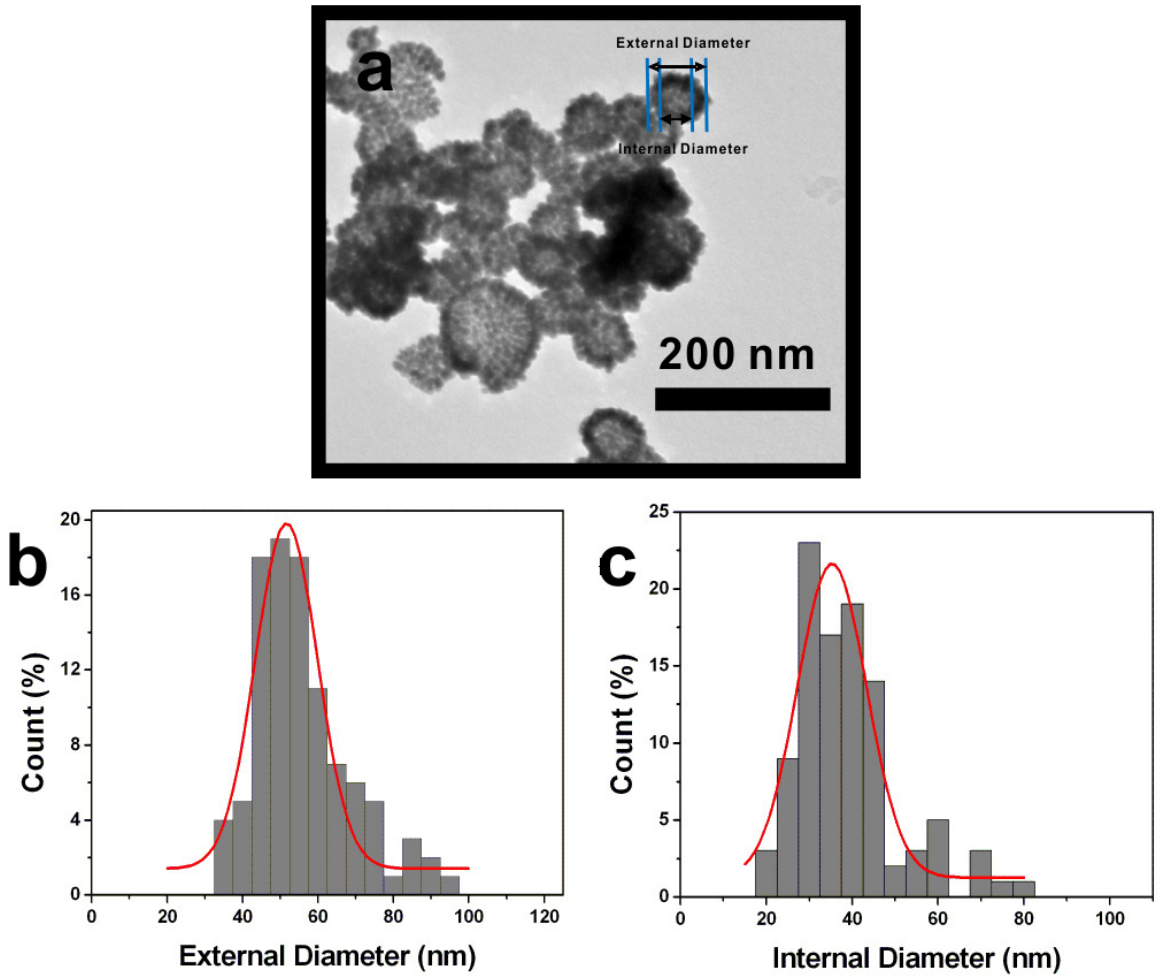


**Figure 4.9.** (a) TEM image indicating the inner and outer diameters of the spherical gold nanoparticle superstructures. (b) Distribution of external diameters of the spherical gold nanoparticle superstructures (based on 100 counts; 51.6 ± 0.8 nm). (c) Distribution of internal diameters of the spherical gold nanoparticle superstructures (based on 100 counts; 35.3 ± 1.0nm).

To further study and gain 3-D information of the spherical structures, electron tomography was used to probe the three-dimensional structure of the nanoparticle assemblies. Tilted images (**Figure 4.10c**) collected at 1° tilt intervals from -70° to 70° were combined computationally to generate a three-dimensional electron density map (tomogram) (**Figure 4.10d**). Sample tomographic slices and the 3-D tomogram definitively reveal that the structures are spherical capsules comprising a single layer of gold nanoparticles.

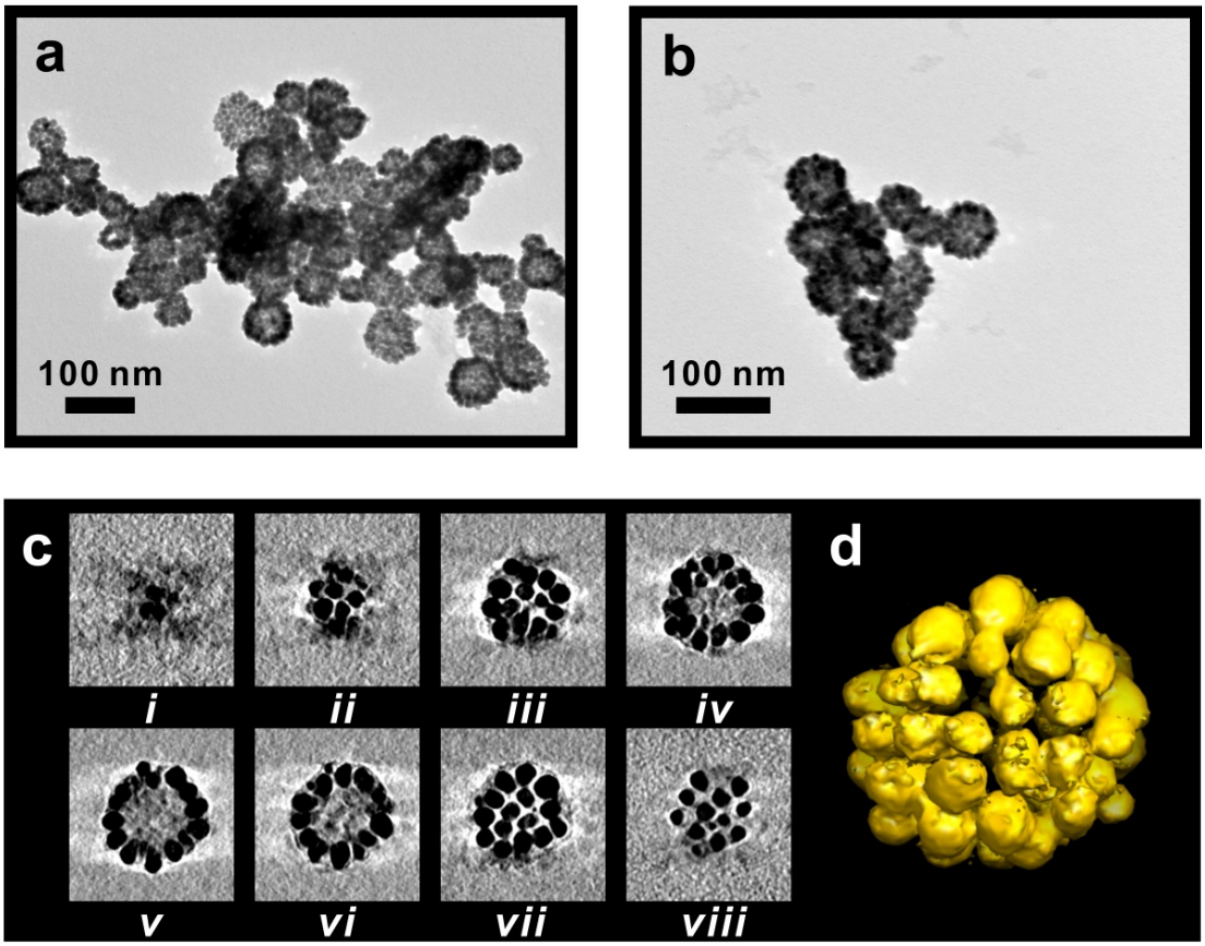


**Figure 4.10**. (a,b) TEM images of spherical gold nanoparticle superstructures. (c) X-Y computational slices (i-viii) of the 3-D tomographic volume containing the nanoparticle assembly (scale bar = 20 nm). (d) 3-D surface rendering of the tomographic volume.

At this stage of our investigation, it was clear that $C_6$-AA-$PEP_{Au}$ directs the assembly of gold nanoparticles into spherical superstructures and that a hollow self-assembled $C_6$-AA-$PEP_{Au}$ structure serves as the underlying structure-directing entity. In fact, when I performed the same reaction but used AA-$PEP_{Au}$ instead of $C_6$-AA-$PEP_{Au}$, random gold nanoparticle aggregates were observed as product (**Figure 4.11**).

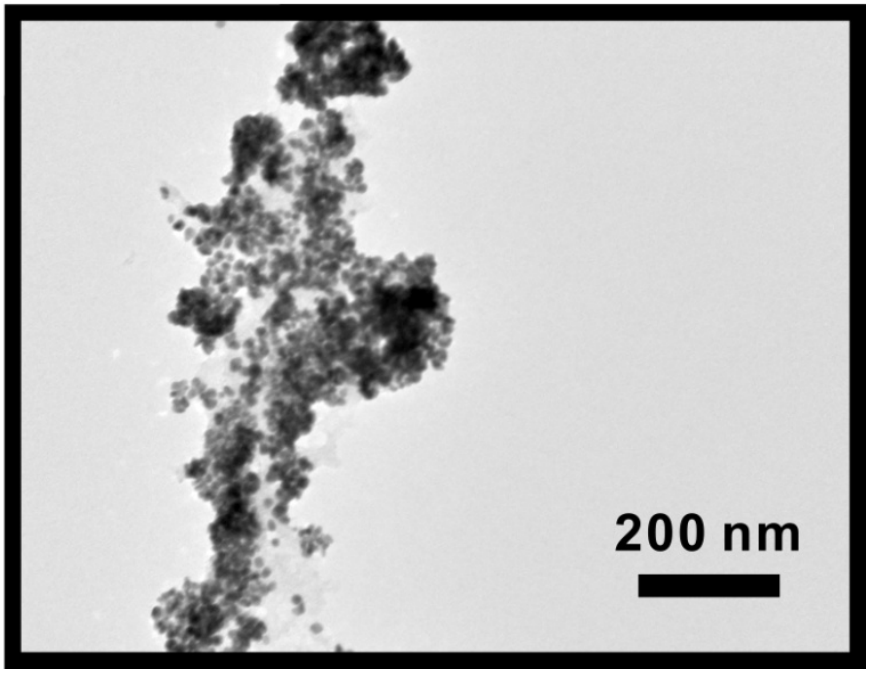


**Figure 4.11.** TEM image of random gold nanoparticle aggregates formed using AA-$PEP_{Au}$ instead of $C_6$-AA-$PEP_{Au}$.

We note that the average diameter of the nanoparticle superstructures is smaller than what one might expect based on the average diameter of the $C_6$-AA-$PEP_{Au}$ nanospheres which self-assemble in water. This suggests that the assembly of $C_6$-AA-$PEP_{Au}$ and the gold nanoparticles may in fact be coupled and that both components could influence the size and shape of the resulting superstructure.

To more completely understand the mechanism of superstructure formation, we studied samples of the reaction mixture at various time points using both TEM and AFM. After ~20 min, we observed islands of nanoparticles containing nanoparticles of uniform diameter (4.7 ± 0.1 nm) (**Figure 4.12a, Figure 4.13**). Over the course of several hours, the nanoparticles within the islands continue to grow (5.4 ± 0.2 nm at 2.5 h, Figure 12b ; 6.2 ± 0.1 nm at 4.5 h **Figure 4.12c**). We hypothesize that as small nanoparticles form in solution, they provide a surface onto which $C_6$-AA-$PEP_{Au}$ can attach and aggregate. Aggregates of $C_6$-AA-$PEP_{Au}$ then attract more nanoparticles, leading to the formation of island structures. At a certain critical point, the island structures accumulate and concentrate enough $C_6$-AA-$PEP_{Au}$ in one area that it becomes favorable for the $C_6$-AA-$PEP_{Au}$ to self-assemble into a spherical structure, thus driving the spherical assembly of the gold nanoparticles (**Figure 4.12d**). We note that this assembly process also results in a small number of incomplete structures (**Figure 4.12d**) which need more nanoparticles to complete their spherical nanoparticle monolayer shell. Detailed studies of the mechanistic aspects of superstructure formation will be addressed in the future.

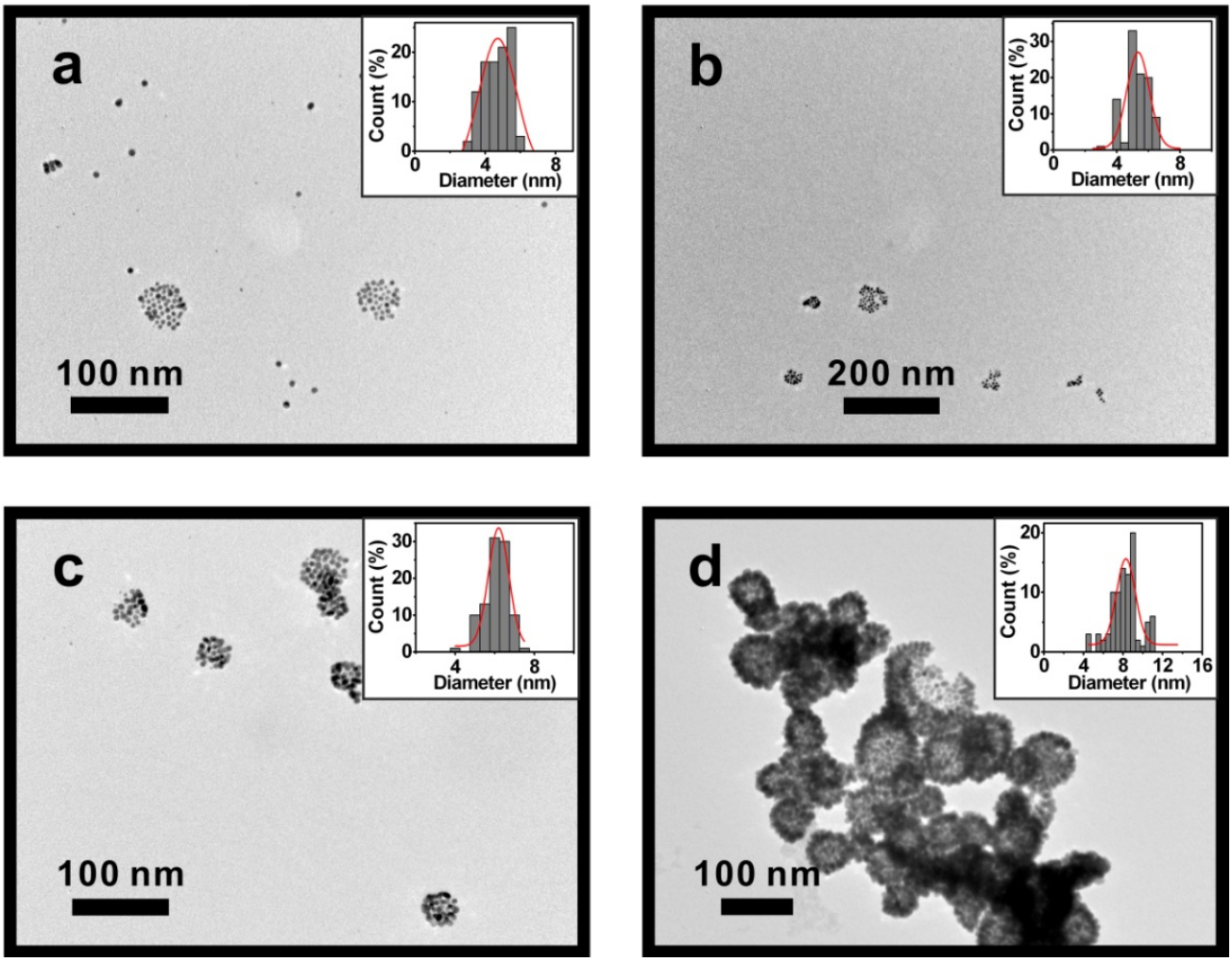


**Figure 4.12**. Progress of superstructure formation. TEM images and particle size distributions after (a) 20 min. of reaction, (b) 2.5 h of reaction, (c) 4.5 h of reaction, and (d) 38 h of reaction. (arrow indicates incomplete nanoparticle superstructures).

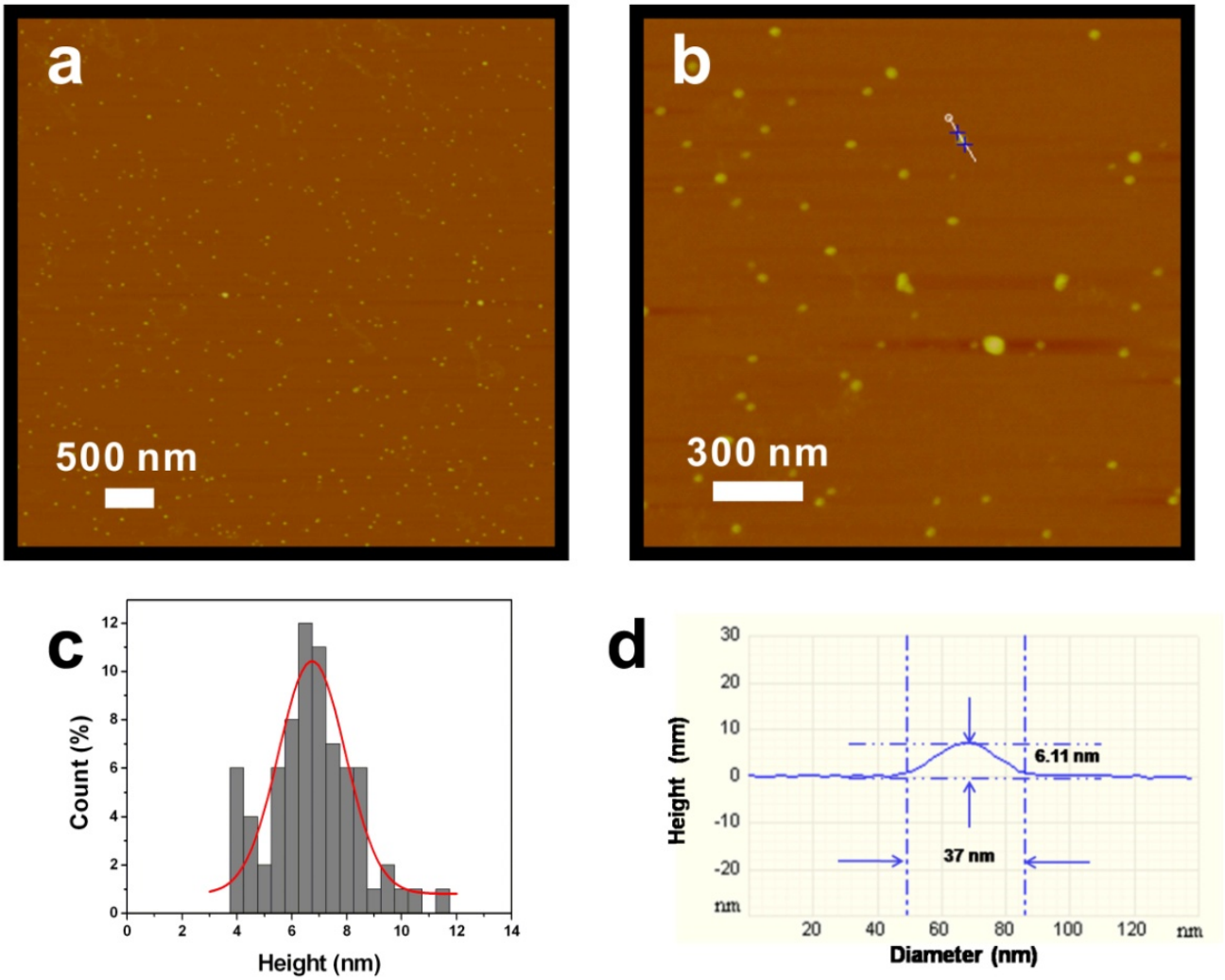


**Figure 4.13.** (a) and (b)AFM height images of samples taken from the reaction mixture used to prepare the spherical gold nanoparticle superstructures. These samples were taken 20 min. after the addition of $HAuCl_4$/TEAA to the $C_6$-AA-$PEP_{Au}$/HEPES solution. (c) Height distribution of structures from (a,b) (based on 75 counts; height = 6.7 ± 0.1 nm). (d) cross-sectional analysis of AFM image (b).

## 4.3 CONCLUSION

We have discovered that $C_6$-AA-$PEP_{Au}$ conjugates direct the formation of well-defined hollow spherical nanoparticle superstructures. Remarkably, $C_6$-AA-$PEP_{Au}$ and $C_{12}$-$PEP_{Au}$,[2a] which have slightly different compositions, direct the formation of dramatically different nanoparticle superstructures (hollow spheres vs. double helices[2a]). This result points toward the versatility of this methodology and the ability to program the shape of the ultimate nanoparticle superstructure simply by programming specific information into the composition of the peptide conjugate.

## 4.4 EXPERIMENTAL SECTION

### 4.4.1 Materials and general methods

All solvents and chemicals were obtained from commercial sources and used without further purification. 0.1M HEPES Buffer (HEPES = 4-(2-hydroxyethyl)-1-piperazineethanesulfonic acid) was made by directly diluting 1.0M HEPES buffer (pH = 7.3 ± 0.1; Fisher Scientific) with water (NANOpure, Barnstead DiamondTM System.; 18.2 MΩ). Peptides with sequences of AYSSGAPPMPPF ($PEP_{Au}$), AAYSSGAPPMPPF (A-$PEP_{Au}$), AAAYSSGAPPMPPF (AA-$PEP_{Au}$) and AAAAYSSGAPPMPPF (AAA-$PEP_{Au}$) were synthesized and purified by New England Peptide with final purity of 99%. Reverse-phase high-pressure liquid chromatography (HPLC) was performed at ambient temperature with an Agilent 1200 liquid chromatographic system equipped with diode array and multiple wavelength detectors using a Grace Vydac protein C4 column (214TP1010, 1.0 cm × 25 cm). Matrix-assisted laser desorption ionization time-of-flight (MALDI-TOF) mass spectra were obtained on an Applied Biosystem Voyager System 6174 MALDI-TOF mass spectrometer using α-cyano-4-hydroxy cinnamic acid (CHCA) as the matrix. Transmission electron microscopy (TEM) samples were prepared by pipetting one drop of solution onto a 3-mm-diameter copper grid coated with carbon film; 2% aqueous phosphotungstic acid was used for negative staining. TEM was conducted on a JEOL 200CX instrument operated at 200 kV and images were collected using a Gatan CCD image system. Samples for atomic force microscopy (AFM) were prepared on freshly peeled MICA substrates. Tapping-mode AFM was performed on a Veeco Dimension V SPM. The projection images from electron tomography studies were recorded with a Gatan 4K × 4K charge-coupled device (CCD) camera mounted on a Tecnai F20 electron microscope (FEI Corporation, Hillsboro, Oreg.)

equipped with a field emission gun (FEG) operating at 200 kV. For electron tomography, a series of images were recorded at room temperature with the Gatan 4K × 4K CCD camera at a nominal magnification of 50,000 by tilting the specimen from −70° to 70° in increments of 1°. Images were recorded at an underfocus value around 2μm along the tilt axis. A back-projection algorithm, as implemented in the IMOD reconstruction package,[1] was used to convert the information present in the series of tilted projection images into three-dimensional density maps. The surface rendering was generated using the Chimera software.

### 4.4.2 Preparation of N-hydroxyl-succinimide ester and peptide conjugate

**N-hydroxyl-succinimide esters.** Caproic acid (696 mg, 6 mmol) and N-hydroxysuccinimide (725 mg, 6.3 mmol) were dissolved in 30 mL dry $CH_3COOC_2H_5$ under an argon atmosphere. After addition of dicyclohexyl carbodiimide (DCC) (1341 mg, 6.5 mmol) at 0ºC, the solution was stirred overnight at room temperature. The reaction mixture was processed by removing the precipitate via filtration. The solvent was removed under reduced pressure and the crystalline residue recrystallized from isopropanol (iPrOH) to yield the N-hydroxyl-succinimide ester (211 mg, 1 mmol, 17%).

**NOTE**: $C_8$ esters syntheses were were prepared, purified, and characterized in a similar fashion.

**Peptide conjugates.** AAAYSSGAPPMPPF (1.20 mg, $8.80 \times 10^{-7}$ mol) was dissolved in 60 μL DMF. After addition of caproic N-hydroxyl-succinimide ester (0.6 mg, $2.81 \times 10^{-6}$ mol) in 60μL DMF and 1 μL $Et_3N$ under stirring, the solution was stirred at room temperature for 12 hours. Pure $C_6$-AA-$PEP_{Au}$ was obtained by conducting reversed-phase HPLC eluting with a linear gradient of 0.05% formic acid in $CH_3CN$ and 0.1% formic acid in water (5/95 to 95/5 over 30

min). The molecular weight for $C_6$-AA-$PEP_{Au}$ was confirmed by MALDI-TOF mass spectrometry. Concentration of the peptide was determined spectrophotometrically in water/acetonitrile (1:1) using the molar extinction coefficient of tyrosine (1280 $M^{-1}cm^{-1}$) at 280 nm.

**NOTE**: $C_6$-$PEP_{Au}$, $C_8$-$PEP_{Au}$, $C_6$-A-$PEP_{Au}$ and $C_6$-AAA-$PEP_{Au}$ were prepared, purified, and characterized in a similar fashion.

### 4.4.3 Preparation of gold nanospherical superstructures

Lyophilized $C_6$-AA-$PEP_{Au}$ (~ $1.87 \times 10^{-8}$ mol) was completely dissolved in 125 µL 0.1 M HEPES buffer in a plastic vial. After 30 mins, 0.5 µL of freshly prepared 0.1M chloroauric acid ($HAuCl_4$) in 1.0 M triethylammonium acetate (TEAA, pH = 7.0) buffer solution was added to the above clear peptide-HEPES solution. The above mixture was vortexed for a few seconds and then left undisturbed at room temperature. Spherical nanoparticle superstructures were observed as product after ~24 h.

**NOTE**: When $C_6$-$PEP_{Au}$ and $C_8$-$PEP_{Au}$, $C_6$-A-$PEP_{Au}$ and $C_6$-AAA-$PEP_{Au}$ were used in attempts to prepare nanoparticle superstructures, similar reaction conditions were employed.

# 5.0 PEPTIDE-DIRECTED SYNTHESIS AND ASSEMBLY OF HOLLOW SPHERICAL COPT NANOPARTICLE SUPERSTRUCTURES

This work, written in collaboration with Yang Wang and Nathaniel L. Rosi*, was published in *Angew. Chem. Int. Ed*. **2013**, 52(14), 3993. 

Yang Wang, working under the direction of Prof. David Waldeck, performed the electrocatalysis experiments.

## 5.1 INTRODUCTION

Controlling the directed assembly of nanoparticles into well-defined nanoparticle superstructures is a significant challenge,[85,168,184-186] and we are working to develop a general methodology to address this challenge. The success and broad applicability of a particular nanoparticle assembly methodology should be assessed according to the following important criteria: i) diverse structural scope; ii) ability to tune and tailor superstructure metrics (e.g. nanoparticle size, nanoparticle shape, interparticle distances, and superstructure diameter); and iii) diverse compositional scope.

In our group's previous work, we developed 1-D and 3-D gold nanoparticle superstructures using our peptide-based methodology.[66] We successfully demonstrated that this methodology

addresses criteria i) and ii) listed above. Specifically, we used this methodology to prepare a diverse set of complex gold nanoparticle superstructures, including double helices,[66] linear belts,[140] and hollow spherical structures,[141] and to tune the metrics of the superstructures.[139] In this contribution, we begin to address criterion iii) above.

Peptide conjugates are the centerpiece molecules in this methodology. They consist of two components: an inorganic-binding peptide and an organic moiety tethered to the peptide terminus. The peptide portion binds to the nanoparticle surface while the organic moiety influences the assembly of the peptide, and therefore the assembly of the nanoparticles.

Numerous peptides exist which have been evolved and selected, naturally or unnaturally, to selectively adhere to specific inorganic surfaces.[62,64] Thus far, we have only utilized a gold-binding peptide in this methodology.[65] In principle, however, we could choose any inorganic-binding peptide, and this would allow us to target and prepare nanoparticle superstructures of variable composition.

In recent years, considerable work has been directed at constructing Co/Pt bimetallic superstructures [89,187,188]. Vasquez et al. prepared hollow spherical CoPt structures using a galvanic replacement method. Chen et al. prepared CoPt hollow spheres by thermolyticly reducing platinum acetylactonate and cobalt (II) acetate in refluxing ethylene glycol and anionic surfactant sodium dodecyl sulfate (SDS) was employed as the capping and structure-directing agent in the reacting mixtures [89].

Here, we introduce, describe, and demonstrate how our peptide-based methodology can be adapted to target and prepare CoPt nanoparticle superstructures. It is established that CoPt nanoparticles are potentially useful in nanomedicine as magnetic resonance imaging (MRI) contrast agents[189] and as electrocatalysts.[190,191] For these applications, individual CoPt

nanoparticles are typically employed. We sought to assemble CoPt nanoparticles into hollow spherical sub-100 nm superstructures, reasoning that they may ultimately be useful as multifunctional bionanomaterials capable of serving both as MRI imaging agents[189] and as cargo[192] (e.g. drug, biomolecule, labeling, etc.) agents or as high surface area electrocatalysts.[190,191]

## 5.2 RESULTS AND DISCUSSION

To prepare hollow spherical CoPt nanoparticle superstructures, we first selected from the literature the Co-binding peptide HYPTLPLGSSTY (Co1-P10), isolated by Naik et al.[193] and hereafter referred to as $PEP_{Co}$. $PEP_{Co}$ was used previously by Naik et al. to prepare both Co nanoparticles and CoPt alloy nanoparticles. The reported syntheses are straightforward and are performed in aqueous media at neutral pH. In order to prepare hollow spherical superstructures, we elected to utilize the conjugate BP-$PEP_{Co}$ ($C_{12}H_9CO$−HYPTLPLGSSTY; BP = biphenyl) (see Supporting Information for synthetic details), because our previous results with biphenyl-based $PEP_{Au}$ conjugates yielded hollow spherical gold nanoparticle superstructures.[142] BP-$PEP_{Co}$, upon dissolution and subsequent incubation in 0.1 M HEPES buffer (HEPES = 4-(2-hydroxyethyl)-piperazineethanesulfonic acid), assembles into well-defined spherical structures (30.9 ± 4.5 nm), as evidenced by transmission electron microscopy (TEM) studies (**Figure 5.1**).

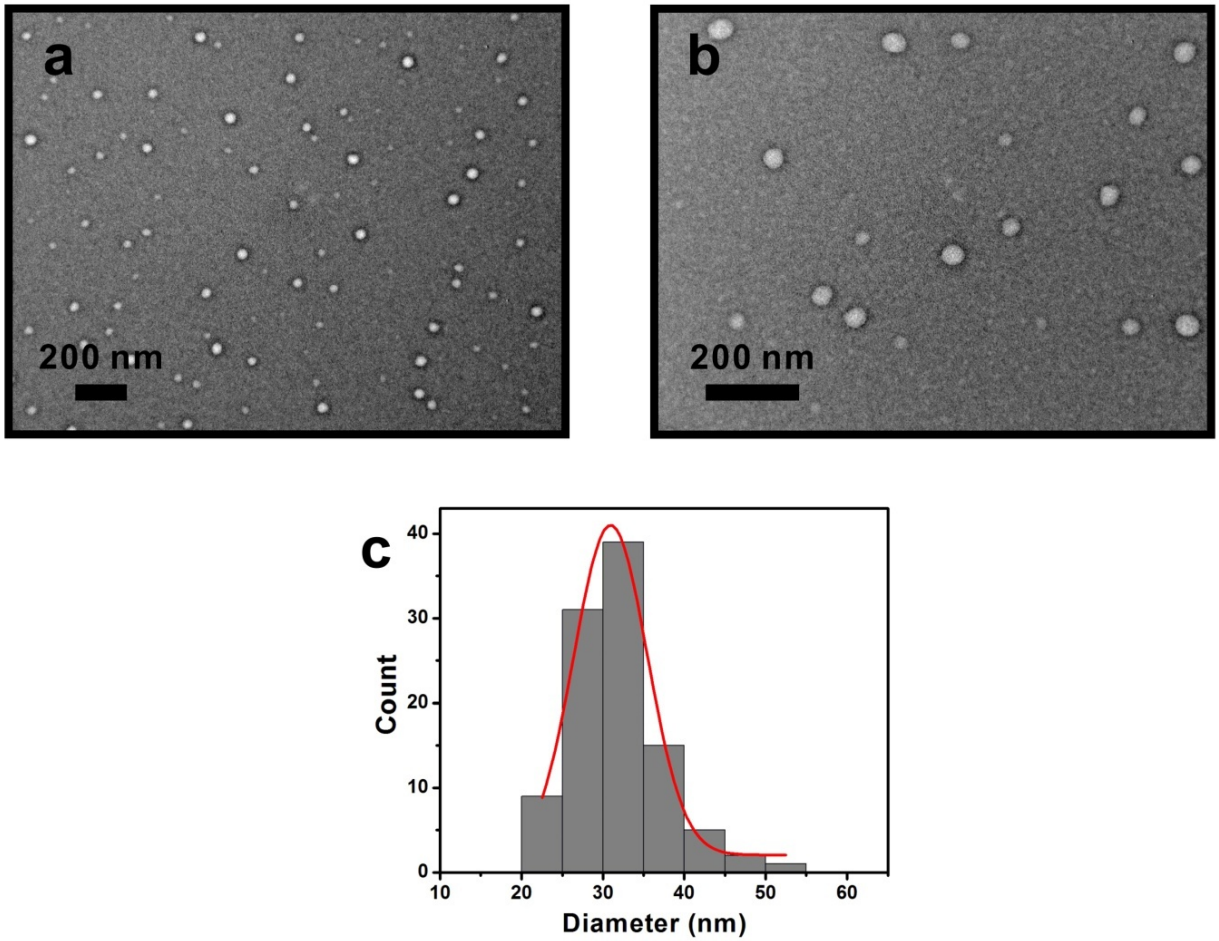


**Figure 5.1**. (a),(b) TEM images of BP-$PEP_{Co}$ nanospherical structures obtained from dissolving BP-$PEP_{Co}$ in HEPES buffer and incubating for one day at room temperature. (c) Diameter distribution of the BP-$PEP_{Co}$ self-assembled spherical structures (based on 102 counts; diameter = 30.9 ± 4.5 nm).

Encouraged by these results, we next adapted the literature synthesis for CoPt nanoparticles by replacing $PEP_{Co}$ with BP-$PEP_{Co}$ to determine whether BP-$PEP_{Co}$ could serve the dual purpose of directing both the synthesis of CoPt nanoparticles and their assembly into spherical superstructures (**Scheme 5.1**). Specifically, a 6.5:1 ratio of cobalt acetate to BP-$PEP_{Co}$ was incubated for four hours at room temperature in HEPES buffer to yield a colorless solution. Thereafter, aliquots of sodium borohydride ($NaBH_4$) and ammonium tetrachloroplatinate [$(NH_4)_2(PtCl_4)$] were added in sequence. Black precipitate appeared in the solution immediately after the addition of the $NaBH_4$, indicating the reduction of the cobalt and platinum ions. After reaction, a sample of the precipitate was collected and analyzed using transmission electron microscopy (TEM).

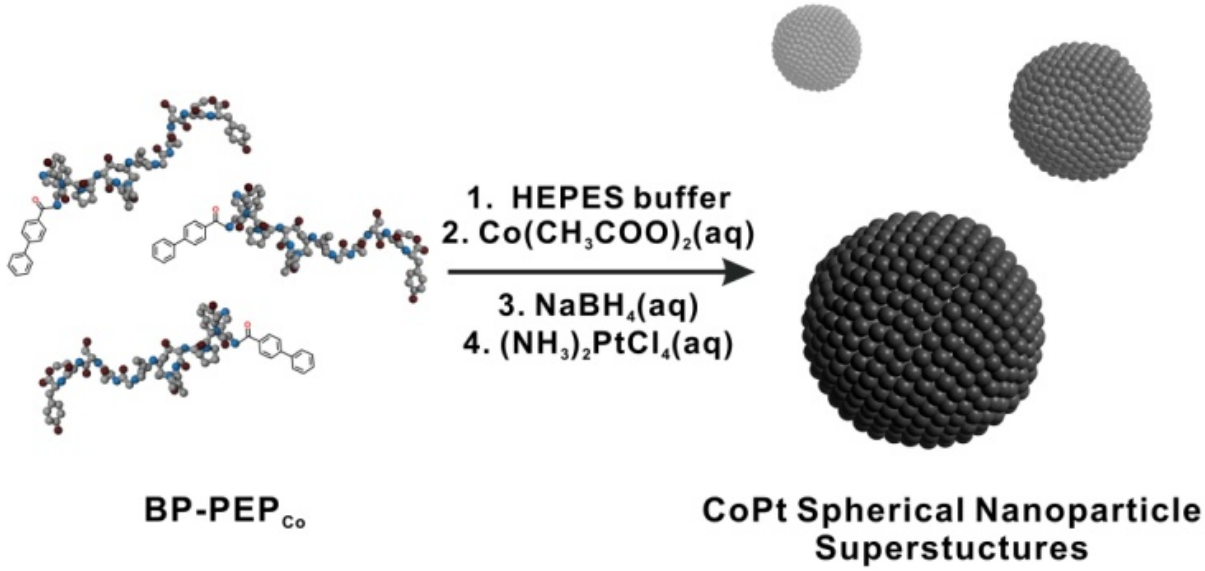


**Scheme 5.1.** Preparation of hollow spherical CoPt nanoparticle superstructures (Small gray spheres = CoPt nanoparticles)

Examination of the TEM images indicated the formation of spherical nanoparticle superstructures (53.9 ± 7.9 nm) (**Figure 5.2**) that consist of individual nanoparticles (3.3 ± 0.5 nm) (**Figure 5.3a**). These structures have dark edges and light cores, which suggests the formation of 'hollow' spherical nanoparticle assemblies. The average diameter of the lighter inner core was 29.5 ± 5.5 nm (**Figure 5.3b**), consistent with the size of the self-assembled peptide structures.

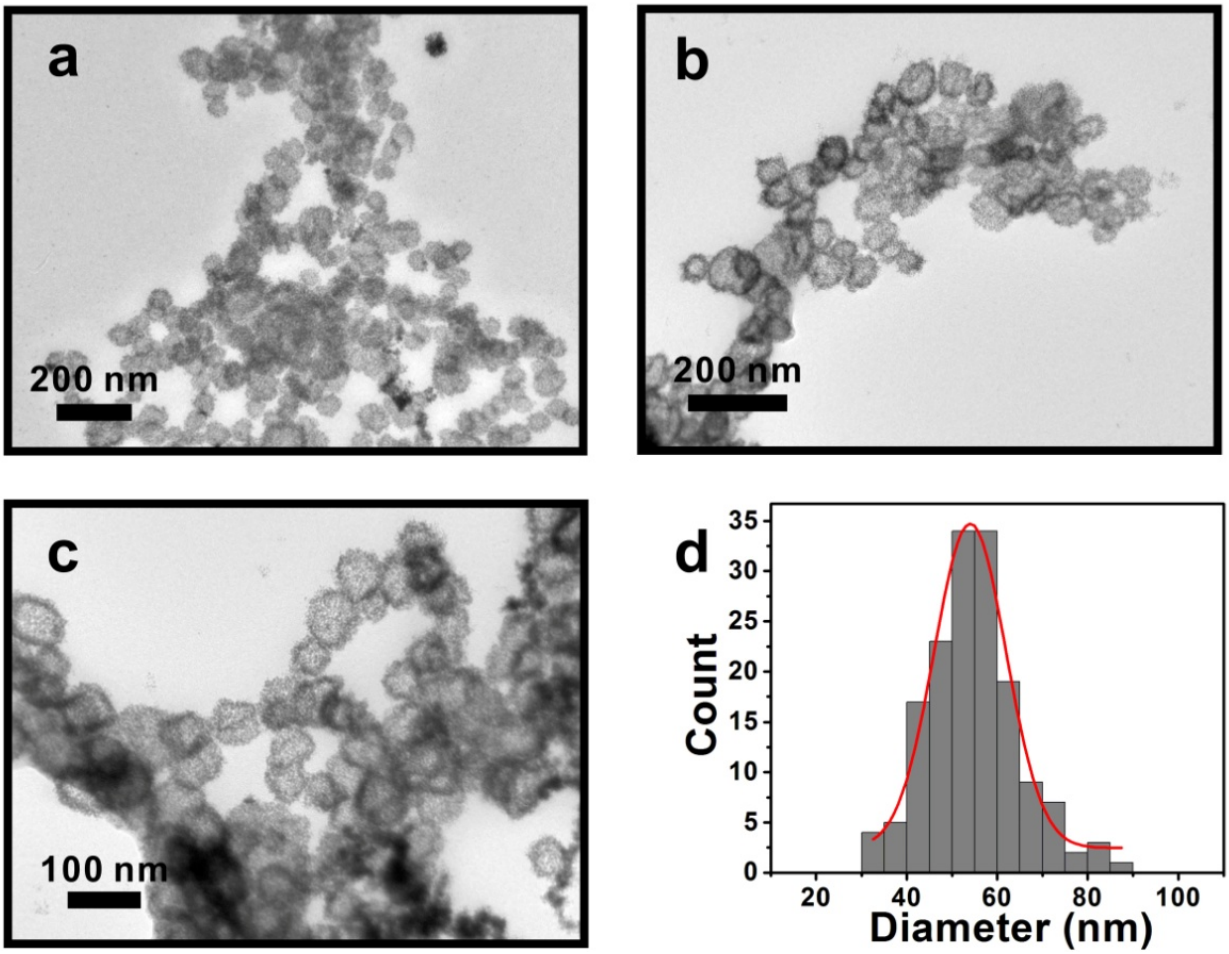


**Figure 5.2.** (a-c) TEM images of hollow spherical CoPt nanoparticle superstructures. (d) The diameter distribution of CoPt nanoparticle superstructures (53.9 ± 7.9 nm; based on 158 counts).

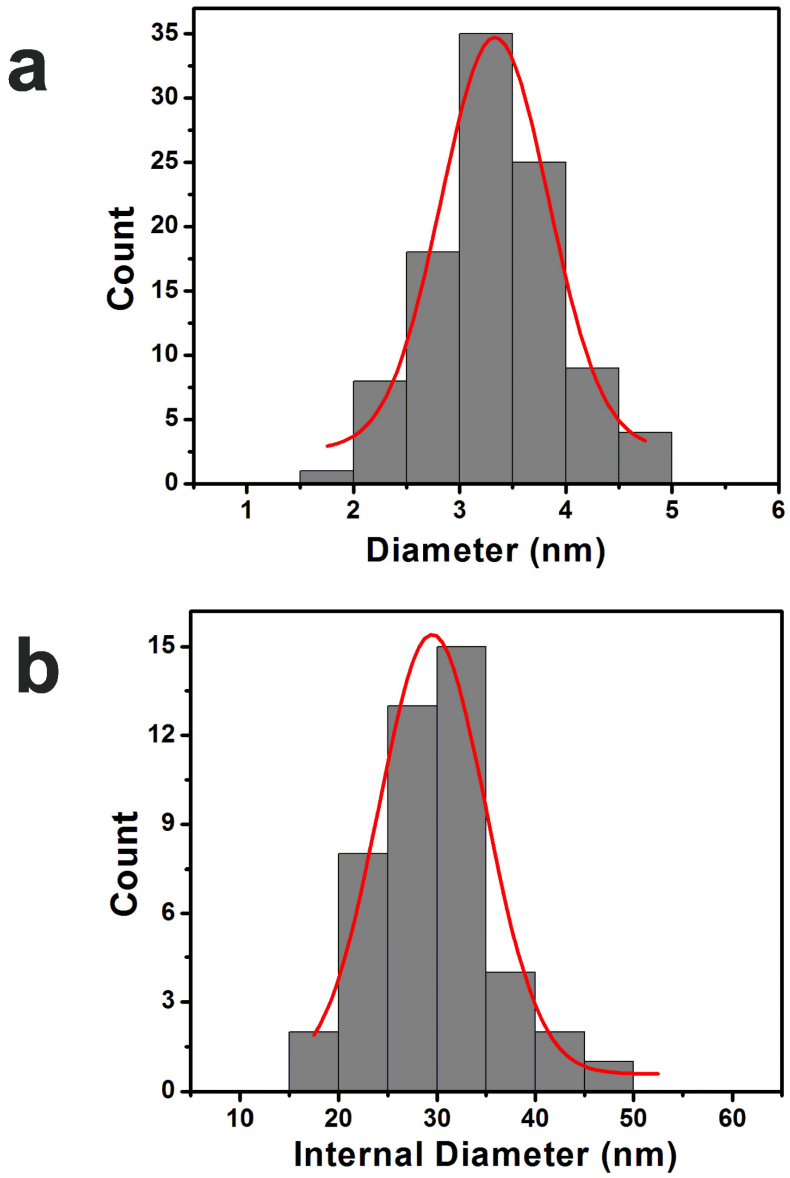


**Figure 5.3.** (a) Distribution of size of individual nanoparticles in the nanoparticle superstructures (based on 100 counts from TEM images; diameter = 3.3 ± 0.5 nm). (b) Distribution of the internal diameter of the hollow nanoparticle superstructures (based on 45 counts from TEM images; internal diameter = 29.5 ± 5.5 nm).

Larger hollow spheres were constructed by halving the concentration of BP-$PEP_{Co}$ in the synthesis (**Figure 5.4**), indicating that one can possibly tune the dimension of the CoPt nanoparticle superstructures using this methodology.

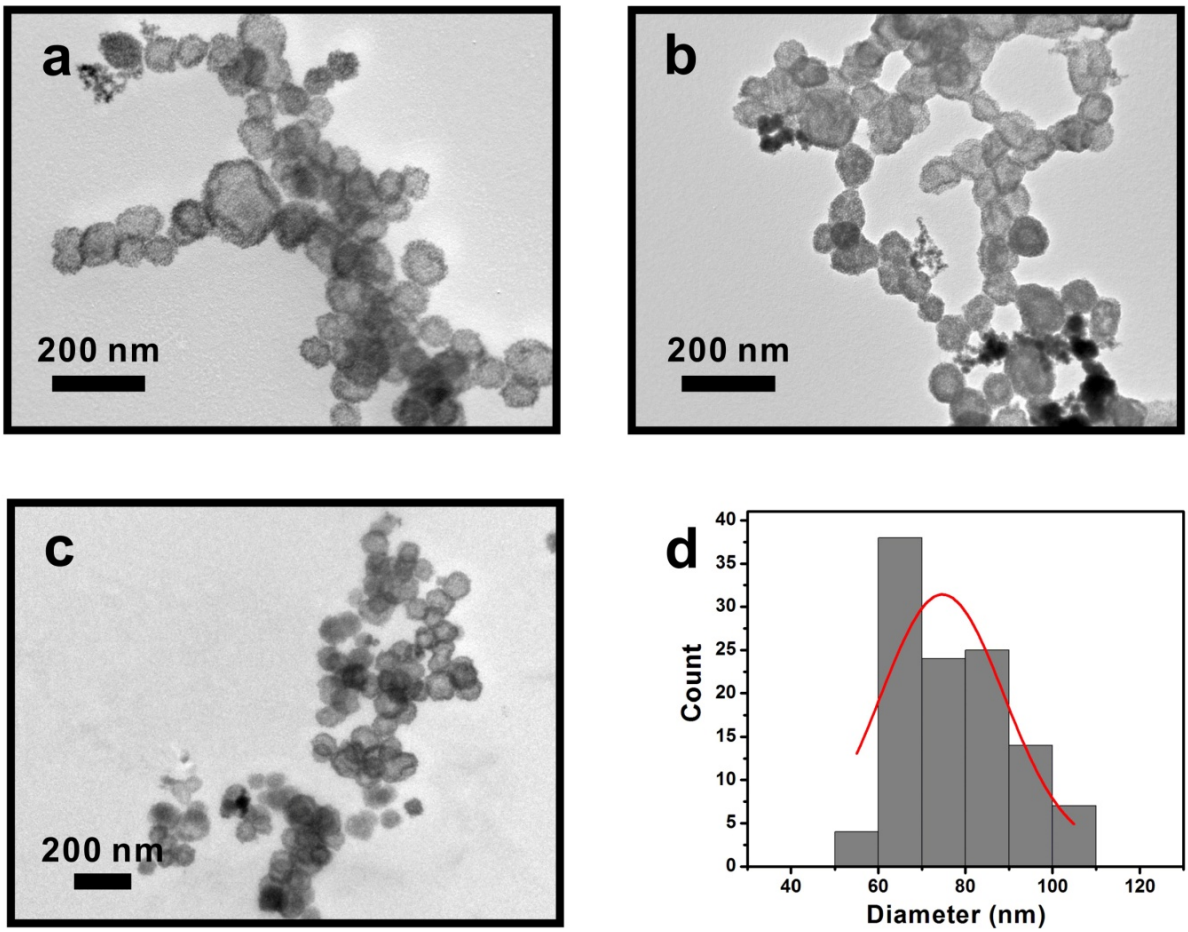


**Figure 5.4.** (a-c) TEM images of large CoPt nanoparticle superstructures synthesized by lowering the concentration of peptide conjugates. (d) Distribution of diameter of large hollow spherical CoPt nanoparticle superstructures (based on 112 counts; 74.7 ±14.1 nm).

Energy dispersive X-ray spectroscopy (EDS) revealed a 45:55 Co:Pt ratio for the assembled superstructures (**Figure 5.5a**). To further confirm the composition of the individual nanoparticles, we used high-resolution TEM to measure their atomic lattice spacing. The measured distance, 0.218 nm (**Figure 5.5b**), is consistent with reported results[193,194] as well as X-ray diffraction data[89] (**Figure 5.6**) collected for the assembled superstructures. When we performed the same reaction using $PEP_{Co}$ instead of BP-$PEP_{Co}$, random aggregates composed of individual nanoparticles (2.61 ± 0.43 nm) were observed (**Figure 5.7**).

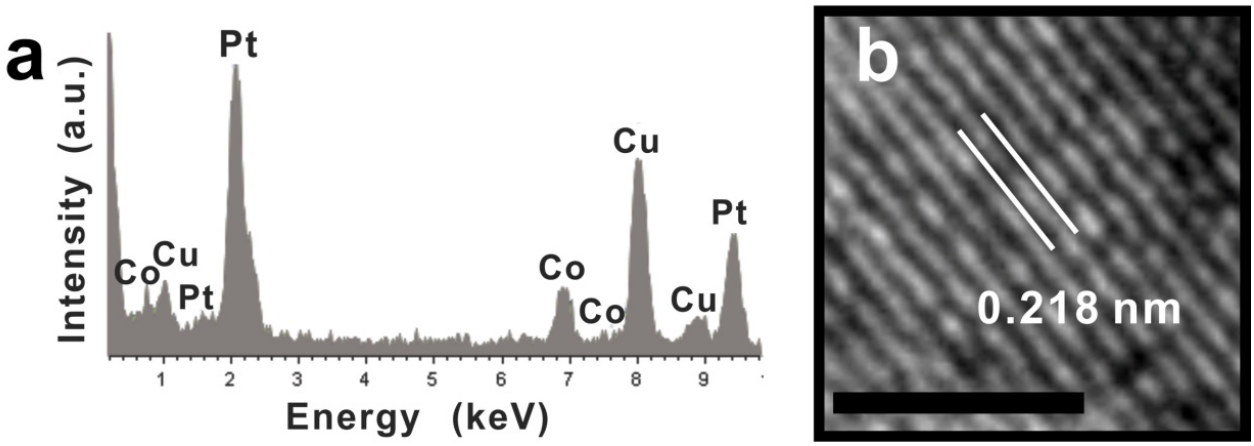


**Figure 5.5.** (a) EDS data for CoPt nanoparticle superstructures (Cu is from the TEM grid). (b) HRTEM of a single CoPt nanoparticle showing the lattice fringes (scale bar, 2 nm).

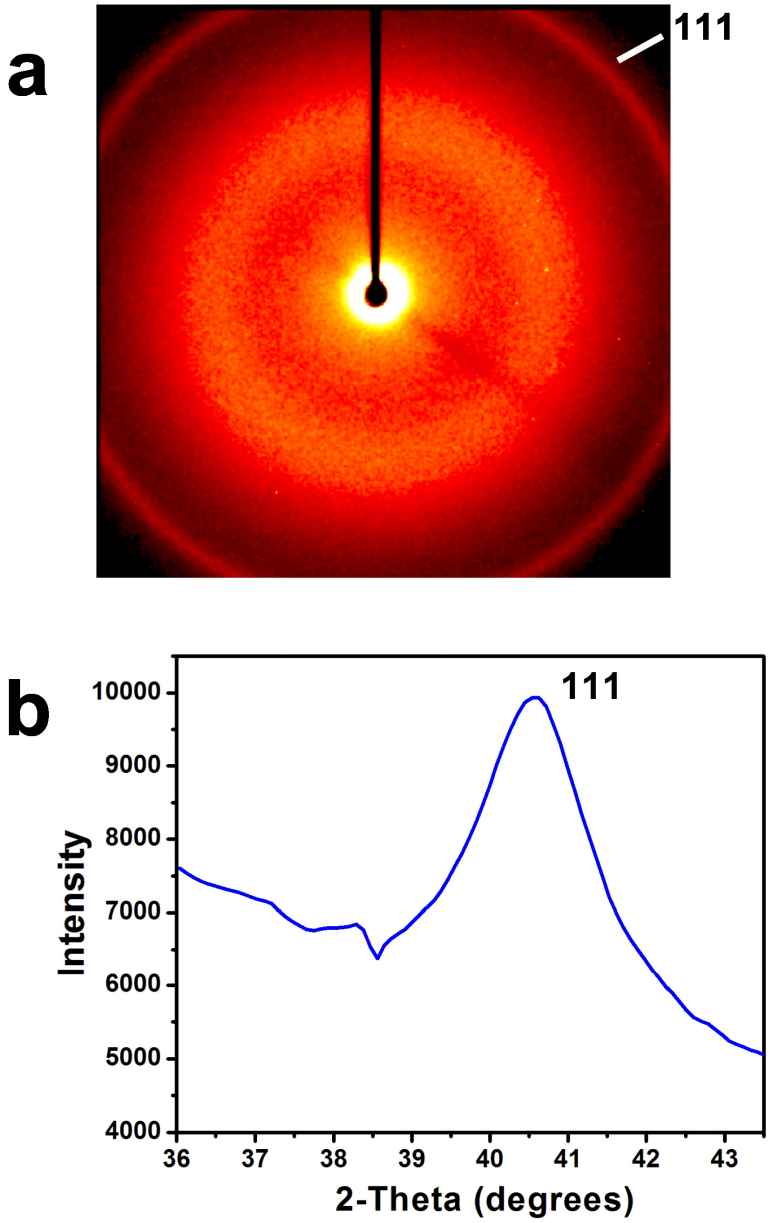


**Figure 5.6.** Powder X-ray diffraction (XRD) pattern (a) and data (b) for hollow CoPt nanospheres show the ring corresponding to diffraction from the [111] plane and the plane corresponds to the lattice fringe 0.22 nm, as calculated using Bragg's law.

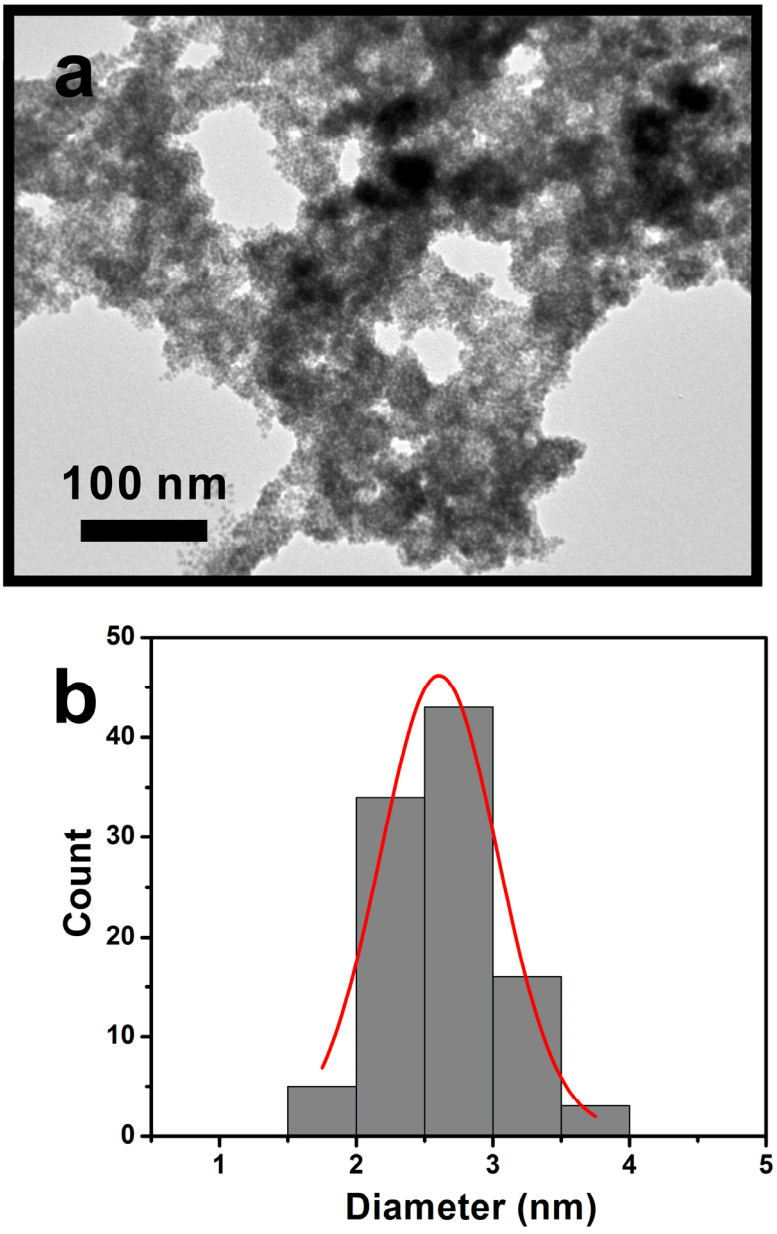


**Figure 5.7.** (a) TEM image of individual CoPt nanoparticles formed using the preparation methods described but replacing BP-PEP$_{Co}$ with PEP$_{Co}$. (b) Distribution of size of the above nanoparticles (based on 100 counts; 2.61 ± 0.43 nm).

Earlier workers reported the synthesis of continuous CoPt nanoshells via a galvanic displacement reaction of Co nanoparticles with platinum salts.[89,195] Our superstructures are distinguished from these reported materials, because they are composed of non-fused discrete nanoparticles. However, given their similarity to the reported nanoshells, we decided to confirm that our structures were indeed the product of a peptide-conjugate directed synthesis rather than a galvanic displacement reaction. Specifically, we performed our synthesis described above, but now in the absence of BP-$PEP_{Co}$. After the addition of $NaBH_4$, we observed, via TEM, the formation of large Co nanoparticles (99.5 ± 19.0 nm) (**Figure 5.8a-c**). The addition of $[(NH_4)_2(PtCl_4)]$ to the reaction solution resulted in the formation of large hollow structures consisting of a continuous shell (96.7 ± 7.4 nm) (**Figure 5.8d-f**), which were similar to those reported by Schaak et al.[89] These results are markedly different from what we observe for our synthesis. Based on these comparison studies, we conclude that our structures are formed via BP-$PEP_{Co}$-directed synthesis and assembly rather than galvanic displacement.

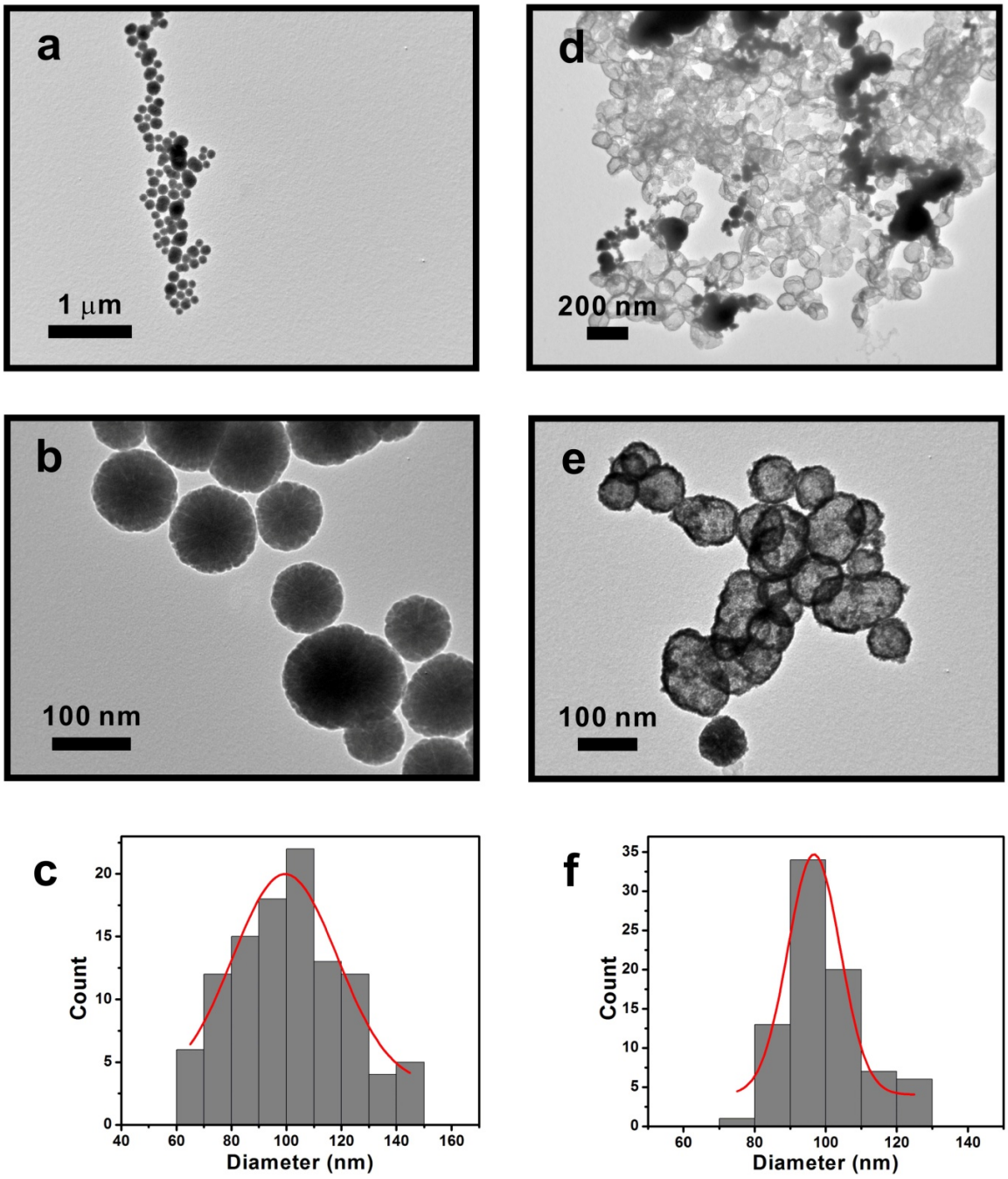


**Figure 5.8**. TEM images (a-b) of spherical Co nanoparticles synthesized in HEPES buffer in the absence of BP-$PEP_{Co}$ (c) Distribution of diameters of (a) spherical Co nanoparticles (based on 107 counts; 99.5 ± 19.0 nm). TEM images (d-e) of hollow nanospheres synthesized by adding an

aliquot of platinum salt to the above HEPES buffer containing solid Co nanoparticles (note: see experimental section for complete details). (f) Distribution of diameters of (d) hollow nanospheres (based on 81 counts; 96.7 ± 7.4 nm).

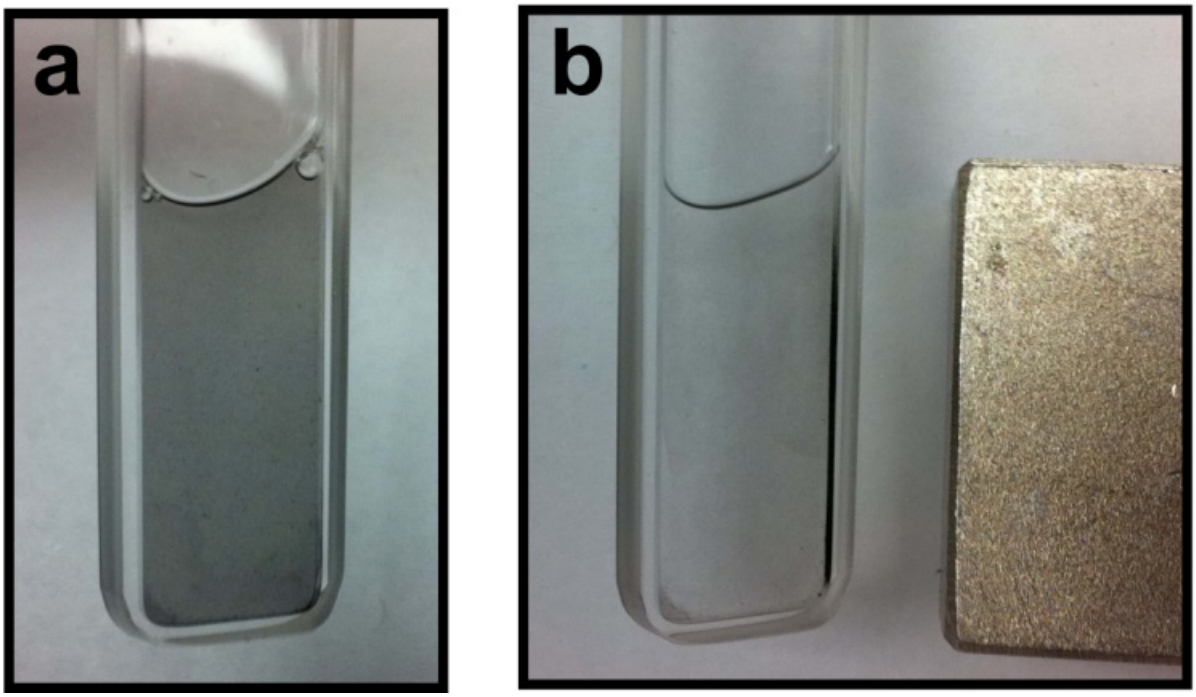


**Figure 5.9**. (a) CoPt nanoparticle superstructures were freshly prepared (see experimental section). (b) A magnet closed to the cuvette contains CoPt nanoparticle superstructures. Black precipitate was drawn to the wall of the cuvette. It indicates that the CoPt nanoparticle superstructures are magnetically-separable.

Peptide-capped Pd nanoparticles have been successfully utilized for catalysis.[87,196] We envision that the 'hollow' spherical CoPt nanoparticle superstructures reported herein could potentially be used as magnetically-separable heterogeneous catalytic reaction vessels.[190,195,197] As a first step in this direction, we have shown that the superstructures drawn to the wall of a reaction flask in the presence of a magnetic field (**Figure 5.9**).

We also examined their activity as methanol oxidation catalysts. Specifically, we monitored the oxidation of methanol in a cyclic voltammetry (CV) experiment. When the surface of a glassy carbon disk electrode was loaded with the hollow CoPt nanoparticle superstructures, significant anodic current (6.72 μA) was observed with an oxidation peak at 0.62 V (vs. Ag/AgCl), which is consistent with literature values for the oxidation of methanol.[31] In comparison, only weak anodic current (1.94 μA) was observed when the electrode was instead coated with an identical loading of CoPt nanoparticles (**Figure 5.10**). To confirm that the CoPt superstructures and CoPt nanoparticles remain intact in the $H_2SO_4$/MeOH solutions used for the electrocatalysis experiments, we soaked samples of the CoPt superstructures and CoPt nanoparticles in a $H_2SO_4$/MeOH solution and then examined the structures using TEM. We found that the superstructures remain intact and retain their spherical shape. The CoPt nanoparticles also remained intact. However, the Co:Pt ratio of the superstructures changes from 45:55 to 20:80 after soaking in the acidic methanol, as evidenced by EDS (**Figure 5.11**); clearly, Co leaches from the structures in the acidic environment. EDS revealed that the Co:Pt ratio of nanoparticles (22:78) is similar to that of superstructures after soaking in the acidic methanol (**Figure 5.12**). Our data suggest that CoPt nanoparticles assembled into hollow spherical superstructures exhibit greater electrocatalytic activity toward the oxidation of methanol compared to non-assembled CoPt nanoparticles. We preliminarily attribute this enhanced activity

to an increase in the exposed surface area of the CoPt particles that results from their assembly. Our current work is focused on examining this enhanced activity in more detail through both tuning and controlling the diameters of the assembled structures and by developing an understanding of the mechanism of the electrocatalytic activity.

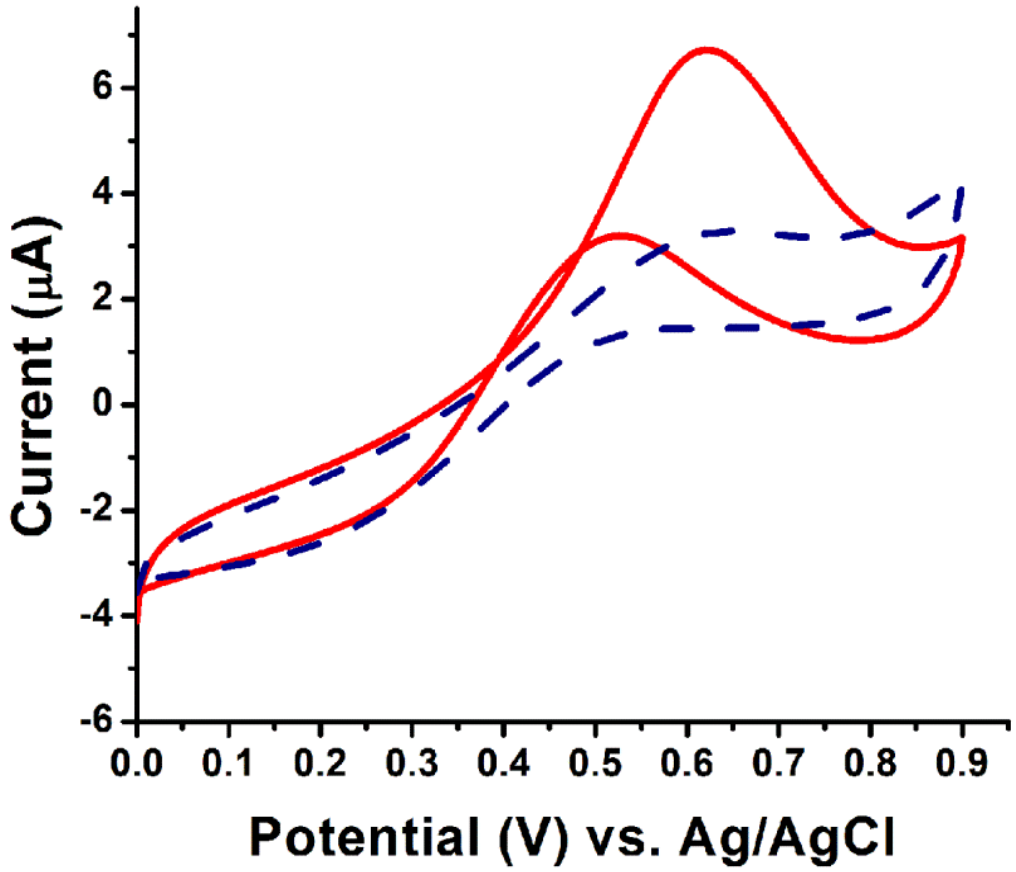


**Figure 5.10.** Cyclic voltammograms of hollow spherical CoPt nanoparticle superstructures (red) and CoPt nanoparticles (blue dash) in $H_2SO_4$ (0.5 M) containing methanol (0.6 M) (note: sweep rate = 0.05 $Vs^{-1}$; loading = ~7.5 μg).

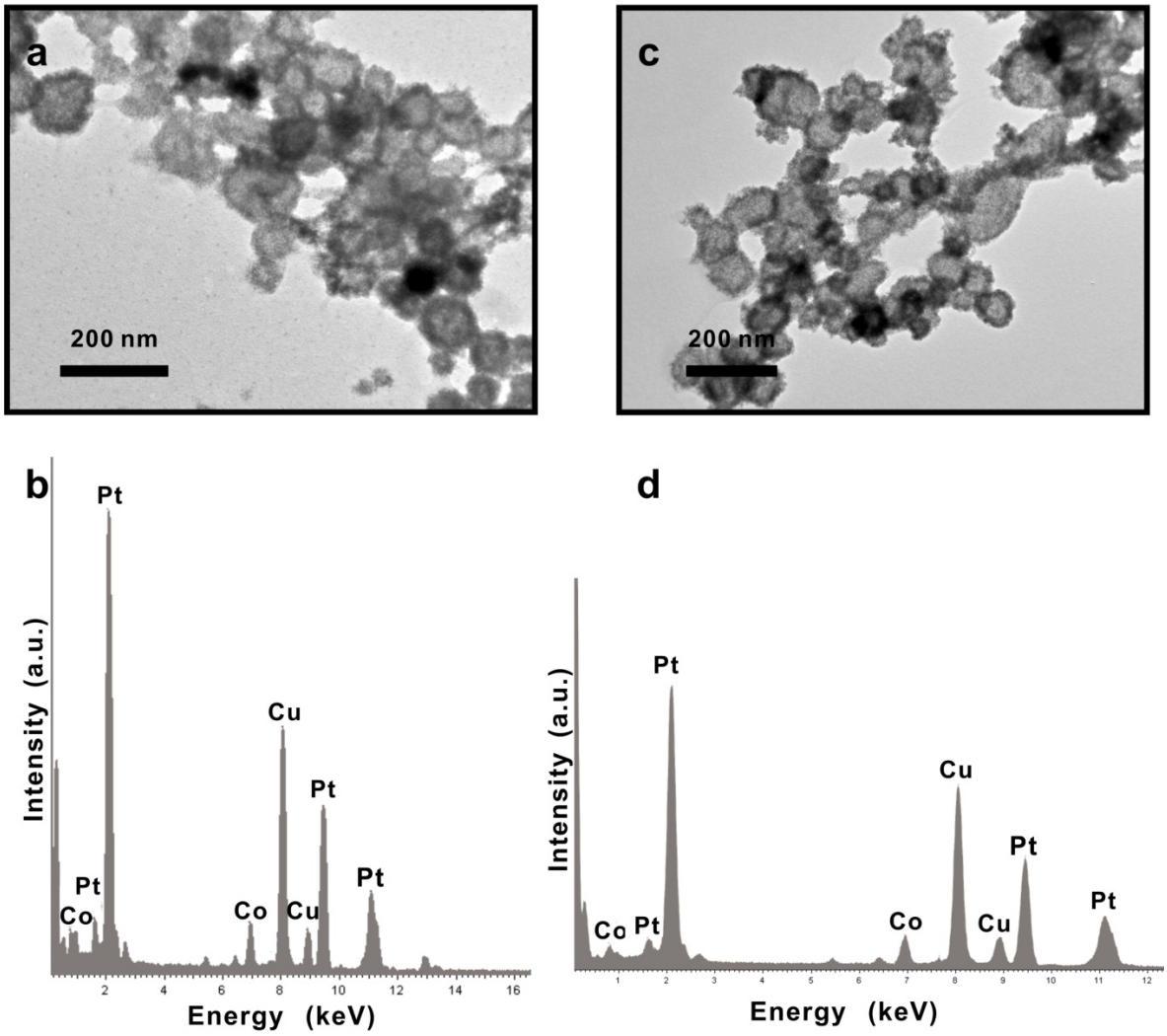


**Figure 5.11**. (a) As synthesized CoPt nanoparticle superstructures were incubated in 0.5 M $H_2SO_4$/0.6 M MeOH solution for 5 minutes. TEM images indicated that the nanoparticle superstructures remain assembled in the above solution. (b) EDS revealed that Co:Pt = 20:80 for the CoPt nanoparticle superstructures in (a). (c) The same nanoparticle superstructures were incubated in the same solution for 4 hours. TEM images revealed that the nanoparticle superstructures remain intact. (d) EDS revealed that Co:Pt = 17:83 for CoPt nanoparticle superstructures in (c).

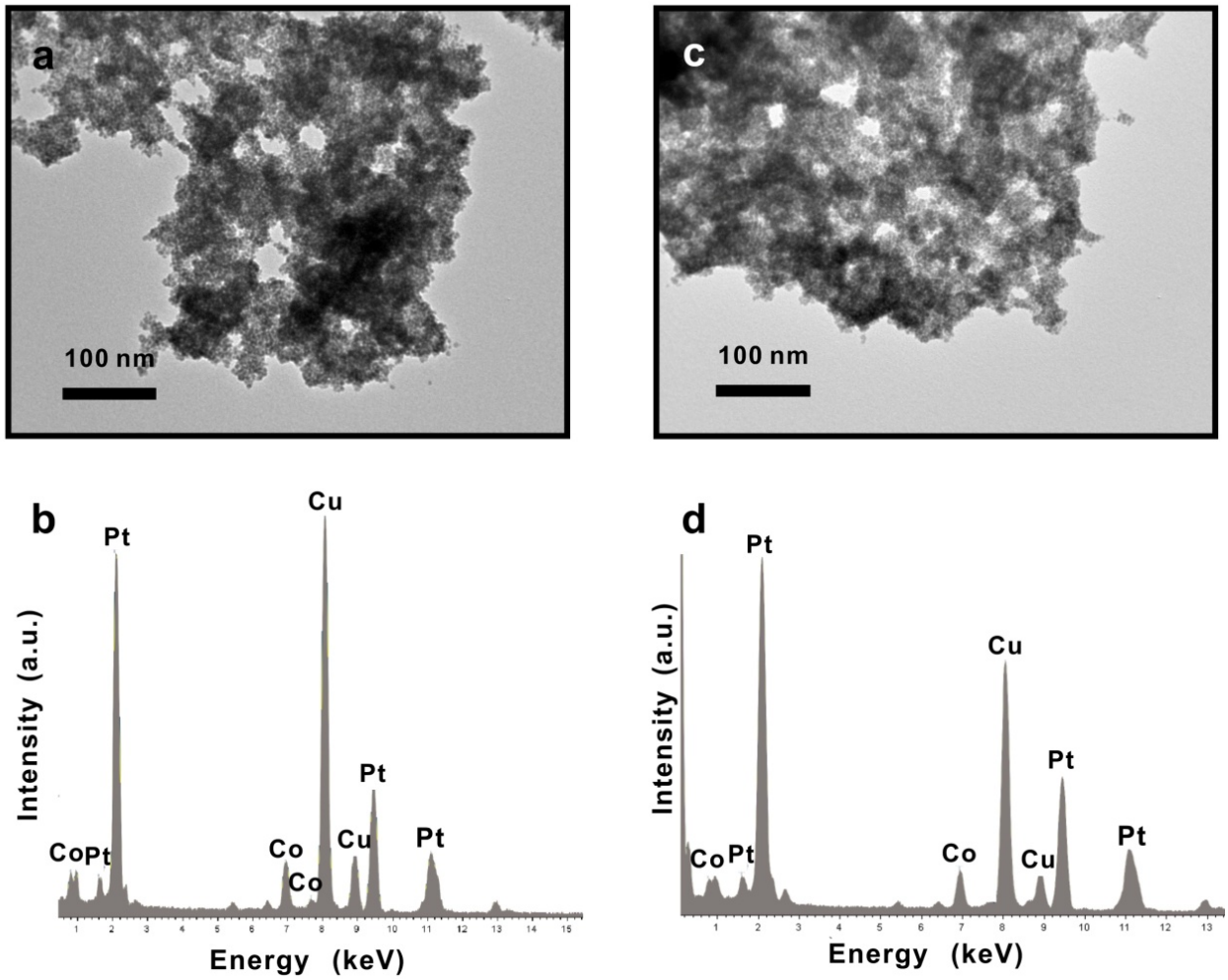


**Figure 5.12**. (a) As synthesized CoPt nanoparticles were incubated in 0.5 M $H_2SO_4$/0.6 M MeOH solution for 5 minutes. TEM images indicated that the individual nanoparticles aggragated in the above solution. (b) EDS revealed that Co:Pt = 22:78 for the CoPt nanoparticles in (a). (c) The same nanoparticles were incubated in the same solution for 12 hours. TEM images revealed that the nanoparticles remain stable. (d) EDS revealed that Co:Pt = 12:88 for CoPt nanoparticles in (c).

## 5.3 CONCLUSION

We have demonstrated that designed peptide conjugate molecules can be used to direct the synthesis and assembly of CoPt nanoparticles into spherical magnetic superstructures which can serve as catalysts for the oxidation of methanol. This work is important from a methodology standpoint because it demonstrates that one can target and prepare functional nanoparticle superstructures of arbitrary composition, provided that one identifies the proper peptide and designs the proper peptide conjugate.

## 5.4 EXPERIMENTAL SECTION

### 5.4.1 Materials and general methods

All solvents and chemicals were obtained from commercial sources and used without further purification. 0.1M HEPES Buffer (HEPES = 4-(2-hydroxyethyl)-1- piperazineethanesulfonic acid) was made by directly diluting 1.0M HEPES buffer (pH = 7.3 ± 0.1; Fisher Scientific) with water (NANOpure, Barnstead DiamondTM System.; 18.2 MΩ). HYPTLPLGSSTY ($PEP_{Co}$) was synthesized and purified by New England Peptide with final purity of 99%. Reverse-phase high-pressure liquid chromatography (HPLC) was performed at ambient temperature with an Agilent 1200 liquid chromatographic system equipped with diode array and multiple wavelength detectors using a Grace Vydac protein C4 column (214TP1010, 1.0 cm × 25 cm). Matrix-assisted laser desorption ionization time-of-flight (MALDI-TOF) mass spectra were obtained on an Applied Biosystem Voyager System 6174 MALDI-TOF mass spectrometer using α-cyano-4-hydroxy cinnamic acid (CHCA) as the matrix. Transmission electron microscopy (TEM) samples were prepared by pipetting one drop of solution onto a 3-mm-diameter copper grid coated with Formvar/Carbon film; 2% aqueous phosphotungstic acid was used for negative staining. TEM was conducted on a JEOL 200CX instrument operated at 200 kV and images were collected using a Gatan CCD image system. High resolution TEM was conducted on a JEM 2100F instrument at 200 kV and images were collected using a Gatan CCD image system.

### 5.4.2 Preparation of N-hydroxyl-succinimide ester and peptide conjugate

**N-hydroxyl-succinimide esters.** Briefly, 4-phenylbenzoic acid (1.0000 g, 5.04 mmol) and N-hydroxysuccinimide (0.5800 g, 5.04 mmol) were dissolved in 15 ml anhydrous

dimethylformamide (DMF) in an argon atmosphere. The solution was stirred for 5 min at room temperature and then cooled to 0ºC in an ice bath. After addition of dicyclohexyl carbodiimide (DCC) (1.1240 g, 5.44 mmol) at 0ºC, the solution was stirred overnight at room temperature. The reaction mixture was processed by removing the precipitate via filtration. The solvent was removed under reduced pressure and the crystalline residue recrystallized from isopropanol to yield the N-hydroxyl-succinimide esters (315.3 mg, 1.069 mmol, 21.2 %).

**Peptide Conjugates.** BP-$PEP_{Co}$ was synthesized and purified using established methods.[140] HYPTLPLGSSTY (0.9 mg, $6.74 \times 10^{-7}$ mol) was dissolved in 60 μL DMF. After addition of 4-phenylbenzoic N-hydroxyl-succinimide ester (0.6 mg, $2.03 \times 10^{-6}$ mol) in 60μL DMF and 1 μL $Et_3N$ under stirring, the solution was stirred at room temperature for 12 hours to yield product. Pure BP-$PEP_{Co}$ was obtained by conducting reversed-phase HPLC eluting with a linear gradient of 0.05% formic acid in $CH_3CN$ and 0.1% formic acid in water (5/95 to 95/5 over 30 min). The molecular weight for BP-$PEP_{Co}$ was confirmed by MALDI-TOF mass spectrometry. Concentration of the peptide was determined spectrophotometrically in water/acetonitrile (1:1) using the molar extinction coefficient of tyrosine (1280 $M^{-1}cm^{-1}$) at 280 nm. Concentration of the peptide conjugate was determined spectrophotometrically in water/acetonitrile (1:1) using the combined molar extinction coefficient of tyrosine (1280 $M^{-1}cm^{-1}$) and 4-phenylbenzoic N-hydroxyl-succinimide ester (26679 $M^{-1}cm^{-1}$) at 280 nm.

### 5.4.3 Preparation of CoPt nanospherical structures

Lyophilized BP-$PEP_{Co}$ (~$3.10 \times 10^{-8}$ mol) was completely dissolved in 250 μL 0.1 M HEPES buffer in a plastic vial. After 1 day, 2 μL of freshly prepared 0.1M cobalt acetate [$Co(CH_3COO)_2$] aqueous solution was added to the above clear peptide-HEPES solution. The

above mixture was vortexed for a few seconds and then left undisturbed at room temperature for 4 hours. Thereafter, 5 μL of a 1.0M $NaBH_4$ solution was added. After ~7-8 seconds, the solution turns slightly black; at this point, 2 μL of 0.1M ammonium tetrachloroplatinate [$(NH_3)_2(PtCl_4)$] aqueous solution was added to the reaction. Spherical nanoparticle superstructures were observed as product after ~30 minutes.

**NOTE**: Large CoPt nanoparticle superstructures were prepared in a similar fashion, except the amount of BP-$PEP_{Co}$ was halved (~$1.55\times10^{-8}$ mol).

### 5.4.4 Preparation of CoPt nanoparticles

Lyophilized $PEP_{Co}$ (~$3.10\times10^{-8}$ mol) was completely dissolved in 250 μL 0.1 M HEPES buffer in a plastic vial. After 1 day, 2 μL of freshly prepared 0.1M cobalt acetate [$Co(CH_3COO)_2$] aqueous solution was added to the above clear peptide-HEPES solution. The above mixture was vortexed for a few seconds and then left undisturbed at room temperature for 4 hours. Thereafter, 5 μL of a 1.0M $NaBH_4$ solution was added. After ~7-8 seconds, 2 μL of 0.1M ammonium tetrachloroplatinate [$(NH_3)_2(PtCl_4)$] aqueous solution was added to the reaction. Individual nanoparticles were observed as product after ~30 minutes.

### 5.4.5 Preparation of hollow CoPt nanospheres (in absence of BP-$PEP_{Co}$)

2 μL of freshly prepared 0.1M cobalt acetate [$Co(CH_3COO)_2$] aqueous solution was added to 250 μL 0.1 M HEPES buffer in a plastic vial. The above mixture was vortexed for a few seconds and then left undisturbed at room temperature for 4 hours. Thereafter, 5 μL of a 1.0M $NaBH_4$ solution was added. The solution turns black immediately; at this point, 2 μL of 0.1M

ammonium tetrachloroplatinate [$(NH_3)_2(PtCl_4)$] aqueous solution was added to the reaction. Hollow nanospheres were observed as product after ~30 minutes.

### 5.4.6 Electrocatalysis experiments

Cyclic voltammetry was used to characterize the electrocatalytic properties of the CoPt nanoparticle superstructures by oxidizing methanol in an aqueous solution of $H_2SO_4$ (0.5 M) and methanol (0.6 M). The measurement was performed in a standard three electrode electrochemical cell with a CHI 618B potentiostat. A Pt wire and a Ag/AgCl electrode was used as the counter electrode and the reference electrode, respectively. The working electrode (6 mm diameter) was a glassy carbon disk with a 3 mm diameter, polished with $Al_2O_3$ paste and washed ultrasonically in water. The scan rate was 0.05 V/s.

As-synthesized CoPt nanoparticle superstructures were centrifuged (3000 rpm for 1 minute), and then the supernatant was removed. The pellet of product was air-dried for 1 hour. Then, 50 μL of MeOH was added to the air-dried pellet of product. This mixture was sonicated for 5 seconds. 5 μl of the CoPt nanoparticle superstructure/MeOH mixture was drop-cast onto a glassy carbon disk working electrode and dried in air.

To determine the amount of superstructures loaded onto the electrode surface, we prepared six CoPt nanoparticle superstructures/MeOH mixtures (50 L) in an identical fashion as above. These samples were air-dried and massed. The average mass of the samples was 74.6 ± 9.5 μg. Based on this calculation, we estimate that the electrode loading was ~7.5 μg.

The loadings of CoPt nanoparticles were determined in a similar fashion. The average mass of the samples was 65.4 ± 5.8 μg. In order to keep the same loading as CoPt nanoparticle superstructures, 44 μL of MeOH was added to the air-dried pellet of CoPt nanoparticles. This

mixture was sonicated for 5 seconds. 5 μL of the CoPt nanoparticles/MeOH mixture was drop-cast onto a glassy carbon disk working electrode and dried in air.

### 5.4.7 XRD measurement

The XRD measurement was conducted on a Bruker X8 Prospector Ultra diffractometer equipped with an Apex II CCD detector and an I*μ*S micro-focus CuK\α X-ray source (λ =0.154178 nm). Specifically, as-synthesized CoPt nanoparticle superstructures were centrifuged (3000 rpm for 2 minutes), most of the supernatant was removed to leave behind a wet pellet of product. 5μL of the pellet was added into a glass capillary tube (0.4 mm O.D.Hampton research, glass 50). The capillary tube was then flame sealed and mounted onto XRD instrument. A 60 seconds rotation frame was collected and integrated to give the powder X-ray diffraction pattern.

# 6.0 SUMMARY OF RESULTS

The work presented in this dissertation focused on developing peptide-based methods to assemble nanoparticles into nanoparticle superstructures with various shapes, compositions, and physical properties.

Fundamental insights into the mechanism of peptide-directed assembly of gold nanoparticle superstructures were developed and these insights were used to improve the yield of gold nanoparticle double helices. With a route for preparing larger quantities of the double helices in hand, we were able to perform CD studies to investigate the chirooptical properties of these unique superstructures. By coupling theory with experiment, we were able to explain and predict the chirooptical behaviour.

Nanoparticle superstructures with various topological shapes can be widely used in numerous disciplines. In Chapter 4, we explored the feasibility of assembling 3-D nanoparticle superstructures via this newly developed methodology. We demonstrated that small modifications to gold-binding peptide conjugates dramatically impact the final topology of nanoparticle superstructures. Transmission electron microscopy (TEM) and electron tomography revealed that the superstructures are uniform and consist of monodisperse gold nanoparticles arranged into a spherical monolayer shell. These hollow gold nanospherical superstructures are potential useful in drug delivery and thermal therapy.

Lastly, another important criterion to assess a nanoparticle-assembly methodology is diverse compositional scope. Chapter 5 presented new cobalt-binding peptides terminated with biphenyl tails, which were used to direct the synthesis and assembly of hollow spherical superstructures consisting of CoPt nanoparticles. These magnetically separable nanoparticle superstructures exhibit electrocatalytic activity for methanol oxidation.

# APPENDIX

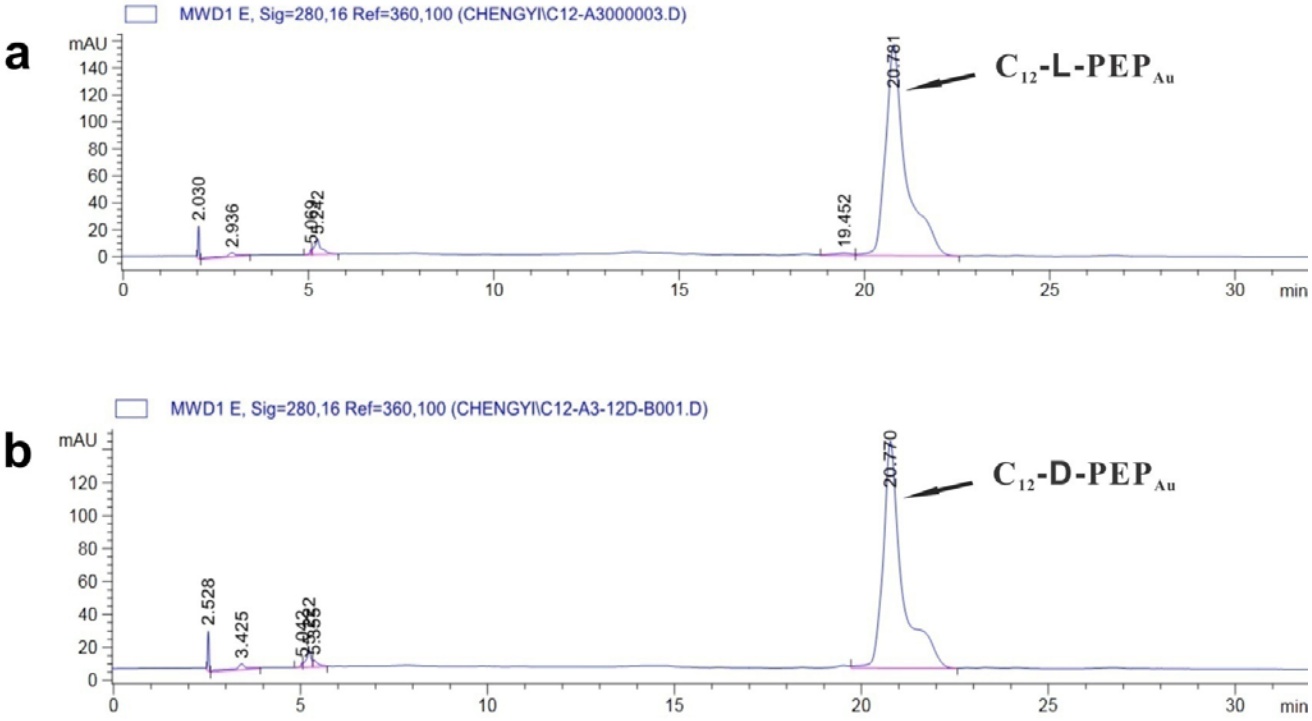


**Figure A1**.(a) Reverse-phase HPLC chart for the coupling reaction of (L)-AYSSGAPPMPPF with dodecanoic N-hydroxyl-succinimide ester. (b)Reverse-phase HPLC chart for the coupling reaction of (D)-AYSSGAPPMPPF with dodecanoic N-hydroxyl-succinimide ester.

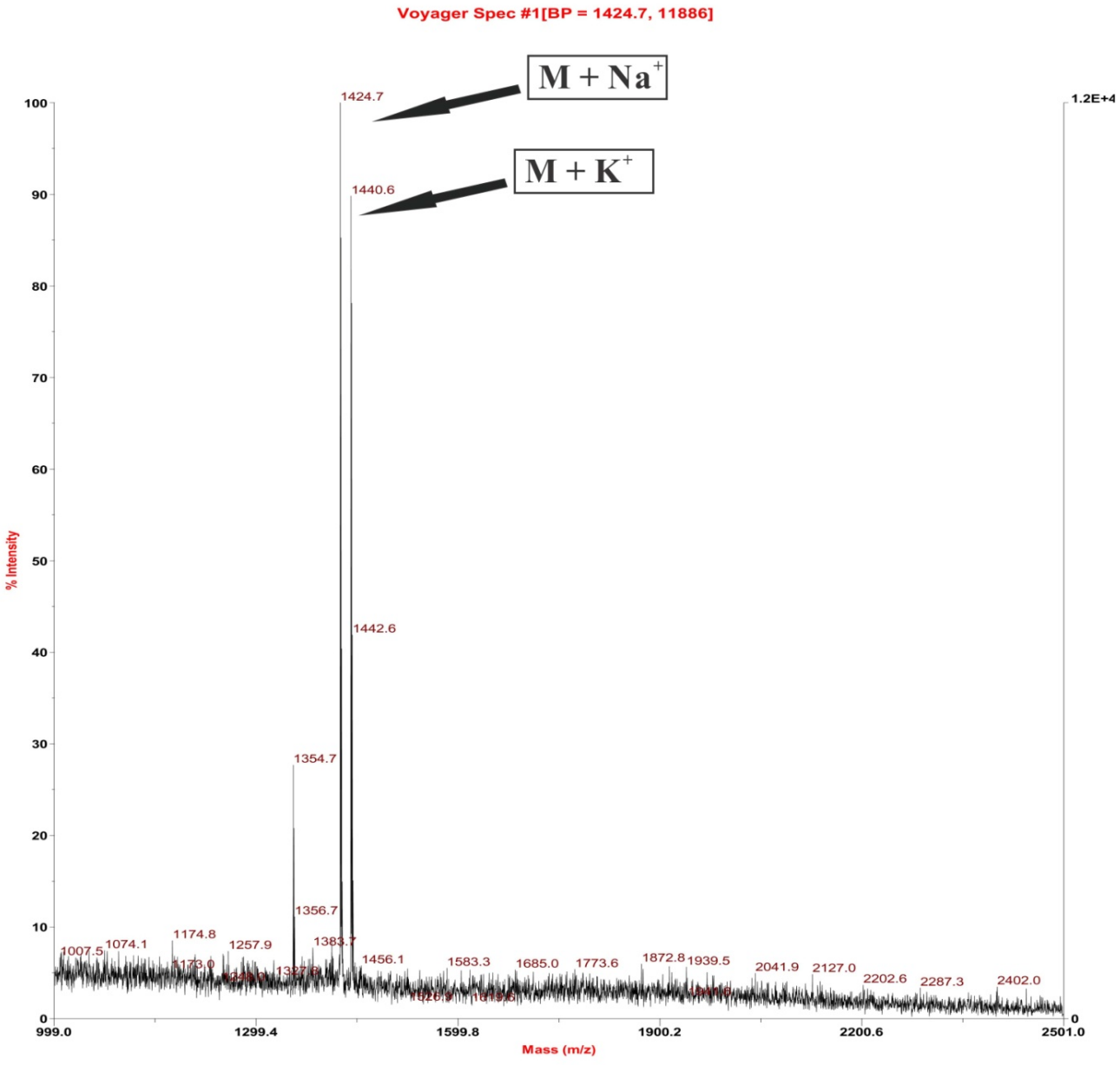


**Figure A2**. MALDI-TOF mass spectrum of purified $C_{12}$-L-$PEP_{Au}$.The molar mass of $C_{12}$-L-$PEP_{Au}$ is 1403 g/mol. [$C_{12}$-L-$PEP_{Au}$ + $Na^+$] = 1424.7 g/ mol and [$C_{12}$-L-$PEP_{Au}$ + $K^+$] =1440.6 g/mol.

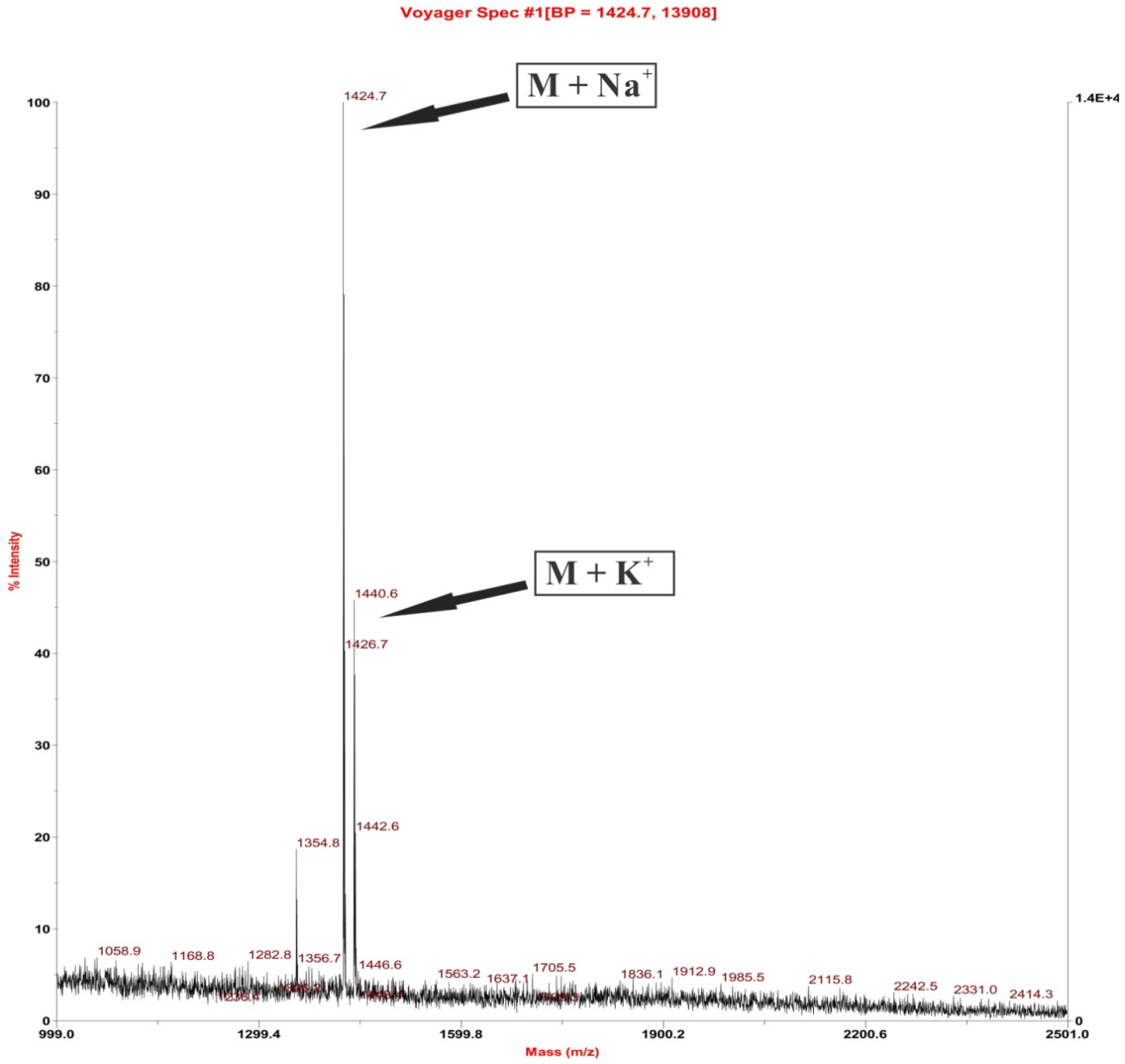


**Figure A3.** MALDI-TOF mass spectrum of purified $C_{12}$-D-$PEP_{Au}$.The molar mass of $C_{12}$-D-$PEP_{Au}$ is 1403 g/mol. [$C_{12}$-D-$PEP_{Au}$ + $Na^+$] = 1424.7 g/ mol and [$C_{12}$-D-$PEP_{Au}$ + $K^+$] =1440.6 g/mol.

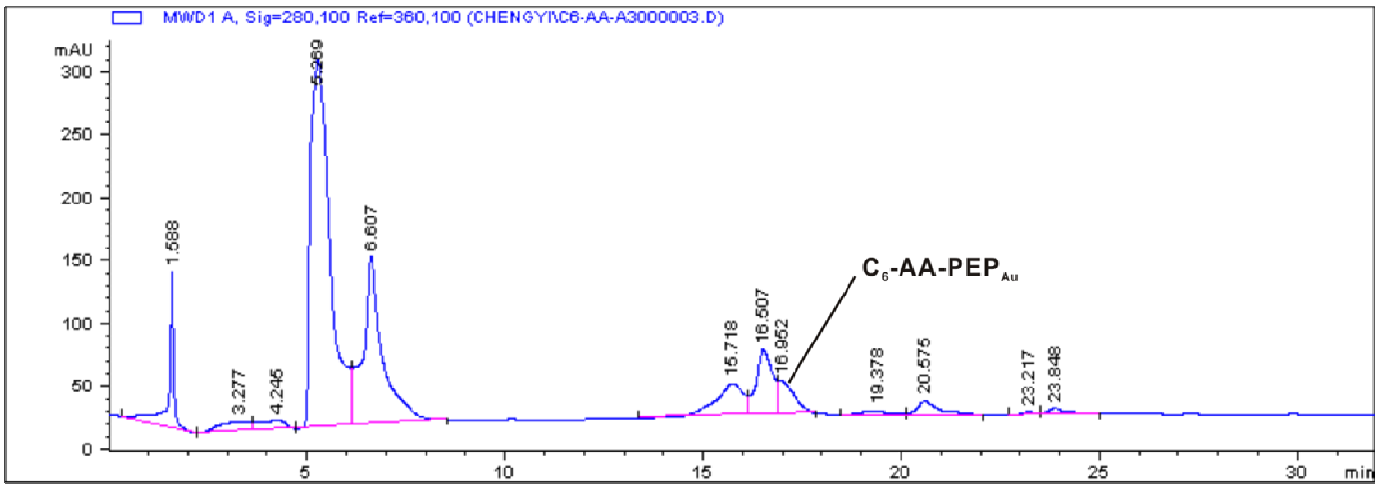


**Figure A4**. The reverse-phase HPLC chart for the coupling reaction of AAAYSSGAPPMPPF with caproic N-hydroxyl-succinimide ester.

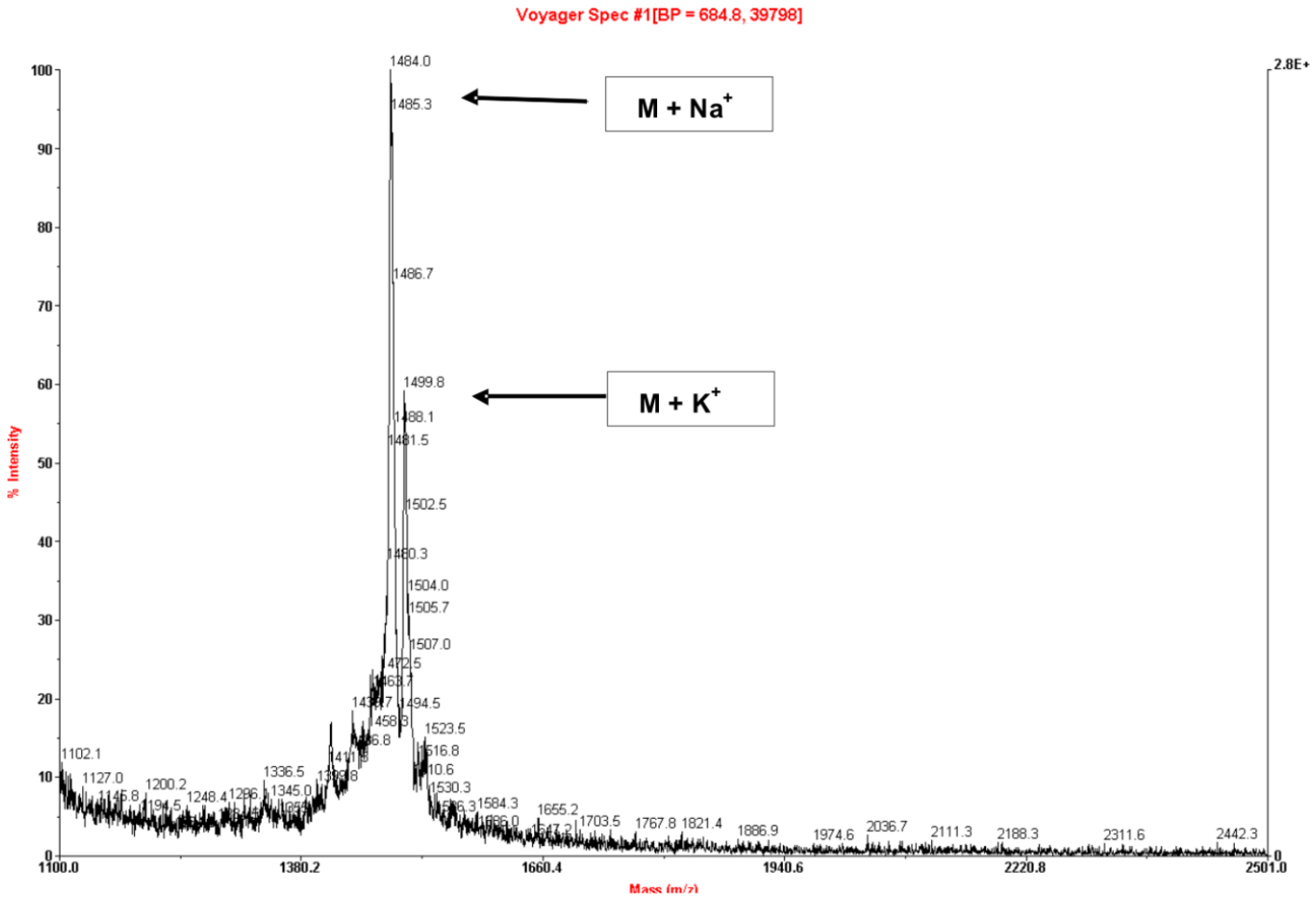


**Figure A5**. MALDI-TOF mass spectrum of purified $C_6$-AA-$PEP_{Au}$.

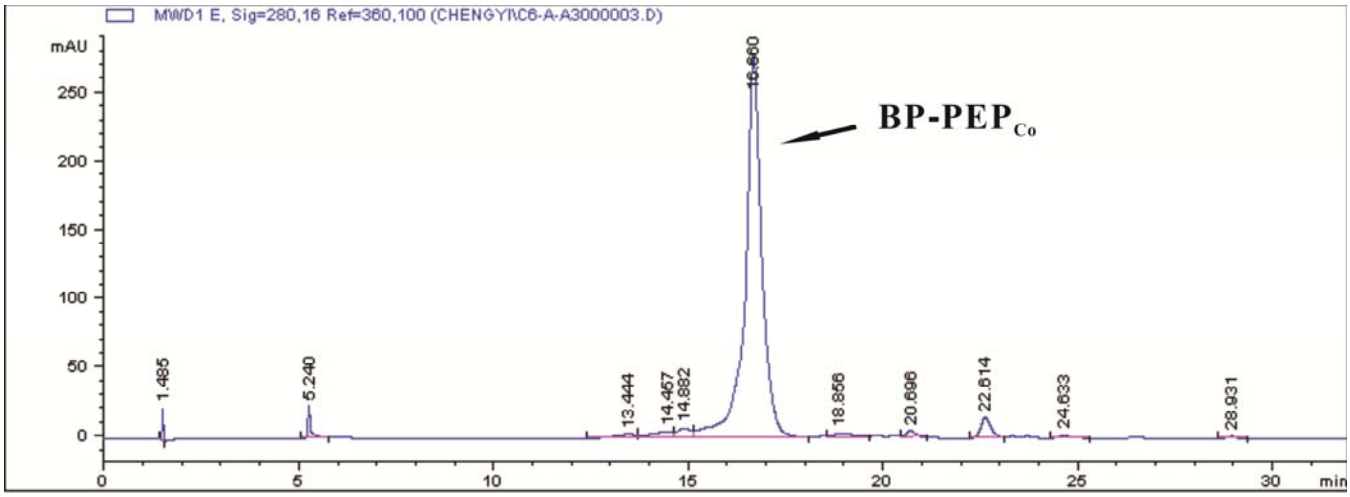


**Figure A6**. The reverse-phase HPLC chart for the coupling reaction of HYPTLPLGSSTY with 4-phenylbenzoic N-hydroxyl-succinimide ester.

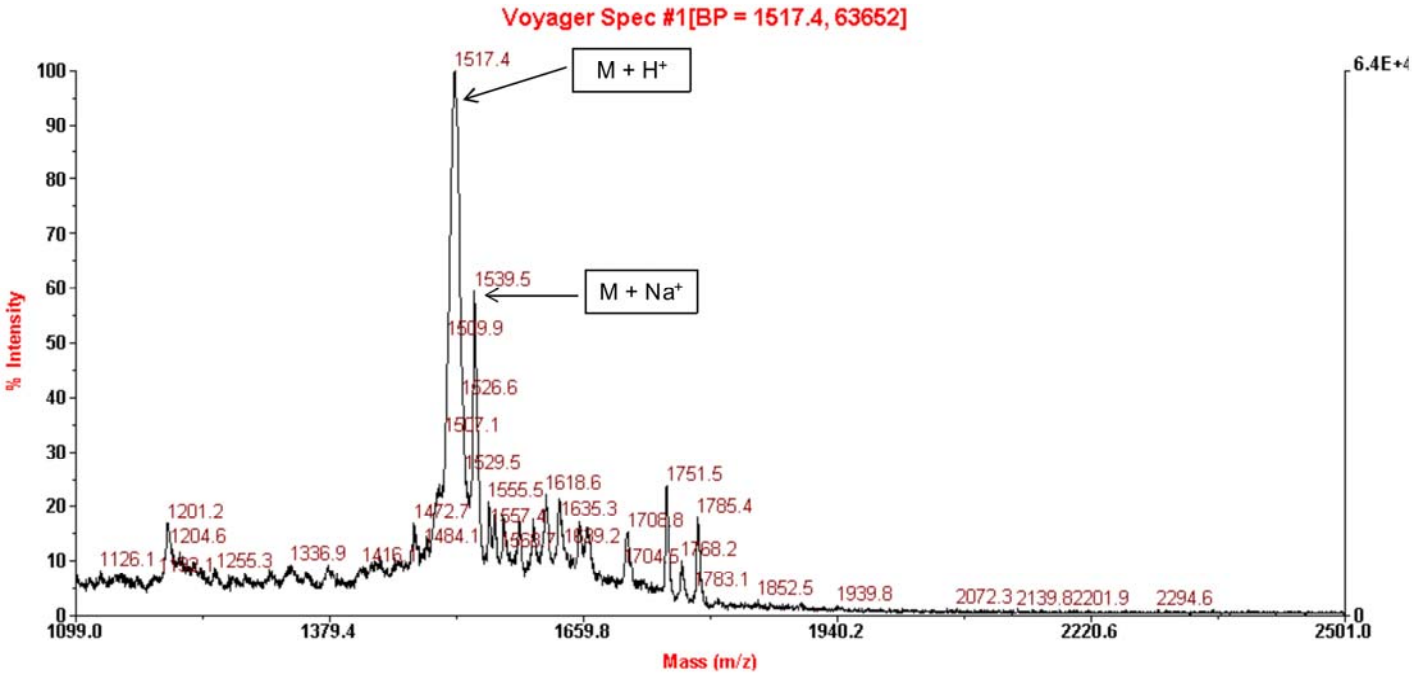


**Figure A7.** MALDI-TOF mass spectrum of purified BP-$PEP_{Co}$. The molar mass of BP-$PEP_{Co}$ is 1517 g/mol. [BP-$PEP_{Co}$ + $H^+$] = 1517.4 g/ mol and [BP-$PEP_{Co}$ + $Na^+$] =1539.5 g/mol.

## BIBLIOGRAPHY


(1) Faraday, M. *Philosophical Transactions of the Royal Society of London* **1857**, *147*, 145.

(2) Daniel, M.-C.; Astruc, D. *Chemical Reviews* **2003**, *104*, 293.

(3) Ghosh, S. K.; Pal, T. *Chemical Reviews* **2007**, *107*, 4797.

(4) Ozbay, E. *Science* **2006**, *311*, 189.

(5) Tang, Z.; Wang, Y.; Podsiadlo, P.; Kotov, N. A. *Advanced Materials* **2006**, *18*, 3203.

(6) Koole, R.; Liljeroth, P.; de Mello Doneg, C.; Vanmaekelbergh, D.; Meijerink, A. *Journal of the American Chemical Society* **2006**, *128*, 10436.

(7) Crooker, S. A.; Hollingsworth, J. A.; Tretiak, S.; Klimov, V. I. *Physical Review Letters* **2002**, *89*, 186802.

(8) Lisiecki, I.; Parker, D.; Salzemann, C.; Pileni, M. P. *Chemistry of Materials* **2007**, *19*, 4030.

(9) Lalatonne, Y.; Motte, L.; Russier, V.; Ngo, A. T.; Bonville, P.; Pileni, M. P. *The Journal of Physical Chemistry B* **2004**, *108*, 1848.

(10) Stewart, M. E.; Anderton, C. R.; Thompson, L. B.; Maria, J.; Gray, S. K.; Rogers, J. A.; Nuzzo, R. G. *Chemical Reviews* **2008**, *108*, 494.

(11) Medintz, I. L.; Uyeda, H. T.; Goldman, E. R.; Mattoussi, H. *Nat Mater* **2005**, *4*, 435.

(12) Tong, L.; Wei, Q.; Wei, A.; Cheng, J.-X. *Photochemistry and Photobiology* **2009**, *85*, 21.

(13) Xia, Y.; Xiong, Y.; Lim, B.; Skrabalak, S. E. *Angewandte Chemie* **2009**, *121*, 62.

(14) Burda, C.; Chen, X.; Narayanan, R.; El-Sayed, M. A. *Chemical Reviews* **2005**, *105*, 1025.

(15) Halas, N. J.; Lal, S.; Chang, W.-S.; Link, S.; Nordlander, P. *Chemical Reviews* **2011**, *111*, 3913.

(16) Dusemund, B.; Hoffmann, A.; Salzmann, T.; Kreibig, U.; Schmid, G. *Z Phys D - Atoms, Molecules and Clusters* **1991**, *20*, 305.

(17) Mirkin, C. A.; Letsinger, R. L.; Mucic, R. C.; Storhoff, J. J. *Nature* **1996**, *382*, 607.

(18) Elghanian, R.; Storhoff, J. J.; Mucic, R. C.; Letsinger, R. L.; Mirkin, C. A. *Science* **1997**, *277*, 1078.

(19) Charrier, A.; Candoni, N.; Thibaudau, F. *The Journal of Physical Chemistry B* **2006**, *110*, 12896.

(20) He, J.; Huang, X.; Li, Y.-C.; Liu, Y.; Babu, T.; Aronova, M. A.; Wang, S.; Lu, Z.; Chen, X.; Nie, Z. *Journal of the American Chemical Society* **2013**, *135*, 7974.

(21) Abu-Shumays, A.; Duffield, J. J. *Analytical Chemistry* **1966**, *38*, 29A.

(22) Greenfield, N. J. *Nat. Protocols* **2007**, *1*, 2876.

(23) Purdie, N.; Swallows, K. A. *Analytical Chemistry* **1989**, *61*, 77A.

(24) Gansel, J. K.; Thiel, M.; Rill, M. S.; Decker, M.; Bade, K.; Saile, V.; von Freymann, G.; Linden, S.; Wegener, M. *Science* **2009**, *325*, 1513.

(25) Kuzyk, A.; Schreiber, R.; Fan, Z.; Pardatscher, G.; Roller, E.-M.; Hogele, A.; Simmel, F. C.; Govorov, A. O.; Liedl, T. *Nature* **2012**, *483*, 311.

(26) Guerrero-Martínez, A.; Auguié, B.; Alonso-Gómez, J. L.; Džolić, Z.; Gómez-Graña, S.; Žinić, M.; Cid, M. M.; Liz-Marzán, L. M. *Angewandte Chemie International Edition* **2011**, *50*, 5499.

(27) Song, H. M.; Anjum, D. H.; Sougrat, R.; Hedhili, M. N.; Khashab, N. M. *Journal of Materials Chemistry* **2012**, *22*, 25003.

(28) Maiyalagan, T.; Alaje, T. O.; Scott, K. *The Journal of Physical Chemistry C* **2011**, *116*, 2630.

(29) Hofstead-Duffy, A. M.; Chen, D.-J.; Sun, S.-G.; Tong, Y. J. *Journal of Materials Chemistry* **2012**, *22*, 5205.

(30) Li, W. S.; Tian, L. P.; Huang, Q. M.; Li, H.; Chen, H. Y.; Lian, X. P. *Journal of Power Sources* **2002**, *104*, 281.

(31) Liang, H.-P.; Zhang, H.-M.; Hu, J.-S.; Guo, Y.-G.; Wan, L.-J.; Bai, C.-L. *Angewandte Chemie International Edition* **2004**, *43*, 1540.

(32) Gates, B. D.; Xu, Q.; Stewart, M.; Ryan, D.; Willson, C. G.; Whitesides, G. M. *Chemical Reviews* **2005**, *105*, 1171.

(33) Gratton, S. E. A.; Williams, S. S.; Napier, M. E.; Pohlhaus, P. D.; Zhou, Z.; Wiles, K. B.; Maynor, B. W.; Shen, C.; Olafsen, T.; Samulski, E. T.; DeSimone, J. M. *Accounts of Chemical Research* **2008**, *41*, 1685.

(34) Kinge, S.; Crego-Calama, M.; Reinhoudt, D. N. *ChemPhysChem* **2008**, *9*, 20.

(35) Shenhar, R.; Rotello, V. M. *Accounts of Chemical Research* **2003**, *36*, 549.

(36) Lu, W.; Lieber, C. M. *Nat Mater* **2007**, *6*, 841.

(37) Stearns, L. A.; Chhabra, R.; Sharma, J.; Liu, Y.; Petuskey, W. T.; Yan, H.; Chaput, J. C. *Angewandte Chemie International Edition* **2009**, *48*, 8494.

(38) Tseng, A. A.; Notargiacomo, A.; Chen, T. P. *Journal of Vacuum Science & Technology B: Microelectronics and Nanometer Structures* **2005**, *23*, 877.

(39) Bishop, K. J. M.; Wilmer, C. E.; Soh, S.; Grzybowski, B. A. *Small* **2009**, *5*, 1600.

(40) Tao, A. R.; Huang, J.; Yang, P. *Accounts of Chemical Research* **2008**, *41*, 1662.

(41) Tao, A.; Sinsermsuksakul, P.; Yang, P. *Nat Nano* **2007**, *2*, 435.

(42) Volinsky, R.; Jelinek, R. *Angewandte Chemie International Edition* **2009**, *48*, 4540.

(43) Shevchenko, E. V.; Talapin, D. V.; Kotov, N. A.; O'Brien, S.; Murray, C. B. *Nature* **2006**, *439*, 55.

(44) Courty, A.; Mermet, A.; Albouy, P. A.; Duval, E.; Pileni, M. P. *Nat Mater* **2005**, *4*, 395.

(45) Cheng, W.; Campolongo, M. J.; Cha, J. J.; Tan, S. J.; Umbach, C. C.; Muller, D. A.; Luo, D. *Nat Mater* **2009**, *8*, 519.

(46) Lin, Y.; Skaff, H.; Emrick, T.; Dinsmore, A. D.; Russell, T. P. *Science* **2003**, *299*, 226.

(47) Kalsin, A. M.; Fialkowski, M.; Paszewski, M.; Smoukov, S. K.; Bishop, K. J. M.; Grzybowski, B. A. *Science* **2006**, *312*, 420.

(48) Jones, M. R.; Mirkin, C. A. *Angewandte Chemie International Edition* **2013**, *52*, 2886.

(49) Auyeung, E.; Macfarlane, R. J.; Choi, C. H. J.; Cutler, J. I.; Mirkin, C. A. *Advanced Materials* **2012**, *24*, 5181.

(50) Correa-Duarte, M. A.; Pérez-Juste, J.; Sánchez-Iglesias, A.; Giersig, M.; Liz-Marzán, L. M. *Angewandte Chemie International Edition* **2005**, *44*, 4375.

(51) Kim, Y.-H.; Nedeljkovi, J. M.; Ahrenkiel, S. P.; Gilbert, K. E. H.; Alleman, J. L.; Zhang, S. B.; Mii, O. I.; Nozik, A. J.; Heben, M. J. *The Journal of Physical Chemistry B* **2006**, *110*, 25153.

(52) Jiang, K.; Eitan, A.; Schadler, L. S.; Ajayan, P. M.; Siegel, R. W.; Grobert, N.; Mayne, M.; Reyes-Reyes, M.; Terrones, H.; Terrones, M. *Nano Letters* **2003**, *3*, 275.

(53) Wang, H.; Lin, W.; Fritz, K. P.; Scholes, G. D.; Winnik, M. A.; Manners, I. *Journal of the American Chemical Society* **2007**, *129*, 12924.

(54) Dujardin, E.; Peet, C.; Stubbs, G.; Culver, J. N.; Mann, S. *Nano Letters* **2003**, *3*, 413.

(55) Ryadnov, M. G.; Woolfson, D. N. *Journal of the American Chemical Society* **2004**, *126*, 7454.

(56) Warner, M. G.; Hutchison, J. E. *Nat Mater* **2003**, *2*, 272.

(57) Artemyev, M.; Kisiel, D.; Abmiotko, S.; Antipina, M. N.; Khomutov, G. B.; Kislov, V. V.; Rakhnyanskaya, A. A. *Journal of the American Chemical Society* **2004**, *126*, 10594.

(58) Zhang, C.-L.; Lv, K.-P.; Cong, H.-P.; Yu, S.-H. *Small* **2012**, *8*, 648.

(59) Djalali, R.; Chen, Y.-f.; Matsui, H. *Journal of the American Chemical Society* **2002**, *124*, 13660.

(60) Huang, J.; Kim, F.; Tao, A. R.; Connor, S.; Yang, P. *Nat Mater* **2005**, *4*, 896.

(61) Dong, L.; Hollis, T.; Connolly, B. A.; Wright, N. G.; Horrocks, B. R.; Houlton, A. *Advanced Materials* **2007**, *19*, 1748.

(62) Dickerson, M. B.; Sandhage, K. H.; Naik, R. R. *Chemical Reviews* **2008**, *108*, 4935.

(63) Shin, H.; Jo, S.; Mikos, A. G. *Biomaterials* **2003**, *24*, 4353.

(64) Sarikaya, M.; Tamerler, C.; Jen, A. K. Y.; Schulten, K.; Baneyx, F. *Nat Mater* **2003**, *2*, 577.

(65) Slocik, J. M.; Stone, M. O.; Naik, R. R. *Small* **2005**, *1*, 1048.

(66) Chen, C.-L.; Zhang, P.; Rosi, N. L. *Journal of the American Chemical Society* **2008**, *130*, 13555.

(67) Naik, R. R.; Stringer, S. J.; Agarwal, G.; Jones, S. E.; Stone, M. O. *Nat Mater* **2002**, *1*, 169.

(68) Lee, S.-W.; Mao, C.; Flynn, C. E.; Belcher, A. M. *Science* **2002**, *296*, 892.

(69) Banerjee, I. A.; Yu, L.; Matsui, H. *Proceedings of the National Academy of Sciences of the United States of America* **2003**, *100*, 14678.

(70) Yu, L.; Banerjee, I. A.; Shima, M.; Rajan, K.; Matsui, H. *Advanced Materials* **2004**, *16*, 709.

(71) Reiss, B. D.; Mao, C.; Solis, D. J.; Ryan, K. S.; Thomson, T.; Belcher, A. M. *Nano Letters* **2004**, *4*, 1127.

(72) Peelle, B. R.; Krauland, E. M.; Wittrup, K. D.; Belcher, A. M. *Acta Biomaterialia* **2005**, *1*, 145.

(73) Sewell, S. L.; Wright, D. W. *Chemistry of Materials* **2006**, *18*, 3108.

(74) Lee, J.-Y.; Choo, J.-E.; Choi, Y.-S.; Park, J.-B.; Min, D.-S.; Lee, S.-J.; Rhyu, H. K.; Jo, I.-H.; Chung, C.-P.; Park, Y.-J. *Biomaterials* **2007**, *28*, 4257.

(75) Hamley, I. W. *Angewandte Chemie* **2007**, *119*, 8274.

(76) Ulijn, R. V.; Smith, A. M. *Chemical Society Reviews* **2008**, *37*, 664.

(77) Lutolf, M. P.; Hubbell, J. A. *Nat Biotech* **2005**, *23*, 47.

(78) Kokkoli, E.; Mardilovich, A.; Wedekind, A.; Rexeisen, E. L.; Garg, A.; Craig, J. A. *Soft Matter* **2006**, *2*, 1015.

(79) Lim, Y.-b.; Moon, K.-S.; Lee, M. *Chemical Society Reviews* **2009**, *38*, 925.

(80) Silva, G. A.; Czeisler, C.; Niece, K. L.; Beniash, E.; Harrington, D. A.; Kessler, J. A.; Stupp, S. I. *Science* **2004**, *303*, 1352.

(81) Niece, K. L.; Hartgerink, J. D.; Donners, J. J. J. M.; Stupp, S. I. *Journal of the American Chemical Society* **2003**, *125*, 7146.

(82) Slocik, J. M.; Zabinski, J. S.; Phillips, D. M.; Naik, R. R. *Small* **2008**, *4*, 548.

(83) Habib, A.; Tabata, M.; Wu, Y. G. *Bulletin of the Chemical Society of Japan* **2005**, *78*, 262.

(84) Xie, J.; Lee, J. Y.; Wang, D. I. C. *Chemistry of Materials* **2007**, *19*, 2823.

(85) Nie, Z.; Petukhova, A.; Kumacheva, E. *Nat Nano* **2010**, *5*, 15.

(86) Hentschel, M.; Saliba, M.; Vogelgesang, R.; Giessen, H.; Alivisatos, A. P.; Liu, N. *Nano Letters* **2010**, *10*, 2721.

(87) Coppage, R.; Slocik, J. M.; Sethi, M.; Pacardo, D. B.; Naik, R. R.; Knecht, M. R. *Angewandte Chemie International Edition* **2010**, *49*, 3767.

(88) Lal, S.; Link, S.; Halas, N. J. *Nat Photon* **2007**, *1*, 641.

(89) Vasquez, Y.; Sra, A. K.; Schaak, R. E. *Journal of the American Chemical Society* **2005**, *127*, 12504.

(90) Euliss, L. E.; Grancharov, S. G.; O'Brien, S.; Deming, T. J.; Stucky, G. D.; Murray, C. B.; Held, G. A. *Nano Letters* **2003**, *3*, 1489.

(91) Jin, Y.; Gao, X. *Journal of the American Chemical Society* **2009**, *131*, 17774.

(92) Chen, C.-L.; Rosi, N. L. *Angewandte Chemie International Edition* **2010**, *49*, 1924.

(93) Zelzer, M.; Ulijn, R. V. *Chemical Society Reviews* **2010**, *39*, 3351.

(94) Chang, W.-S.; Slaughter, L. S.; Khanal, B. P.; Manna, P.; Zubarev, E. R.; Link, S. *Nano Letters* **2009**, *9*, 1152.

(95) Oh, H. S.; Liu, S.; Jee, H.; Baev, A.; Swihart, M. T.; Prasad, P. N. *Journal of the American Chemical Society* **2010**, *132*, 17346.

(96) Shemer, G.; Krichevski, O.; Markovich, G.; Molotsky, T.; Lubitz, I.; Kotlyar, A. B. *Journal of the American Chemical Society* **2006**, *128*, 11006.

(97) Shen, X.; Song, C.; Wang, J.; Shi, D.; Wang, Z.; Liu, N.; Ding, B. *Journal of the American Chemical Society* **2011**, *134*, 146.

(98) Slocik, J. M.; Govorov, A. O.; Naik, R. R. *Nano Letters* **2011**, *11*, 701.

(99) Gao, X.; Matsui, H. *Advanced Materials* **2005**, *17*, 2037.

(100) Li, L.-s.; Stupp, S. I. *Angewandte Chemie International Edition* **2005**, *44*, 1833.

(101) Ostrov, N.; Gazit, E. *Angewandte Chemie International Edition* **2010**, *49*, 3018.

(102) Mafuné, F. *Chemical Physics Letters* **2004**, *397*, 133.

(103) Link, S.; El-Sayed, M. A. *The Journal of Physical Chemistry B* **1999**, *103*, 4212.

(104) Logunov, S. L.; Ahmadi, T. S.; El-Sayed, M. A.; Khoury, J. T.; Whetten, R. L. *The Journal of Physical Chemistry B* **1997**, *101*, 3713.

(105) Dulkeith, E.; Niedereichholz, T.; Klar, T. A.; Feldmann, J.; von Plessen, G.; Gittins, D. I.; Mayya, K. S.; Caruso, F. *Physical Review B* **2004**, *70*, 205424.

(106) Kuo, P.-L.; Chen, C.-C. *Langmuir* **2006**, *22*, 7902.

(107) Zakaria, H. M.; Shah, A.; Konieczny, M.; Hoffmann, J. A.; Nijdam, A. J.; Reeves, M. E. *Langmuir* **2013**.

(108) Kühnle, R. I.; Börner, H. G. *Angewandte Chemie International Edition* **2011**, *50*, 4499.

(109) Dublin, S. N.; Conticello, V. P. *Journal of the American Chemical Society* **2007**, *130*, 49.

(110) Lee, O.-S.; Stupp, S. I.; Schatz, G. C. *Journal of the American Chemical Society* **2011**, *133*, 3677.

(111) Zhang, X.; Chen, J.; Yang, P.; Yang, W. *Journal of Inorganic Biochemistry* **2005**, *99*, 1692.

(112) Tong, G. J.; Hsiao, S. C.; Carrico, Z. M.; Francis, M. B. *Journal of the American Chemical Society* **2009**, *131*, 11174.

(113) Velichko, Y. S.; Stupp, S. I.; de la Cruz, M. O. *The Journal of Physical Chemistry B* **2008**, *112*, 2326.

(114) Reboul, J.; Nugay, T.; Anik, N.; Cottet, H.; Ponsinet, V.; In, M.; Lacroix-Desmazes, P.; Gerardin, C. *Soft Matter* **2011**, *7*, 5836.

(115) Pandey, R. B.; Heinz, H.; Feng, J.; Farmer, B. L.; Slocik, J. M.; Drummy, L. F.; Naik, R. R. *Physical Chemistry Chemical Physics* **2009**, *11*, 1989.

(116) Yu, J.; Becker, M. L.; Carri, G. A. *Small* **2010**, *6*, 2242.

(117) Heinz, H.; Farmer, B. L.; Pandey, R. B.; Slocik, J. M.; Patnaik, S. S.; Pachter, R.; Naik, R. R. *Journal of the American Chemical Society* **2009**, *131*, 9704.

(118) Jana, N. R.; Gearheart, L.; Murphy, C. J. *Advanced Materials* **2001**, *13*, 1389.

(119) Ji, X.; Song, X.; Li, J.; Bai, Y.; Yang, W.; Peng, X. *Journal of the American Chemical Society* **2007**, *129*, 13939.

(120) Hu, J.; Wang, M.; Weier, H. U. G.; Frantz, P.; Kolbe, W.; Ogletree, D. F.; Salmeron, M. *Langmuir* **1996**, *12*, 1697.

(121) Pendry, J. B. *Science* **2004**, *306*, 1353.

(122) Zhu, Y.; Xu, L.; Ma, W.; Xu, Z.; Kuang, H.; Wang, L.; Xu, C. *Chemical Communications* **2012**, *48*, 11889.

(123) Fan, Z.; Govorov, A. O. *Nano Letters* **2010**, *10*, 2580.

(124) Govorov, A. O.; Gun'ko, Y. K.; Slocik, J. M.; Gerard, V. A.; Fan, Z.; Naik, R. R. *Journal of Materials Chemistry* **2011**, *21*, 16806.

(125) Tan, S. J.; Campolongo, M. J.; Luo, D.; Cheng, W. *Nat Nano* **2011**, *6*, 268.

(126) George, J.; Thomas, K. G. *Journal of the American Chemical Society* **2010**, *132*, 2502.

(127) Yan, W.; Xu, L.; Xu, C.; Ma, W.; Kuang, H.; Wang, L.; Kotov, N. A. *Journal of the American Chemical Society* **2012**, *134*, 15114.

(128) Fu, X.; Wang, Y.; Huang, L.; Sha, Y.; Gui, L.; Lai, L.; Tang, Y. *Advanced Materials* **2003**, *15*, 902.

(129) Mastroianni, A. J.; Claridge, S. A.; Alivisatos, A. P. *Journal of the American Chemical Society* **2009**, *131*, 8455.

(130) Sharma, J.; Chhabra, R.; Cheng, A.; Brownell, J.; Liu, Y.; Yan, H. *Science* **2009**, *323*, 112.

(131) Chen, W.; Bian, A.; Agarwal, A.; Liu, L.; Shen, H.; Wang, L.; Xu, C.; Kotov, N. A. *Nano Letters* **2009**, *9*, 2153.

(132) Guha, S.; Drew, M. G. B.; Banerjee, A. *Small* **2008**, *4*, 1993.

(133) Gerard, V. A.; Gun'ko, Y. K.; Defrancq, E.; Govorov, A. O. *Chemical Communications* **2011**, *47*, 7383.

(134) Wang, R.-Y.; Wang, H.; Wu, X.; Ji, Y.; Wang, P.; Qu, Y.; Chung, T.-S. *Soft Matter* **2011**, *7*, 8370.

(135) Qi, H.; Shopsowitz, K. E.; Hamad, W. Y.; MacLachlan, M. J. *Journal of the American Chemical Society* **2011**, *133*, 3728.

(136) Wang, Y.; Wang, Q.; Sun, H.; Zhang, W.; Chen, G.; Wang, Y.; Shen, X.; Han, Y.; Lu, X.; Chen, H. *Journal of the American Chemical Society* **2011**, *133*, 20060.

(137) Sone, E. D.; Zubarev, E. R.; Stupp, S. I. *Angewandte Chemie International Edition* **2002**, *41*, 1705.

(138) Yang, M.; Kotov, N. A. *Journal of Materials Chemistry* **2011**, *21*, 6775.

(139) Chen, C.-L.; Rosi, N. L. *Journal of the American Chemical Society* **2010**, *132*, 6902.

(140) Hwang, L.; Chen, C.-L.; Rosi, N. L. *Chemical Communications* **2011**, *47*, 185.

(141) Song, C.; Zhao, G.; Zhang, P.; Rosi, N. L. *Journal of the American Chemical Society* **2010**, *132*, 14033.

(142) Hwang, L.; Zhao, G.; Zhang, P.; Rosi, N. L. *Small* **2011**, *7*, 1939.

(143) Song, C.; Wang, Y.; Rosi, N. L. *Angewandte Chemie International Edition* **2013**, *52*, 3993.

(144) Link, S.; El-Sayed, M. A. *The Journal of Physical Chemistry B* **1999**, *103*, 8410.

(145) Fan, Z.; Govorov, A. O. *The Journal of Physical Chemistry C* **2011**, *115*, 13254.

(146) Draine, B. T.; Flatau, P. J. *J Opt Soc Am A* **1994**, *11*, 1491.

(147) Draine, B. T.; Flatau, P. J. *arXiv:1202.3424 [physics.comp-ph]* **2012**.

(148) Du, Q.; Faber, V.; Gunzburger, M. *SIAM Review* **1999**, *41*, 637.

(149) Hardin, D. P.; Saff, E. B. *Notices of the American Mathematical Society* **2004**, *51*, 1186.

(150) Renka, R. J. *Acm T Math Software* **1997**, *23*, 416.

(151) Saff, E. B.; Kuijlaars, A. B. J. *Mathematical Intelligencer* **1997**, *19*, 5.

(152) Brongersma, M. L.; Hartman, J. W.; Atwater, H. A. *Physical Review B* **2000**, *62*, 16356.

(153) Jain, P. K.; Huang, W. Y.; El-Sayed, M. A. *Nano Letters* **2007**, *7*, 2080.

(154) Pinchuk, A. O.; Schatz, G. C. *Materials Science and Engineering B-Advanced Functional Solid-State Materials* **2008**, *149*, 251.

(155) Zou, S. L.; Schatz, G. C. *Nanotechnology* **2006**, *17*, 2813.

(156) Arnold, M. D.; Blaber, M. G.; Ford, M. J.; Harris, N. *Optics Express* **2010**, *18*, 7528.

(157) Harris, N.; Arnold, M. D.; Blaber, M. G.; Ford, M. J. *J Phys Chem C* **2009**, *113*, 2784.

(158) Arnold, M. D.; Blaber, M. G. *Optics Express* **2009**, *17*, 3835.

(159) Kremer, J. R.; Mastronarde, D. N.; McIntosh, J. R. *Journal of Structural Biology* **1996**, *116*, 71.

(160) Pettersen, E. F.; Goddard, T. D.; Huang, C. C.; Couch, G. S.; Greenblatt, D. M.; Meng, E. C.; Ferrin, T. E. *Journal of Computational Chemistry* **2004**, *25*, 1605.

(161) Yang, W. H.; Schatz, G. C.; Van Duyne, R. P. *Discrete dipole approximation for calculating extinction and Raman intensities for small particles with arbitrary shapes*; AIP, 1995; Vol. 103.

(162) Gutkowicz-Krusin, D.; Draine, B. T. *arXiv:astro-ph* **2004**, *0403082v1*.

(163) Draine, B. T.; Goodman, J. *Astrophys J* **1993**, *405*, 685.

(164) Johnson, P. B.; Christy, R. W. *Phys Rev B* **1972**, *6*, 4370.

(165) Kreibig, U.; Fragstein, C. v. *Zeitschrift fur Physik A Hadrons and Nuclei* **1969**, *224*, 307.

(166) Brioude, A.; Jiang, X. C.; Pileni, M. P. *J. Phys. Chem. B* **2005**, *109*, 13138.

(167) Goodman, J. J.; Draine, B. T.; Flatau, P. J. *Opt. Lett.* **1991**, *16*, 1198.

(168) Kotov, N. A.; Stellacci, F. *Advanced Materials* **2008**, *20*, 4221.

(169) Nie, Z. H.; Petukhova, A.; Kumacheva, E. *Nature Nanotechnology* **2010**, *5*, 15.

(170) Chang, W. S.; Slaughter, L. S.; Khanal, B. P.; Manna, P.; Zubarev, E. R.; Link, S. *Nano Letters* **2009**, *9*, 1152.

(171) Chen, C. L.; Zhang, P. J.; Rosi, N. L. *J. Am. Chem. Soc.* **2008**, *130*, 13555.

(172) Chen, C. L.; Rosi, N. L. *J. Am. Chem. Soc.* **2010**, *132*, 6902.

(173) Chen, C. L.; Rosi, N. L. *Angew. Chem. Int. Ed.* **2010**, *49*, 1924.

(174) Caruso, F.; Caruso, R. A.; Mohwald, H. *Science* **1998**, *282*, 1111.

(175) Wong, M. S.; Cha, J. N.; Choi, K. S.; Deming, T. J.; Stucky, G. D. *Nano Letters* **2002**, *2*, 583.

(176) Park, S.; Lim, J. H.; Chung, S. W.; Mirkin, C. A. *Science* **2004**, *303*, 348.

(177) Rana, R. K.; Murthy, V. S.; Yu, J.; Wong, M. S. *Advanced Materials* **2005**, *17*, 1145.

(178) Liu, B.; Zeng, H. C. *J. Am. Chem. Soc.* **2004**, *126*, 8124.

(179) Jin, Y. D.; Gao, X. H. *J. Am. Chem. Soc.* **2009**, *131*, 17774.

(180) Wu, G. H.; Milkhailovsky, A.; Khant, H. A.; Fu, C.; Chiu, W.; Zasadzinski, J. A. *J. Am. Chem. Soc.* **2008**, *130*, 8175.

(181) Habib, A.; Tabata, M.; Wu, Y. G. *Bull. Chem. Soc. Jpn.* **2005**, *78*, 262.

(182) Xie, J. P.; Lee, J. Y.; Wang, D. I. C. *Chem. Mater.* **2007**, *19*, 2823.

(183) Jahnke, E.; Lieberwirth, I.; Severin, N.; Rabe, J. P.; Frauenrath, H. *Angew. Chem. Int. Ed.* **2006**, *45*, 5383.

(184) Jones, M. R.; Osberg, K. D.; Macfarlane, R. J.; Langille, M. R.; Mirkin, C. A. *Chemical Reviews* **2011**, *111*, 3736.

(185) Mann, S. *Nat Mater* **2009**, *8*, 781.

(186) Ofir, Y.; Samanta, B.; Rotello, V. M. *Chemical Society Reviews* **2008**, *37*, 1814.

(187) Chen, G.; Xia, D.; Nie, Z.; Wang, Z.; Wang, L.; Zhang, L.; Zhang, J. *Chemistry of Materials* **2007**, *19*, 1840.

(188) Chinnasamy, C. N.; Jeyadevan, B.; Shinoda, K.; Tohji, K. *Journal of Applied Physics* **2003**, *93*, 7583.

(189) Meng, X.; Seton, H. C.; Lu, L. T.; Prior, I. A.; Thanh, N. T. K.; Song, B. *Nanoscale* **2011**, *3*, 977.

(190) Chen, G.; Xia, D.; Nie, Z.; Wang, Z.; Wang, L.; Zhang, L.; Zhang, J. *Chemistry of Materials* **2007**, *19*, 1840.

(191) Xu, Y.; Yuan, Y.; Ma, A.; Wu, X.; Liu, Y.; Zhang, B. *ChemPhysChem* **2012**, *13*, 2601.

(192) Holme, M. N.; Fedotenko, I. A.; Abegg, D.; Althaus, J.; Babel, L.; Favarger, F.; Reiter, R.; Tanasescu, R.; Zaffalon, P.-L.; Ziegler, A.; Muller, B.; Saxer, T.; Zumbuehl, A. *Nat Nano* **2012**, *7*, 536.

(193) Naik, R. R.; Jones, S. E.; Murray, C. J.; McAuliffe, J. C.; Vaia, R. A.; Stone, M. O. *Advanced Functional Materials* **2004**, *14*, 25.

(194) Zheng, F.; Alayoglu, S.; Guo, J.; Pushkarev, V.; Li, Y.; Glans, P.-A.; Chen, J.-l.; Somorjai, G. *Nano Letters* **2011**, *11*, 847.

(195) Zhai, Y.; Zhai, J.; Dong, S. *Chemical Communications* **2010**, *46*, 1500.

(196) Pacardo, D. B.; Sethi, M.; Jones, S. E.; Naik, R. R.; Knecht, M. R. *ACS Nano* **2009**, *3*, 1288.

(197) Stevens, P. D.; Fan, J.; Gardimalla, H. M. R.; Yen, M.; Gao, Y. *Organic Letters* **2005**, *7*, 2085.